

بِسْمِ اللَّهِ الرَّحْمَنِ الرَّحِيمِ

إِنَّ فِي خَلْقِ السَّمَوَاتِ وَالْأَرْضِ وَأَخْتِلَافِ اللَّيْلِ وَالنَّهَارِ
وَالْفُلْكِ الَّتِي تَجْرِي فِي الْبَحْرِ بِمَا يَنْفَعُ النَّاسَ وَمَا أَنْزَلَ اللَّهُ
مِنَ السَّمَاءِ مِنْ مَّاءٍ فَأَحْيَا بِهِ الْأَرْضَ بَعْدَ مَوْتِهَا وَبَثَّ فِيهَا
مِنْ كُلِّ دَابَّةٍ وَتَصْرِيفِ الرِّيْحِ وَالسَّحَابِ الْمُسَخَّرِينَ
السَّمَاءِ وَالْأَرْضِ لآيَاتٍ لِقَوْمٍ يَعْقِلُونَ ﴿١٦٤﴾ سُورَةُ الْبَقَرَةِ

164. Verily! In the creation of the heavens and the earth, and in the alternation of night and day, and the ships which sail through the sea with that which is of use to mankind, and the water (rain) which Allah sends down from the sky and makes the earth alive therewith after its death, and the moving (living) creatures of all kinds that He has scattered therein, and in the veering of winds and clouds which are held between the sky and the earth, are indeed Ayat (proofs, evidences, signs, etc.) for people of understanding. Qur'an (2:164)

الْمُرْتَانَ اللَّهُ يُرْجِي ﴿٤٣﴾

سَحَابًا ثُمَّ يُؤَلِّفُ بَيْنَهُ ثُمَّ يَجْعَلُهُ رُكَّامًا فَتَرَى الْوَدْقَ يَخْرُجُ مِنْ
خَلَلِهِ ۗ وَيُنَزِّلُ مِنَ السَّمَاءِ مِنْ جِبَالٍ فِيهَا مِنْ بَرَدٍ فَيُصِيبُ بِهِ مَنْ يَشَاءُ
وَيَصْرِفُهُ ۗ وَعَنْ مَنْ يَشَاءُ يَكَادُ سَنَا بَرْقِهِ ۗ يَذْهَبُ بِالْأَبْصَارِ ﴿٤٣﴾
سُورَةُ الْوَاوِ

43. See you not that Allah drives the clouds gently, then joins them together, then makes them into a heap of layers, and you see the rain comes forth from between them. And He sends down from the sky hail (like) mountains, (or there are in the heaven mountains of hail from where He sends down hail), and strike therewith whom He will, and averts it from whom He wills. The vivid flash of its (clouds) lightning nearly blinds the sight. [Tafsir At-Tabari]. Qur'an (24:43)

اللَّهُ الَّذِي يُرْسِلُ الرِّيحَ فَتُثِيرُ سَحَابًا فَيَبْسُطُهُ
 فِي السَّمَاءِ كَيْفَ يَشَاءُ وَيَجْعَلُهُ كِسْفًا فَنَرَى الْوَدْقَ يَخْرُجُ مِنْ
 خَلَلِهِ ۗ فَإِذَا أَصَابَ بِهِ ۗ مَنْ يَشَاءُ مِنْ عِبَادِهِ إِذَا هُمْ يَسْتَبْشِرُونَ

سُورَةُ الرُّومِ



48. Allah is He Who sends the winds, so they raise clouds, and spread them along the sky as He wills, and then break them into fragments, until you see rain drops come forth from their midst! Then when He has made them fall on whom of His slaves as He will, lo! they rejoice! Qur'an (30:48)

مَا مِنْ عَامٍ بِأَكْثَرَ مَطْرًا مِنْ عَامٍ وَلَكِنَّ اللَّهَ يُصَرِّفُهُ بَيْنَ خَلْقِهِ [حَيْثُ يَشَاءُ] . ثُمَّ قَرَأَ : وَلَقَدْ صَرَّفْنَا لَهُمْ لِيَذَكَّرُوا

الراوي: عبدالله بن عباس المحدث: الألباني - المصدر: السلسلة الصحيحة - الصفحة أو الرقم: ٢٤٦١
 خلاصة حكم المحدث: صحيح على شرط الشيخين

From Ibn Abbas who said, “No year has more rain than another, but Allâh distributes it between His Creation wherever He wishes.’ Then he recited, “*And we have distributed it amongst them, in order that they may remember [the Grace of Allah] ...*” *al-Albaani (Silsilah | 2461 | Saheeh)*

”I wanted to know the best of the life of one who holds today an undisputed sway over the hearts of millions of mankind.... I became more than ever convinced that it was not the sword that won a place for Islam in those days in the scheme of life. It was the rigid simplicity, the utter self--effacement of the Prophet the scrupulous regard for pledges, his intense devotion to his friends and followers, his intrepidity, his fearlessness, his absolute trust in God and in his own mission.” Mahatma Gandhi, statement published in 'Young India' 1924.

”My choice of Muhammad to lead the list of the worlds most influential persons may surprise some readers and may be questioned by others, but he was the only man in history who was supremely successful on both the secular and religious level. ...It is probable that the relative influence of Muhammad on Islam has been larger than the combined influence of Jesus Christ and St. Paul on Christianity.” Michael Hart, (1978) 'The 100, A Ranking of the Most Influential Persons In History,' New York

University of Alberta

Teleconnection, Modeling, Climate Anomalies Impact and
Forecasting of Rainfall and Streamflow of the Upper Blue Nile
River Basin

by

Mohamed Helmy Mahmoud Moustafa Elsanabary

A thesis submitted to the Faculty of Graduate Studies and Research in partial
fulfillment of the requirements for the degree of

Doctor of Philosophy

in

Water Resources Engineering

Department of Civil and Environmental Engineering

©Mohamed Helmy Mahmoud Moustafa Elsanabary
Fall 2012
Edmonton, Alberta

Permission is hereby granted to the University of Alberta Libraries to reproduce single copies of this thesis and to lend or sell such copies for private, scholarly or scientific research purposes only. Where the thesis is converted to, or otherwise made available in digital form, the University of Alberta will advise potential users of the thesis of these terms.

The author reserves all other publication and other rights in association with the copyright in the thesis and, except as herein before provided, neither the thesis nor any substantial portion thereof may be printed or otherwise reproduced in any material form whatsoever without the author's prior written permission.

To ...

Allah, the Most Merciful, the Most Compassionate,

Prophet Muhammad (Peace be upon him),

My beloved Mother,

My Father,

My brother Ayman,

My sincere wife, Doaa,

My beloved kids Mohamed, Yusuf, and Zaynab,

For all their love and generosity

Abstract

The Nile River, the primary water resource and the life artery for its downstream countries such as Egypt and Sudan, exhibits strong seasonal fluctuations. The Upper Blue Nile basin (UBNB), the most significant tributary of the Nile, contributes more than half of the Nile's streamflow. Prompted by a lack of knowledge on the nonstationarity of hydro-climatic processes in the Ethiopian Highlands (EH), this thesis employed the non-stationary techniques of Wavelet principal component analysis (WPCA) and coherence analysis to identify the spatial, temporal and frequency variability regimes of these hydro-climatic processes of UBNB.

A fully distributed, physically-based model, a modified version of the Interactions Soil-Biosphere-Atmosphere model of Météo France (MISBA), and a lumped, conceptual rainfall-runoff model, SAC-SMA of the US National Weather Service, was used to simulate the streamflow of UBNB. To study the potential hydrologic effect of climate anomalies on the UBNB, rainfall and temperature data observed when climate anomalies were active, were re-sampled and used to drive MISBA and SAC-SMA. The results provide useful information on the effects of global oceanic anomalies on the hydrology of UBNB.

An artificial neural network calibrated by a genetic algorithm (ANN-GA) model, was developed to forecast the seasonal rainfall of UBNB through teleconnection with selected oceanic sectors

of SST. Results show that seasonal rainfall predicted by the ANN-GA agrees well with the observed rainfall data of UBNB. The Valencia and Schaake model was used to disaggregate the forecasted seasonal rainfall to weekly rainfall, which was found to reasonably capture the UBNB observed weekly rainfall characteristics.

ANN-GA was also forced with seasonal oceanic SST to directly forecast seasonal streamflow which was then disaggregated to weekly streamflow. Results indicate that forecasts with up to four months lead time based on climate indices achieve reasonable skill (correlation of 0.66), while combining rainfall and SST as predictors achieved better results (correlation of 0.83).

Knowledge gained on teleconnecting the climate of UBNB to oceanic SST and the possible impact of climate anomalies on the streamflow of UBNB will be useful for the planning and management of its water resources, especially during the threat of impending droughts.

Preface

The Greek historian Herodotus wrote; “Egypt is the gift of the Nile”. The Nile is a continuous source of sustenance; it played the main role in the development of Egyptian civilization. Egypt is a dry country; therefore, water is the main factor in any social and economic development. The Egyptian Ministry of Water Resources and Irrigation (MWRI) plays a key-role in the development and management of the water system in the country. MWRI has established the Egyptian National Water Resources Plan - 2017 (NWRP) to upgrade the water policies and plans. NWRP depends on the integrated water resources principals which makes it as a national plan. For improving her water resources, Egypt has improved the deep underground water in the western desert and reaching 3.5 Billion m^3 per year. Some other resources can be developed such as rain harvesting, storm water collection, reduce ground water salinity. According to the fifth year of the five year plan (2002-2007), “by increasing the scholarships to highly ranked specialized universities in the new technologies”, Egypt could improve her water resources and create sustainable plans for the future.

This thesis has been written for water resources managers and decision makers at all levels of the management program, from leaders working directly with their department to regional leadership to professionals. Also, it provides guidance for developing the Nile Basin water resources in an equitable way to ensure security, prosperity, and peace for all the riparian countries.

The thesis covers the basics of water resources management. It will familiarize the reader with the Nile basin water resources, specifically the Upper Blue Nile River Basin (UBNB), and how they affected by the climate variability represented by the oceanic anomalies. The thesis will also touch on some of the hydrologic modeling using both physically-distributed vs.

lumped hydrologic models. This thesis represents the highest level of work and learning that has taken place over a period of almost six years (2006-2012). Early work proceeded with my “PhD program proposal” to the Department of Civil and Environmental Engineering, University of Alberta in 2005. As I developed ideas concurrently with my experience in irrigation projects that I gained during my Master degree and hydrological knowledge. A critical mass was reached when I finished my PhD courses at the University of Alberta, Fall 2007. When I was preparing my term paper at my office within the University of Alberta one morning in November 2007, I reached a conclusion that, if I want to study the hydrology of Nile River Basin and its water resources, then what I need is a substantial and ordered hydro-climate data set. It took a year to achieve, and it was with this data set, that this thesis began.

Dealing with such enormous basin was a tough decision. With lack of data and conflicts between the riparian countries sharing the basin, it was extremely difficult to find suitable temporal scale data for the basin. Using the wavelet analysis to study the spatial, temporal and frequency of the UBNB rainfall was a crucial part of the thesis. I have been working in collaboration with Dr. Davison Mwale in order to investigate the spatial temporal and frequency variability of the Ethiopian Highlands, where UBNB is located. To date this collaborative work has lead to the submission for publication of one paper. From the other chapters of the thesis, I am planning to submit three more papers. The task of preparing this thesis has been to produce from these activities a one piece of work, and one that I can call my property.

Mohamed Elsanabary

Edmonton, AB, June, 2012

Acknowledgements

I am greatly indebted first and foremost to Allah (swt) (God), the Almighty, Creator and Sustainer of the universe and to whom everything will return. I admit I have been totally impressed with three “*āyāt*” from the Quran and the one of Prophet Muhammad’s narrations, which deal with the phenomena of rain formation and the hydrologic cycle as signs from God to humanity. I ask Allah that he accept this tiny work, and it becomes beneficial to all mankind in this area and others, “*Āmīn*”. I would like to thank my supervisor Dr. Thian Yew Gan for his supervision, guidance and encouragement during this work. My sincere appreciation goes to the members of my examination committee: Dr. Mohamed Al-Hussein, Dr. Evan Davies, Dr. Paul Myers, Dr. Yang Liu, Dr. Marwan El-Rich, and Prof. D. J. (Dave) Sauchyn for their valuable comments and suggestions.

I gratefully acknowledge the Egyptian Ministry of Higher Education and Scientific Research, Egypt, for the financial support provided to this research work. I am grateful to the Student Financial Resources Centre, University of Alberta for providing some financial support. I would like to thank Dr. Declan Conway for provided me with El Diem station, Ethiopia, monthly streamflow. Dr. Davison Mwale introduced me to much of the guidance and feedbacks on the work in the thesis and offered his time to discuss the applications of Wavelet Analysis. Also, my special thanks go to the Research Support Group at the University of Alberta, specifically: Mr. Masao Fujinaga, Mr. Jon Johansson, Mr. Edmund Sumbar, and Ms. Denise Thornton of Computing and Network Services for their cheerful assistance in compiling the UNIX programs and *Matlab*[®] codes used in processing various data. Thanks are due to Mr. Perry Fedun for helping with the computing facilities in the Water Resources Engineering group.

The data from Digital Elevation Model were provided by USGS, Météo France provided the Ecoclimap land surface data set, and ECMWF provided the ERA-40 atmospheric re-analysis dataset. Without these datasets, none of this work would have started. I would like to acknowledge the thousands of individuals who have coded for the L^AT_EX project for free. It is due to their efforts that we can generate professionally typeset “pdf” files now.

I am forever indebted to my beloved mother for her continuous sacrifice, continuous prayers and support. I wish to extend a warm thank you to my brother Ayman and all my family members who have been encouraging me all through my study. I am indebted to my sincere wonderful wife, Doaa, for her patience, understanding, encouragement, and support throughout the course of this study. Also, I like to dedicate this thesis to dear daughter Zaynab, and dear sons Mohamed, and Yusuf, for their love, encouragement, and for playing quietly while Dad was studying. My gratitude goes to the members of Muslim community in Edmonton, friends, for their support and encouragement throughout my stay in Canada. Thank you to my fellow graduate students in the Water Resources program, specially, Ali Kiyani, for the valuable discussions throughout my study.

Last but not least, I wish to thank many people and my elementary school teachers from my small city and my professors at the faculty of Engineering, Suez Canal University (currently, Port Said University), Port Said, Egypt, as well as the professors at the University of Alberta from whom I gained all the knowledge that I have.

Contents

List of Figures	xv
List of Tables	xxiv
List of Abbreviations	xxv
1 Introduction	1
1.1 Problem statement	1
1.2 Research objectives	6
1.3 Geography of the Nile River Basin	7
1.4 Research Contributions	8
1.5 Dissertation outline	9
References	10
2 Teleconnection between Nonstationary Character of Ethiopian Rainfall and Global Sea Surface Temperature	19
2.1 Introduction	19
2.2 Research Objectives	23
2.3 Brief Climatology of Ethiopian Rainfall	24
2.4 Rainfall and Sea Surface Temperature Data	24
2.5 Research Methodology	25
2.5.1 Wavelet analysis	25
2.5.2 Wavelet Empirical Orthogonal Functions Analysis	27
2.6 Data Analysis and Results	29
2.6.1 Dominant Oscillations	29
2.6.2 How Many Signals in Rainfall or SST Data?	29
2.6.3 Spatial Patterns of June-September Rainfall	30
2.6.4 Temporal Patterns of June-September Rainfall	32
2.6.5 Spatial Patterns of February-May (FMAM) Rainfall	34
2.6.6 Temporal Patterns of February-May Rainfall	35
2.6.7 Global Sea Surface Temperature Variations	35
2.6.8 Spatial Patterns of Global SST	36

2.6.9	Temporal patterns-Sea Surface Temperature	37
2.6.10	Teleconnecting Rainfall and Sea Surface Temperature	38
2.7	Observations and Conclusions	38
	References	40
3	Hydrologic impacts of climate anomalies on the Upper Blue Nile	64
3.1	Introduction	64
3.2	Research Objectives	67
3.3	Upper Blue Nile Basin	68
3.4	Data	69
3.4.1	Meteorological Data	69
3.4.2	Temperature Data	69
3.4.3	DEM Data	70
3.4.4	Land cover Data	70
3.4.5	Hydrometric Data	70
3.5	Research Methodology	71
3.5.1	MISBA Model	71
3.5.2	SAC-SMA Model	74
3.5.3	Assessment of Model Performance	76
3.5.4	Bootstrap Resampling method	77
3.6	Discussions of Results	78
3.6.1	Physically-based and Fully Distributed MISBA Model	78
3.6.2	Lumped, Conceptual SAC-SMA Model	80
3.6.3	Climate anomalies effects	81
3.7	Summary and Conclusions	85
	References	88
4	The Upper Blue Nile Basin Rainfall, Teleconnection, and Prediction by an Artificial Neural Network	116
4.1	Introduction	116
4.2	Research Objectives	119
4.3	Study site	120
4.3.1	Upper Blue Nile Basin(UBNB)	120
4.3.2	Climatetic regime of UBNB	120
4.4	Climate data	121
4.4.1	Rainfall Data	121
4.4.2	Sea Surface Temperature Data	122
4.5	Research Procedure and Methodology	122
4.5.1	Wavelet Analysis	122

4.5.2	Principal component analysis	124
4.5.3	ANN-GA for forecasting seasonal rainfall	125
4.5.4	Statistical Measures	127
4.5.5	Disaggregation of Seasonal precipitation	129
4.6	Discussion of Results	130
4.6.1	Wavelet analysis of seasonal rainfall	130
4.6.2	Wavelet analysis of seasonal SST	132
4.6.3	Teleconnection between WPC1 of JJAS rainfall WPC1 and SAWP of global FMAM SST	132
4.6.3.1	Wavelet coherence and phase differences	134
4.6.4	Seasonal rainfall forecasting	136
4.6.5	Seasonal rainfall disaggregation	137
4.7	Summary and Conclusions	138
	References	140

5 Weekly Streamflow Forecasting for the Upper Blue Nile Basin, Ethiopia 164

5.1	Introduction	164
5.2	Research Objectives	167
5.3	Upper Blue Nile Basin (UBNB)	168
5.4	Hydro-Climate data	169
5.4.1	Rainfall Data	169
5.4.2	SST Data	169
5.4.3	Streamflow Data	169
5.5	Modeling Components and framework	170
5.5.1	Wavelet transformation	170
5.5.2	Principal component analysis	172
5.5.3	ANN-GA for predicting seasonal streamflow	173
5.5.4	Forecasting skill	174
5.5.5	Disaggregation of Seasonal streamflow	174
5.6	Discussion of Results	175
5.6.1	Wavelet analysis of seasonal streamflow	175
5.6.2	Teleconnection between SAWP of JASO streamflow and SAWP of global SST	176
5.6.3	Seasonal streamflow forecasting	177
5.6.4	Seasonal streamflow disaggregation	179
5.7	Summary and Conclusions	179
	References	181

6	Summary, Conclusions and Recommendations	199
6.1	Summary and Conclusions	199
6.2	Recommendations	203
6.2.1	Nonlinear-Nonstationary techniques	203
6.2.2	For Climate Variability Effects	204
6.2.3	For Better Rainfall Forecasting	204
6.2.4	For Better streamflow Forecasting	205
6.2.5	General recommendations	205
6.3	Suggestions for Future Work	206
6.3.1	The Zero Padding (Truncation problem)	206
6.3.2	Application of WPCA to Global Scales and other Atmospheric Variables	206
6.3.3	Seasonal forecasting	207
6.3.4	Climate change effects	207
	References	207

List of Figures

1.1	The River Nile Basin relative to Africa. The ten riparian countries are shown and the three boxes identifying the three major sub-basins, which are: The Upper Blue Nile Basin (UBNB), The White Nile basin (WNB) and the Victoria Lake Basin (VLB) (Map Drawn using ArcGIS).	16
1.2	SST anomalies are shaded (red color is for warm anomalies and blue is for cold). White patches indicate increased convective activities and arrows indicate anomalous wind directions during IOD events (courtesy of JAMSTEC website: http://www.jamstec.go.jp/frsgc/research/d1/iod/)	17
1.3	Spatial displays of the correlation between the first Wavelet principal component (WPC1) of the gridded seasonal rainfall during the four seasons, December-February (DJF), March-May (MAM), June-August (JJA) and September-November (SON), and the scale average wavelet power (SAWP) of the entire Nile River Basin rainfall.	18
2.1	Ethiopian Highlands map showing grid points of monthly rainfall data of University of East Anglia at $2.5^\circ \times 3.75^\circ$ resolution used in this study. Notice irregular grid points with total 23 grid points due to missing surrounding stations.	44
2.2	Correlation-distance plots of Pearson correlation versus inter-grid distance between gridded data of UEA and UoD are presented, such that specific grid points of UEA data, (a) to (p), are selected as the reference while grid points of UoD data considered are those located within a circle of 233 km radius and centered at these selected grid points of UEA. . .	45
2.2	continued	46

2.3	Scatter plots of Pearson correlation versus inter-grid distance between gridded data of UEA and UoD are presented, such that specific grid points of UEA data, (a) to (p), are selected as the reference while grid points of UoD data considered are those located within a circle of 233 km radius and centered at these selected grid points of UEA.	47
2.3	continued	48
2.4	Examples of Continuous wavelet and global spectra of a) Ethiopian rainfall during June-September (JJAS) at grid point (12.5° N-41.25° E), b) Ethiopian rainfall during February-May (FMAM) at grid point (5° N-33.75° E, and c) global SST during January-March at a grid point located in the Tropical Pacific Ocean (0.5° N-98.5° W) . Each example presents the standardized time series anomaly, Morlet wavelet power spectrum, where the dashed line is the cone of influence beyond which the energy is contaminated by the effect of zero-padding and the thick black contours represent the 95% confidence level of local power relative to a red noise background, Global wavelet power spectrum (solid line) with the 95% confidence level (dashed line), and the Scale-average wavelet power over 2-8 yrs. band with the dashed line is the 95% significance level.	49
2.4	continued	50
2.4	continued	51
2.5	Scree plots of the 23 WPCs of Ethiopian Highlands rainfall for the 2-8 yrs. band during (a) FMAM and (b) JJAS seasons. Notice 35 points in the figures because of filling the missing grid points from the data. The heavy dashed vertical line separating the first two WPCs.	52
2.6	Scree plots of global sea surface temperature for about 65,000 WPCs for the 2-8 yrs. band during (a) JFM, (b) AMJ, (c) JAS, and (d) OND.	53

2.7	Contours of spatial Pearson’s correlation between (a) WPC1 and (b) WPC2, and SAWP of gridded, Ethiopian rainfall data of June-September (JJAS) computed using the 2-8 year frequency band. Also, between WPC1 (c and e) and WPC2 (d and f), and SAWP of gridded, Ethiopian rainfall data of June-September (JJAS) computed using 2-4 years (c and d) and 5-7 years (e and f) frequency bands, respectively. Notice Eritrea borders are not shown in the maps. All the PCA have been done on the wavelet transformed rainfall time series. Also, the correlation values are shown in colors and contour values have been smoothed using linear interpolation and are written on the maps.	54
2.8	Temporal variation of WPC1 and WPC2 time series of Ethiopian June-September (JJAS) rainfall computed using 2-8 year (a and b), 2-4 year (c and d) and 5-7 years (e and f) frequency bands, respectively.	55
2.9	Contours of spatial Pearson’s correlation between (a) WPC1 and (b) WPC2, and SAWP of gridded, Ethiopian rainfall data of June-September (FMAM) computed using the 2-8 year frequency band. Also, between WPC1 (c and e) and WPC2 (d and f), and SAWP of gridded, Ethiopian rainfall data of June-September (JJAS) computed using 2-4 years (c and d) and 5-7 years (e and f) frequency bands, respectively. Notice Eritrea borders are not shown in the maps. All the PCA have been done on the wavelet transformed rainfall time series. Also, the correlation values are shown in colors and contour values have been smoothed using linear interpolation and are written on the maps.	56
2.10	Temporal variation of WPC1 and WPC2 time series of Ethiopian, February-May (FMAM) rainfall computed using 2-8 year (a and b), 2-4 year (c and d) and 5-7 years (e and f) frequency bands, respectively.	57
2.11	Spatial correlation between WPC1 and WPC2, and SAWP of gridded global sea surface temperature of 1° resolution computed for OND (a and b), JFM (c and d), AMJ (e and f) and JAS (g and h) using the 2-8 year frequency band.	58
2.11	continued	59
2.11	continued	60
2.11	continued	61

2.12	Temporal variation of WPC1 and WPC2 time series of global sea surface temperature computed for JFM (a and b), AMJ (c and d), JAS (e and f) and OND (g and h), using the 2-8 year frequency band.	62
2.13	Correlation between (a) WPC1 and (b) WPC2 of Ethiopian rainfall and SAWP of the gridded global sea surface temperature computed using the 2-8 year frequency band.	63
3.1	The study site, showing the Upper Blue Nile Basin, topography and the nine grid points of ERA-40 used for the hydrologic modeling.	98
3.2	Schematic diagram of surface energy budget and hydrology in ISBA standard model. R_g (incoming solar radiation), R_{at} (incoming longwave atmospheric radiation), αR_g (outgoing shortwave radiation), R_l (outgoing longwave atmospheric radiation), H (sensible heat flux), L_E (latent heat flux), G (ground heat flux), T_s (surface temperature), T_2 (deep soil temperature), P_r (total precipitation), P_n (snowfall), P_s (precipitation reaching soil), P_v (precipitation intercepted by vegetation), P_g (infiltration), Q_r (surface runoff), D (surface/deep soil water diffusion), K (gravitational drainage), E_n (sublimation), E_g (bare soil evaporation), E_r (evaporation from interception), E_{tr} (transpiration), W_r (canopy water store), W_n (snowpack SWE), w_s (surface soil volumetric water content), w_2 (root layer soil volumetric water content), d_s (surface soil depth), d_2 (root depth). Source Météo France http://www.cnrmmeteo.fr/isbadoc/model/schemstd.html	99
3.3	Schematic diagram of the Sacramento-Soil Moisture Accounting (SAC-SMA) Model (Gan and Burges, 1990)	100
3.4	Flow diagram of the Sacramento-Soil Moisture Accounting (SAC-SMA) Model. About 15 model parameters need calibration (Gan and Burges, 1990)	101
3.5	Scatterplots of the gauge rainfall data at Debremarcos station and two rainfall data sets (a) ERA-40 data, and (b) NCEP data.	102
3.6	Comparison of Monthly rainfall time series between Gauge rainfall data at Debremarcos, ERA-40, and NCEP rainfall data.	103

3.7	Streamflow simulation from MISBA model at daily time scale before rainfall, elevation, temperature corrections.	104
3.8	The UBNB streamflow simulation from MISBA model at daily time scale after adjusting the rainfall data by 3% increase with elevation	105
3.9	The UBNB streamflow simulation from MISBA model at daily time scale after modifying the evapotranspiration scheme.	106
3.10	Scatterplots of the rainfall at each grid point of the ERA-40 data (Pt1 to Pt8) that cover the UBNB versus the whole basin average rainfall.	107
3.11	Scatterplots of the potential evapotranspiration (PET) at four different grid points (Pt1, Pt4, Pt5 and Pt8) of the UBNB versus the whole basin PET	108
3.12	The UBNB streamflow simulation from SAC-SMA model.	109
3.13	Monthly precipitation for grid point at 10° N-37.5° E resampled by El Niño, La Niña, and IOD years.	110
3.14	Monthly temperature for grid point at 10° N-37.5° E resampled by El Niño, La Niña, and IOD years.	111
3.15	Composite analysis of the UBNB rainfall using the ERA-40 data at the eight grid points covering the basin. (a-b) for FMAM and JJAS for the whole grid points. (c-d) FMAM and JJAS averaging over three longitudes (35° E, 37.5° E, and 40° E).	112
3.15	continued	113
3.16	Box plot comparing the simulated streamflow distribution for the UBNB associated with El Niño, La Niña, and IOD periods (a) from MISBA simulation and (b) from SAC-SMA model.	114
3.17	Average monthly of the UBNB streamflow hydrograph for the period (1970-2002) under different climate anomalies.	115
4.1	The Upper Blue Nile river basin, topography, UEA 23 grid points used for Wavelet analysis and ERA-40 nine grid points used for the hydrologic model. the closed circles indicating the two grid points (#4 and #7) out of nine, used for JJAS rainfall forecasting.	149

4.2	Seasonal rainfall variation at one grid point located at 10° N-37.5° E for the period (1950-1998) from the UEA monthly gridded rainfall data.	150
4.3	850-hPa winds over Africa showing the prevailing atmospheric circulation and moisture transport in terms of wind speed (m/s) and direction throughout different seasons as indicated on each figure for a particular time period (ERA-40 data). (a-d) OND, JFM, AMJ and JAS for the period 1970-1990, (f-h) ONDJ, FMAM and JJAS for the period 1970-1990, and (i-k) ONDJ, FMAM and JJAS for the period 1990-2002.	151
4.3	continued	152
4.4	Flow chart of three-layer (input, hidden, and output) of the ANN-GA model. Three operations are shown: Selection, Crossover, and Mutation.	153
4.5	Seasonal disaggregation to weekly rainfall.	154
4.6	Examples of Continuous wavelet and global spectra of Ethiopian rainfall during June-September (JJAS) at two grid point: a) 17.5° N-37.5° E and b) 12.5° N-45° E. Each example presents the Morlet wavelet power spectrum, where the dashed line is the cone of influence beyond which the energy is contaminated by the effect of zero-padding and the thick black contours represent the 95% confidence level of local power relative to a red noise background, and Global wavelet power spectrum (solid line) with the 95% confidence level (dashed line).	155
4.7	Contours of spatial correlation patterns between gridded rainfall SAWP and WPC1 of 2-8 year spectral band for the Kiremt season of UEA monthly gridded data (1900-1998).	156
4.8	Power Hovmöller of 2-8 yrs. SAWP of the JJAS precipitation at lat. 10.25° N. the thick contour is the 95% confidence level, using the corresponding white noise spectrum at each longitude; (b) the average of (a) over all longitudes; (c) the average of (a) over all times. The data source is the UoD 0.5° × 0.5° for the period (1900-2006).	157
4.9	Contours of spatial correlation patterns between gridded SST SAWP and WPC1 from the SSTs of 2-8 year spectral band during FMAM season of 1870-2007	158

4.10	Contours of spatial correlation patterns between WPC1 of JJAS Ethiopian rainfall for 2-8 year spectral band during 1900-1998 and gridded SST SAWP during (a) JFM, and (b) FMAM.	159
4.11	Wavelet Power Spectra of the leading first principal component for JFM seasonal Oceanic SST sectors (a) Equatorial Pacific Ocean (EPO), (b) South Pacific Ocean (SPO), (c) North Atlantic Ocean (NAO) and (d) South Indian Ocean (SIO). The thick black contours enclose statistically significant wavelet power at the 5% level of a red noise process, and the thin black curve is the cone of influence.	160
4.12	Wavelet Power Spectra of the leading first principal component for FMAM seasonal Oceanic SST sectors (a) Equatorial Indian Ocean (EIO), (b) South Indian Ocean (SIO), (c) South Atlantic Ocean (SAO) and (d) South Pacific Ocean (SPO). The thick black contours enclose statistically significant wavelet power at the 5% level of a red noise process, and the thin black curve is the cone of influence.	161
4.13	Wavelet coherence and phase difference between the UBNB rainfall PC1 and the leading PC1 for JFM seasonal Oceanic SST sectors (a) Equatorial Pacific Ocean (EPO), (b) South Pacific Ocean (SPO), (c) North Atlantic Ocean (NAO) and (d) South Indian Ocean (SIO). The thick black contours enclose statistically significant wavelet power at the 5% level of a red noise process, and the thin black curve is the cone of influence. The phase difference is plotted only for time periods and scales coherence over 0.5. Right pointing arrows indicate in-phase signals while left pointing arrows indicate anti phase signals.	162

4.14	Wavelet coherence and phase difference between the UBNB rainfall PC1 and the leading PC1 for JFM seasonal Oceanic SST sectors (a) Equatorial Indian Ocean (EIO), (b) South Indian Ocean (SIO), (c) South Atlantic Ocean (SAO) and (d) South Pacific Ocean (SPO). The thick black contours enclose statistically significant wavelet power at the 5% level of a red noise process, and the thin black curve is the cone of influence. The phase difference is plotted only for time periods and scales coherence over 0.5. Right pointing arrows indicate in-phase signals while left pointing arrows indicate anti phase signals.	163
4.15	The observed (solid line) and forecasted (doted and dashed) for JJAS seasonal rainfall at (a) grid point #4, (b) grid point #7. Calibration period is (1975-1995) and validation period is (1996-2001).	164
4.16	scatter plots for observed vs disaggregated weekly rainfall during JJAS rainy season at (a) grid point #4, (b) grid point #7.	165
4.17	Observed and disaggregated weekly rainfall (mm) for grid point #4.	166
4.18	Observed and disaggregated weekly rainfall (mm) for grid point #7.	167
5.1	The Upper Blue Nile basin, location of the main streamflow gauge station at El Diem near to Ethiopia-Sudan boarder and the $2.5^{\circ} \times 2.5^{\circ}$ grid pints from ERA-40	188
5.2	Streamflow time series at El Diem station, (1912-2001); (a) average monthly streamflow; (b) average monthly rainfall for each grid point in Figure 5.1; (c) Seasonal (annual) streamflow with solid (dashed) line and historical seasonal (annual) average solid (dashed) horizontal line.	189
5.3	The flowchart of the study.	190
5.4	Seasonal disaggregation to weekly streamflow.	191

5.5	wavelet decomposition of the July-October streamflow of the UBNB. (a) Streamflow anomaly time series, (b) Wavelet power spectrum, (c) Global wavelet power spectrum. The solid lines in (b) enclose regions in the time-frequency domain where the streamflow power was statistically significant against a red-noise spectrum at the 10% level. The dashed line in (b) is the cone of influence outside which the effect of zero-padding may suppress the wavelet power. The dashed line in (c) is the 90% confidence level for the global wavelet power spectrum.	192
5.6	Contours of spatial correlation patterns between WPC1 of 2-8 year spectral band during JASO season of 1913-2001 and gridded SST SAWP during (a) FMAM, and (b) JFM. . . .	193
5.7	Scree plot from the principal component analysis of the four sectors from the global Oceans SST.	194
5.8	Observed and forecasted seasonal streamflow during JASO in BM^3 , a) using the SST predictors, b) using combined SST predictors and forecasted rainfall.	195
5.9	Scatter plots of Observed vs forecasted seasonal streamflow during JASO in BM^3 , a) using the SST predictors, b) using combined SST predictors and forecasted rainfall.	196
5.10	Observed and disaggregated weekly seasonal streamflow during JASO in BM^3 , a) using the SST predictors, b) using combined SST predictors and forecasted rainfall.	197
5.11	Scatter plots of Observed vs disaggregated weekly seasonal streamflow during JASO in BM^3 , a) using the SST predictors, b) using combined SST predictors and forecasted rainfall. . . .	198

List of Tables

3.1	Correlation between observed monthly rainfall data at De- bremarcos station and ECMWF and NCEP rainfall data . . .	95
3.2	Optimized SAC-SMA model parameters for the Upper Blue Nile Basin.	96
3.3	Summary statistics of MISBA and SAC-SMA forecasting skill using the simulated streamflow	97
4.1	Summary statistics of the forecasted JJAS rainfall season at the two grid points #4, #7	147
4.2	Summary statistics of the statistically disaggregated weekly rainfall during JJAS rainy season at the two grid points #4, #7	148
5.1	Summary statistics of the forecasted seasonal streamflow during JASO season	186
5.2	Summary statistics of the statistically disaggregated weekly streamflow during JASO season	187

List of Abbreviations

AMJ	April-May-June
ANN	Artificial Neural Network
ANN-GA	Artificial Neural Network - Genetic Algorithm
BN	Blue Nile
CI	Cone of Influence
DEM	Digital Elevation Model
DJF	December-January-February
EA	East Africa
ECMWF	European Centre for Mid-range Weather Forecasts
EH	Ethiopian Highlands
ENSO	El Niño-Southern Oscillation
FMAM	February-March-April-May
GA	Genetic Algorithm
GCM	General Circulation Model
GHCDN	Global Hydro Climate Data Network
HHT	Hilbert Huang Transformation
HK	Hanssen-Kuipers
IOD	Indian Ocean Dipole
ISBA	Interactions Soil-Biosphere-Atmosphere
JASO	July-August-September-October

JFM January-February-March

JJA June-July-August

JJAS June-July-August-September

MAM March-April-May

MISBA Modified Interactions Soil-Biosphere-Atmosphere

MWRI Egyptian Ministry of Water Resources and Irrigation

NCAR National Center for Atmospheric Research Reanalysis

NCEP National Centers for Environmental Prediction

NMA Ethiopian National Meteorology Agency

NR Nile River

NRB Nile River Basin

NS Nash-Sutcliffe

NWRP Egyptian National Water Resources Plan

ONDJ October-November-December-January

PCA Principal Component Analysis

PET Pan Evapotranspiration

PH Power Hovmöller

RMSE Root Mean Square Error

SAC-SMA Sacramento, Soil Moisture Accounting model

SAWP Scale Average Wavelet Power

SOI Southern Oscillation Index

SON September-October-November

SST Sea Surface Temperature

SVAT Soil-Vegetation-Atmosphere Transfer model

UBNB Upper Blue Nile Basin

UEA University of East Anglia
UoD University of Delaware
VS Valencia and Schaaake model
WA Wavelet Analysis
WEOF Wavele Emperical Orthogonal Function
WOM World Metrological Organization
WPC Wavele Principal Component

Chapter 1

Introduction

1.1 Problem statement

There has been a growing concern over the potential impacts of global warming ([Houghton and Syvitski, 2009](#); [Barry and Gan, 2011](#)) as in recent decades, severe weather has been occurring more frequently and in greater severity world wide, which could affect the reliability of water supply on various continents ([Bate, 2000](#); [Congress, 2009](#)). In the midst of dwindling water resources, increasing demand from the growing population, widespread pollution, and increasing extreme weather events, the world is facing a more and more serious water crisis since the beginning of the 21st Century ([BBC, 2010](#)). [Arnell \(1999\)](#) estimated that by about 2030, several billion people across the world could face water stress, including people who rely on the Nile River for their water supply. Therefore, competition among different users over diminishing water resources could spark conflicts.

The Nile River, the longest river in the world ([Duiker and Spielvogel, 2009](#)), is an “international” river as its water resources is shared by ten countries, namely, Tanzania, Uganda, Rwanda, Burundi, Congo, Kenya, Ethiopia, Eretria, Sudan and the Arab Republic of Egypt. In particular, the Nile River provides the primary water resource and so it is the life artery for its downstream countries such as Egypt and Sudan. One of the

main problems facing the ten riparian countries sharing the Nile River is the lack of a comprehensive agreement between the countries (Howell and Allan, 1994). The first Nile waters “geopolitical” agreement between Egypt and the Anglo-Egyptian Sudan was signed in 1929, which specified agreed amount of water to be allocated to both countries (Shahin, 1985). The construction of the Aswan High Dam led to another agreement between Egypt and Sudan in 1959, which allows Egypt to use 75% of the water coming from the Aswan High Dam (i.e. 55.5 Billion m^3), while Sudan takes the remaining 25%, based on an estimated mean annual flow of 84 km^3 for 1900-59 (Conway and Hulme, 1996).

Several attempts have been made to establish agreements between the countries sharing the Nile waters. It is very difficult to have all these countries agree with each other given the self interest of each country and their political, strategic, and social differences. On 14th of May 2010 (at Entebbe, Uganda), Ethiopia, Rwanda, Tanzania and Uganda signed a new agreement on sharing the Nile water even though this agreement raised strong opposition from Egypt and Sudan. Ideally, such international agreements should promote equitable and efficient usage of the Nile basin’s water resources. Without a better understanding about the availability of the future water resources of the Nile River, we could expect more conflicts between these countries relying on the Nile for their water supply, economic and social developments. However, geographically, the Nile flows through diverse landscapes and different climatic regimes, posing a pertinacious challenge to streamflow forecasters of the Nile.

Because of flow variability of the Nile River (NR), there could be water shortages during the dry season for downstream countries such as Egypt and Sudan (Abu-Zeid and Biswas, 1991). Even though the Nile River has four tributaries (White Nile, Sobat, Blue Nile, and Atbara), the Blue Nile which begins from the Ethiopian highlands (EH) contributes more than

60% of the Nile streamflow (see Figure 1.1). The Blue Nile has annual streamflow of about 48 Billion m^3 , that means EH deliver more than 85% of the flow in the Nile in Egypt (Bishop, 2012). The The streamflow of the Blue Nile is highly variable (Sutcliffe et al., 1999), partly because of the summer monsoon. Also, the boreal summer rainfall can contribute up to 80% of the annual streamflow of the Upper Blue Nile basin (UBNB). Thus, a diagnostic analysis of the Upper Blue Nile's hydroclimatic variability and its relationship to the dominant modes of oceanic variability of nearby oceans can potentially be used to predict the rainfall/ streamflow over the upper Blue Nile, which is vital for efficient water resources management for the Nile River basin.

The primary source of moisture for rainfall during the boreal summer season is the South Atlantic Ocean and the Indian circulation coming from the Indian Ocean (Awadallah and Rousselle, 2000). The teleconnection between the large-scale oceanic-atmospheric circulation patterns and the variability of streamflow has been a research topic of increasing interest. The monthly Sea Surface Temperature (SST) over the oceans is now accepted as one of the crucial factors that govern the monthly, global atmospheric activity (Pan and Oort, 1983).

The dominant source of interannual tropical climate variability is the El Niño/Southern Oscillation (ENSO) (Philander, 1990) which is a coupled ocean-atmosphere circulation anomaly that originates from the Tropical Pacific Ocean. For the last several decades, various studies have documented the relationships between ENSO and interannual hydroclimatic/streamflow variability in the Nile River and specifically the western regions of Ethiopia, including the UBNB (e.g. Eltahir, 1996; Amarasekera et al., 1997; Bekele, 1997; Wang and Eltahir, 1999; Eltahir and Wang, 1999; Awadallah and Rousselle, 2000; Conway, 2000; Eldaw, 2001; Eldaw et al., 2003; Gissila et al., 2004; Eltahir et al., 2004; Delude, 2005; Block, 2006; Abteu et al.,

2009).

The Pacific Ocean climate system represented by the Niño3 index, exhibits strong low-frequency variability modes at both interannual and inter-decadal scales (Torrence and Compo, 1998). Typically, the UBNB low-flow years appear to be associated with warm ENSO events (El Niño) while high-flow years are associated with cold ENSO events (La Niña). However, not every low (high-flow) year in the Nile River is induced by El Niño (La Niña). For example, 1918, 1925, 1939, 1972, 1982, 1984, 1995, and 1997 were low-flow years, but they were not El Niño years. Likewise, 1935, 1938, 1946, 1961, 1964, 1988 and 1998 were high-flow years, but they were not La Niña years. Other regional SSTs, such as those related to the Atlantic and Indian Oceans, sometimes may exert a significant influence on the climate of UBNB. Therefore, it may be necessary to identify predictors from the global oceans in order to adequately determine signals that contribute to the variability of the UBNB.

Another oceanic climate anomaly relevant to the climate of UBNB is the Indian Ocean Dipole (IOD), which is a coupled ocean-atmosphere phenomenon in the Indian Ocean. It is characterized by anomalous cooling of SST in the south, eastern equatorial Indian Ocean and anomalous warming of SST in the western equatorial Indian Ocean. The cooling and the warming (dipole) of the Ocean alters the normal upper air flow situated the eastern Indian Ocean, which causes a warm pool of moisture to shift to the west, bringing abundant rainfall over eastern Africa and devastating droughts over the Indonesian archipelago (Saji et al., 1999) (see Figure 1.2).

Although the Nile River Basin has been well-studied in the past, there is still a room for more investigations. Some previous studies have depended heavily on stationary techniques such as direct correlation analysis, harmonic analysis, and/or event-based compositing to find the tele-

connection between anomalous Ocean/atmosphere circulation patterns and hydroclimatic variables (e.g. [Eldaw, 2001](#); [Gissila et al., 2004](#); [Block and Rajagopalan, 2007](#); [Korecha and Barnston, 2007](#)). There are still possible spatial patterns in the global SST-UBNB streamflow relationships that have yet to be objectively identified.

Several studies have shown that large-scale climate anomalies such as ENSO and IOD are non-stationary (that does not include a trend-like behavior) (e.g. [Torrence and Compo, 1998](#); [Saji et al., 1999](#)). Therefore, there is a growing trend of using non-stationary approaches such as the Hilbert Huang transform and wavelet transforms for the analysis of hydroclimatic variability in different parts of the world. Wavelet transform has recently been used to study the interannual variability of East, central and South Africa (e.g. [Mwale et al., 2004](#); [Mwale and Gan, 2005](#); [Mwale, 2005](#); [Mwale et al., 2005, 2007](#); [Mwale and Gan, 2009](#); [Mwale et al., 2009](#)). Also, the technique has been used to study the variability of Canadian annual and seasonal streamflows and their relationships with some large-scale climate patterns ([Coulibaly and Burn, 2004, 2005](#); [Gobena and Gan, 2006](#); [Gobena, 2008](#)).

Past studies have mainly focused on establishing links between hydroclimatic variations and individual global oceanic anomalies which are assumed to be independent of each another. This may not be true because two oceanic anomalies with different characteristic time scales may have a constructive or destructive effect on each other, depending on whether they are in phase or out of phase with each other. Thus, it is desirable to understand possible interactions (i.e. statistical and dynamic-physical) between large scale climate anomalies because constructive interactions between them may produce extreme hydroclimatic events such as droughts and floods.

Because the Nile basin is vast and has different rainfall regimes, it would

be difficult to deal with the rainfall over the whole basin as one regime. Figure 1.3 shows the spatial correlation map (first wavelet principal component, WPC1, vs. scale average wavelet power, SAWP, for each season) of the wavelet transformed seasonal rainfall over the entire Nile River basin. The figure shows how the rainfall power is variable spatially and temporally. Therefore, it is appropriate to divide the basin into sub-basins.

This dissertation deals with a systematic analysis of interannual to interdecadal scale precipitation and streamflow variability in the UBNB, with the objective of advancing our understanding of the climate and hydrology of UBNB, and eventually to develop a statistical forecasting system at one season lead time that incorporates large-scale climate information. Questions that are of interest are such as:

- What are the dominant spatial and/or temporal modes of hydroclimatic variability of the Upper Blue Nile River basin (UBNB)?
- How are these modes teleconnected to large-scale oceanic anomalies?
- How to improve modeling the rainfall of the UBNB?
- How to improve modeling the streamflow of the UBNB?

To address these questions, statistical characteristics of precipitation and streamflow of the UBNB will be analyzed using wavelets, compositing and correlation analysis. From these findings, the feasibility of using large-scale climate information for accurate forecasting of the sub-basin-scale weekly seasonal rainfall and streamflow volumes will be examined.

1.2 Research objectives

Using selected sea surface temperature data, and large scale, climate anomalies, the key objectives of this research are summarized as follows:

1. To investigate the dominant spatial and/or temporal modes of variability of low-frequency (e.g. 2-8, 16, and 32 yrs.) rainfall across the major sub-basin of the Nile River (UBNB);
2. To investigate the dominant spatial and/or temporal modes of low frequency Sea Surface Temperature (SST) of the global Oceans;
3. To investigate the possible influence of global oceanic SST indices on UBNBs hydroclimatic variability;
4. To explore modeling streamflows of the UBNB using ERA-40 re-analysis data produced by a physically-based, fully distributed land surface scheme MISBA and a lumped-parameter, conceptual hydrologic model, the Sacramento model of National Weather Service of USA;
5. To assess the possible hydrologic impacts of climate anomalies on the historical rainfall/ streamflow of the UBNB;
6. To develop and verify weekly seasonal rainfall forecast model for UBNB driven by SST predictors identified from those global oceanic indices;
7. To develop and verify weekly seasonal streamflow forecast model that incorporates predictors identified from those global oceanic indices of importance to UBNB.

1.3 Geography of the Nile River Basin

The Nile gets its name from the Greek word “Nelios” which means River Valley. The Nile River extends from the most remote source to its mouth at the Mediterranean with total length about 6695 Km ([Davies and Walker, 1986](#)), draining a basin area of about 2.9 million km^2 , approximately one

third that of the United States and one-tenth that of Africa. It extends from 4° S to 31° N and from 21° E to 41° E. Figure 1.1 shows the hydrological boundaries of the basin (Shahin, 1985). Despite of the river length and catchment area, the Nile has the lowest specific discharge in comparison to other major world rivers. The Nile River's average discharge is about 0.3 billion m^3 per day (i.e. $3,500 m^3/s$) at its mouth.

The Nile basin is comprised of three main sub-basins: The eastern part (the Upper Blue Nile, Sobat, and Atbara), the western part (the White Nile), and the southern part (the Equatorial lakes) (see the three dotted boxes in Figure 1.1). Finally, the Nile discharges to the Mediterranean Sea. The UBNB is one of the most important tributaries of the Nile River because of it contributes about 60% of the Nile's streamflow that reaching Aswan High dam, Egypt. Roughly 70% of the annual rainfall in the UBNB is delivered during the Kiremt season, June-September, Kiremt season (Conway, 2000). During this season, 85%-95% of annual crops are produced (Degefu, 1987).

1.4 Research Contributions

The contributions of this research to climate and hydrology include the followings:

1. Application and demonstration of the wavelet principal component analysis (WPCA) methodology for multivariate nonstationary data analysis. The method is a new direction in climate research and has helped us to gain new understanding in the nonlinearity and nonstationary variability of global oceanic SST and the various climate processes of Africa and other continents;
2. Simulating the UBNB streamflow using two different hydrologic models; a physically-distributed model and a lumped model with less in-

put hydroclimatic data;

3. Reproduction and demonstration of the effects of climatic anomalies on the historical streamflows in the UBNB. The method is a new direction in climate research and has helped us to gain new understanding in the effects of global oceanic indices on the UBNB streamflow;
4. Development and application of the non-linear statistical model for climate and hydrologic forecasting based on an artificial neural networks (ANNs) trained by genetic algorithms (GAs). The combined model is known as the ANN-GA and as far as we know, this combination of models (ANNs and GAs) has contributed to an improved forecasting of hydroclimatic variables;
5. Development and demonstration of the weekly seasonal rainfall framework by integrating ANN-GA, and a disaggregation model, for forecasting weekly rainfall from disaggregated seasonal rainfall. This system has predicted accurate weekly rainfall from seasonal oceanic variability;
6. Development and demonstration of the weekly seasonal streamflow framework by integrating ANN-GA, and a disaggregation model, for forecasting weekly rainfall from disaggregated seasonal rainfall. This system has predicted accurate weekly rainfall from seasonal oceanic variability;

1.5 Dissertation outline

The dissertation is divided into six quasi independent chapters. The first chapter is the introduction that discusses statements of problems, research objectives, the geography of the Nile River Basin (NRB), and the research contribution. The second chapter presents the diagnostic analysis of low-

frequency seasonal rainfall variability of the Ethiopian Highlands (EH) and its teleconnection to the global Oceanic SST. The third chapter discusses the effects of climate anomalies of oceanic origins, such as ENSO and IOD, on the UBNB streamflow variability. In the fourth Chapter, an ANN-GA teleconnection model is developed to forecast seasonal rainfall for the Ethiopian portion of the NRB and disaggregation of seasonal to weekly scale rainfall. The fifth chapter deals with the understanding obtained from the climate diagnostics through the development and application of weekly seasonal streamflow forecasting models for the UBNB by combining two different approaches. Finally, the general summary, overall conclusions and recommendations for future research are presented in the sixth Chapter.

References

- Abteu, W., Melesse, A. M., and Dessalegne, T. (2009). El Niño Southern Oscillation link to the Blue Nile river basin hydrology. *Hydrol. Processes*, 23(26), 3653-3660.
- Abu-Zeid, M. A., and Biswas, A. K. (1991). Some major implications of climatic fluctuations on water management. *Int. J. Water Resour. Dev.*, 7(2), 74.
- Amarasekera, K. N., Lee, R. F., Williams, E. R., and Eltahir, E. A. B. (1997). ENSO and the natural variability in the flow of tropical rivers. *J. Hydrol.*, 200(1-4), 24-39.
- Arnell, N. W. (1999). Climate change and global water resources. *Global Environ. Change*, 9(Supplement 1), S31-S49.
- Awadallah, A. G., and Rousselle, J. (2000). Improving forecasts of Nile flood using SST inputs in TFN model. *J. Hydrol. Eng.*, 5(4), 371-379.

- Barry, R., and Gan, T. (2011). *The global Cryosphere: Past, present and future*. Cambridge University Press.
- Bate, R. (2000). *Life's adventure: Virtual risk in a real world*. Butterworth-Heinemann.
- BBC. (2010, May). *East Africa seeks more Nile water from Egypt*. Retrieved from <http://news.bbc.co.uk/2/hi/8682387.stm> (Accessed: 06/01/2010)
- Bekele, F. (1997). Ethiopian use of ENSO information in its seasonal forecasts. *Internet Journal of African Studies*, 2(5). Retrieved from <http://ccb.colorado.edu/ijas/ijasno2/bekele.html> (Accessed: 11/26/2008)
- Bishop, K. (2012, July). The relationship between land use and water, water as the mirror of landscapes: How useful a hypothesis for resource management? *EOS*, 93(28), 259.
- Block, P. (2006). *Integrated management of the Blue Nile basin in Ethiopia: Precipitation forecast, hydropower, and irrigation modeling*. PhD thesis, University of Colorado, Colorado, United States.
- Block, P., and Rajagopalan, B. (2007). Interannual variability and ensemble forecast of Upper Blue Nile basin Kiremt season precipitation. *Journal of Hydrometeorology*, 8(3), 327-343.
- Congress. (2009). *Congressional record, v. 150, pt. 11, june 25, 2004 to july 14, 2004*. United States Congress. Retrieved from <http://books.google.ca/books?id=FtNW4skCGBUC> (Accessed: 06/20/2012)
- Conway, D. (2000). The climate and hydrology of the Upper Blue Nile river. *The Geographical Journal*, 166(1), 49-62.

- Conway, D., and Hulme, M. (1996). The impacts of climate variability and future climate change in the Nile basin on water resources in Egypt. *Int. J. Water Resour. Dev.*, 12(3), 277-296.
- Coulibaly, P., and Burn, D. (2004). Wavelet analysis of variability in annual Canadian streamflows. *Int. J. Climatol.*, 40(3), 1509-1530.
- Coulibaly, P., and Burn, D. (2005). Spatial and temporal variability of Canadian seasonal streamflows. *J. Clim.*, 18(1), 191-210.
- Davies, B., and Walker, K. F. (1986). *The ecology of river systems*. Boston: W. Junk.
- Degefu, W. (1987). Some aspects of meteorological drought in Ethiopia. In M. H. Glantz (Ed.), *Drought and hunger in Africa: Denying famine a future* (p. 23-36). Cambridge, England: Cambridge University Press.
- Delude, C. M. (2005, February). *Tropical seesaw: Flooded Amazon means drought in Congo* (Vol. 49) (No. 16). Retrieved from <http://web.mit.edu/newsoffice/2005/techtalk49-16.pdf> (Accessed: 05/15/2008)
- Duiker, W. J., and Spielvogel, J. J. (2009). *World history: to 1500* (Vol. 5). Australia: Wadsworth.
- Eldaw, A. K. (2001). *Long range forecasting of the Nile river flow using large scale oceanic atmospheric forcings*. PhD thesis, Colorado State University, Colorado, United States.
- Eldaw, A. K., Salas, J. D., and Garcia, L. A. (2003). Long-range forecasting of the Nile river flows using climatic forcing. *J. Appl. Meteorol.*, 42(7), 890-904.
- Eltahir, E. A. B. (1996). El Niño and the natural variability in the flow of the Nile river. *Water Resour. Res.*, 32(1), 131-137.

- Eltahir, E. A. B., Loux, B., Yamana, T. K., and Bomblies, A. (2004). A see-saw oscillation between the Amazon and Congo basins. *Geophys. Res. Lett.*, *31*(23), L23201.
- Eltahir, E. A. B., and Wang, G. (1999). Nilometers, el Niño, and climate variability. *Geophys. Res. Lett.*, *26*(4), 489-492.
- Gissila, T., Black, E., Grimes, D. I. F., and Slingo, J. M. (2004). Seasonal forecasting of the Ethiopian summer rains. *Int.J.Climatol.*, *24*(11), 1345-1358.
- Gobena, A. K. (2008). *The analysis of hydroclimatic variability and predictability in western Canada*. PhD thesis, University of Alberta, Edmonton, Alberta, Canada.
- Gobena, A. K., and Gan, T. (2006). Low-frequency variability in southwestern Canadian streamflow: links with large-scale climate anomalies. *Int.J.Climatol.*, *26*(13), 1843-1869.
- Houghton, J., and Syvitski, J. (2009). Global warming: The complete briefing. *Oceanography*, *22*(3), 191-205.
- Howell, P., and Allan, J. (1994). *The Nile: Sharing a scarce resource: a historical and technical review of water management and of economic and legal issues*. Cambridge University Press.
- Korecha, D., and Barnston, A. (2007). Predictability of June-September rainfall in Ethiopia. *Mon. Wea. Rev.*, *135*(2), 628-650.
- Mwale, D. (2005). *Nonstationary and nonlinear approaches for the analysis and prediction of hydroclimatic variables in eastern and southern Africa*. PhD thesis, University of Alberta, Edmonton, Alberta, Canada.

- Mwale, D., and Gan, T. (2009). Integrating Wavelet empirical orthogonal functions and statistical disaggregation for predicting weekly runoff for the Upper Kafue basin in Zambia, Africa. *J.Hydrol.Eng.*, 15, 822.
- Mwale, D., and Gan, T. Y. (2005). Wavelet analysis of variability, teleconnectivity, and predictability of the September-November East African rainfall. *J. Appl. Meteorol.*, 44(2), 256-269.
- Mwale, D., Gan, T. Y., Devito, K., Mendoza, C., Silins, U., and Petrone, R. (2009). Precipitation variability and its relationship to hydrologic variability in Alberta. *Hydrol. Processes*, 23(21), 3040-3056.
- Mwale, D., Gan, T. Y., and Shen, S. S. P. (2004). A new analysis of variability and predictability of seasonal rainfall of central southern Africa for 1950-94. *Int.J.Climatol.*, 24(12), 1509-1530.
- Mwale, D., Gan, T. Y., Shen, S. S. P., Shu, T. T., and Kim, K.-M. (2007). Wavelet empirical orthogonal functions of space-time-frequency regimes and predictability of southern Africa summer rainfall. *J.Hydrol.Eng.*, 12(5), 513-523.
- Mwale, D., Shen, S., and Gan, T. (2005). Integration of wavelet or Hilbert transforms and disaggregation for weekly streamflow prediction from seasonal oceanic variability. *Proceeding conference, AMS Forum: Living with a Limited Water Supply*.
- Pan, Y., and Oort, A. (1983). Global climate variations connected with sea surface temperature anomalies in the eastern equatorial Pacific Ocean for the 1958-73 period. *Mon.Wea.Rev*, 111, 1244-1258.
- Philander, S. (1990). *El Niño, La Niña, and the Southern Oscillation* (Vol. 46 of International Geophysics Series). London: Academic Press.
- Saji, N., Goswami, B. N., Vinayachandran, P. N., and Yamagata, T. (1999). A dipole mode in the tropical Indian Ocean. *Nature*, 401(6751), 360-363.

- Shahin, M. (1985). *Hydrology of the Nile basin* (Vol. 21). Amsterdam: Elsevier.
- Sutcliffe, J., Parks, Y., and of Hydrological Sciences, I. A. (1999). *The hydrology of the Nile*. International Association of Hydrological Sciences.
- Torrence, C., and Compo, G. P. (1998). A practical guide to Wavelet analysis. *Bulletin of the American Meteorological Society*, 79(1), 61.
- Wang, G., and Eltahir, E. A. B. (1999). Use of ENSO information in medium- and long-range forecasting of the Nile floods. *Journal of Climate*, 12(6), 1726-1737.

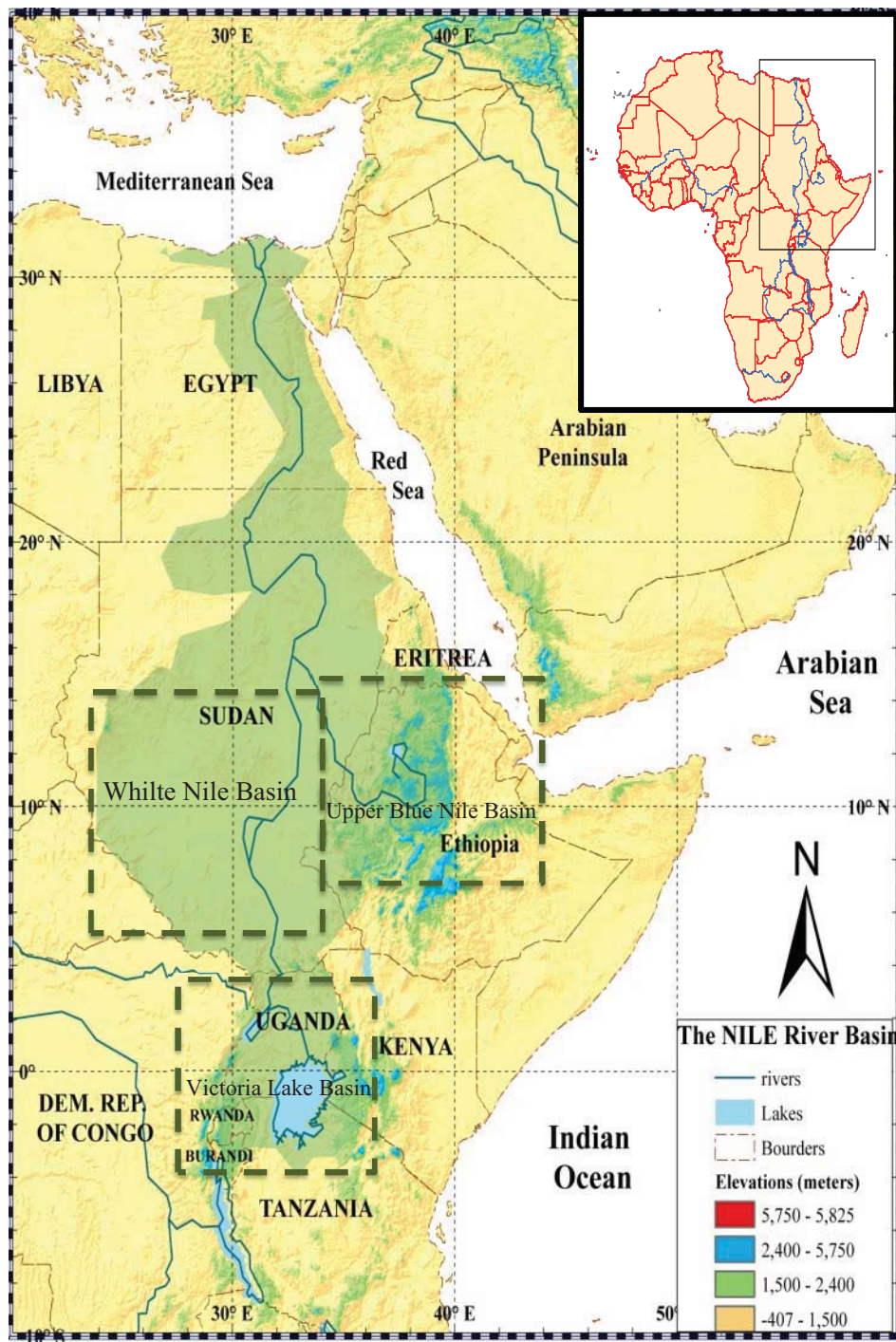
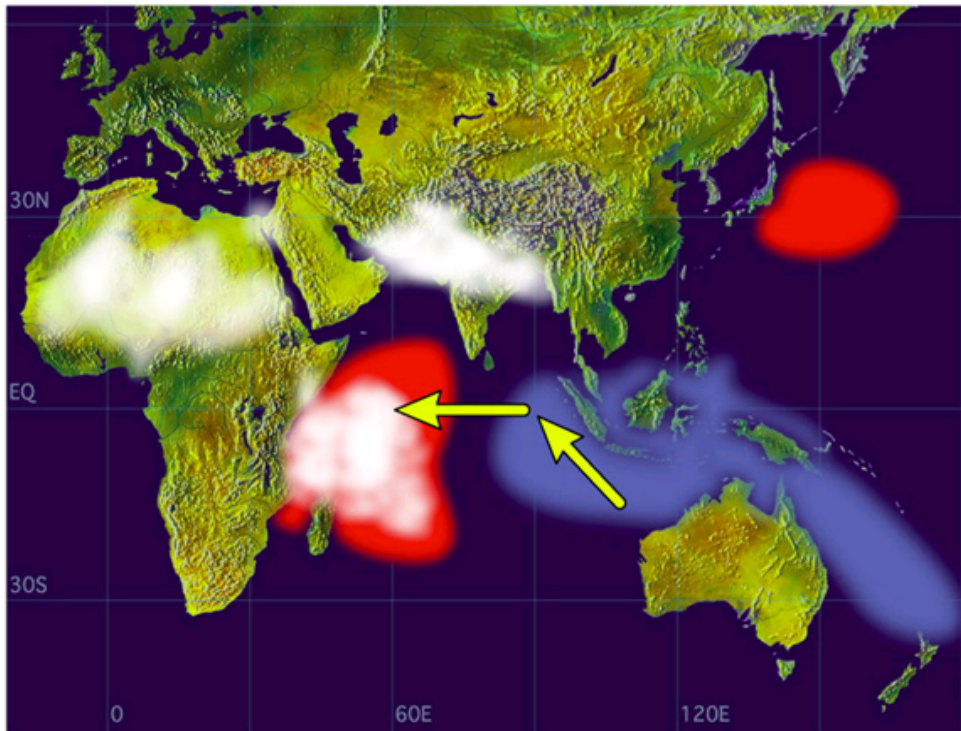


Figure 1.1: The River Nile Basin relative to Africa. The ten riparian countries are shown and the three boxes identifying the three major sub-basins, which are: The Upper Blue Nile Basin (UBNB), The White Nile basin (WNB) and the Victoria Lake Basin (VLB) (Map Drawn using ArcGIS).

Positive Dipole Mode



Negative Dipole Mode

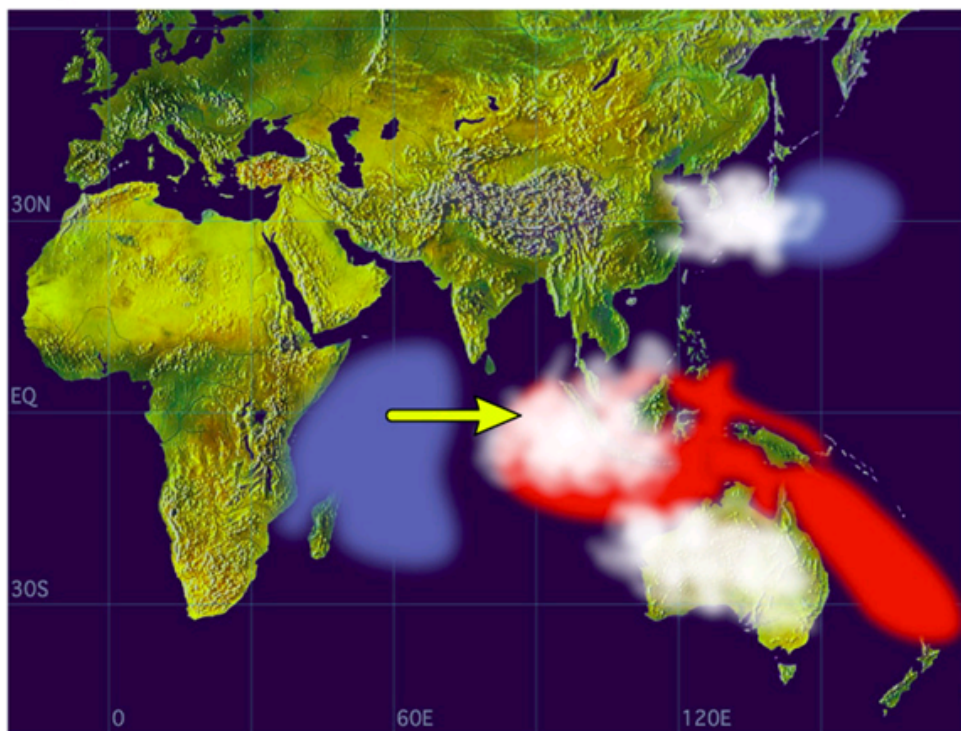


Figure 1.2: SST anomalies are shaded (red color is for warm anomalies and blue is for cold). White patches indicate increased convective activities and arrows indicate anomalous wind directions during IOD events (courtesy of JAMSTEC website: <http://www.jamstec.go.jp/frsgc/research/d1/iod/>)

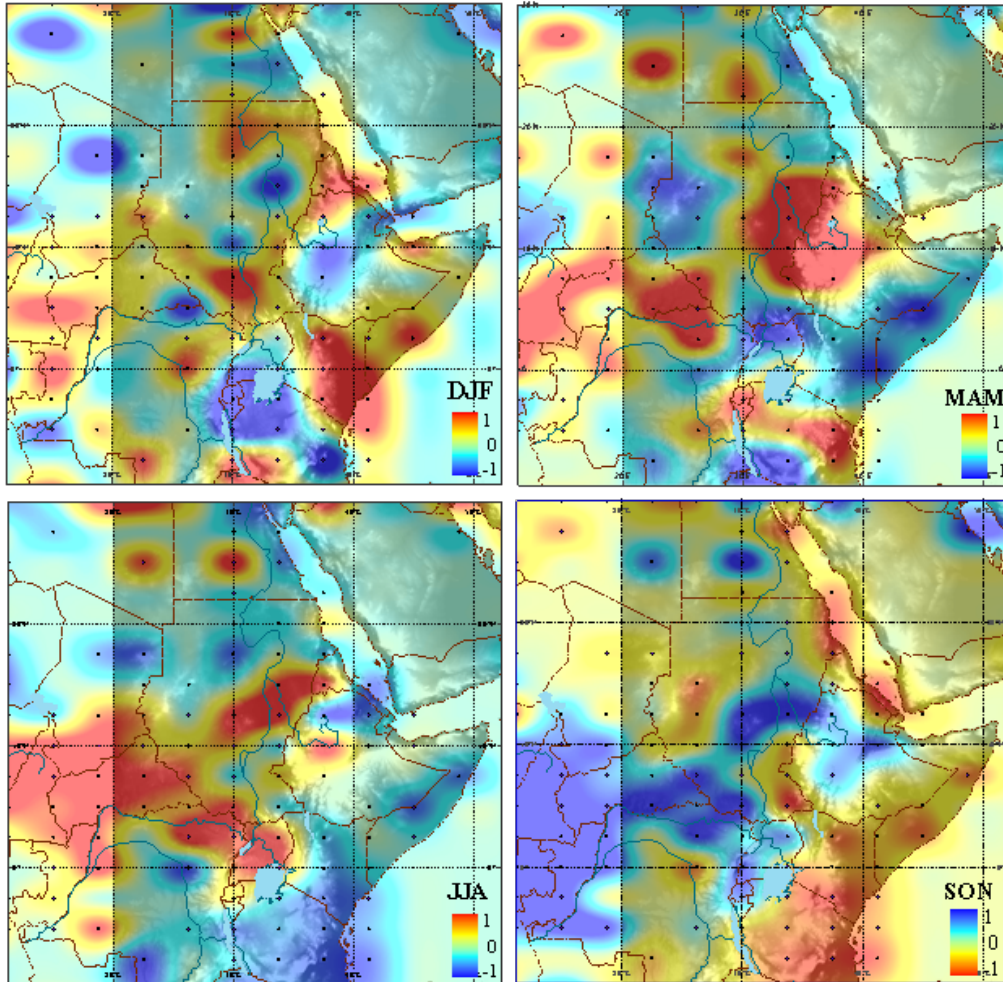


Figure 1.3: Spatial displays of the correlation between the first Wavelet principal component (WPC1) of the gridded seasonal rainfall during the four seasons, December-February (DJF), March-May (MAM), June-August (JJA) and September-November (SON), and the scale average wavelet power (SAWP) of the entire Nile River Basin rainfall.

Chapter 2

Teleconnection between Nonstationary Character of Ethiopian Rainfall and Global Sea Surface Temperature ¹²

2.1 Introduction

Ethiopia's climate variability, in particular that of rainfall, is nonstationary (Segele et al., 2009). Because of the nonstationary characteristics inherent in rainfall data, nonstationary techniques are needed to analyze the variability of rainfall in space and time. To understand the nonstationary knowledge of Ethiopia's rainfall variability, it is also necessary to understand similar variability in global ocean Sea Surface Temperatures (SST), known to be linked to (Diro et al., 2011). As demonstrated by Mwale et al. (2004, 2005, 2007), an important by-product of the nonstationary analysis of rainfall and SST is the ability to teleconnect seemingly

¹A version of this chapter has been submitted for publication to the International Journal of Climatology and is under review.

²Part of this chapter was accepted in the Proceeding conference, 2012 CSCE Annual General Conference, June 6-9, 2012, Edmonton, AB, CA.

remote nonstationary spatial and temporal patterns of these climatic variations, making it possible to reliably predict rainfall from SST. The ability to understand and teleconnect the nonstationary variations of rainfall and SST should be useful to Ethiopia, a country where droughts and famines are notoriously endemic (Degefu, 1987). Droughts and famines are endemic because agriculture, which accounts for approximately 50% of Ethiopia's Gross Domestic Product and employs 80% of Ethiopia's population, is heavily dependent on rainfall (Abegaz et al., 2007), which has been found to exhibit considerable spatial and temporal variability (Shanko and Camberlin, 1998; Bewket and Conway, 2007). Since nonstationary climatic information shows dominant events irregularly distributed in space and time (Torrence and Compo, 1998), the dominant events can reveal rainfall droughts and floods, and warming or cooling of ocean SST. As shown by Mwale et al. (2004), the complementary interaction of dominant events in rainfall and SST, simultaneous or lagged, evolve over time and space. Knowledge of this interaction would create the potential for Ethiopia to improve its rainfall prediction capabilities and adapt its agriculture practices wisely. Further, Ethiopia is also the headwaters of the Nile River and its tributaries, which endow Egypt and Sudan with 60% of its streamflow (Seleshi and Demaree, 1995). Understanding the nonstationary variations of rainfall across the Blue Nile basin has the potential to assist Egypt and Sudan, downstream of the Blue Nile, to understand the nonstationary character of streamflow and plan for their water supplies accordingly.

The catastrophic nature of persistent droughts and famines across Ethiopia (see Table 2.1 of (Degefu, 1987), pages 29-31) has in the last three decades rekindled efforts aimed at understanding the nature of rainfall variability, so as to better prepare the population to these climatic extremes. Such efforts include those of (Diro et al., 2011; Segele et al., 2009; Bewket and Conway, 2007; Gissila et al., 2004; Bekele, 1997; Eklundh and Pilesjö, 1990).

Among all these studies, only [Segele et al. \(2009\)](#) applied the nonstationary techniques of wavelet analysis to analyze Ethiopian rainfall. Using pentad time series, [Segele et al. \(2009\)](#) showed that rainfall in Ethiopia is dominated by inter annual cycles of 0.57-1.42, 1.41-3.04 and 3.04-4.6-years, which they determined were caused by local and regional atmospheric circulation mechanisms and global SST anomaly patterns. [Segele et al.'s \(2009\)](#) identification of rainfall oscillations and their variations in time and across Ethiopia was a valuable contribution to understanding the nonstationary character of Ethiopia's rainfall. However, their study utilized only 30 years of rainfall data (1979-2008). With longer datasets, there is potential to uncover the temporal evolution and interaction of lower (e.g. 5-7) and higher frequencies (e.g. 2-4) in rainfall, which can reveal how droughts and floods evolve over long periods of time, which is not possible when short datasets are used. Hence, the first goal of this study is to re-analyze Ethiopian rainfall using 99 years of monthly rainfall and SST data (1900-1998). As shown by [Mwale et al. \(2005\)](#), although rainfall data before the Second World War was scarce for large parts of Africa, which include Ethiopia, the few datasets that were available (and have since been interpolated) give very meaningful results of rainfall variation in both space and time, especially when most of the noise is removed, such as through computing the scale averaged wavelet power of rainfall data ([Torrence and Compo, 1998](#)). Further, instead of using composite analysis, this study employs a technique reported by [Mwale et al. \(2004\)](#) called wavelet based-empirical orthogonal function (WEOF) analysis to study simultaneous nonstationary variations of rainfall and SST and their teleconnectivity.

Besides understanding the spectral characteristics of Ethiopian rainfall, Ethiopia has also been delineated into several homogenous rainfall regions. For example, [Diro et al. \(2011\)](#) used composite analysis to divide Ethiopia into six homogenous zones of rainfall and showed that different

mechanisms linked to SST controls rainfall variations in various zones. [Eklundh and Pilesjö \(1990\)](#) applied the principal component analysis (PCA) and common factor analysis (CFA) to regionalize annual Ethiopian rainfall into seven homogeneous zones. Generally, these regions were identified as southern Ethiopia, south of the Great Rift Valley (GRV), western half of Ethiopia north of the GRV, eastern half of Ethiopia north of the GRV and the GRV. Further, [Bekele \(1997\)](#) regionalized Ethiopia into three zones of the rainy seasons and found that the central and eastern regions of Ethiopia had bimodal rainfall (i.e., February-May, FMAM, and June-September, JJAS), the western parts of Ethiopia have an unimodal rainfall distribution while the southern and southeastern had rainfall almost all year round (i.e., December- February, March-May, June-August and September-November). A delineation of Ethiopia into homogenous zones of rainfall helped the country to create a reliable database of rainfall. To our understanding, all the studies that delineated Ethiopian rainfall into homogenous zones did not use nonstationary approaches, and hence the zones identified are not dependent on nonstationary characteristics of rainfall. Further, these studies also did not relate the nonstationary rainfall zones to nonstationary zones of global SST variability, meaning that there is room to understanding Ethiopia's rainfall variations and its teleconnections to SST. In this study, not only is the dominant nonstationary characteristics of Ethiopian rainfall and global SST variations determined, their spatial and temporal patterns are also teleconnected. Identifying dominant SST and rainfall patterns that are teleconnected has been shown to be critical for predicting spatial and temporal patterns of rainfall in eastern, central southern and southern Africa (e.g. [Mwale et al., 2004, 2005, 2007](#)). This is the second goal of the chapter.

2.2 Research Objectives

To meet the above goals, the following are the objectives of this study:

- i) Analyze the nonstationary variations of seasonal (June-September and February-May, respectively JJAS and FMAM) Ethiopian rainfall by employing wavelet analysis and wavelet based empirical orthogonal function analysis (WEOF);
- ii) Using results from (i), delineate Ethiopia into homogenous zones of non-stationary rainfall variability, determine the leverage topographic terrain and other factors have on Ethiopian rainfall and understand the frequency of droughts and their spatial localization;
- iii) Using the non-stationary techniques of wavelet analysis and wavelet based principal component analysis (WPCA), analyze the nonstationary character of seasonal (January-March-JFM, April-June-AMJ, July-September-JAS and October-December- OND) global sea surface temperature (SST);
- iv) Using results from (iii.), identify the spatial character of dominant nonstationary global ocean SST regions;
- v) Using results from (iv) identify the nonstationary global SSTs that are teleconnected to seasonal rainfall across Ethiopia, especially the region of the upper Blue Nile basin the source of the Nile River.

To achieve the above goals and objectives, this chapter is outlined as follows: Ethiopian rainfall climatology is briefly outlined in section 2.3, rainfall and SST data is presented in section 2.4, research methodology is presented in section 2.5, results are presented and discussed in section 2.6 and observations and conclusions are given in Section 2.7.

2.3 Brief Climatology of Ethiopian Rainfall

Ethiopia has generally three rainy seasons. These are the June to September (JJAS) rainy season, locally called the Kiremt and the February/March-June (F/MAM-J) rainy season, locally called the Belg and the October-January (ONDJ) rainy season, locally called the Bega. Most of the rainfall occurs during the Kiremt rainy season, when 60-90% of the rainfall occurs. and when 90-95% of all food of Ethiopia is produced during the Kiremt rainy season. The Kiremt rainy season occurs in the western half of Ethiopia, central and most eastern parts, while the Belg and Bega rainy season mainly occurs to the south and south eastern parts of Ethiopia. The Belg rainy season is the main rainy season for southern Ethiopia and coincides with the MAM rainfall of East Africa (Mwale et al., 2005).

2.4 Rainfall and Sea Surface Temperature Data

Historical monthly precipitation data (1900-1998), '*gu23wld0098.dat*', Version 1.0, was supplied by Dr. Mike Hulme at the Climatic Research Unit, University of East Anglia (UEA) in the United Kingdom. The data, gridded at a resolution of 2.5° latitude \times 3.75° longitude was extracted from the region 18° N- 2° N to 33° E- 48° E over Ethiopia and the surrounding areas (Figure 2.1). Data was extracted for 23 grid points and filling the missing grid points with zeros to form 35 grid points, just for facilitating the correlation maps plotting. This data is part of historical monthly precipitation dataset for global land areas from 1900 to 1998. These data were constructed from station data using Thiessen polygon weights. No topographic weighting has been applied to the interpolation scheme. Because the method interpolates anomalies and not precipitation values, it is rea-

sonable to exclude the effects of elevation. The data quality control of these gridded data is described in [Hulme \(1992\)](#); [Hulme et al. \(1998\)](#), [Hulme and New \(1997\)](#) and [Hulme \(1994\)](#). Since this study focuses on the *Belg* and *Kiremt* seasons, the seasonal, averaged data for February to May (FMAM) and June to September (JJAS) were computed for each year. A longer (1900-2006) and high resolution ($0.5^\circ \times 0.5^\circ$) rainfall data set was also collected from the University of Delaware (UoD) in the USA. Comparison between the University of East Anglia and the University of Delaware data showed major disagreements, and the latter data was discarded (see distance correlation plots in [Figure 2.2](#) and scatterplots in [Figure 2.3](#)). Some of the grids points are with low correlation and scattered, which are near to the Red Sea (e.g. [Figure 2.2](#) and [2.3c, f, g, and o](#)). Also point in the west (e.g. [Figure 2.2](#) and [2.3h, and m](#)) these are the worst. The latter data was discarded in favor of the former because the former has been extensively used and shown to be reliable.

Global mean monthly SST data of 1870-2008, at $1^\circ \times 1^\circ$ grid resolution was extracted for all the global oceans, about 65,000 grids from Hadley Centre, Version 1.1 of HadISST from United Kingdom Met Office. The monthly SST anomaly grid data were transformed into seasonal SST (October-December, OND, January-March, JFM, April-June, AMJ and July-September, JAS) anomalies.

2.5 Research Methodology

2.5.1 Wavelet analysis

[Torrence and Compo \(1998\)](#) defined the wavelet transform of an observed time series, O with respect to the mother wavelet, $\psi_o(\eta)$, as a convolution integral:

$$\psi_{\circ}(\eta) = \pi^{-1/4} e^{i\omega_{\circ}\eta} e^{-\eta^2/2}, \quad (2.1)$$

$$Z(t, b) = \frac{1}{\sqrt{b}} \int_0^n O\psi^* \left(\frac{n-t}{b} \right) dn, \quad (2.2)$$

Where ψ^* is the complex conjugate of (ψ) , and n is the total length of the observation, and $Z(t, b)$ is a wavelet spectrum of the decomposed time series at scale b and time t . The quantity $\frac{1}{\sqrt{b}}$ in Equation (2.2) is an energy normalization term, which ensures that the energy of the mother and daughter wavelets remain the same over all scales, making it possible to directly compare wavelet transforms of one time series with another (Torrence and Compo, 1998).

The wavelet function (ψ) can be constructed so that it can easily be used to match a time series. For analyzing rainfall or SST time series, Mwale et al. (2004) suggested using a Morlet wavelet. Convoluting a rainfall or SST time series with a Morlet wavelet over time gives a wavelet spectrum, whose coefficients show how well the wavelet matches with the time series. Therefore, at each scale the magnitude of the spectrum coefficients depict the amplitude of a time series.

When the wavelet spectrum coefficients at each scale are summed over the length of a time series, they give a new representation of a wavelet spectrum called a global wavelet spectrum. A global wavelet spectrum is similar to a Fourier spectrum. Both spectra show periodic cycles present in the time series, but not their localized occurrence in time.

Having computed the wavelet spectrum, the scale averaged wavelet power (SAWP), which represents the mean variance of wavelet coefficients

over a range of scales, may also be computed from the wavelet spectrum. The range of scales (e.g. 2-8 years) can be visually identified from the significant power found in the continuous wavelet spectrum. This is done in order to examine the variation of rainfall and SST over a range of statistically significant oscillations, as follows:

$$\overline{W}_t^2 = \frac{\delta_j \delta_t}{C_\delta} \sum_{j=j_1}^{j_2} \frac{|W_t(b, a_j)|^2}{a_j}, \quad (2.3)$$

Where C_δ is 0.776 for the Morlet wavelet, δ_j is a factor for scale averaging, and δ_t is the sampling period (Torrence and Compo, 1998). Since SAWP is a time series of average variance in a certain frequency band, SAWP can also be used to examine the modulation of one time series by another (e.g., variation of rainfall due to SST variations) or the modulation of one frequency by another within the same time series.

2.5.2 Wavelet Empirical Orthogonal Functions Analysis

Wavelet empirical orthogonal function (WEOF) analysis or wavelet principal component analysis (WPCA) transforms an “ $n \times k$ ” data of scale averaged wavelet power (SAWP) into another “ $n \times k$ ” data of SAWP signals and noise. Here, n and K represent the length of the rainfall/ SST time series and the number of data grid points, respectively. The signals and noise are called wavelet principal components, WPCs, designated here as U . U accounts for all the variability in the SAWP and some noise due to minor errors (i.e., extra energy introduced into the SAWP because δ_t the sampling period is discrete and may include spurious energy into the wavelet spectrum). If the rainfall or SST variability were the same at all grid points, the matrix U would contain one SAWP signal (WPC1), which

would account for all the variations of the SAWP. Mwale et al. (2009) pointed out this is never the case because SST in different parts of the oceans will vary differently. Similarly, rainfall varies differently from place to place. Hence, there are usually a few U (or u_m) to account for the majority of the SAWP variation. The SAWP signals (u_m) are computed as follows:

$$u_m = e_m^T O' = \sum_{k=1}^K e_{km} O'_k, \quad m = 1, \dots, m, (\text{where } m \ll K), \quad (2.4)$$

Where, e_{km} are the eigenvectors, are the k SAWP anomalies, and m represents a small subset of the k possible signals. The signals, u_m , are usually the major spatial and temporal patterns that account for the majority of the variations in the SAWP, and can be used to spatially delineate rainfall or SST variations into independent zones.

It is generally useful to have an idea about the number of signals present in a group of observed time series. This can be done by computing Eigenvalues and Eigenvectors of the time series and showing their relative values in a plot (called a Scree plot). The relative size of the Eigenvalues represents how “independent” the Eigenvectors are; the farther apart the Eigenvalues, the more distinct their corresponding Eigenvectors and vice versa. This is one subjective way to check how many signals are present in the time series. The other way is to look for an “elbow” or sudden change in the gradient of the Scree plot. Eigenvalues to the left of the “elbow” are subjectively considered to represent Eigenvectors that correspond to signals in the time series, while the ones to the right of the elbow are essentially “noise”.

2.6 Data Analysis and Results

2.6.1 Dominant Oscillations

Before the 1900-1998 scale averaged wavelet power (SAWP) was computed for each rainfall or SST grid, the range of dominant periodic cycles (i.e., oscillations above the 95% confidence level of a red noise process) in the rainfall and SST time series were identified using the time domain wavelet spectra and the frequency fixed global spectra. Figure 2.4 a (b). shows an example wavelet and global spectra of Ethiopian rainfall from 12°N and 41.25°E (5°N and 33.75°E) during JJAS (FMAM). Using this and other figures (not shown), statistically significant power in JJAS and FMAM Ethiopian rainfall was found to show statistically significant oscillations at 2-8 year, and about 32 year frequency bands.

Equally, since there were 65,000 grid points of SST data, we could not show wavelet and global spectra for all the SST data. An example wavelet spectrum of SST extracted at 0.5°N - 98.5°W , which shows dominant oscillations of SST within the 2-8 year range is given in Figure 2.4c. However, some SST data (not shown) exhibited frequencies with the 2-16 year range for the 95% significance level in the continuous wavelet spectrum. To be able to simultaneously analyze rainfall and SST, only the 2-8 year frequency range could be used. Hence, the SAWP for both the SST and rainfall was computed using the 2-8 year frequency range.

2.6.2 How Many Signals in Rainfall or SST Data?

When using a filtered time series, such as the SAWP, a useful way to determine the number of signals present in a time series can be done by observing spatial patterns of the Eigen vectors (Mwale et al., 2004). Mwale et al. (2004, 2009) found that rainfall spatial patterns may reflect the regional physiographic or topographic characteristics, localized climatic

processes or warming and cooling of regional ocean current systems. Some Eigenvectors, especially the ones that cover very small areas are discarded, because they are considered as “noise” or meaningless. Figure 2.5 shows the Scree plot of the Ethiopian Highlands rainfall, for the 2-8 yrs. during, (JJAS and FMAM). Notice 35 points in the Figures 2.5 (a) and (b), because of filling the missing grid points from the original data. Figure 2.6 shows the Scree plot of global oceanic SST for the 2-8 yrs. scale band, Hadley SST dataset, for the seasons of October-December (OND), January-March (JFM), April-June (AMJ) and July-September (JAS). From Figures 2.5 and 2.6, Ethiopian rainfall (both JJAS and FMAM) may have up to four (4) distinct signals and global SSTs appear to have three (3) distinct signals.

2.6.3 Spatial Patterns of June-September Rainfall

Although Figure 2.5 showed that the June-to-September (JJAS) rainfall over Ethiopia appeared to have four signals that account for the majority of rainfall variability, only the first two leading wavelet principal components (WPCs), i.e., WPC1 and WPC2, were retained for analysis, because the other two WPCs could not explain any further spatial details (Figures not shown). The first two WPCs jointly accounted for 41% of the total rainfall SAWP variability, with WPC1 explaining 23% and WPC2 18%. Figures 2.7(a) and 2.7(b) show the spatial patterns formed by correlating WPC1 and WPC2 to the rainfall SAWP at each of the 23 points, with contours outside Ethiopia trimmed off. WPC1 is positively correlated to SAWP from the Great Rift Valley (GRV) to northern Ethiopia (excluding an area north 12.5°N , between 37.5°N and 43°N) and negatively correlated to southern Ethiopia, south of the GRV. The strongest positive correlations were in the western half of Ethiopia. The correlations decrease northwards, eastwards and southwards, all towards the GRV. The tightness of contours along the GRV showed decreasing correlation between WPC1 and SAWP (i.e.,

variation of rainfall in the GRV is different) highlighting the leverage the topography of GRV has on the Ethiopian rainfall. In Ethiopia, the GRV is a geographic trench 50-100 km wide (see Figure 2.1), which cuts Ethiopia diagonally from the southwestern corner of the country. From the middle of the country and stretching northeast-wards, the GRV funnels out into a triangular depression (the Afar Triangle) with its base stretching from the Gulf of Aden to the Red Sea (see Figure 2.1). Rainfall variability in the Afar Triangle region and an area north of 12.5°N (between 37.5°N and 43°N) was not accounted for by WPC1, because the rainfall in this area varies independently of rainfall to the rest of Ethiopia. The variability of rainfall in the Afar Triangle and the area north of 12.5°N (between 37.5°N and 43°N) is shown in Figure 2.7(b). Figure 2.7(b) shows that WPC2 is negatively correlated to SAWP in the region (12.5°N - 17.5°N and 37.5°N - 44°N), and positively correlated to the Afar Triangle region, with a boundary at about 10°N - 41.2°N , which separates the two regions.

Figures 2.7(c), 2.7(d), 2.7(e) and 6(f) shows the spatial patterns of Ethiopian rainfalls WPC1 and WPC2 using energy extracted from the 2-4 and 5-7-year frequency bands. Figure 2.7(e) appears more similar to Figure 2.7(a) than does Figure 2.7(c) to Figure 2.7(a), showing that spatially 5-7 year frequency periods are more dominant within the 2-8 year frequency band than the 2-4 year frequencies. Figure 2.7(c) show that the 2-4 year frequency energy is dominant in the whole of Ethiopia, north of the GRV, and much weaker south of the GRV. The similarity of spatial patterns corresponding to WPC1, among all frequency bands, north of the GRV shows that, except along the GRV, where correlations between WPC1 and SAWP are weak or zero, all frequencies in the 2-8 year bands are important in the JJAS Ethiopia rainfall. Similarly, Figure 2.7(d) and Figure 2.7(f) appears similar to Figure 2.7(b), showing also that the 2-4 year and 5-7 year frequencies are dominant within the 2-8 year frequency band.

From the spatial patterns of three spectral bands (i.e., 2-4, 5-7 and 2-8 years), Ethiopia's JJAS rainfall may generally be delineated into three nonstationary rainfall zones. These zones are western Ethiopia north of the GRV, southern Ethiopia, south of GRV and the GRV from southwestern Ethiopian to the Afar Triangle. The steep gradient along the GRV shows that while JJAS rainfall occurs all over Ethiopia; its variability is attenuated by the valley, and it is out of phase between western Ethiopia and southern Ethiopia. Since the rainfall pattern is negatively correlated to southern Ethiopia, WPC1 shows that when JJAS rainfall increases for the rest of Ethiopia, it decreases in southern Ethiopia and vice versa.

2.6.4 Temporal Patterns of June-September Rainfall

Figure 2.8 shows the temporal variations of the leading Eigenvector time series of JJAS Ethiopian rainfall (i.e., WPC1 and WPC2) for frequency bands, 2-8 years, 2-4 years and 5-7 years. Since SAWP was created from a convolution of rainfall by a periodically adjusted wavelet, the positive gradients in the SAWP are interpreted as increasing rainfall and vice versa.

Figure 2.8 (a) shows that apart from the two periods of 1910-1917 and 1990-1998, which showed positive gradient in WPC1, Ethiopian rainfall was in the doldrums for much of the 20th century, with the lowest rainfall in the 1980, followed by 1941-2. Decreasing rainfall leading up to 1980 and 1941-2 is shown as low energy troughs in WPC1. Table 2.1 of [Degefu \(1987\)](#) chronicles droughts in Ethiopia, as depicted by famines and levels of the river Nile from 253 BCE. The table documented droughts during 1913-14, 1921-22, 1932-34, 1953, 1957-1958, 1960, 1964-1966, 1968-1978, 1982-1985, and 1991-1992. Those periods are depicted in WPC1 as troughs or plateaus. The three "peaks" of WPC1 (i.e., 1917, the two decades of 1945-1965 and 1990) do not show any regularity, espousing the fact that Ethiopian rainfall exhibits a truly non-stationary character. Hence, by looking at WPC1, it is

not possible to predict when the next anomalously wet or dry rainfall period will occur. Although data was limited for most of global land areas before 1945, including Ethiopia, the few data that are available and interpolated for 1900-1998 by [Hulme \(1992\)](#) appears to have captured the variation of Ethiopian rainfall and validated the use of this data in Ethiopia for periods before 1945. Figure 2.8 (b) shows the temporal variations of WPC2. This Figure shows that rainfall consistently decreased from 1900 to about 1963, with a brief increase between 1963 and 1975 and exhibited strong regular variations between 1965 and 1998. WPC2 is positively correlated to the Afar Triangle region of Ethiopia and represents the calamitous regime of rainfall variability for this region.

A closer look at the narrower bands of frequency energy in the SAWP (i.e., 2-4 year and 5-7 year of Figures 2.8(c)- 2.8(f)) showed that the JJAS 2-8 year WPC1 was largely dominated by the 2-4 year cycles and modulated by 5-7 year cycles, while WPC2 was dominated by 5-7 year cycles and modulated by 2-4 year cycles. The correlation between the 2-4 year WPC1 and 2-8 year WPC1 is 0.62, (i.e., the 2-4 year frequency band explains $(0.62^2=38\%$ variance in the 2-8 year band), while WPC2 (5-7 year) explained 57% of WPC2 (2-8 year). This means that in western Ethiopia, the 2-4 year rainfall frequencies dominates rainfall variation within the 2-8 year frequency band (see Figure 2.8(a) and 2.8(c)), but their trends are dominated by the 5-7 year frequency band (see Figure 2.8(a), 2.8(c) and 2.8(e)), which explains the suppression of the 1940-1965 peak in the WPC1 of the 2-8 year frequency band. This result re-affirms that when low frequency energy (i.e. 5-7 yrs.) is propagating towards the trough, the 2-4 year (inter-annual) rainfall variations appears to not have enough energy to offset the 5-7 year energy propagation of the Ethiopian rainfall. This result is similar to that of [Segele et al. \(2009\)](#) who found that major climatic system processes contributing to the annual mode get augmented

or suppressed by seasonal, quasi biennial and ENSO time-scale variability. Hence, when analyzing Ethiopian rainfall, it is necessary to simultaneously look at both low (5-7) and high (2-4) frequency bands, to figure out the direction of propagation of the composite 2-8 year rainfall.

On the other hand, in northeastern Ethiopia, the 5-7 year frequencies dominate the rainfall (see Figure 2.8(b) and 2.8(f)), while the 2-4 year frequencies have limited influence in the variation of the 2-8 year frequency band (see Figure 2.8(b), 2.8(d), and 2.8(f)). This means that between 1900 and 1998, north eastern Ethiopia (Afar Triangle), experienced decreasing rainfall for over 60 years (1900-1963).

2.6.5 Spatial Patterns of February-May (FMAM) Rainfall

Figure 2.9 shows the spatial patterns of FMAM rainfall. Figure 2.9(a) shows that WPC1 is positively correlated to southern Ethiopia and negatively correlated elsewhere in Ethiopia, while Figure 2.9(b) shows that WPC2 is negatively correlated to almost all parts of Ethiopia, except the northernmost region. The two spatial patterns resemble those of JJAS rainfall and also divide Ethiopian into three zones. Because of similarity between the FMAM and JJAS rainfall patterns, the former are not discussed further.

Figures 2.9(c), 2.9(d), 2.9(e) and 2.9(f) show spatial patterns of WPC1 and WPC2, computed from 2-4 and 5-7 year frequency bands. These figures show similar patterns as that of WPC1 of 2-8 year. Similar to the JJAS rainfall, energy within the 2-4 and 5-7 year for FMAM rainfall also dominated the Ethiopian rainfall.

2.6.6 Temporal Patterns of February-May Rainfall

Figure 2.10 shows the temporal variations of WPC1 and WPC2 for the FMAM rainfall, for 2-8 years, 2-4 years and 5-7 years frequency bands. Figure 2.10(a) shows that WPC1 exhibited highly irregular variations, generally with less energy between 1900 and 1943, positive energy between 1944 and until about 1980, and after which it shows a dramatic decrease in energy. Since WPC1 is positively correlated to southern Ethiopia and negatively correlated to all other areas of the country, the variations in energy show that southern Ethiopia suffered from a serious decrease of rainfall for 1920-1945 and 1980-1998.

WPC2 (Figure 2.10(b)) also shows an irregular variation of energy, which generally decreases from 1900 to 1998 with the worst being 1965 and 1998. Decreases in the FMAM rainfall have impacted southern Ethiopia, where it is the main rainy season.

When the power within the 2-4 year (Figure 2.10(c) and 2.10(d)) and 5-7 year (Figure 2.10(e) and 2.10(f)) bands is examined, it is clear that the temporal variation of WPC1 computed using 2-8 year frequency bands was dominated by power in the 2-4 year range, but not by the 5-7 year cycles. WPC1 (WPC2) of the 2-4-year band explain 88%(86%) of the energy variation in 2-8 year frequency band, while the 5-7 WPC1(WPC2) bands explain 11%(41%) of the energy variation in the 2-8 year frequency band. This means that for FMAM rainfall the 2-4 year frequencies show more rainfall variations than that of the 5-7 year.

2.6.7 Global Sea Surface Temperature Variations

SST spatial and temporal patterns were computed for January-March (JFM), April-June (AMJ), July-September (JAS), and October-December (OND). Only the first two WPCs were retained for further analysis. The JFM SST was chosen to see if there was a 3-month lead time to help with

future prediction of JJAS Ethiopian rainfall from SST variations.

2.6.8 Spatial Patterns of Global SST

Figures 2.11(a), 2.11(c), 2.11(e) and 2.11(g) show the leading SST SAWP spatial variations of (2-8 yrs.) frequency band as represented by WPC1 of global SST, for OND, JFM, AMJ and JAS, while Figures 2.11(b), 2.11(d), 2.11(f) and 2.11(h) show similar variations represented by WPC2. Of the total seasonal SST SAWP variability, WPC1 (WPC2) accounted for 30% (15%) in OND, 29% (14%) in JFM, 31% (13%) in AMJ and 27% (13%) in JAS. Figures 2.11(a), 2.11(c), 2.11(e) and 2.11(g) show that regardless what time of the year, the strongest contributions to global SST variations occur in the Antarctic Ocean region (50° S- 70° S), the El Niño region of south America (5° N- 5° S and 150° W- 160° E) and the southwestern Pacific Ocean region. As expected, in Antarctica, the widest (Figure 2.11c) and strongest variations occur during JFM and narrowest variations (Figure 2.11g) occur during JAS. Because JFM is the summer in the southern hemisphere, therefore it has strong variation. WPC2 shows that the second leading global SST variations are dominant in the Atlantic and Indian Oceans and part of the Pacific (i.e., ocean areas located on either side of the El Niño region in South America).

Figures 2.11(a), 2.11(c), 2.11(e) and 2.11(g) show the nonstationary, migratory patterns of ocean SST variations of the El Niño, Atlantic and Antarctic Ocean basins. The figures show that during the OND period, SST variations show El Niño developing from the Pacific Ocean towards the south American coast (i.e., 140° W- 100° W and 5° N- 5° S). By JFM, SST variations intensify and develop along the South American coastlines, extending roughly from 80° W- 160° W and 10° N- 10° S and by AMJ, SST variations are fully developed both along the coastline and extend to 160° W. By JAS, variations in the El Niño region begin to dissipate, starting

at 160° W. The SST variations and migration patterns in the Atlantic and Indian Oceans are similar to that found by [Mwale et al. \(2005\)](#) and so are not discussed further.

2.6.9 Temporal patterns-Sea Surface Temperature

Figures [2.12\(a\)](#), [2.12\(c\)](#), [2.12\(e\)](#) and [2.12\(g\)](#) show the temporal variations of the leading Eigenvectors of global SST from 1870 to 2006 for OND, JFM, AMJ and JAS. These figures show that generally between 1870 and 1960, low energy variations dominated the nonstationary characteristics of the global SST. However, between 1960 and 1998 there was a sharp increase in the energy of WPC1, which peaked in 1980 for OND, 1985 for JFM, 1985 for AMJ and 1990 for JAS. Since WPC1 is positively correlated to the Antarctic Ocean, it shows that the Antarctic Ocean underwent considerable warming for about four decades (1960–1998). However, after 1980, there appears to be a dramatic decrease in SST for this region of the earth.

Figures [2.12\(b\)](#), [2.12\(d\)](#), [2.12\(f\)](#) and [2.12\(h\)](#) also show the variations of the second leading Eigenvectors (WPC2) of global SST from 1900 to 1998 for OND, JFM, AMJ and JAS, respectively. Similar to Figures [2.12\(a\)](#), [2.12\(c\)](#), [2.12\(e\)](#) and [2.12\(g\)](#), these figures show that between 1900 and 1940, low energy dominated the nonstationary characteristics of global SST, which sharply increased between 1940 and 1975, peaking in 1970 for all seasons of OND, JFM, AMJ and JAS, and sharply decreasing between 1975 and 1998, confirming [Mwale et al.’s \(2004\)](#) finding. This means that ocean regions positively correlated to WPC2 experienced warming between 1940 and 1975 and experienced cooling between 1975 and 1998. A comparison of WPC1 and WPC2 shows that increase in SST started in the Atlantic and Indian Oceans spread to the Antarctic Ocean region, which had probably contributed to the melting of sea ice in the Antarctic because of the large

specific heat capacity of the oceans.

2.6.10 Teleconnecting Rainfall and Sea Surface Temperature

Figure 2.13 shows the spatial correlation patterns between gridded precipitation WPC1 and WPC2 and each of the 65,000 SAWP of gridded global SST, during JFM. Figure 2.13(a) shows that JJAS rainfall is correlated to the El Niño region and the northern Atlantic Ocean (west of the Sahara desert). Some other areas include areas east and west of South America and areas south of Indian Ocean. The correlations between SST SAWP and rainfall WPCs show that SST explains up to 16% (i.e. correlation of 0.4) of the rainfall variability. The WPCs that defined the rainfall zones explained up to 64% (i.e. correlation of 0.8) of the rainfall SAWP variation. Therefore, correlation between rainfall WPC1 and SST SAWP in the El Niño region appear comparatively weak (up to 16% of the explained variation), showing a causal relationship, but nonetheless a weak one. Figure 2.13(b) shows that JJAS rainfall over the Afar triangle is correlated to the Gulf of Aden and the southern Pacific Ocean (west of South America).

2.7 Observations and Conclusions

Ethiopia's climate variation, in particular rainfall, is known to be non-stationary. Because of its nonstationarity, nonstationary analyses techniques of wavelet empirical orthogonal function analysis (WEOF) were employed to analyze the variability of rainfall in space and time. To complement the nonstationarity of Ethiopia's rainfall variability, the techniques were also applied to global ocean SST variations, which are known to be linked to Ethiopian's rainfall variations. Other than examining the non-stationarity of Ethiopian rainfall and global SST variations, the aim is to

teleconnect the two climatic variables.

The study revealed that both the June-September (JJAS) and February-May (FMAM) global SST variations espouse nonstationary characteristics. From a nonstationary perspective, rainfall variability in Ethiopia was delineated into three zones. These are western half of Ethiopia north of the Great Rift Valley (GRV), southern Ethiopia south of the GRV, and the GRV from the south west to the Afar Triangle (see [Eklundh and Pilesjö, 1990](#); [Bekele, 1997](#); [Diro et al., 2011](#)).

Temporal characteristics of the leading wavelet principal component signals showed Ethiopian rainfall, during JJAS, in the doldrums for most of the Twentieth century (1900-1998), with major periods of drought during the 1940s and 1980s. The temporal characteristics also showed that despite of three peaks in the rainfall data (1913-1917, 1945-1955 and 1990-1998); these peaks were so irregular that Ethiopian rainfall exhibits a strong non-stationary character.

The dominant frequencies in the Ethiopian rainfall ranged between 2 and 8 years. In western Ethiopia north of the GRV, the 2-4 year rainfall frequencies dominated the rainfall variation within the 2-8 year frequency band, but their trends are modulated by the 5-7 year frequency band. Hence, when analyzing Ethiopian rainfall, it is necessary to simultaneously examine both the low (5-7 years) and the high (2-4 years) frequency regimes, to understand the nonstationary behavior. On the other hand, in northeastern Ethiopia (Afar Triangle region), the 5-7 year frequencies dominate the rainfall but the 2-4 year frequencies have limited influence in the variation of the 2-8 year frequency band. This means that between 1900 and 1998, the north eastern Ethiopia experienced decreasing rainfall for 60 years (1900-1960), following the 5-7 year cycles of drought.

The non-stationary characteristic of seasonal global SST (January-March-JFM, April-June-AMJ, July-September-JJS and October-December- OND)

revealed that regardless of the time of the year, the strongest contributions to global SST variations occur in the Antarctic Ocean region, the El Niño region of south America and the south western Pacific Ocean region. The next dominant oceanic regions were the Atlantic and the Indian oceans. Interesting findings of this study include the annual migration patterns of SST variation in the El Niño region, the Antarctic Ocean and the Atlantic which show the varying predictor data locations throughout the year. A comparison of leading signals in the oceans showed that increase in SST started in the Atlantic and Indian oceans, which spread to the Antarctic Ocean, which probably contributed to the melting of Antarctic sea ice because of the large specific heat capacity of the oceans.

It was also found that the correlation between rainfall wavelet principal components (WPC1) and SST-SAWP in the El Niño region were comparatively weak, which means a weak relationship between El Niño SST and the Ethiopian rainfall, and so it will be difficult for us to relate individual El Niño events to the rainfall deficits or droughts in Ethiopia.

Acknowledgements

This research was funded by the Egyptian Ministry of Higher education (MHE). The Wavelet software was provided by Torrence and Compo. It may be downloaded from the following website. <http://atoc.colorado.edu/research/wavelets/>

References

Abegaz, A., Keulen, H., Haile, M., and Oosting, S. (2007). Nutrient dynamics on smallholder farms in Teghane, Northern Highlands of Ethiopia. In A. Bationo, B. Waswa, J. Kihara, and J. Kimetu (Eds.), *Advances in*

- integrated soil fertility management in sub-Saharan Africa: Challenges and opportunities* (p. 365-378). Springer Netherlands.
- Bekele, F. (1997). Ethiopian use of ENSO information in its seasonal forecasts. *Internet Journal of African Studies*, 2(5). Retrieved from <http://ccb.colorado.edu/ijas/ijasno2/bekele.html> (Accessed: 11/26/2008)
- Bewket, W., and Conway, D. (2007). A note on the temporal and spatial variability of rainfall in the drought-prone Amhara region of Ethiopia. *Int.J.Climatol.*, 27(11), 1467-1477.
- Degefu, W. (1987). Some aspects of meteorological drought in Ethiopia. In M. H. Glantz (Ed.), *Drought and hunger in Africa: Denying famine a future* (p. 23-36). Cambridge, England: Cambridge University Press.
- Diro, G., Grimes, D., and Black, E. (2011). Teleconnections between Ethiopian summer rainfall and sea surface temperature: part I- observation and modelling. *Clim.Dyn.*, 37(1), 103-119.
- Eklundh, L., and Pilesjö, P. (1990). Regionalization and spatial estimation of Ethiopian mean annual rainfall. *Int.J.Climatol.*, 10(5), 473-494.
- Gissila, T., Black, E., Grimes, D. I. F., and Slingo, J. M. (2004). Seasonal forecasting of the Ethiopian summer rains. *Int.J.Climatol.*, 24(11), 1345-1358.
- Hulme, M. (1992). A 1951-80 global land precipitation climatology for the evaluation of General Circulation Models. *Clim. Dyn.*, 7, 57-72.
- Hulme, M. (1994). Validation of large-scale precipitation fields in General Circulation Models. In M. Desbois and F. Desalmand (Eds.), *Global precipitations and climate change*. Springer-Verlag.

- Hulme, M., and New, M. (1997). Dependence of large-scale precipitation climatologies on temporal and spatial sampling. *J.Clim.*, 10(5).
- Hulme, M., Osborn, T., and T.C.Johns. (1998). Precipitation sensitivity to global warming: Comparison of observations with HadCM2 simulations. *Geophys. Res. Letts.*, 25, 3379-3382.
- Mwale, D., Gan, T. Y., Devito, K., Mendoza, C., Silins, U., and Petrone, R. (2009). Precipitation variability and its relationship to hydrologic variability in Alberta. *Hydrol. Processes*, 23(21), 3040-3056.
- Mwale, D., Gan, T. Y., and Shen, S. S. P. (2004). A new analysis of variability and predictability of seasonal rainfall of central southern Africa for 1950-94. *Int.J.Climatol.*, 24(12), 1509-1530.
- Mwale, D., Gan, T. Y., Shen, S. S. P., Shu, T. T., and Kim, K.-M. (2007). Wavelet empirical orthogonal functions of space-time-frequency regimes and predictability of southern Africa summer rainfall. *J.Hydrol.Eng.*, 12(5), 513-523.
- Mwale, D., Shen, S., and Gan, T. (2005). Integration of wavelet or Hilbert transforms and disaggregation for weekly streamflow prediction from seasonal oceanic variability. *Proceeding conference, AMS Forum: Living with a Limited Water Supply*.
- Segele, Z., Lamb, P., and Leslie, L. (2009). Seasonal-to-Interannual variability of Ethiopia/Horn of Africa Monsoon. part I: Associations of Wavelet-filtered large-scale atmospheric circulation and global Sea Surface Temperature. *J.Clim.*, 22(12), 3396-3421.
- Seleshi, Y., and Demaree, G. (1995). Rainfall variability in the Ethiopian and Eritrean highlands and its links with the Southern Oscillation Index. *J.Biogeogr.*, 945-952.

Shanko, D., and Camberlin, P. (1998). The effects of the southwest Indian Ocean tropical cyclones on Ethiopian drought. *Int.J.Climatol.*, 18(12), 1373-1388.

Torrence, C., and Compo, G. P. (1998). A practical guide to Wavelet analysis. *Bulletin of the American Meteorological Society*, 79(1), 61.

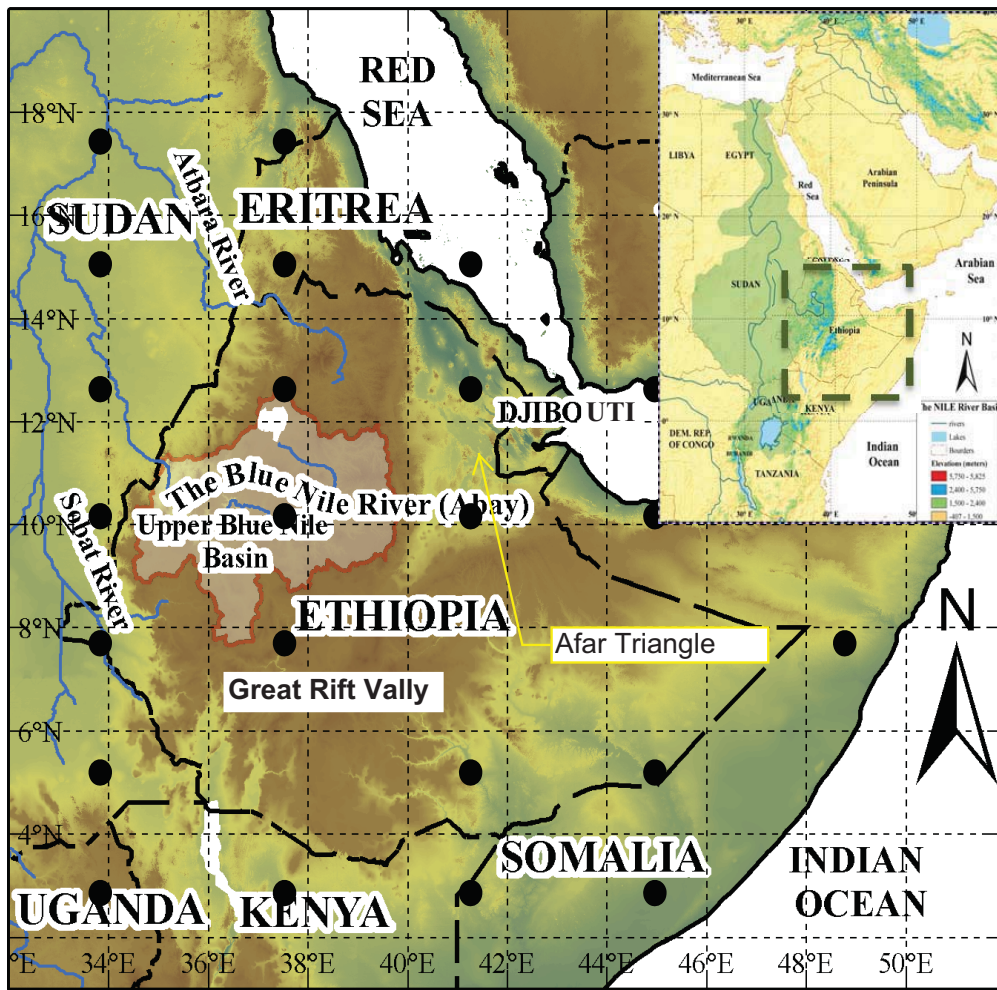


Figure 2.1: Ethiopian Highlands map showing grid points of monthly rainfall data of University of East Anglia at $2.5^\circ \times 3.75^\circ$ resolution used in this study. Notice irregular grid points with total 23 grid points due to missing surrounding stations.

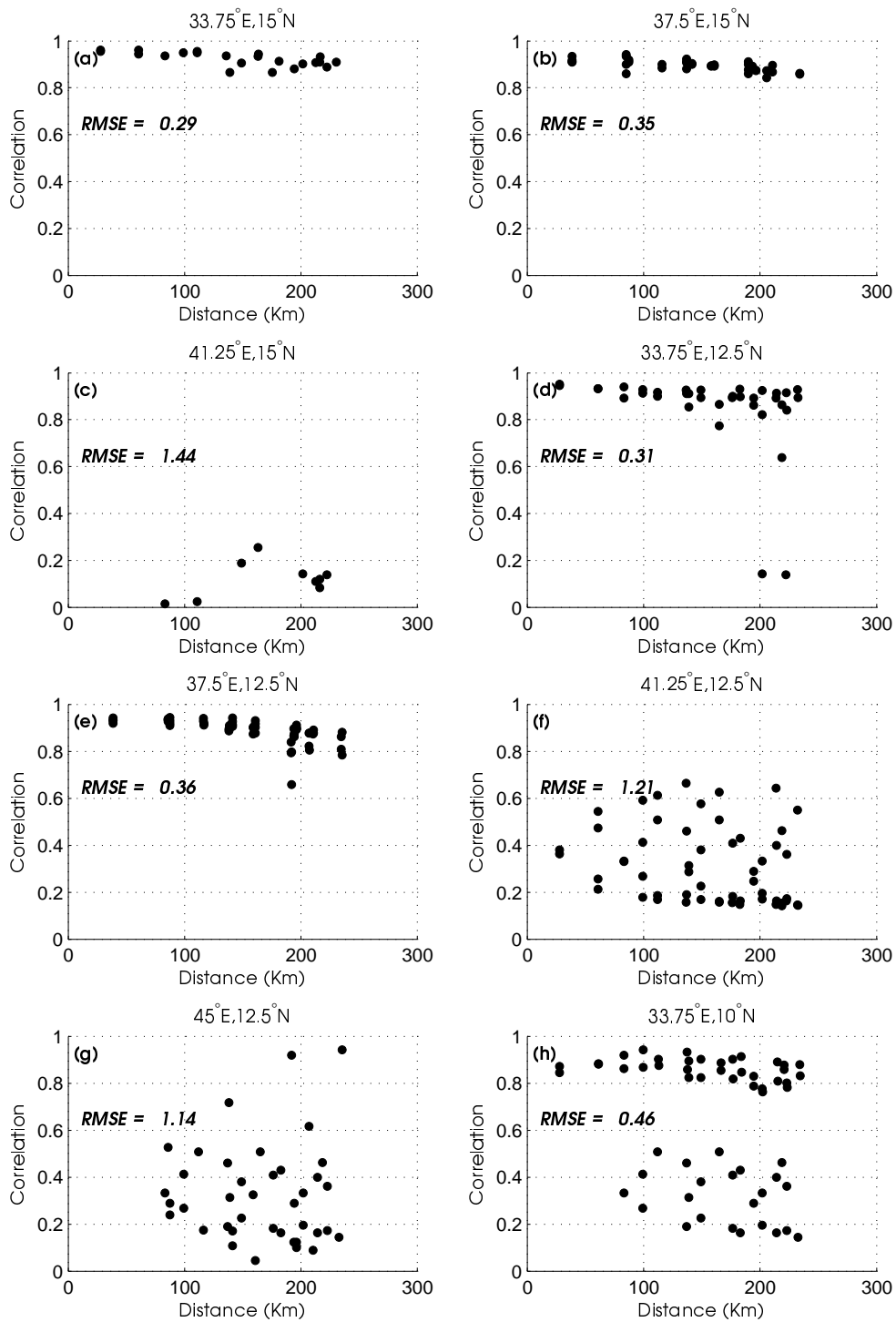


Figure 2.2: Correlation-distance plots of Pearson correlation versus inter-grid distance between gridded data of UEA and UoD are presented, such that specific grid points of UEA data, (a) to (p), are selected as the reference while grid points of UoD data considered are those located within a circle of 233 km radius and centered at these selected grid points of UEA.

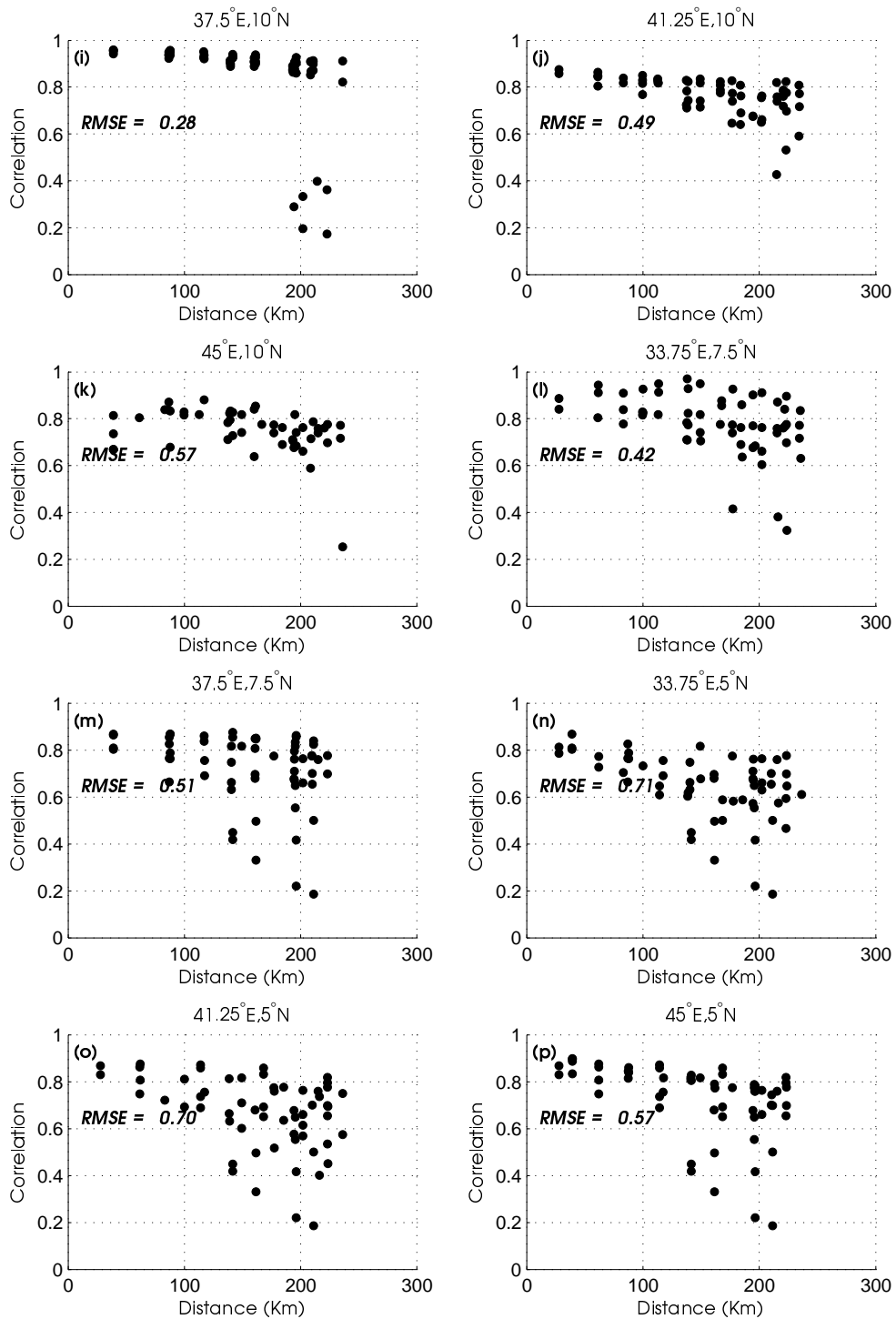


Figure 2.2: continued

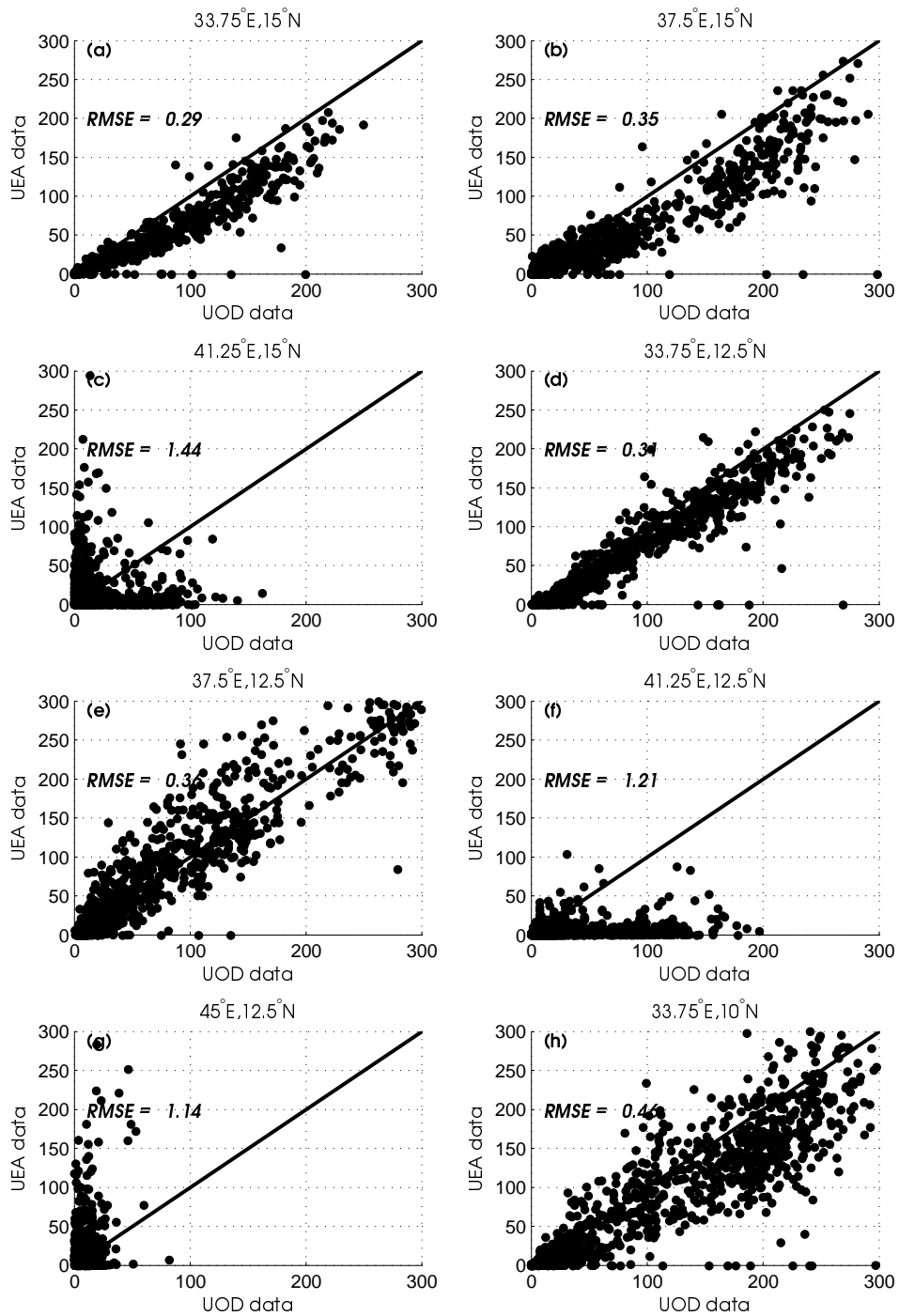


Figure 2.3: Scatter plots of Pearson correlation versus inter-grid distance between gridded data of UEA and UoD are presented, such that specific grid points of UEA data, (a) to (p), are selected as the reference while grid points of UoD data considered are those located within a circle of 233 km radius and centered at these selected grid points of UEA.

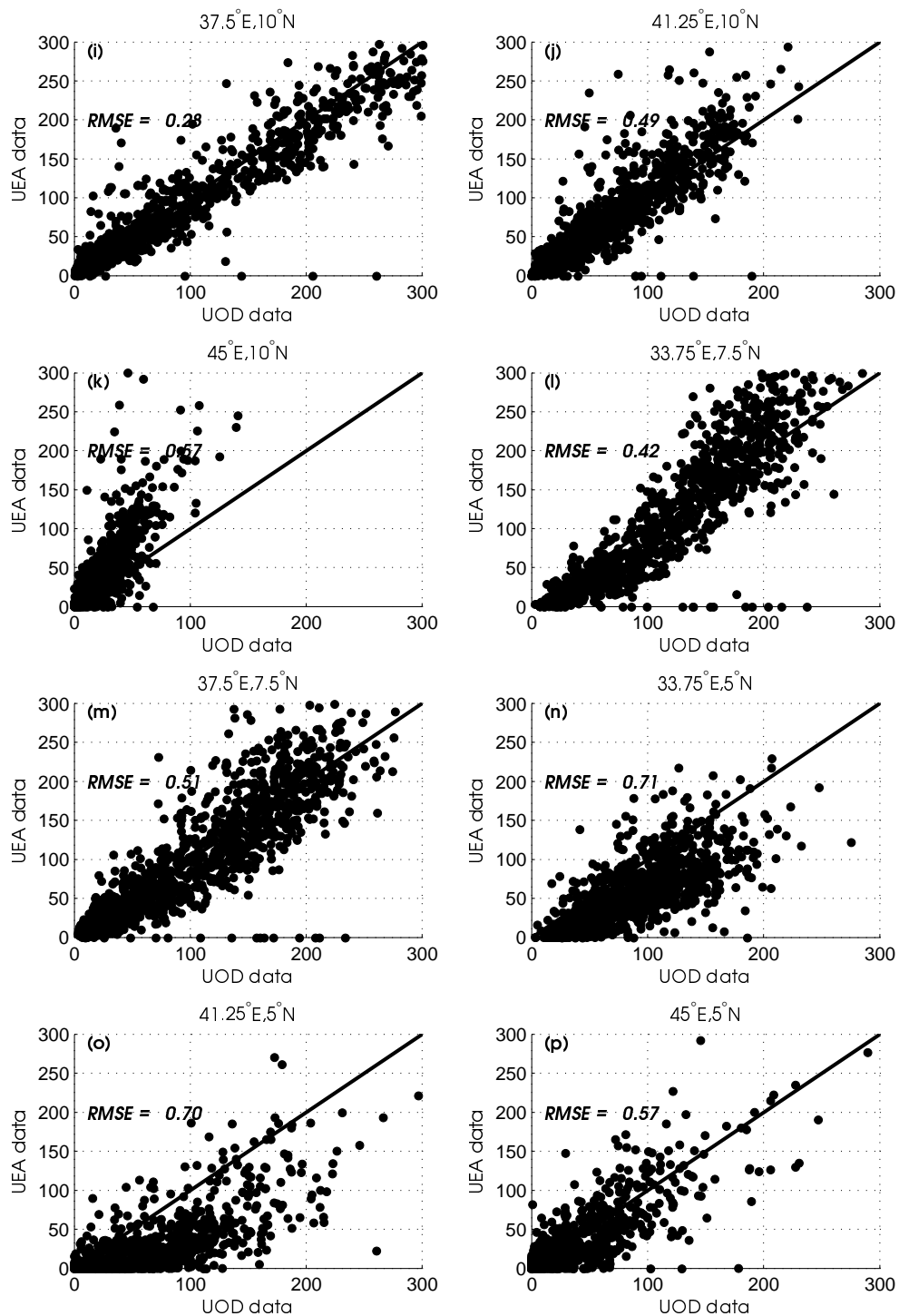


Figure 2.3: continued

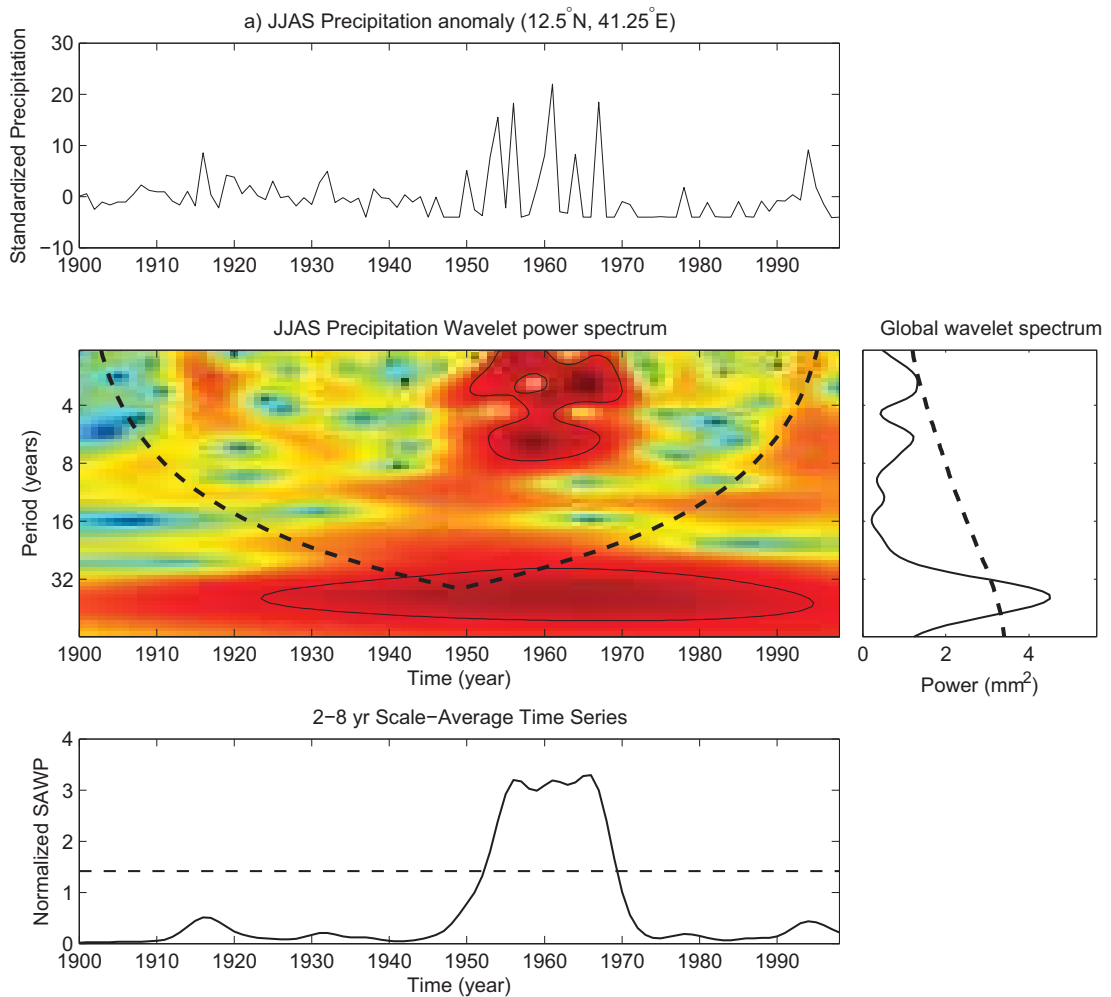


Figure 2.4: Examples of Continuous wavelet and global spectra of a) Ethiopian rainfall during June-September (JJAS) at grid point (12.5° N- 41.25° E), b) Ethiopian rainfall during February-May (FMAM) at grid point (5° N- 33.75° E, and c) global SST during January-March at a grid point located in the Tropical Pacific Ocean (0.5° N- 98.5° W) . Each example presents the standardized time series anomaly, Morlet wavelet power spectrum, where the dashed line is the cone of influence beyond which the energy is contaminated by the effect of zero-padding and the thick black contours represent the 95% confidence level of local power relative to a red noise background, Global wavelet power spectrum (solid line) with the 95% confidence level (dashed line), and the Scale-average wavelet power over 2-8 yrs. band with the dashed line is the 95% significance level.

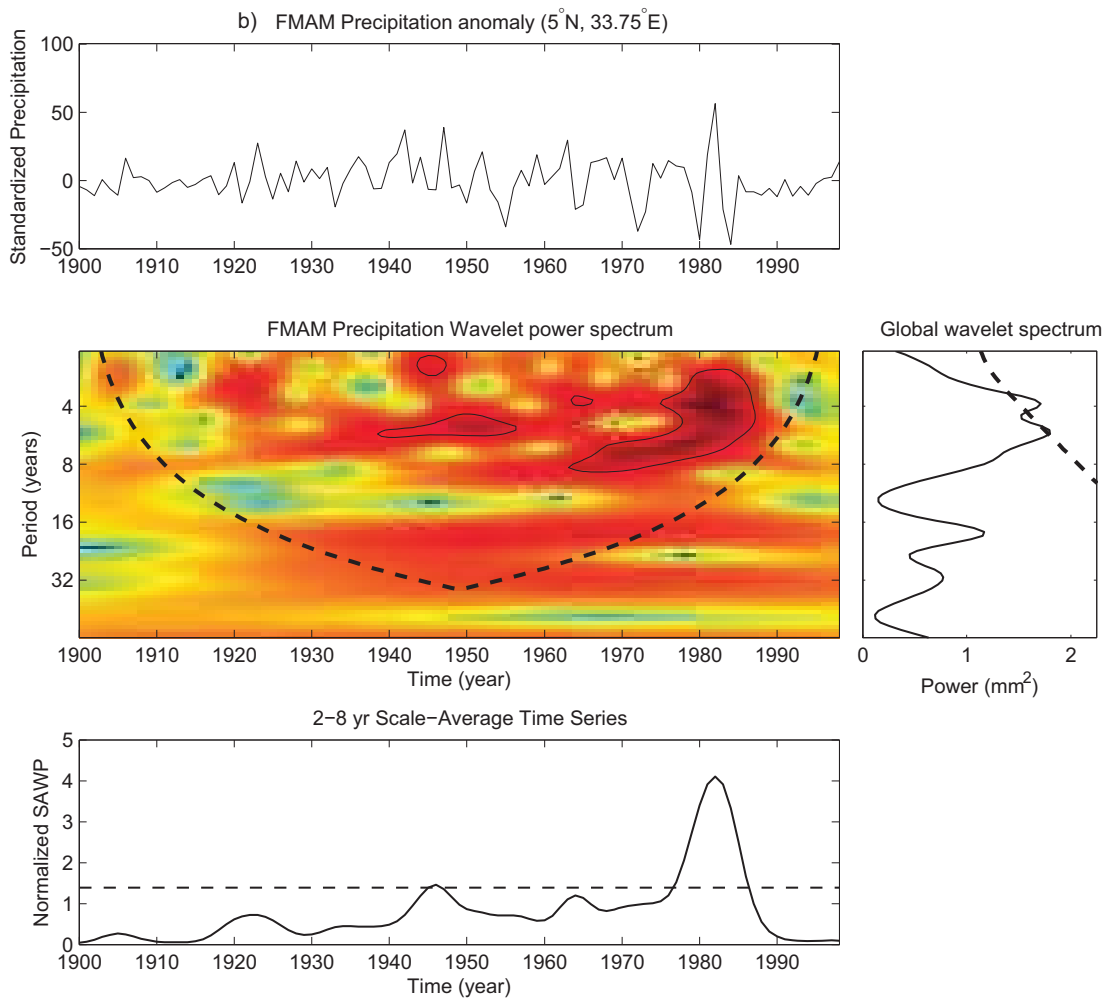


Figure 2.4: continued

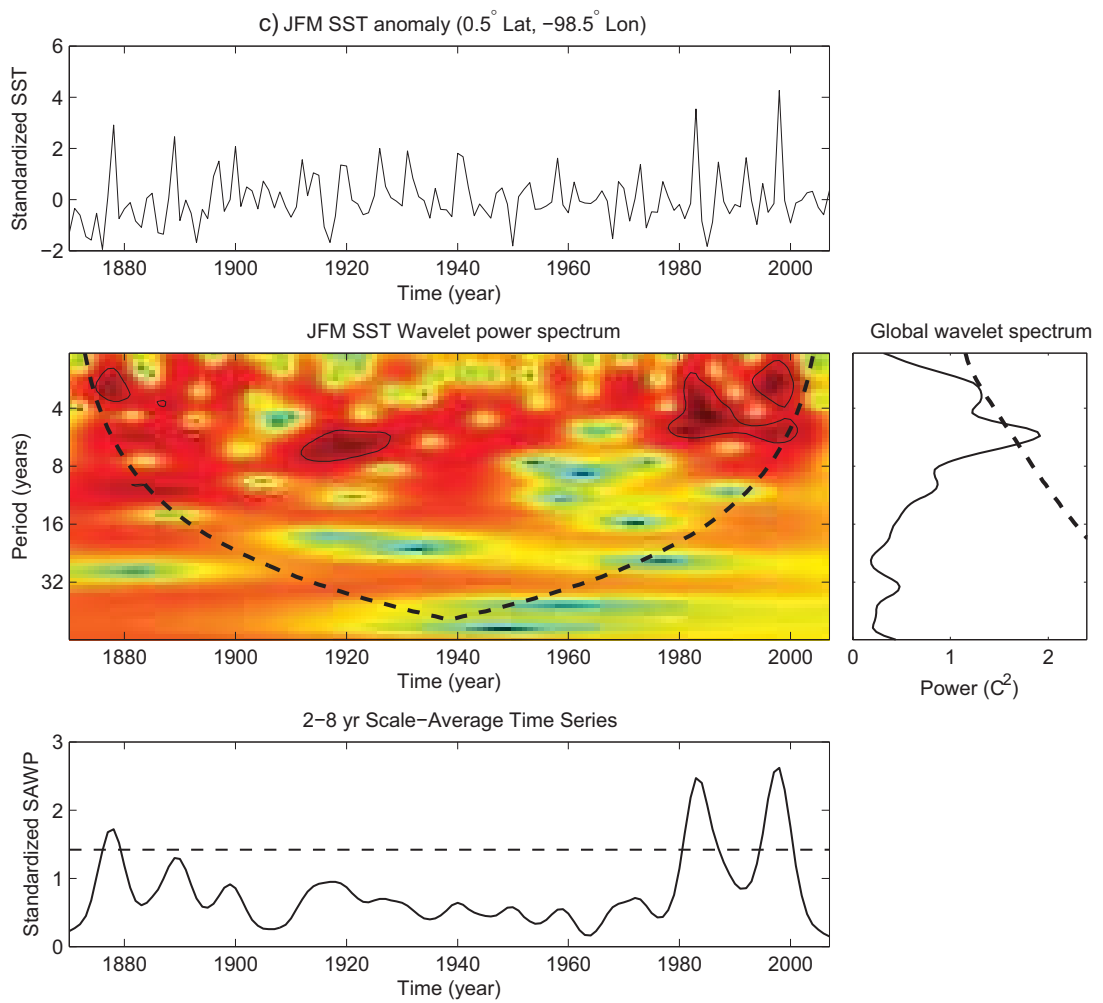


Figure 2.4: continued

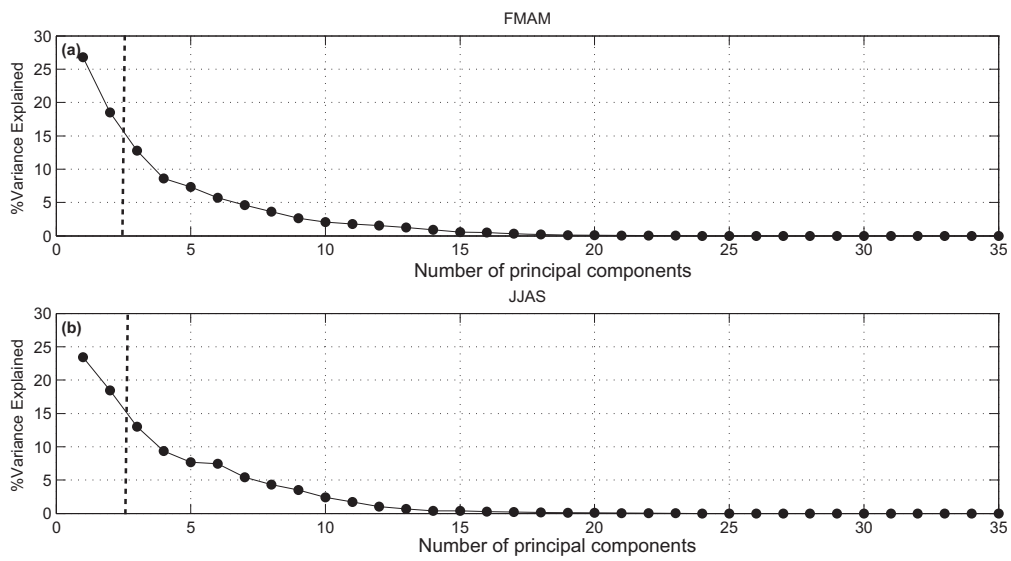


Figure 2.5: Scree plots of the 23 WPCs of Ethiopian Highlands rainfall for the 2-8 yrs. band during (a) FMAM and (b) JJAS seasons. Notice 35 points in the figures because of filling the missing grid points from the data. The heavy dashed vertical line separating the first two WPCs.

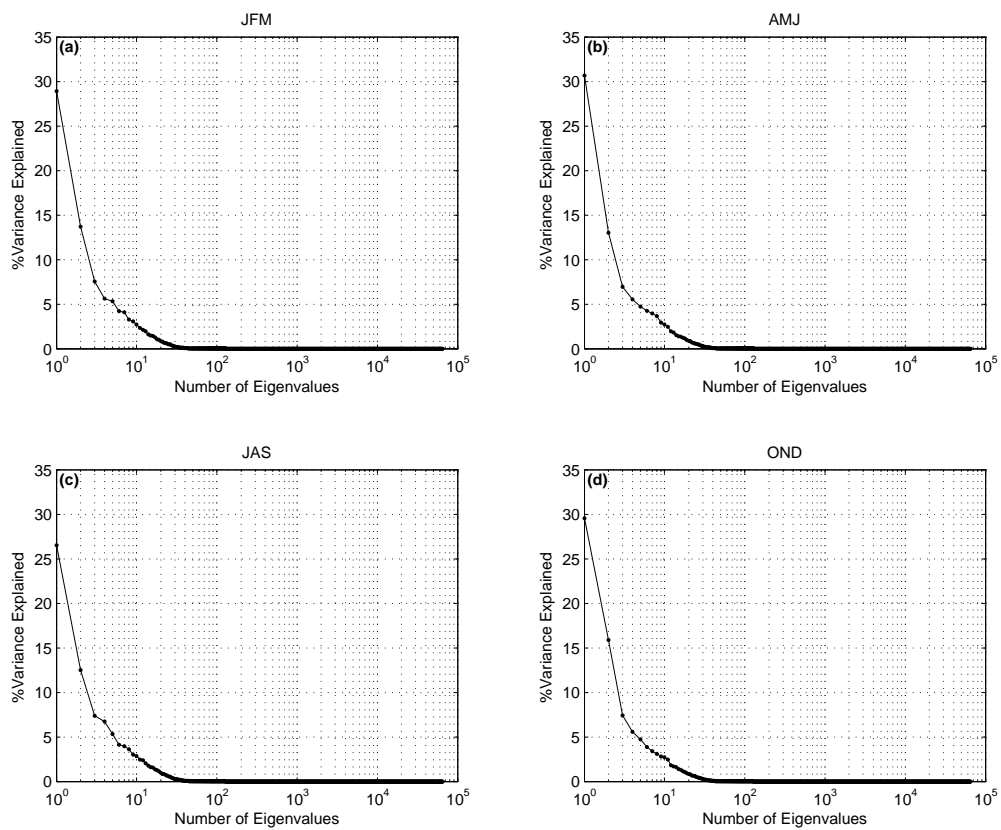


Figure 2.6: Scree plots of global sea surface temperature for about 65,000 WPCs for the 2-8 yrs. band during (a) JFM, (b) AMJ, (c) JAS, and (d) OND.

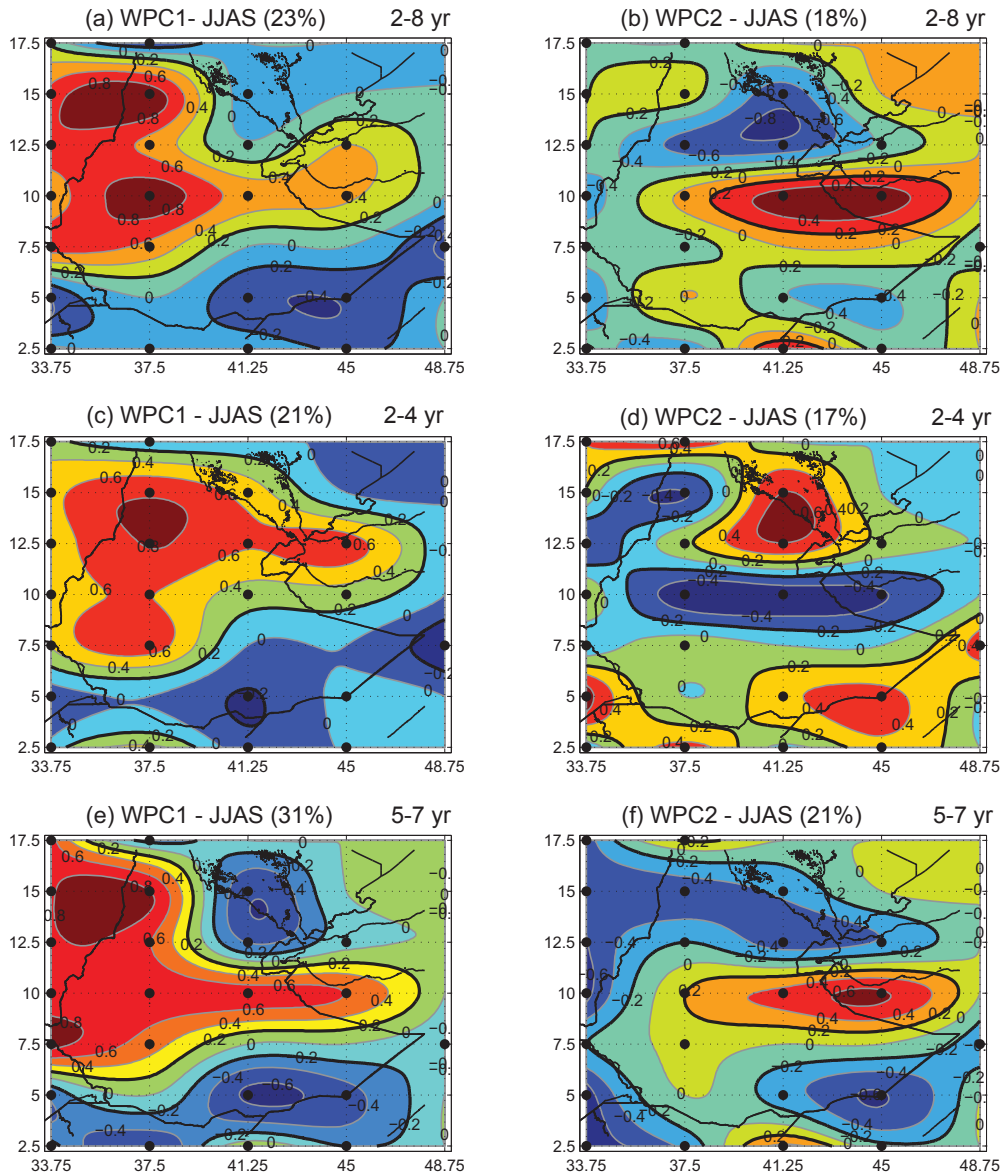


Figure 2.7: Contours of spatial Pearson's correlation between (a) WPC1 and (b) WPC2, and SAWP of gridded, Ethiopian rainfall data of June-September (JJAS) computed using the 2-8 year frequency band. Also, between WPC1 (c and e) and WPC2 (d and f), and SAWP of gridded, Ethiopian rainfall data of June-September (JJAS) computed using 2-4 years (c and d) and 5-7 years (e and f) frequency bands, respectively. Notice Eritrea borders are not shown in the maps. All the PCA have been done on the wavelet transformed rainfall time series. Also, the correlation values are shown in colors and contour values have been smoothed using linear interpolation and are written on the maps.

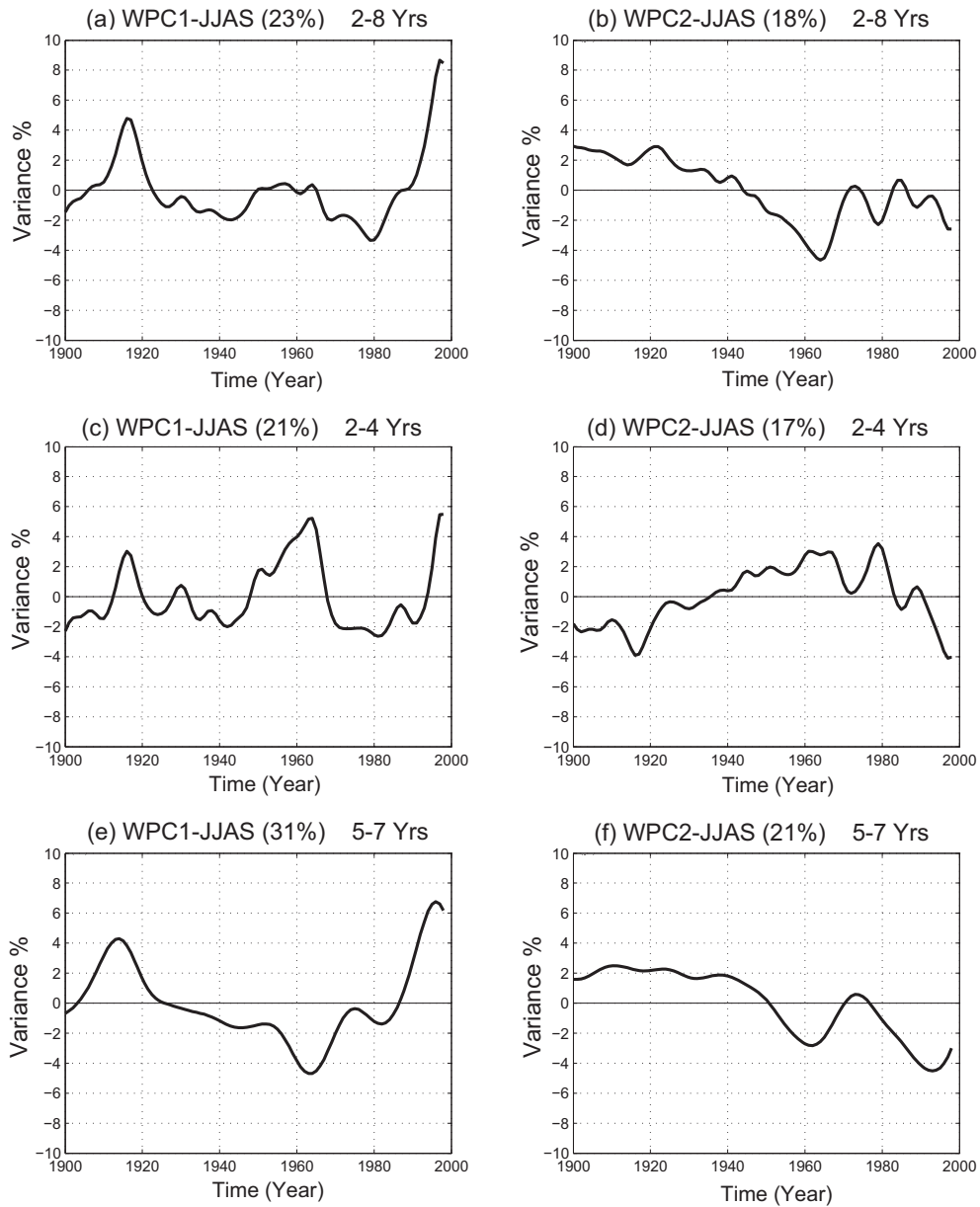


Figure 2.8: Temporal variation of WPC1 and WPC2 time series of Ethiopian June-September (JJAS) rainfall computed using 2-8 year (a and b), 2-4 year (c and d) and 5-7 years (e and f) frequency bands, respectively.

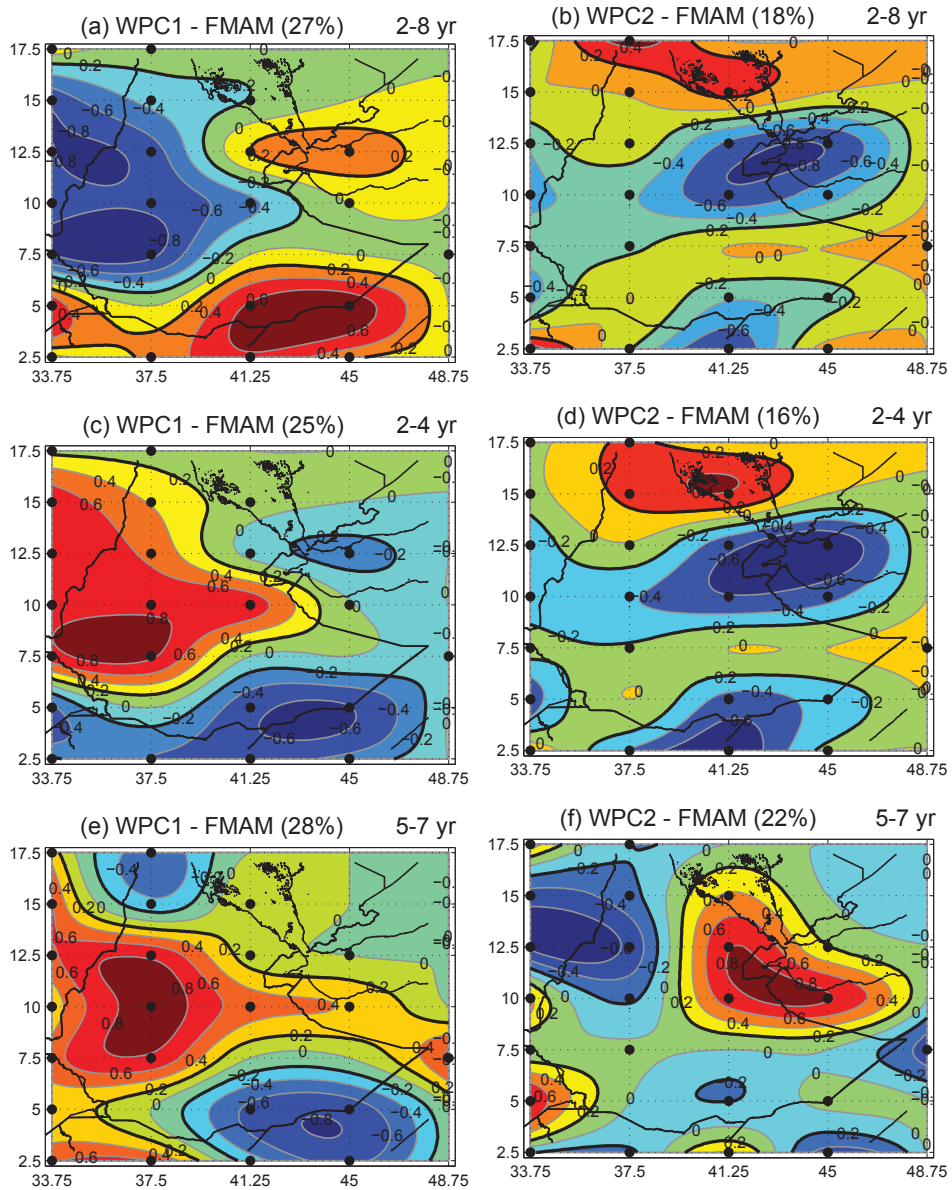


Figure 2.9: Contours of spatial Pearson's correlation between (a) WPC1 and (b) WPC2, and SAWP of gridded, Ethiopian rainfall data of June-September (FMAM) computed using the 2-8 year frequency band. Also, between WPC1 (c and e) and WPC2 (d and f), and SAWP of gridded, Ethiopian rainfall data of June-September (JJAS) computed using 2-4 years (c and d) and 5-7 years (e and f) frequency bands, respectively. Notice Eritrea borders are not shown in the maps. All the PCA have been done on the wavelet transformed rainfall time series. Also, the correlation values are shown in colors and contour values have been smoothed using linear interpolation and are written on the maps.

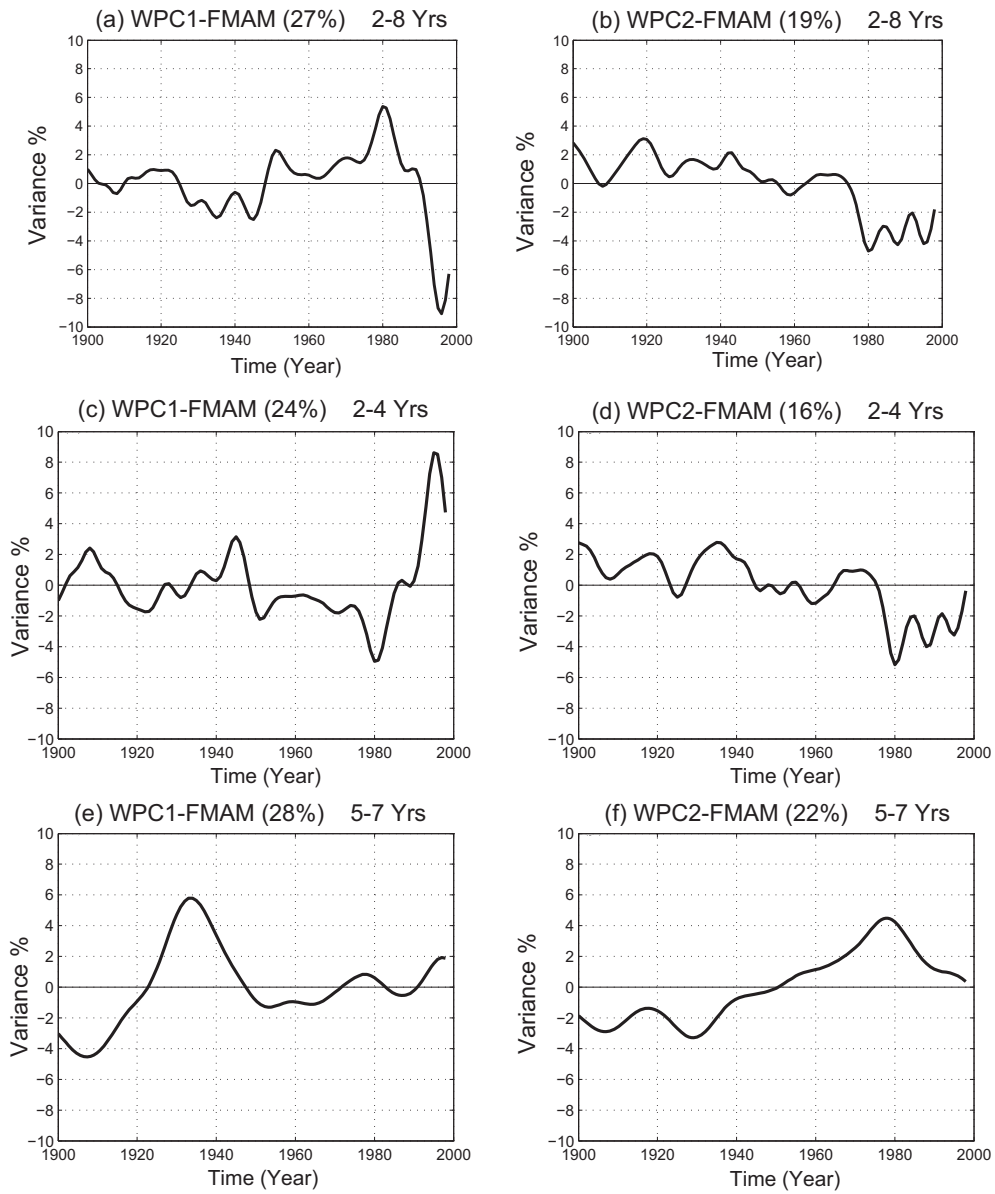


Figure 2.10: Temporal variation of WPC1 and WPC2 time series of Ethiopian, February-May (FMAM) rainfall computed using 2-8 year (a and b), 2-4 year (c and d) and 5-7 years (e and f) frequency bands, respectively.

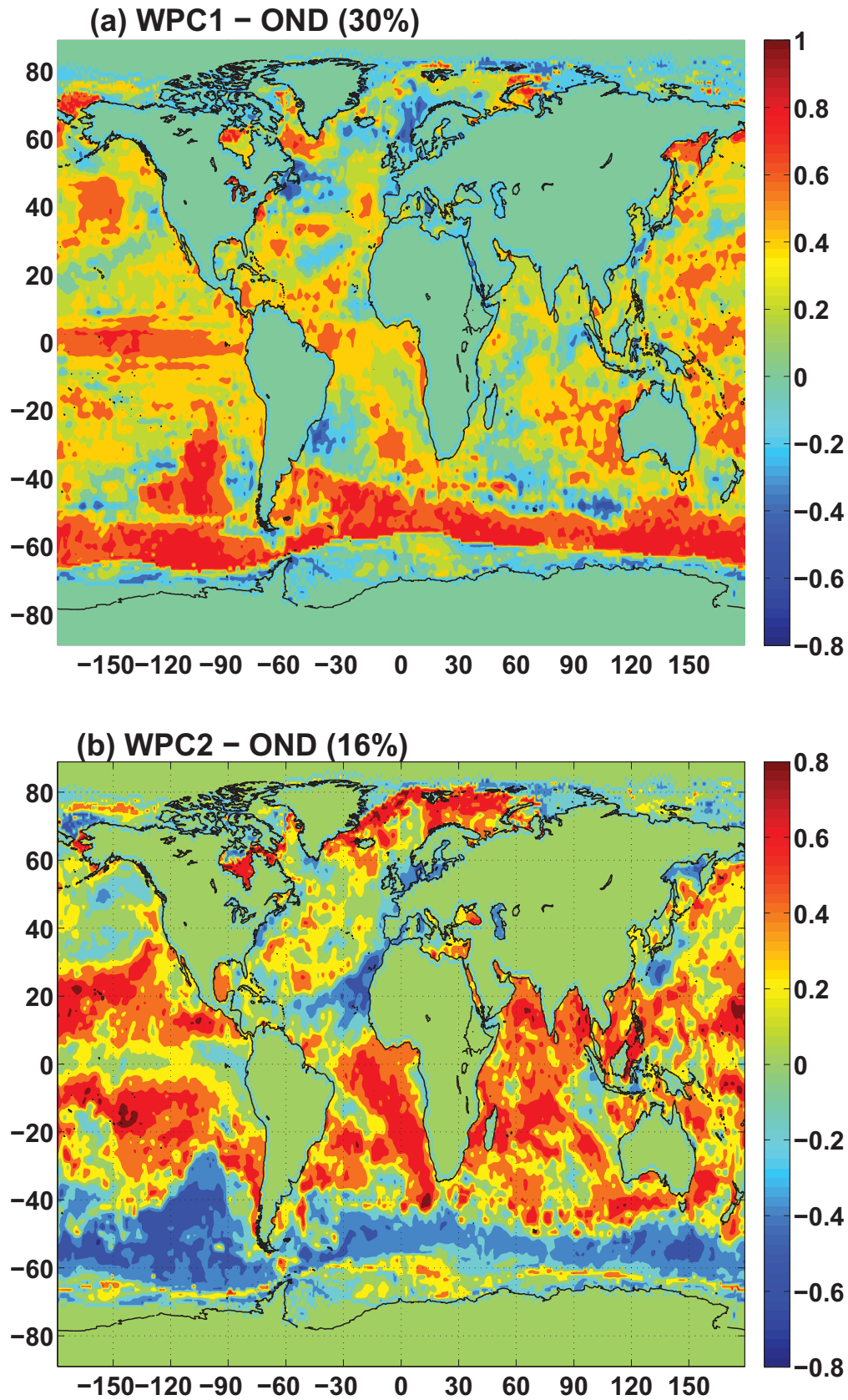
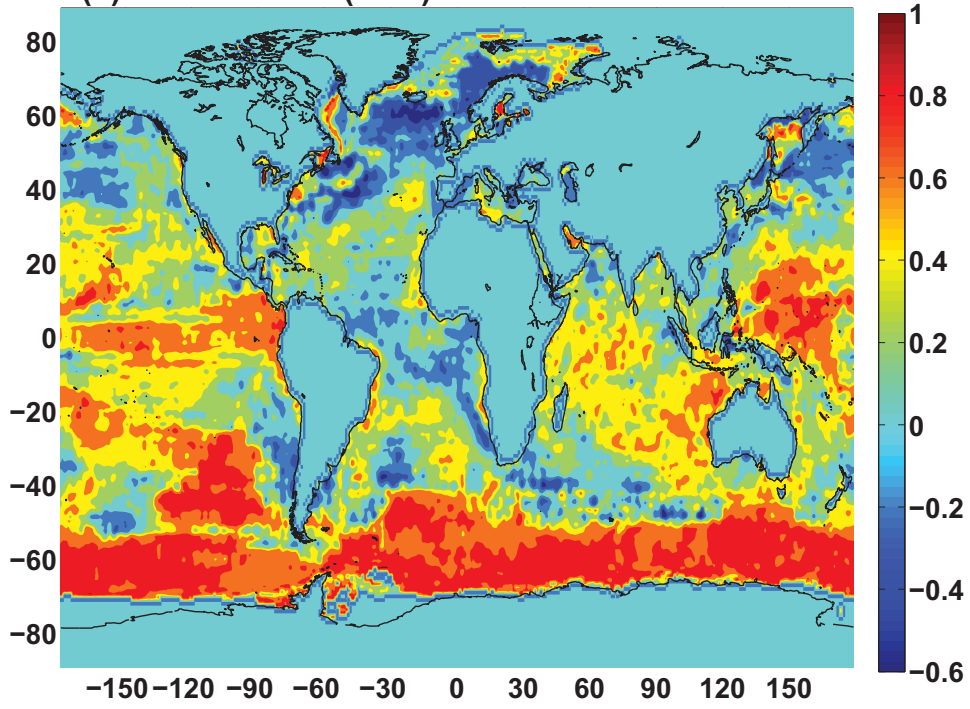


Figure 2.11: Spatial correlation between WPC1 and WPC2, and SAWP of gridded global sea surface temperature of 1° resolution computed for OND (a and b), JFM (c and d), AMJ (e and f) and JAS (g and h) using the 2-8 year frequency band.

(c) WPC1 – JFM (29%)



(d) WPC2 – JFM (14%)

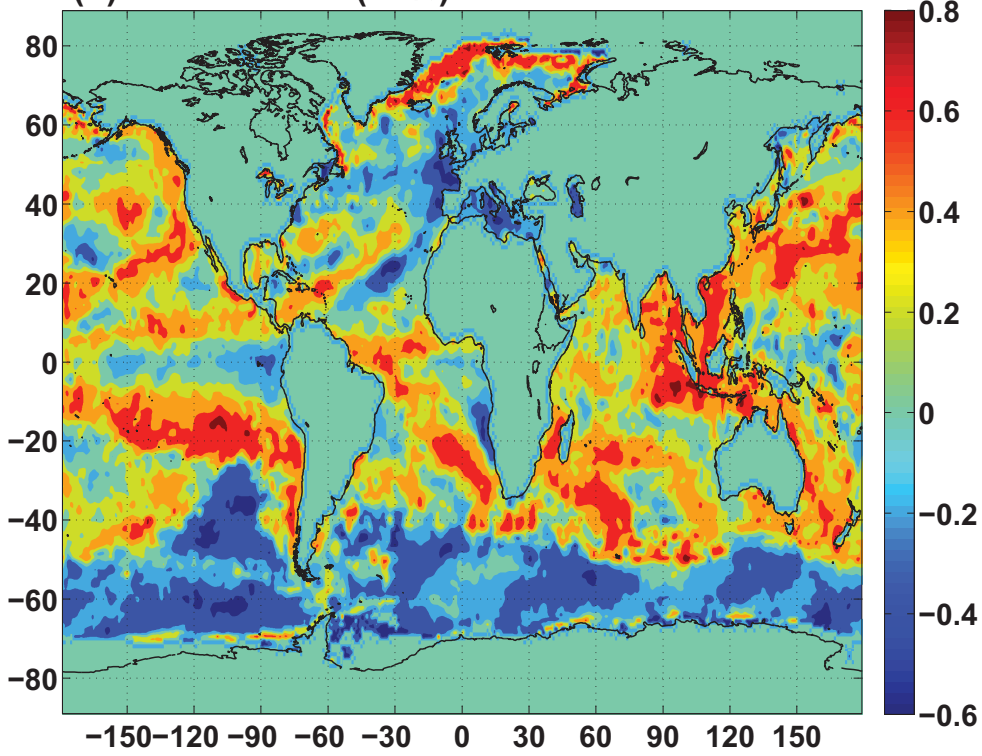


Figure 2.11: continued

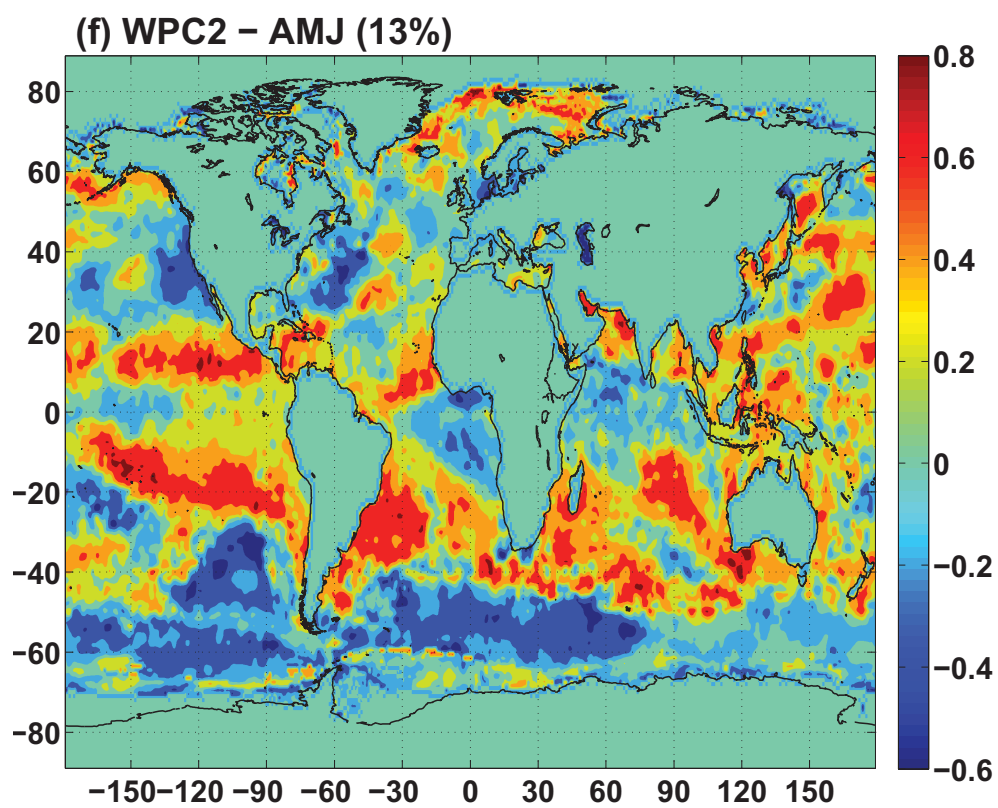
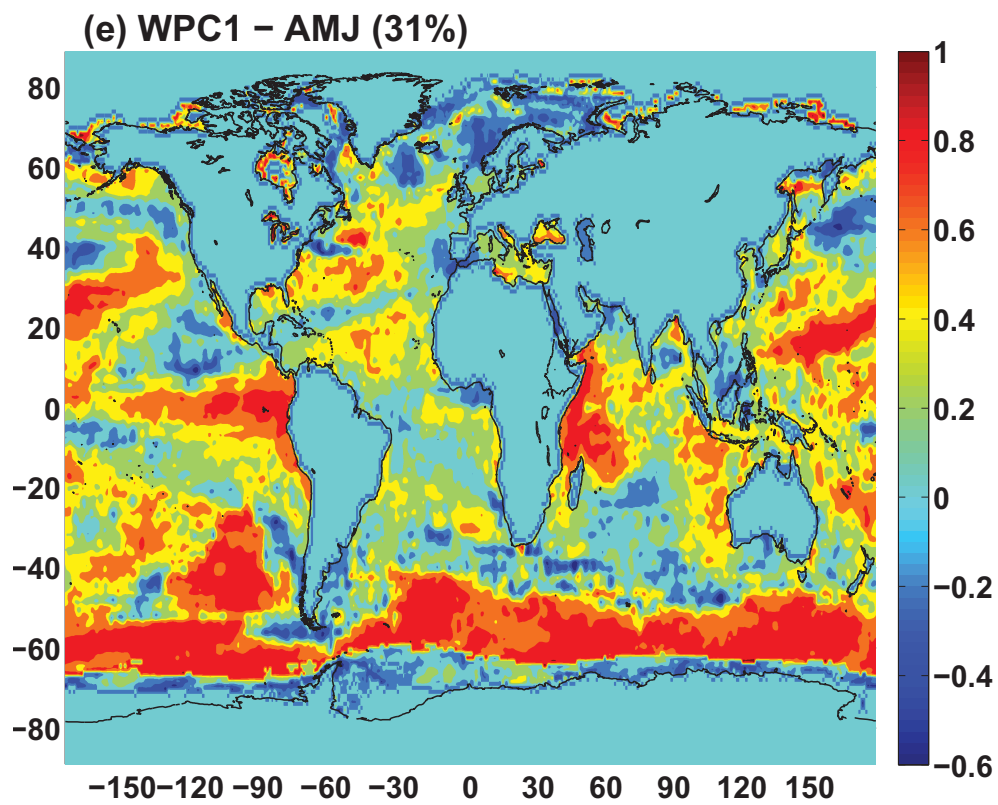
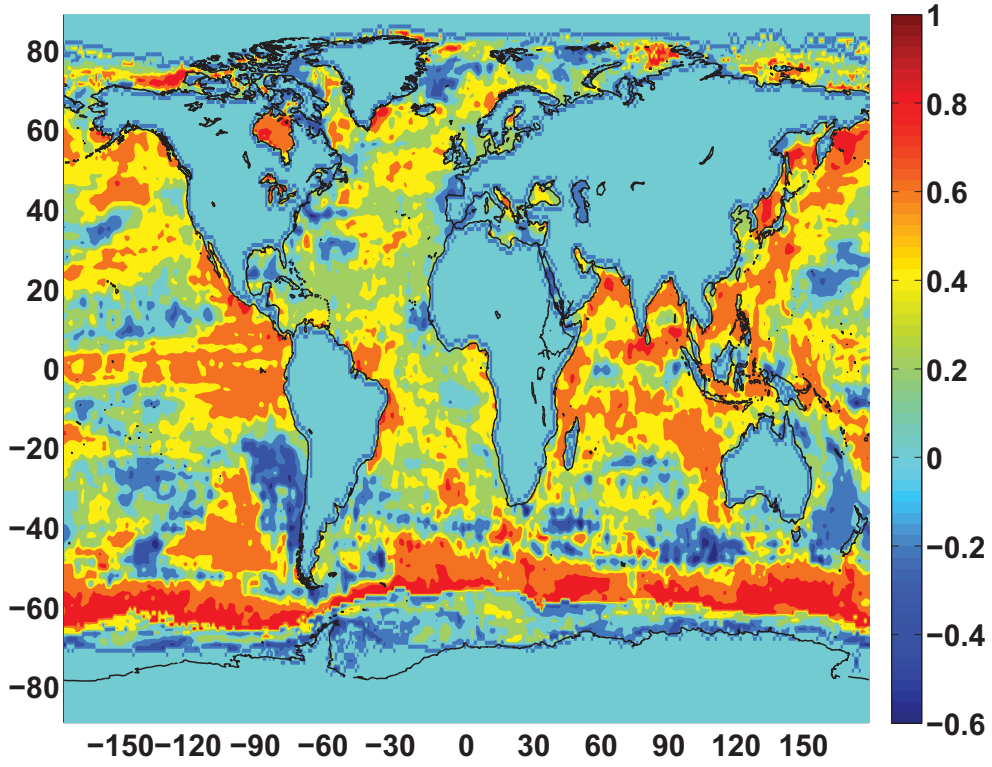


Figure 2.11: continued

(g) WPC1 – JAS (27%)



(h) WPC2 – JAS (13%)

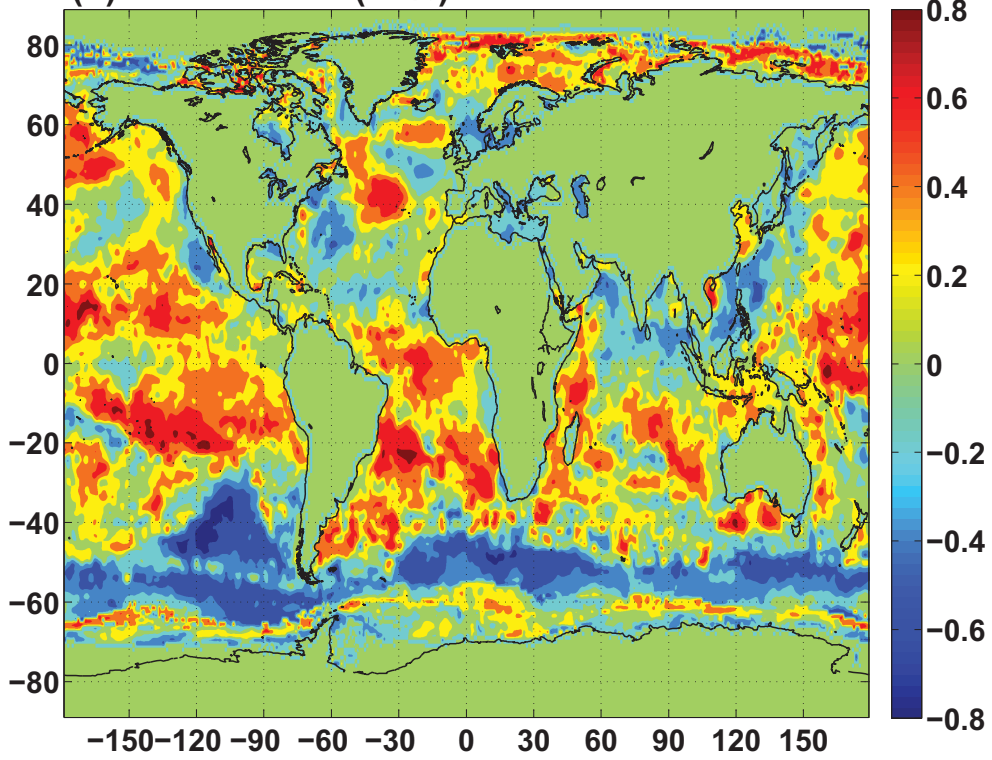


Figure 2.11: continued

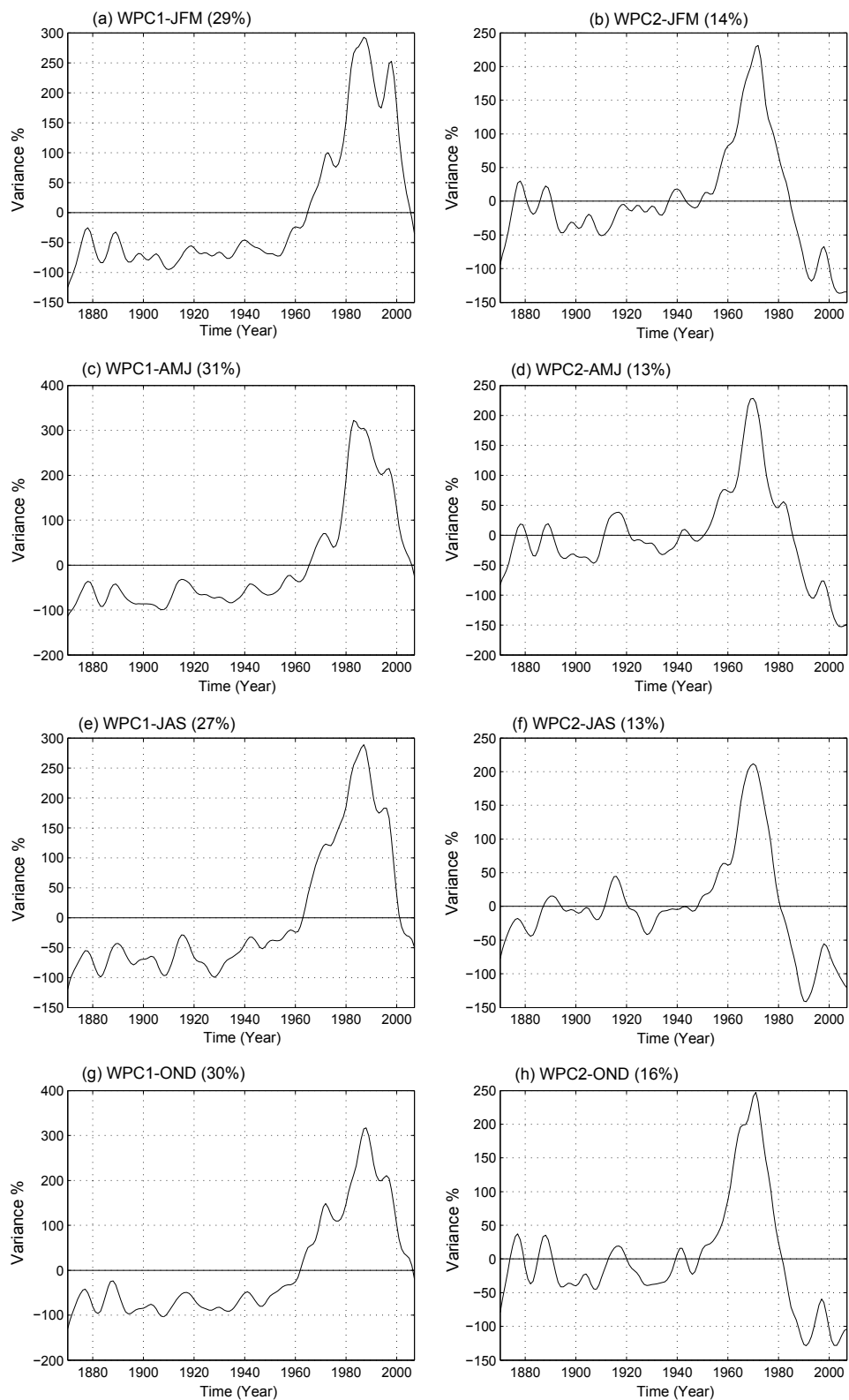


Figure 2.12: Temporal variation of WPC1 and WPC2 time series of global sea surface temperature computed for JFM (a and b), AMJ (c and d), JAS (e and f) and OND (g and h), using the 2-8 year frequency band.

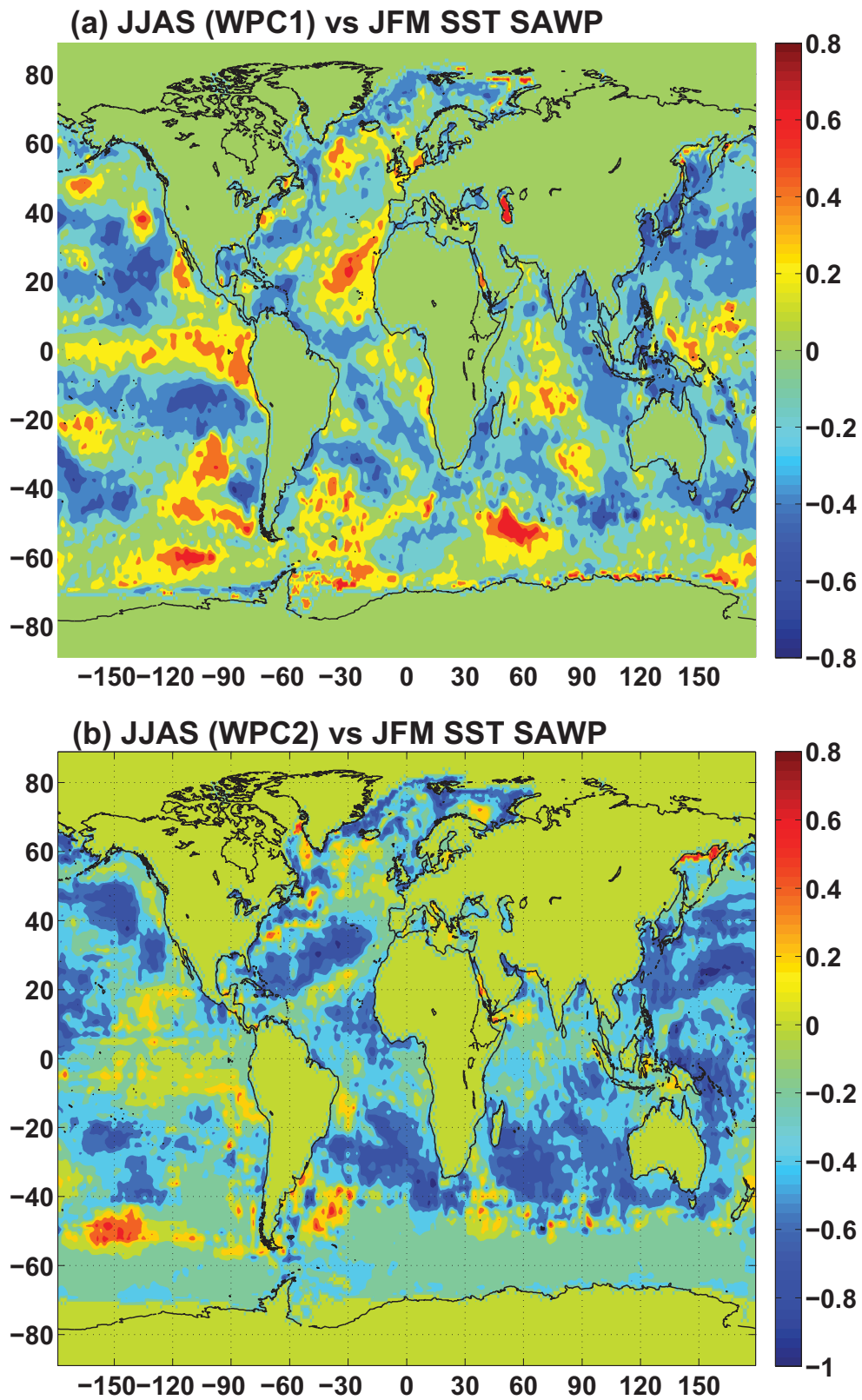


Figure 2.13: Correlation between (a) WPC1 and (b) WPC2 of Ethiopian rainfall and SAWP of the gridded global sea surface temperature computed using the 2-8 year frequency band.

Chapter 3

Hydrologic impacts of climate anomalies on the Upper Blue Nile¹

3.1 Introduction

If there will be a 3rd World War, it could be a war over water (<http://watervideo.com>, Dr. Terje Tvedt). In recent decades, there has been growing concern over the possible impacts of global warming to our climate ([Houghton and Syvitski, 2009](#); [Barry and Gan, 2011](#)) as severe weather has been occurring more frequently and in greater severity world wide, which could affect the reliability of water supply on various continents ([Bate, 2000](#); [Congress, 2009](#)). In the midst of dwindling water resources, increasing demand for water from growing population, widespread pollution, and increasing extreme weather events, the world is facing a more and more serious water crisis since the beginning of the 21st Century ([BBC, 2010](#)). It has been estimated that, by about 2030, several billion people across the world could face water stress ([Arnell, 1999](#); [IPCC, 2012](#)), including peo-

¹Aversion of this chapter is being submitted for publication to the Advances in Water Resources

ple who rely on the world's longest river, the Nile ([Duiker and Spielvogel, 2009](#)), for their water supply. The Nile River (NR) has strong seasonal and annual fluctuations which may cause water shortage problems to riparian users relying on the natural flow of the Nile.

Because of its scale, the Nile River Basin (NRB) is rather diversified hydrologically and so it will be difficult to model the hydrology of the NRB in a lumped manner. The Upper Blue Nile Basin (UBNB), which is located in the Ethiopian Highlands, is one of the most important sub-basins of the NRB. Typically, during July-October, the Blue Nile (Abay) river contributes about 60% of the total flow of the Nile River. Approximately, 70% of the annual rainfall of the UBNB occurs in the Kiremt season (June-September) ([Conway, 2000](#)). In this season, 85%-95% of the annual crops of Ethiopia are produced ([Degefu, 1987](#)). Therefore, when suffering from droughts, famines can be endemic because agriculture, which accounts for approximately 50% of Ethiopia's Gross Domestic Product and employs 80% of Ethiopia's population, is heavily dependent on rainfall ([Abegaz et al., 2007](#)).

According to [Shahin \(1985\)](#), climate and topography are the two causative factors that have strong effect on the discharge of the Nile. In this chapter, the focus is to compare modeling the hydrology of UBNB using one physically based distributed model, and one lumped, conceptual hydrologic model, and then using both hydrologic models to assess the possible effects of climate anomalies on the hydrology of UBNB.

There have been studies conducted on the vulnerability of the Nile basin to climatic change (e.g. [Gleick, 1992](#); [Strzepek et al., 1996](#)). The physically-based, distributed model used in this study to model the UBNB is the MISBA model which [Kerkhoven and Gan \(2006\)](#) modified from the land surface scheme, ISBA of Météo France ([Noilhan and Planton, 1989](#)).

Due to the limitations of data availability in the UBNB, e.g., UBNB

has limited meteorological coverage with long-term rainfall and temperature records, in the past relatively simple hydrological models that have modest data requirements had been used to model the UBNB (e.g. [Conway, 1997](#)). Other than data limitations, the complex nature of the Blue Nile also adds complications to model the UBNB with complex, physically-based hydrologic models in a grid-based framework. Such models generally require detailed land cover and digital elevation model (DEM) data, and observed climate data or re-analysis data that are derived from combining observed and climate model simulated data.

Given that Indian and Atlantic Oceans are the primary sources of moisture responsible for most of the precipitation occurring over UBNB and Ethiopia, we expect certain climate anomalies of the oceans to also affect the climate of UBNB and Ethiopia. Besides modeling the hydrology of the UBNB, another objective of this study is to investigate the possible effect of climate anomalies on UBNB, such as El Niño Southern Oscillation (ENSO) and Indian Ocean Dipole (IOD) which could significantly affect the climate of UBNB, and which in turn affect the livelihood of people living in UBNB. There have been various studies conducted on the relationships of climate anomalies to the hydrology of UBNB and Ethiopian Highlands, (e.g. [Degefu, 1987](#); [Kassahun, 1991](#); [Wolde-Georgis et al., 2001](#)).

[Ogallo \(1979\)](#) investigated the rainfall variability of Africa and found the African rainfall to generally oscillate at interannual (3-5 years) to interdecadal scale (10-12 years), and [Nicholson and Entekhabi \(1986\)](#) found that the rainfall over the Sahel and western part of Ethiopia exhibited 10-18 year variability, which could be attributed to the effect of certain climate anomalies. For example, [Amarasekera et al. \(1997\)](#); [Seleshi and Zanke \(2004\)](#) found a negative correlation between the annual discharge of the Nile River and the warm phase of ENSO; [Abteu et al. \(2009\)](#) found that strong El Niño (La Niña) events tend to produce extremely dry (wet)

years over the UBNB; [Conway \(2000\)](#) found heavy rainfall over the UBNB to be associated with positive SOI (i.e. La Niña), when a strong low pressure system extends over India and the Arabian Sea, causing heavy rainfall and high runoff in the UBNB; and [\(Eltahir, 1996\)](#) showed that 25% of the natural variability of the annual streamflow of the Nile is connected to ENSO.

While previous studies on the runoff variability of NRB have provided details on the possible effects of ENSO, as far as we know, there has been no study on the possible impacts of Indian Ocean Dipole (IOD) on the climate of UBNB. IOD is a coupled ocean and atmosphere phenomenon in the equatorial Indian Ocean that affects the climate of countries that surround the Indian Ocean basin ([Saji et al., 1999](#)). IOD is commonly measured by the Dipole Mode Index (DMI) which is the difference between sea surface temperature (SST) in the western (50° E to 70° E and 10° S to 10° N) and eastern (90° E to 110° E and 10° S to 0° S) equatorial Indian Ocean.

Given that the Indian Ocean is a crucial source of moisture source to the spring-summer rainy seasons over Ethiopia (when the temperature is high and the air is full of water vapor), it is important to investigate the possible impact of IOD on the streamflow of UBNB. The results will be valuable to water resources planners of UBNB, given that climatic fluctuations should be considered as an essential part of any water resources planning process in the world ([Abu-Zeid and Biswas, 1991](#)).

3.2 Research Objectives

In light of the above literature review, this study has two objectives:

- i) To explore modeling the UBNB streamflow using a physically based (distributed) hydrologic model MISBA with high data demand, and a

lumped, conceptual hydrologic model, the Sacramento Model of National Weather Service of USA with a modest data demand;

- ii) To investigate the effects of climate anomalies such as ENSO and IOD on the streamflow of UBNB and the implications of such effects to its water resources, and that of the Nile River.

To achieve the above objectives, this chapter is presented as follows: UBNB's physical characteristics and climatology are briefly outlined in Section 3.3, hydroclimatic data in Section 3.4, research procedure and methodology in Section 3.5, discussions of results in Section 3.6, and summary and conclusions in Section 3.7.

3.3 Upper Blue Nile Basin

The UBNB, of 176,000 km^2 in area, occupies 17% of Ethiopia, and has a mean annual streamflow volume of 48.5 Billion cubic meters (BM^3) (Conway, 2000). The Blue Nile (Abay) begins at the Tana Lake (2150 km^2 area) of an approximate elevation of 1800 a.m.s.l, with the water leaving the lake at the Tississat Falls that drop over 50 m vertically (Shahin, 1985). The UBNB, which forms the western part of the Ethiopian Highlands, receives more precipitation (a mean annual precipitation of 1600mm with a range of \pm 600-800 mm/year, (Sutcliffe et al., 1999) than the eastern, northern and southern parts of the Ethiopian Highlands. This is expected since the western part is higher than other parts of the Highlands and precipitation generally increases with altitude because of orographic effects (Kloos and Legesse, 2010). UBNB essentially has two rainy seasons, a small rain season (called Belg) during February-May (FMAM) and a big rain season (called Kiremt) during June-September (JJAS) (Kloos and Legesse, 2010).

3.4 Data

The data required for driving the hydrologic models and for evaluating the climate anomaly effects are meteorological data, topographic data, land use data and hydrometric data.

3.4.1 Meteorological Data

The meteorological data used in this study comprises of rain gauge data, global atmospheric reanalysis data of ERA-40 developed by the European Centre for Mid-range Weather Forecasts (ECMWF) which has a global coverage from January 1961 to August 2002 (ECMWF, 2009). The ERA-40 data has a spatial resolution of 2.5° latitude and 2.5° longitude and a temporal resolution of 6 hours. The reanalysis fields include surface temperature (at 2m above the ground), specific humidity, sea level pressure, wind speed (horizontal and vertical), mean precipitation rate, mean long wave radiation downwards and mean short wave radiation downwards. The National Centers for Environmental Prediction (NCEP) and the National Center for Atmospheric Research Reanalysis (NCAR) precipitation data provided by the NOAA/OAR/ESRL PSD, Boulder, Colorado, USA, has also been considered in this study (Kalnay et al., 1996) <http://www.esrl.noaa.gov/psd/data/gridded/data.ncep.reanalysis.html>

3.4.2 Temperature Data

The temperature data used for calculating the potential evapotranspiration is taken from the ERA-40 data and from the global surface summary day product produced by the National Climatic Data Center (NCDC) in Asheville, NC. The daily summaries are developed out of the Integrated Surface Data which includes global data obtained from the USAF Climatology Center of NCDC. The daily average, maximum and minimum

air temperature data of 1975-2001 for the Debremarcos station (10.33° N, 37.5° E) was obtained from (<http://www.ncdc.noaa.gov/cgi-bin/res40.pl?page=gsod.html>).

3.4.3 DEM Data

The DEM data set of UBNB was extracted from the Global 30 Arc-Second (1km) Elevation Data Set (GTOPO30), a global raster Digital Elevation Model (DEM) with a horizontal grid resolution of 30 arc seconds (approximately 1 km). The data is expressed in latitude and longitude and is referenced to the World Geodetic Survey (WGS) system of 1984 (WGS84) (see Figure 3.1). The DEM data was used to determine the drainage area, drainage network and flow direction of the rivers and streams of the UBNB.

3.4.4 Land cover Data

The Ecoclimap land use data set (Masson et al., 2003; Masson and Faroux, 2010), which has been widely used in Soil-Vegetation-Atmosphere-Transfer schemes (SVATs) of climate models, was used to determine the land surface information required by the MISBA model. The Ecoclimap data set was derived from combining land cover maps, climate maps and AVHRR satellite data, and has a 30 arc seconds (approximately 1 km) horizontal resolution.

3.4.5 Hydrometric Data

Daily natural streamflow (1971-2001) for the El Diem station was provided by Mr. Tazebe Beyenne of University of Washington. Monthly river flow data were collected from the Global Hydro Climate Data Network (GHCDN) of UNESCO/IHP (<http://dss.ucar.edu/datasets/ds553.2/data/>), which came from several sources: Cairo University Shahin (1985),

Massachusetts Institute of Technology (1977), and Global Runoff Data Center of the World Metrological Organization (WOM) funded by Germany (<http://grdc.bafg.de/>). Two monthly precipitation gauge datasets were used: data provided by Dr. Declan Conway (University of East Anglia) and data by [Sy and Gupta \(2004\)](#), <http://www7.ncdc.noaa.gov/CD0/cdoselect.cmd?datasetabbv=GS0D&countryabbv=&georegionabbv=>

Because atmospheric, DEM and Ecoclimap data are of different resolutions, in order to apply them in MISBA, a cross referencing system was developed to link these three layers of data together, such that each DEM square was linked to its nearest land cover data square which was then linked to its nearest Meteorological grid square.

3.5 Research Methodology

3.5.1 MISBA Model

In theory, physically based distributed hydrologic models have an advantage over lumped conceptual models because the former are based on known physical laws, driven by spatially distributed data (climate, land use and DEM), while the latter are based on simplified concepts of physical laws and point data. Ideally, if detailed data are available, physically-based models are preferred over conceptual hydrologic models which require calibrations of model parameters because these parameters may become invalid when extended beyond the hydroclimatic regime used in the calibration experience. The physically-based model, MISBA [Kerkhoven and Gan \(2006\)](#) used in this study is a modified version of the soil-vegetation-atmosphere transfer model (SVAT) called Interactions between the Soil-Biosphere-Atmosphere (ISBA) land surface scheme developed by ([Noilhan and Planton, 1989](#); [Noilhan and Mahfouf, 1996](#)) at Météo-France.

ISBA is a physics/process based SVAT which considers the exchange

of heat and water between the lower atmosphere, the vegetation, and the soil. This model includes both water and an energy budgets to simulate different components of energy and water fluxes. Figure 3.2 represents schematic diagrams of the mass (water), energy pathways and reservoirs for ISBA. The main advantage of ISBA is that it requires minimum number of parameters without affecting the basic physics that controls the energy and water budgets. ISBA has three soil layers with two basic types of parameters - four primary and 22 secondary parameters. The primary parameters are percentage of sand, percentage of clay, vegetation and land-water ratio that are specified at each grid points. ISBA uses a sub-grid runoff scheme (Habets et al., 1999) that considers sub-grid variation of soil moisture, y , by the Xinanjiang distribution,

$$F(y) = 1 - \left(1 - \frac{y}{y_{max}}\right)^\beta \quad 0 \leq y \leq y_{max}, \quad (3.1)$$

$$\frac{\bar{y}}{y_{max}} = \frac{1}{\beta + 1}, \quad (3.2)$$

Where, $F(y)$ is the cumulative probability distribution of y , defined by the maximum (y_{max}) and the mean \bar{y} values of y , and β is an empirical parameter. ISBA tends to drain too quickly leading to high peaks and steep recession limbs suitable for moist regions. For drier regions, recessions will be more modest as water tends to be retained in dry soil and runoff would start after the soil is saturated. For the modified ISBA of (Kerkhoven and Gan, 2006), β is calculated internally using,

$$\beta = \frac{1}{S} - 1, \quad (3.3)$$

Where, S , is the soil water retention, is computed using the following equation:

$$S = \frac{w - w_r}{w_{sat} - w_r}, \quad (3.4)$$

Where, w_r is the residual water content, and w_{sat} is the saturated water content. [Kerkhoven and Gan \(2006\)](#) successfully applied MISBA to the regional scale, Athabasca River Basin (ARB) of about 133,000 km^2 in area, which showed a better performance in predicting the sub-surface runoff of ARB than the original ISBA. The modification of ISBA also involves implementing a highly nonlinear formulation for surface and sub-surface runoff to statistically account for sub-grid heterogeneity of soil moisture and precipitation. The nonlinear, soil water function for the sub-surface runoff to accurately account for interflow is given as:

$$Q = C_3 D(S)^{3+\frac{2}{\lambda}} = C_3 D(S)^n, \quad (3.5)$$

Where, λ is the Brooks-Corey pore-size distribution parameter, which can also be calculated from the soil texture using a pedo-transfer function, D is the depth of the deep soil layer and C_3 is a coefficient.

MISBA accounts for sub-grid variability of land cover, soil moisture, precipitation, and topography using two steps. The first is to divide grids into sub-grids or mosaics, each with its own set of parameters and data. The second is to get MISBA to simulate fluxes for all mosaics and then combine them through an area-weighted average method. By integrating equation 3.5 with the Xinanjiang probability density function, the runoff

is:

$$Q = C_3 D \frac{\Gamma(n+1)\Gamma(\beta+1)}{\Gamma(n+\beta+1)}, \quad (3.6)$$

A Muskingum-Cunge scheme was used to route the streamflow from each grid to obtain discharge at the basin outlet. In this study, MISBA was applied to simulate the streamflow of UBNB and to study the potential impact of climate anomalies in the basin. This is the first time to test the modified ISBA in an African highland, the UBNB.

3.5.2 SAC-SMA Model

Since climatic data in Africa are generally scarce, we also tested the performance of a lumped conceptual model with modest data requirements. The Sacramento Soil Moisture Accounting model (Burnash et al., 1973). Figure 3.3 represents schematic diagrams of the mass (water), soil layers and reservoirs for SAC-SMA. The model consists of two conceptual, upper and lower zones to simulate interflow, direct flow, Horton overland flow, evaporation, and subsurface flow. The soil moisture is distributed between the two layers through certain soil moisture accounting (SMA) algorithm. The upper zone represents top soils and basin interception layers while the lower zone represents groundwater reservoirs. Each zone stores soil moisture as “*tension water*” that remains closely bound to the soil particles and “*free water*” that fills up the interstitial soil pores.

As SAC-SMA is one of the most studied conceptual, hydrologic models for basin scale streamflow simulation, it is chosen for this study, e.g., (Gan and Burges, 1990; Gan and Biftu, 1996; Bashar and Zaki, 2005). SAC-SMA is generally applied to river basins ranging from 300 km^2 in to 5000 km^2 in size. The appropriate basin size will depend on the hydrologic region, geomorphology, and forecast point requirements (Finnerty et al., 1997).

Input to the model includes precipitation, temperature, and pan evapotranspiration (PET) data. The model parameters require calibration which can be of manual or automatic approach or both. The model treats the basin as a closed system. Therefore, the precipitation input returns as a combination of storm streamflow, evapotranspiration and soil moisture. Given that parameter values can vary over a wide range, the search for model parameters by the manual approach can be tedious. In this study, PET data were estimated using the Hargreaves model (Hargreaves et al., 1985; Hargreaves, 1994) modified by Droogers and Allen (2002). This model has been used by Ravazzani et al. (2011) and others.

$$PET = 0.0013 \times 0.408 R_A (T_{avg} + 17.0) (T_{rang} - 0.0123P)^{0.76}, \quad (3.7)$$

Where R_A is the extraterrestrial radiation expressed in ($M J m^{-2} d^{-1}$), T_{avg} is the average daily temperature (C°) defined as the average of the mean daily maximum and mean daily minimum temperature, and T_{rang} (C°) is the temperature range, computed as the difference between mean daily maximum and mean daily minimum temperature. R_A can be estimated (e.g. Duffie and Beckman, 1980) or measured.

Model calibration is an important step for the application of SAC-SMA model which has more than 20 parameters (see Figure 3.4) that can be calibrated by manual and automatic calibration procedures (Duan et al., 1992; Gan and Biftu, 1996). The idea is to achieve physically meaningful parameters so that realistic streamflow values agree with the observed streamflow at both the calibration and validation stage. In this study, a combination of manual and automatic calibration was done. Summary statistics of the calibration (based on 15 years of historical data, (1975-1996) and validation runs are shown in Table 3.3.

3.5.3 Assessment of Model Performance

The performance of MISBA and SAC-SMA were assessed against streamflow data observed at the El Diem station located near the Sudan-Ethiopia borders for UBNB over several periods. The summary statistics used to assess the performance of both models are: Coefficient of determination (R^2) which is the square of the Pearson correlation (r), root mean square error ($RMSE$), Nash-Sutcliffe coefficient of efficiency (Ns) or N_f , and $Bias$:

$$r = \frac{1}{k} \frac{\sum_{i=1}^k (X_i - \bar{X})(O_i - \bar{O})}{\sqrt{\sum_{i=1}^k (X_i - \bar{X})^2 \sum_{i=1}^k (O_i - \bar{O})^2}}, \quad (3.8)$$

$$RMSE = \frac{1}{k} \sqrt{\sum_{i=1}^k (X_i - O_i)^2}, \quad (3.9)$$

$$NS = 1 - \frac{\sum_{i=1}^k (X_i - O_i)^2}{\sum_{i=1}^k (X_i - \bar{X})^2}, \quad (3.10)$$

$$Bias = \frac{1}{k} \sum_{i=1}^k (X_i - O_i), \quad (3.11)$$

Where O_i and X_i are the observed and model simulated streamflow respectively; \bar{X} and \bar{O} are their respective mean values; and K is the total number of data points. The Pearson correlation ranges from -1 to 1 with a

correlation of 1 (-1) being a perfect linear positive (negative) relationship between O_i and X_i , and a correlation of zero indicating no relationship between O_i and X_i . A R^2 of 1 means perfect agreement. The $RMSE$ has the same units as the streamflow, with small $RMSE$ indicating promising simulation. The Nash-Sutcliffe coefficient efficiency (Ns) may range from $-\infty$ to 1, with an efficiency of 1 corresponding to a perfect match, an efficiency of 0 indicating model simulation that are only as good as the mean of O_i , and an efficiency less than zero indicating that the simulation is as good as random. A positive $Bias$ means over-simulation while a negative $Bias$ means under-simulation.

3.5.4 Bootstrap Resampling method

By repeated computer manipulations of certain observations, the idea behind bootstrap resampling is to generate datasets out of limited observations, which is generally done without knowing or assuming a theoretical distribution of the data (Wilks, 2006). The resampling process of a dataset of n years can be represented by having n balls of different colors in a box. Essentially, bootstrap resampling with replacement is to randomly pick a ball from the box, record its color and return the ball to the box. This process is repeated many times until a new time series is generated out of the original sample, the box of colored balls. In our case, the box of colored balls represent those anomalous years between January 1961 and August 2002 when climate anomaly such as ENSO was active. Out of 42 years of data, there were 8 El Niño years, 8 La Niña years and 9 IOD years. By resampling these three sub-samples 42 times respectively, we generated three separate time series of climate data, each of which represent climate data expected of the particular climate anomaly. More details about this resampling approach can be found in Wilks (2006) and Efron and Tibshirani (1998).

3.6 Discussions of Results

For MISBA model, all model parameters such as (β and w_{drain}) were derived from the Ecoclimap dataset and so no model calibration was necessary (Kerkhoven and Gan, 2006). On the other hand, model parameters of the Sacramento model was derived through a combination of manual and automatic calibration base on the Schuffe Complex Evolution Method (Duan et al., 1992).

3.6.1 Physically-based and Fully Distributed MISBA Model

Precipitation data extracted from NCEP and ERA-40 reanalysis data of January 1961-August 2002 for UBNB were compared against gauged rainfall data of the Debremarcos station located at 10.25° N - 37.75° E (Sy and Gupta, 2004). The results for a selected grid point #4 of Figure 3.1 are presented as scatterplots in Figure 3.5 and as time series in Figure 3.6, which together with Table 3.1 show that ERA-40 precipitation data agrees reasonably well with the observed gauge data ($R^2 \approx 0.72-0.83$) but not the NCEP data ($R^2 \approx 0.26-0.54$). Apparently, in comparison to the observed precipitation data, the accuracy of both sets of reanalysis data for 1961-1990 is poorer compared to reanalysis data for 1991-2002. Because ERA-40 reanalysis data is better than that of NCEP, MISBA is driven using the ERA-40 data, which includes temperature, humidity, long and shortwave radiation, sea level pressure, wind speed and precipitation.

Using the raw ERA-40 data, MISBA tends to over-simulate the stream-flow of UBNB (see Figure 3.7) especially during the earlier years partly because ERA-40 data is of relatively coarse resolution ($2.5^\circ \times 2.5^\circ$) and the precipitation data should be downscaled before application to MISBA. Figure 3.7 shows that MISBA's simulation agree better with the observed

streamflow after 1990 which could be because ERA-40 data is more accurate after 1990s or because rainfall of UBNB was more variable in 1961-1990 than in 1992-2006, according to [Elshamy et al. \(2009\)](#).

Next, to correct the over-simulation problem of MISBA, the ERA-40 precipitation data was first arbitrarily reduced by 25% for 1961-1990 and by 10% for 1990-2002 which lead to MISBA under simulating the streamflow of UBNB instead of over-simulation. It turns out that by reducing the 1961-1990 precipitation by 15% and the 1990-2002 precipitation by 5%, MISBA simulated streamflow that agree better with the observed data (see [Figure 3.8](#)) where $RMSE = 0.42$ and $R^2=0.65$.

Even though this simple-minded approach seems to improve the model performance, MISBA may not be simulating the hydrology of UBNB correctly because the over-simulation problem could be attributed to MISBA under-simulating the evaporation loss of UBNB. According to [Shahin \(1985\)](#), the annual evaporation loss of UBNB is about 1100-1500mm. Further, given the coarse resolution of ERA-40 data and the mountainous characteristics of UBNB, it is probably more logical to enhance the evaporation process simulated by MISBA than to reduce the precipitation data of ERA-40.

Next, the model has been run for the period 1961-2002 where the rainfall data has been corrected due to orography effect by 1.5% increase for every 12.5 m while [Kerkhoven and Gan \(2006\)](#) have used 1% for every 12.5 m (Golder Associates, Canada) for the orographic effects. The model responded very similar to the previous one with higher $RMSE=0.53$ and $R^2=0.68$.

In MISBA, the water holding capacity of canopy is specified by the W_{rmax} parameter for each vegetation type. If the liquid water retained on the foliage of the vegetation at time t (W_r) is greater than W_{rmax} , water will spill to the ground and so runoff is generated. MISBA has the option

to turn on or off evaporation loss from the canopy. By allowing MISBA to evaporate from the canopy, more evaporation loss will be simulated by MISBA. Therefore, by statistically downscaling the precipitation data of ERA-40 and by allowing evaporation loss from canopy, MISBA could more realistically simulate the runoff of UBNB, as shown in Figure 3.9 for 1970-2002. The overall performance of MISBA has improved, $NS = 0.52$, $RMSE = 0.34 \text{ m}^3/\text{sec}$, but there is still over-simulation in 1971-1990.

3.6.2 Lumped, Conceptual SAC-SMA Model

Because SAC-SMA is a lumped-parameter model, it accepts only point input data as contrast to spatially distributed input data required by MISBA. However, ERA-40 reanalysis data are gridded data and UBNB encompasses eight grid points of ERA-40. Figure 3.10 shows the scatterplots between rainfall data of the eight grid points and the basin wide average rainfall estimated from the Thiessen polygon method applied to these gridded data. It is clear from Figure 3.10 that rainfall data of the grid point nearest to the Debremarcos station (Grid point #4) has the highest correlation with the basin wide average rainfall where $R^2 = 0.85$. Therefore, Grid point #4 and the basin wide average rainfall data are considered to be most representative of UBNB and these data were used to drive SAC-SMA model.

Another required input of SAC-SMA is the PET computed from the modified Hargraves Equation (Eq. 3.7) based on the daily T_{avg} temperature and extraterrestrial radiation R_A data. Again, Figure 3.11 shows the scatterplots of PET between that of four grid points covering central, northern and southern of the UBNB and PET estimated from basin wide average data. Again, PET estimated at the Debremarcos station (close to grid point #4) is more closely correlated with PET estimated from basin wide average data. The latter was used as input to the SAC-SMA model.

Table 3.2 shows the optimized parameters of SAC-SMA calibrated through

a combination of automatic (Duan et al., 1992) and manual calibrations for UBNB. The optimized upper zone tension moisture capacity (UZTWM) and the free water storages (UZFWM) of the UBNB were found to be 4.08 and 9 mm respectively, which are relatively small according to Gan and Burges (1990). However, the range of values recommended by Gan and Burges (1990) were mainly based on their experience with North American basins. These low upper zone conceptual storage parameters probably reflect the low upper soil storage capacity of UBNB dominated by igneous and sedimentary rocks (Friis et al., 2010). However, the optimized lower zone conceptual storage parameters, LZTWM, LZFSM and LZFPFM are relatively high (Table 3.2), which are within the upper and lower bounds for lower zone storage parameters recommended by Gan and Burges (1990).

With respect to the observed streamflow of the El Diem station of UBNB, the performance of SAC-SMA at the calibration run (based on climate data of 1975-1996) and the validation run are better than that of MISBA (Table 3.3), such that R^2 is 78.6% for calibration and 82.3% for validation even though it models the hydrology of UBNB in a lumped, conceptual framework as against the physically-based, fully distributed framework of MISBA. Figure 3.12 shows that the simulated runoff hydrograph of SAC-SMA generally agrees with the observed counterparts. However, SAC-SMA tends to under simulate the peak flows between 1990 and 2001. Apparently partly due to the coarse resolution of ERA-40 reanalysis data, the mountainous characteristics of UBNB, more difficulties had been encountered to model the hydrology of UBNB in a physics-based approach.

3.6.3 Climate anomalies effects

Various studies have shown that climate of African river basins are subjected to the effects of climate anomalies and climate change, (e.g. Ntale et al., 2003; Ntale and Gan, 2004). ENSO years observed in the Twentieth

Century are as follows: El Niño years (e.g., 1912, 1913, 1915, 1919, 1920, 1926, 1927, 1930, 1931, 1940, 1942, 1952, 1954, 1958, 1959, 1966, 1970, 1973, 1977, 1983, 1987, 1992, 1998), and La Niña years (1917, 1918, 1925, 1929, 1939, 1951, 1956, 1957, 1965, 1971, 1972, 1974, 1976, 1989, 1996, 1999) (see [Shabbar et al., 1997](#); [Gan et al., 2007](#)). According to [Saji et al. \(1999, 2005\)](#); [Meyers et al. \(2007\)](#) and a website of [of Meteorology-Australia \(2011\)](#), Australia, IOD years observed in the last fifty years were 1961, 1963, 1967, 1972, 1977, 1982, 1983, 1994, 1997, 2006, 2007. To simulate the possible effect of climate anomalies such as ENSO and IOD on the UBNB since 1961, selected years of ERA-40 re-analysis data (1961-2002) when ENSO or IOD were active are re-sampled using the bootstrap method (see [Wilks, 2006](#)). Figure [3.13](#) and [3.14](#) showing the resampled rainfall and temperature for one grid point in the basin area at 10°N-37.5°E, respectively. These two figures show the reader what the resampled data looks like, but doesn't mean that these are the actual temperature data (i.e. should not represent actual time series).

A composite analysis was used to explore the impacts of ENSO and IOD on the spring (February-May; FMAM) and summer (June-September; JJAS) rainfall of the UBNB. El Niño (La Niña) composites were based on years in which the 5-month moving average of Southern Oscillation index (SOI) remained in the lower (higher) 25% of the distribution for a period ≥ 5 consecutive months ([Shabbar et al., 1997](#)). The composite rainfall of El Niño years for a given grid point was computed as the ratio of the mean of the FMAM (JJAS) rainfall for the anomalous years (e.g., the 8 El Niño years) relative to the long-term mean seasonal rainfall of FMAM (JJAS) for that grid point computed from the ERA-40 data of 1961-2002. Figure [3.15](#) (a-b) show the composites for all 8 grid points, where a composite value greater than unity means that the climate anomaly is associated with a positive FMAM (JJAS) rainfall anomaly, and vice versa. The composite

analysis shows considerable variations from grid to grid. 3.15 (a) shows that El Niño (La Niña) is typically associated with negative (positive) FMAM rainfall in the southwestern of the UBNB but positive (negative) impact for the northern part of the basin. For JJAS rainfall, El Niño (La Niña) is generally associated with negative (positive) composite across the UBNB (see Figure 3.15 (b)).

Due to the orographic effect of the basin, we tried to study the composite along three longitudes (35° E, 37.5° E, and 40° E). El Niño decreases the JJAS rainfall in the UBNB and boosts the FMAM rainfall. These results agree with (Wolde-Georgis et al., 2001) who noted that weather in some parts of Ethiopia might not be correlated with El Niño events because of diversity in Ethiopia's microclimates.

Figure 3.15 (c) shows that El Niño (La Niña) is typically associated with strong positive (negative) FMAM rainfall anomaly across the eastern part of UBNB but the rainfall anomaly on the western part associated with El Niño (La Niña) is relatively modest even though similar. Apparently the central part of UBNB along the 37.5° E longitude was relatively un-affected by El Niño (La Niña) but strongly affected by IOD. Similarly, Figure 3.15 (d) shows that the JJAS rainfall across the central and western parts (i.e. 35° E, 37.5° E) of UBNB were also relatively marginally affected by El Niño (La Niña). On the other hand, the eastern part of the UBNB is typically associated with positive (negative) JJAS rainfall with El Niño (La Niña).

Given that ENSO and IOD could lead to significant rainfall anomalies (both positive and negative) in some parts of UBNB, a procedure is proposed to simulate the effect of these climate anomalies on the streamflow of UBNB. The climate data re-sampled from ERA-40 reanalysis data that correspond to anomalous, El Niño, La Niña, and IOD years were used to drive MISBA of (Kerkhoven and Gan, 2006) and the Sacramento model to simulate the potential impact of these climate anomalies on the streamflow

of the UBNB. The results are compared with the historical record.

Under different climate anomalies (El Niño, La Niña, and IOD), both La Niña and IOD are responsible for generating more streamflow than El Niño, which has quite an effect of the UBNB streamflow. Figure 3.16 a (b) shows boxplots of streamflow simulated by MISBA (SAC-SMA) under the three climate anomalies in comparison with the observed streamflow. The results show that on a whole all three climate anomalies increase the streamflow variability of UBNB, particularly the IOD. While La Niña is expected to give rise to more positive than negative streamflow anomaly, El Niño and IOD do not seem to exert similar effect on the streamflow of UBNB given the 50th percentile of El Niño and IOD are similar to that of observed streamflow.

In comparison to the boxplot of observed streamflow, the corresponding boxplots for streamflow simulated by SAC-SMA for the three climate anomalies also show that these climate anomalies are expected to increase the streamflow variability of UBNB. However, on the whole, El Niño (La Niña) is expected to exert some drying (wetting) effect on the streamflow of UBNB but IOD is expected to exert fairly significant wetting effect on the streamflow of UBNB. More research is needed before we can conclude the overall wetting effect of IOD on UBNB (see Figure 1.2).

Figure 3.17 shows the monthly hydrograph which is averaged for the entire period (1961-2001). Also, it is clear that La Niña and IOD are expected to exert fairly significant wetting effect while El Niño is exerting some drying effect on the streamflow of UBNB. In general, The IOD and La Niña positively affecting the UBNB streamflow while El Niño adversely affect the UBNB streamflow which agree with [Eltahir \(1996\)](#) who found the same relationship between the main stream of the Nile and ENSO.

3.7 Summary and Conclusions

This study investigated hydrologic modeling of the upper Blue Nile basin (UBNB) and the possible impact of climate variability on the water availability of the UBNB. The fully distributed, physically-based surface scheme called modified Interactions Soil-Biosphere-Atmosphere (MISBA) of (Kerkhoven and Gan, 2006) and the lumped-parameter, conceptual Sacramento model of the National Weather Service of the USA were applied to simulate the hydrologic effects of climate anomalies on the UBNB. One of the key input data to basin scale hydrologic models is representative and accurate rainfall data which is generally variable spatially. This can be a challenge for the UBNB with a basin area of $176,000 \text{ km}^2$, of mountainous terrain and with few rain gauges. For the UBNB, its complex terrain and rainfall dominated by local scale convective storms likely means, a highly variable rainfall field spatially and temporally. To overcome the problem of limited and possibly non-representative gauge measurements, precipitation from the ERA-40 reanalysis data were downscaled and used to drive the hydrologic models tested in this study.

To simulate the hydrologic impact of a particular climate anomaly, ENSO or IOD, for those anomalous years between January 1961 and August 2002 when a particular climate anomaly was active, climate data of those anomalous years were randomly resampled by a bootstrap approach to generate a time series of climate data, which represent climate data affected by that particular anomaly. By forcing a hydrologic model with these resampled climate data, we can simulate the possible impact of the climate anomaly on the hydrology of UBNB. Conclusions based on results obtained for this study are summarized below:

1. There are more discrepancies between rainfall data of ERA-40 and the gauged data before 1990 than after, but it was accurate more

than the NCEP data;

2. Partly due to the coarse resolution of GCM scale ($2.5^{\circ} \times 2.5^{\circ}$) ERA-40, the data should be downscaled (bias correction) before it is applied to a hydrologic model; the data was also corrected for the orographic effect of the mountainous terrain of UBNB;
3. The UBNB is very sensitive to the rainfall variability;
4. For any physically based distributed models, corrections for altitude are mandatory specifically for basins in mountainous areas. A 3% increase factor for every 25 m rise is needed to correct the rainfall over the UBNB for the orographic effects;
5. Modifications were made to the modified land surface MISBA model of [Kerkhoven and Gan \(2006\)](#) so that the modified model, could better simulate the sub-surface streamflow of the UBNB dominated by rainfall-runoff hydrology with an emphasis on the treatment of the evapotranspiration scheme;
6. The performance of MISBA applied to UBNB improved after MISBA was modified so that it could simulate evaporation loss from the canopy. Compared to the observed streamflow of UBNB, $R^2 = 0.58$, $RMSE = 0.34 \text{ m}^3/\text{sec}$. In contrast, the performance of SAC-SMA at the calibration run and the validation run are better than that of MISBA, such that R^2 is 78.6% for calibration and 82.3% for validation even though it models the hydrology of UBNB in a lumped, conceptual framework as against the physically-based, fully distributed framework of MISBA. This is because the SAC-SMA is a simple moisture accounting model while MISBA is a physically based model involving both energy and water fluxes in addition to the effects of data accuracy on the model performance;

7. ENSO warm and cold phases have variable effects on western Ethiopia (UBNB) rainfall spatially and temporally (i.e. from season to season). El Niño tends to decrease the JJAS rainfall in the UBNB and boosts the FMAM rainfall, while La Niña has opposite effect to the rainfall of UBNB, which agrees with [Elsanabary and Gan \(2012\)](#) finding;
8. In general, based on the simulations of MISBA and SAC-SMA for UBNB, La Niña and IOD tend to have a wetting effect while El Niño has a drying effect on streamflow of the UBNB, as found by [Eltahir \(1996\)](#). In addition, apparently ENSO and IOD increase the streamflow variability more than changing the magnitude of streamflow.

In conclusion, MISBA model demonstrates reliability for climate variability studies, assuming the UBNB's physical conditions remain basically unchanged to the end of the 21st century. A reliable water resources management guided by such streamflow simulation, especially during low flow season could be crucial for an optimal allocation of water usage among various competing users. Finally, a study that combined the impacts of climate change and climate variability on the UBNB is currently conducted by the authors.

Acknowledgements

This research was funded by the Egyptian Ministry of Higher education (MHE). The first author was also partly funded by a graduate teaching assistantship of the Department of Civil and Environmental Engineering, University of Alberta. The authors thank Dr. Ernst Kerkhoven for providing the MISBA source code. The Ecoclimap dataset was provided by Météo France http://www.cnrn.fr/gmme/PROJETS/ECOCLIMAP/page_recoclimap.htm. The ERA-40 re-analysis dataset was obtained from the European Centre for Medium-Range Weather Forecasts (ECMWF) data

server. The 1 km Digital Elevation Model of the upper Blue Nile basin was provided by USGS http://eros.usgs.gov/#/FindData/Products_and_Data_Available/HYDR01K. Great appreciation is expressed to the two anonymous reviewers of this paper for their comments and suggestions.

References

- Abegaz, A., Keulen, H., Haile, M., and Oosting, S. (2007). Nutrient dynamics on smallholder farms in Teghane, Northern Highlands of Ethiopia. In A. Bationo, B. Waswa, J. Kihara, and J. Kimetu (Eds.), *Advances in integrated soil fertility management in sub-Saharan Africa: Challenges and opportunities* (p. 365-378). Springer Netherlands.
- Abteu, W., Melesse, A. M., and Dessalegne, T. (2009). El Niño Southern Oscillation link to the Blue Nile river basin hydrology. *Hydrol. Processes*, 23(26), 3653-3660.
- Abu-Zeid, M. A., and Biswas, A. K. (1991). Some major implications of climatic fluctuations on water management. *Int. J. Water Resour. Dev.*, 7(2), 74.
- Amarasekera, K. N., Lee, R. F., Williams, E. R., and Eltahir, E. A. B. (1997). ENSO and the natural variability in the flow of tropical rivers. *J. Hydrol.*, 200(1-4), 24-39.
- Arnell, N. W. (1999). Climate change and global water resources. *Global Environ. Change*, 9(Supplement 1), S31-S49.
- Barry, R., and Gan, T. (2011). *The global Cryosphere: Past, present and future*. Cambridge University Press.
- Bashar, K., and Zaki, A. (2005). *SMA based continuous hydrologic simulation of the Blue Nile*. UNESCO Cairo Office, Cairo, Egypt.

- Retrieved from http://www.unesco.org/new/fileadmin/MULTIMEDIA/FIELD/Cairo/pdf/SMA_Based_Continuous_Hydrologic_Simulation_Of_The_Blue_Nile.pdf (Accessed: 04/17/2012)
- Bate, R. (2000). *Life's adventure: Virtual risk in a real world*. Butterworth-Heinemann.
- BBC. (2010, May). *East Africa seeks more Nile water from Egypt*. Retrieved from <http://news.bbc.co.uk/2/hi/8682387.stm> (Accessed: 06/01/2010)
- Burnash, R., Ferral, R., McGuire, R., and Center, J. F.-S. R. F. (1973). *A generalized streamflow simulation system: conceptual modeling for digital computers*. U. S. Dept. of Commerce, National Weather Service.
- Congress. (2009). *Congressional record, v. 150, pt. 11, june 25, 2004 to july 14, 2004*. United States Congress. Retrieved from <http://books.google.ca/books?id=FtNW4skCGBUC> (Accessed: 06/20/2012)
- Conway, D. (1997). A water balance model of the Upper Blue Nile in Ethiopia. *Hydrol. Sci. J.*, 42(2), 265-286.
- Conway, D. (2000). The climate and hydrology of the Upper Blue Nile river. *The Geographical Journal*, 166(1), 49-62.
- Degefu, W. (1987). Some aspects of meteorological drought in Ethiopia. In M. H. Glantz (Ed.), *Drought and hunger in Africa: Denying famine a future* (p. 23-36). Cambridge, England: Cambridge University Press.
- Droogers, P., and Allen, R. (2002). Estimating reference evapotranspiration under inaccurate data conditions. *Irrig.Drain.Syst.*, 16(1), 33-45.
- Duan, Q., Sorooshian, S., and Gupta, V. (1992). Effective and efficient global optimization for conceptual rainfall-runoff models. *Water Resour.Res.*, 28(4), 1015-1031.

- Duffie, J. A., and Beckman, W. A. (1980). *Solar engineering of thermal processes hydrology of the Nile basin*. New York: Wiley.
- Duiker, W. J., and Spielvogel, J. J. (2009). *World history: to 1500* (Vol. 5). Australia: Wadsworth.
- ECMWF. (2009, September). *ECMWF-ERA-40*. Retrieved from http://data-portal.ecmwf.int/data/d/era40_daily/ (Accessed: 02/15/2009)
- Efron, B., and Tibshirani, R. (1998). *An introduction to the Bootstrap*. Boca Raton, Fla.: Chapman and Hall/CRC.
- Elsanabary, M. H., and Gan, T. Y. (2012). Investigation of seasonal rainfall variability over the Ethiopian Highlands: Teleconnection between the Upper Blue Nile basin rainfall and the oceanic anomalies. *Proc. CSCE General Annual Conference, Canadian Society for Civil Engineering*. (Edmonton, Alberta, June 6-9, 2012)
- Elshamy, M. E., Seierstad, I. A., and Sorteberg, A. (2009). Impacts of climate change on Blue Nile flows using bias-corrected GCM scenarios. *Hydrol. Earth Syst. Sci.*, 13(5), 551-565.
- Eltahir, E. A. B. (1996). El Niño and the natural variability in the flow of the Nile river. *Water Resour. Res.*, 32(1), 131-137.
- Finnerty, B., Smith, M., Seo, D., Koren, V., and Moglen, G. (1997). Space-time scale sensitivity of the Sacramento model to radar-gage precipitation inputs. *J. Hydrol.*, 203(1), 21-38.
- Friis, I., Demissew, S., and Breugel, P. (2010). *Atlas of the potential vegetation of Ethiopia*. Det Kongelige Danske Videnskabernes Selskab.

- Gan, T. Y., and Biftu, G. (1996). Automatic calibration of conceptual rainfall-runoff models: Optimization algorithms, catchment conditions, and model structure. *Water Resour. Res.*, 32(12), 3513-3524.
- Gan, T. Y., and Burges, S. J. (1990). An assessment of a conceptual rainfall-runoff models ability to represent the dynamics of small hypothetical catchments: I models, model properties, and experimental-design. *Water Resour. Res.*, 26(7), 1595-1604.
- Gan, T. Y., Gobena, A. K., and Wang, Q. (2007). Precipitation of southwestern Canada: Wavelet, scaling, multifractal analysis, and teleconnection to climate anomalies. *J. Geophys. Res. Atmos.*, 112(D10), D10110.
- Gleick, P. (1992). *The vulnerability of runoff in the Nile basin to climatic changes* (Vol. 5). Oxford: International Association of Hydrological Sciences.
- Habets, F., Noilhan, J., Golaz, C., Goutorbe, J., Lacarrère, P., Leblois, E., ... Vidal-Madjar, D. (1999). The ISBA surface scheme in a macroscale hydrological model applied to the Hapex-Mobilhy area: Part I: Model and database. *J. Hydrol.*, 217(1-2), 75-96.
- Hargreaves, G. (1994). Defining and using reference evapotranspiration. *J. Irrig. Drain. Eng.*, 120(6), 1132-1139.
- Hargreaves, G., Hargreaves, G., and Riley, J. (1985). Agricultural benefits for Senegal river basin. *J. Irrig. Drain. Eng.*, 111(2), 113-124.
- Houghton, J., and Syvitski, J. (2009). Global warming: The complete briefing. *Oceanography*, 22(3), 191-205.
- IPCC. (2012). *Renewable energy sources and climate change mitigation, special report of the Intergovernmental Panel on Climate Change*. Cambridge University Press.

- Kalnay, E., Kanamitsu, M., Kistler, R., Collins, W., Deaven, D., Gandin, L., . . . Woollen, J. (1996). The NCEP/NCAR 40-year reanalysis project III.
- Kassahun, B. (1991). Climate change and forecast in Ethiopia. *Conference Proceedings: a Meeting organized by the DPPC on Nehasel 1991 (Ethiopian calendar)*, 42(2), 265-286.
- Kerkhoven, E., and Gan, T. (2006). A modified ISBA surface scheme for modeling the hydrology of Athabasca river basin with GCM-scale data. *Adv. Water Resour.*, 29(6), 808-826.
- Kloos, H., and Legesse, W. (2010). *Water resources management in Ethiopia : implications for the Nile basin*. Amherst, NY: Cambria Press.
- Masson, V., Champeaux, J.-L., Chauvin, F., Meriguet, C., and Lacaze, R. (2003). A global database of land surface parameters at 1-km resolution in meteorological and climate models. *J. Clim.*, 16(9), 1261-1282.
- Masson, V., and Faroux, S. (2010, 06/10). *Ecoclimap data*. Retrieved from http://www.cnrm.meteo.fr/gmme/PROJECTS/ECOCLIMAP/page_ecoclimap.htm (Accessed: 06/17/2009)
- Meyers, G., McIntosh, P., Pigot, L., and Pook, M. (2007). The years of El Niño, La Niña, and interactions with the tropical Indian Ocean. *J. Clim.*, 20(13), 2872-2882.
- Nicholson, S. E., and Entekhabi, D. (1986). The quasi-periodic behavior of rainfall variability in Africa and its relationship to the Southern Oscillation. *Meteorol. Atmos. Phys.*, 34(3), 311-348.
- Noilhan, J., and Mahfouf, J. F. (1996). The ISBA land surface parameterisation scheme. *Global Planet. Change*, 13(1-4), 145-159.

- Noilhan, J., and Planton, S. (1989). A simple parameterization of land surface processes for meteorological models. *Mon. Wea. Rev.*, *117*, 536-549.
- Ntale, H. K., and Gan, T. Y. (2004). East African rainfall anomaly patterns in association with El Niño/Southern Oscillation. *J. Hydrol. Eng.*, *9*(4), 257-268.
- Ntale, H. K., Gan, T. Y., and Mwale, D. (2003). Prediction of east African seasonal rainfall using Simplex Canonical correlation analysis. *Journal of Climate*, *16*(12), 2105-2112.
- of Meteorology-Australia, T. B. (2011, August). *Positive iod.* Retrieved from <http://www.bom.gov.au/climate/IOD/positive/> (Accessed 08/11/2011)
- Ogallo, L. (1979). Rainfall variability in Africa. *Mon. Wea. Rev.*, *107*(9), 1133-1139.
- Ravazzani, G., Corbari, C., Morella, S., Gianoli, P., and Mancini, M. (2011). Modified Hargreaves Samani equation for the assessment of reference evapotranspiration in Alpine river basins. *J.Irrig.Drain.Eng.*, *1*(6), 261.
- Saji, N., Ambrizzi, T., and Ferraz, S. T. (2005). Indian Ocean Dipole mode events and Austral surface air temperature anomalies. *Dynamics of Atmospheres and Oceans*, *39*(1-2), 87- 01.
- Saji, N., Goswami, B. N., Vinayachandran, P. N., and Yamagata, T. (1999). A dipole mode in the tropical Indian Ocean. *Nature*, *401*(6751), 360-363.
- Seleshi, Y., and Zanke, U. (2004). Recent changes in rainfall and rainy days in Ethiopia. *Int.J.Climatol.*, *24*(8), 973-983.

- Shabbar, A., Bonsal, B., and Khandekar, M. (1997). Canadian precipitation patterns associated with the Southern Oscillation. *J.Clim.*, 10(12), 3016-3027.
- Shahin, M. (1985). *Hydrology of the Nile basin* (Vol. 21). Amsterdam: Elsevier.
- Strzepek, K. M., Yates, D. N., and El Quosy, D. (1996). Vulnerability assessment of water resources in Egypt to climatic change in the Nile basin. *Climate Research*, 6(2), 89-92.
- Sutcliffe, J., Parks, Y., and of Hydrological Sciences, I. A. (1999). *The hydrology of the Nile*. International Association of Hydrological Sciences.
- Sy, B. K., and Gupta, A. (2004). *Information-statistical data mining : Warehouse integration with examples of oracle basics*. Boston, USA: Kluwer Academic Publishers.
- Wilks, D. S. (2006). *Statistical methods in the atmospheric sciences*. Burlington, MA; London: Academic Press.
- Wolde-Georgis, T., Aweke, D., and Hagos, Y. (2001). The case of Ethiopia: reducing the impacts of environmental emergencies through early warning and preparedness. In G. MH (Ed.), . United Nations University Press.

Table 3.1: Correlation between observed monthly rainfall data at Debre-marcos station and ECMWF and NCEP rainfall data

	1961-2002	1961-1990	1970-2002	1991-2002
ECMWF	0.73	0.72	0.74	0.83
NCEP	0.29	0.26	0.40	0.54

Table 3.2: Optimized SAC-SMA model parameters for the Upper Blue Nile Basin.

No.	Param.	Value	Description
1	UZWWM	4.08	Upper zone tension water maximum capacity (mm).
2	UZFWM	9	Upper zone free water maximum capacity (mm).
3	UZK	0.517	Lateral drainage rate of upper zone free water expressed as a fraction of contents per day.
4	PCTIM	0	The fraction of the catchment which produces impervious runoff during low flow conditions.
5	ADIMP	0	The additional fraction of the catchment which exhibits impervious characteristics when the catchment's tension water requirements are met.
6	LZWWM	147.7	Lower zone tension water maximum capacity (mm).
7	LZFSM	142.8	Lower zone supplemental free water maximum capacity (mm).
8	LZFPM	486.9	Lower zone primary free water maximum capacity (mm).
9	LZSK	0.097	Lateral drainage rate of lower zone supplemental free water expressed as a fraction of contents per day.
10	LZPK	0.023	Lateral drainage rate of lower zone primary free water expressed as a fraction of contents per day.
11	UHG(1)	0.001	Unit graph Ordinate 1
12	UHG(2)	0.001	Unit graph Ordinate 2
13	UGH(3)	0.001	Unit graph Ordinate 3

Table 3.3: Summary statistics of MISBA and SAC-SMA forecasting skill using the simulated streamflow

	R^2	RMSE (m^3/sec)	E_f %	Bias (m^3/sec)
MISBA	0.58	0.34	52	16.22
SAC-SMA				
Calibration	0.79	83.35	60.02	0.34
Validation	0.82	76.92	66.24	-13.24

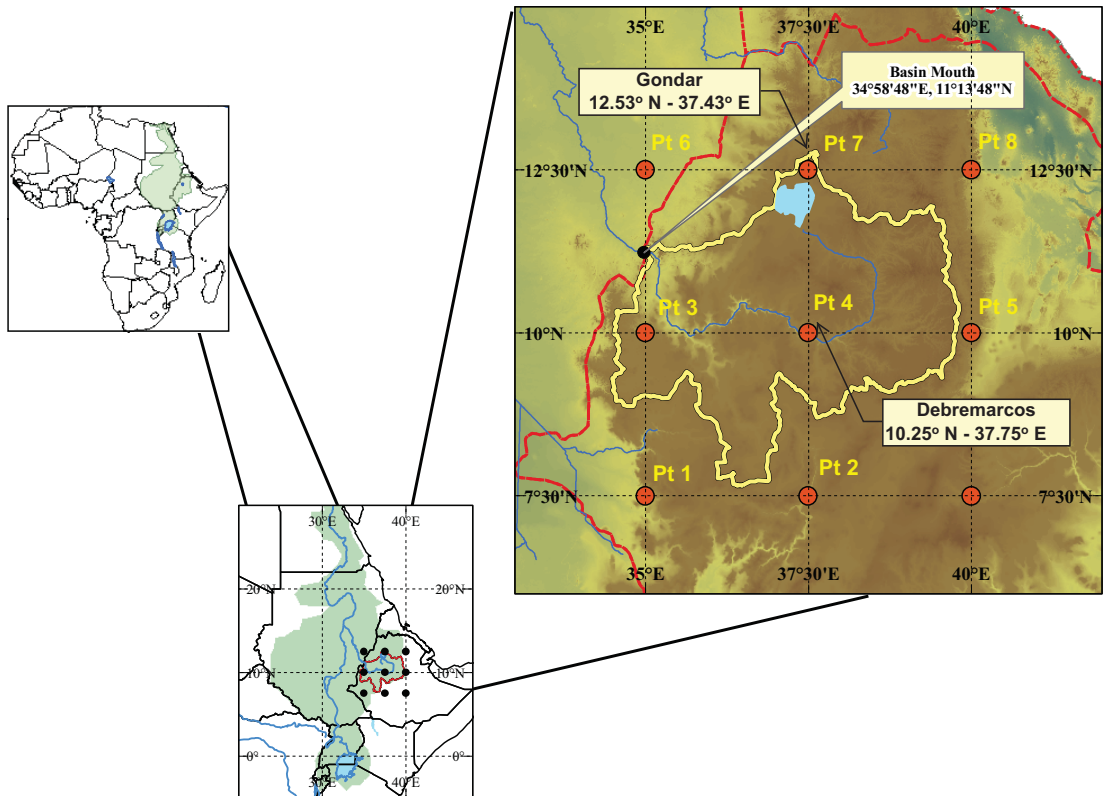


Figure 3.1: The study site, showing the Upper Blue Nile Basin, topography and the nine grid points of ERA-40 used for the hydrologic modeling.

Surface Energy budget/Fluxes

Incoming fluxes are in blue, outgoing are in green, turbulent exchanges with the atmosphere are in purple. Sub-surface heat fluxes are in red.

Hydrology

Water sources due to the various components of the precipitation are in blue, evapotranspiration sources/sinks are in green, and canopy drip, snowmelt runoff, surface runoff, drainage and soil water fluxes are in red.

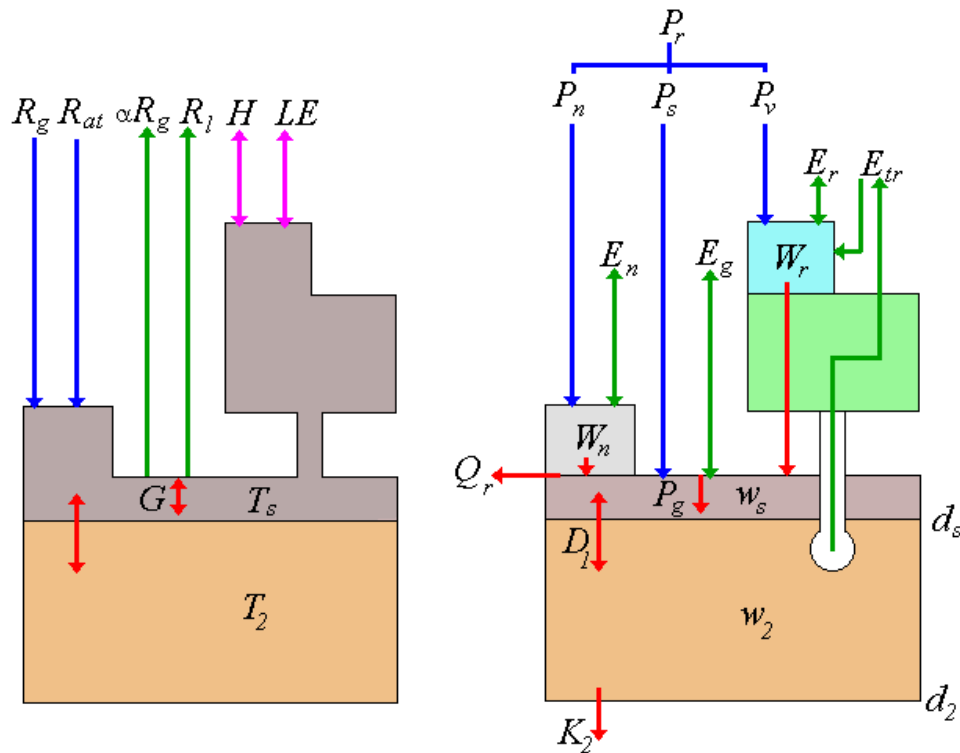


Figure 3.2: Schematic diagram of surface energy budget and hydrology in ISBA standard model. R_g (incoming solar radiation), R_{at} (incoming longwave atmospheric radiation), αR_g (outgoing shortwave radiation), R_l (outgoing longwave atmospheric radiation), H (sensible heat flux), L_E (latent heat flux), G (ground heat flux), T_s (surface temperature), T_2 (deep soil temperature), P_r (total precipitation), P_n (snowfall), P_s (precipitation reaching soil), P_v (precipitation intercepted by vegetation), P_g (infiltration), Q_r (surface runoff), D (surface/deep soil water diffusion), K (gravitational drainage), E_n (sublimation), E_g (bare soil evaporation), E_r (evaporation from interception), E_{tr} (transpiration), W_r (canopy water store), W_n (snowpack SWE), w_s (surface soil volumetric water content), w_2 (root layer soil volumetric water content), d_s (surface soil depth), d_2 (root depth). Source Météo France <http://www.cnrm.meteo.fr/isbadoc/model/schemstd.html>

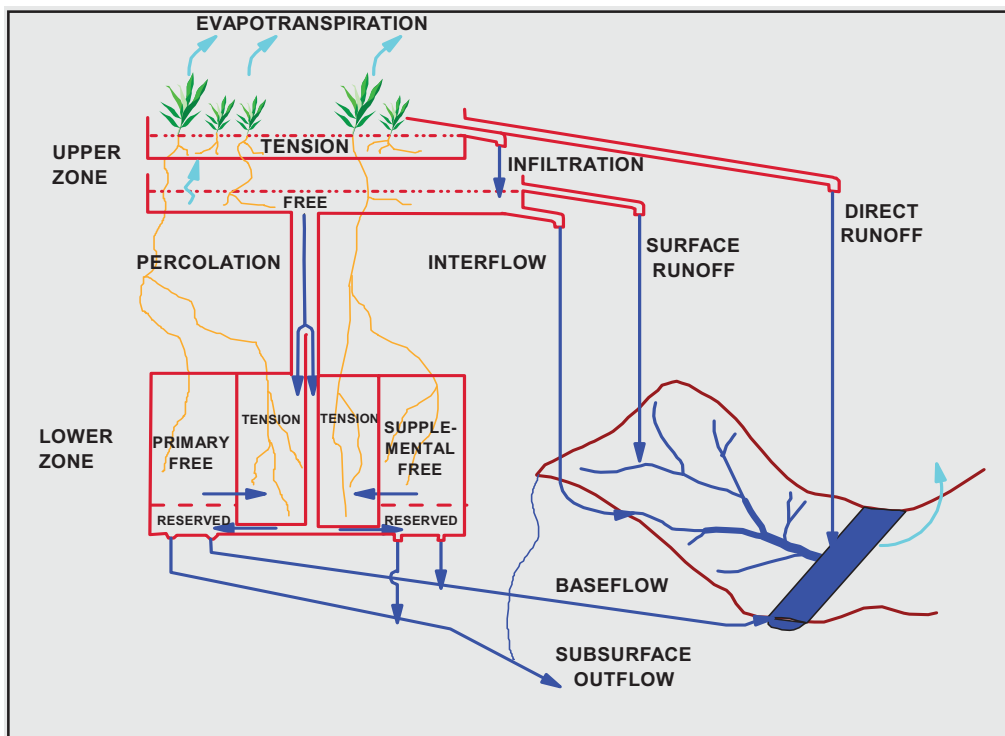


Figure 3.3: Schematic diagram of the Sacramento-Soil Moisture Accounting (SAC-SMA) Model (Gan and Burges, 1990)

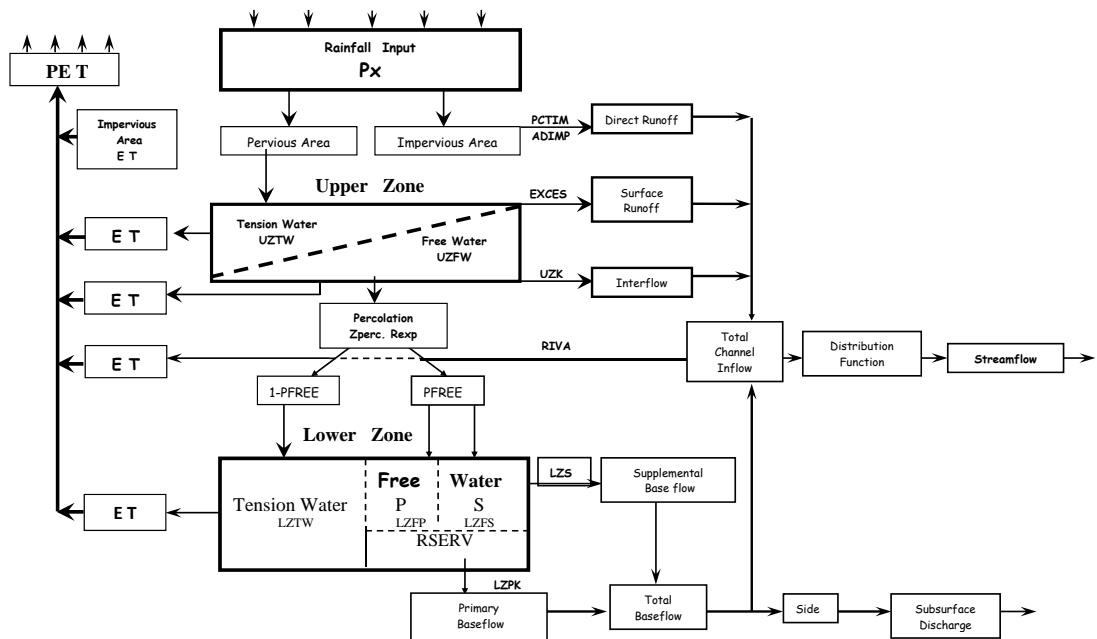


Figure 3.4: Flow diagram of the Sacramento-Soil Moisture Accounting (SAC-SMA) Model. About 15 model parameters need calibration (Gan and Burges, 1990)

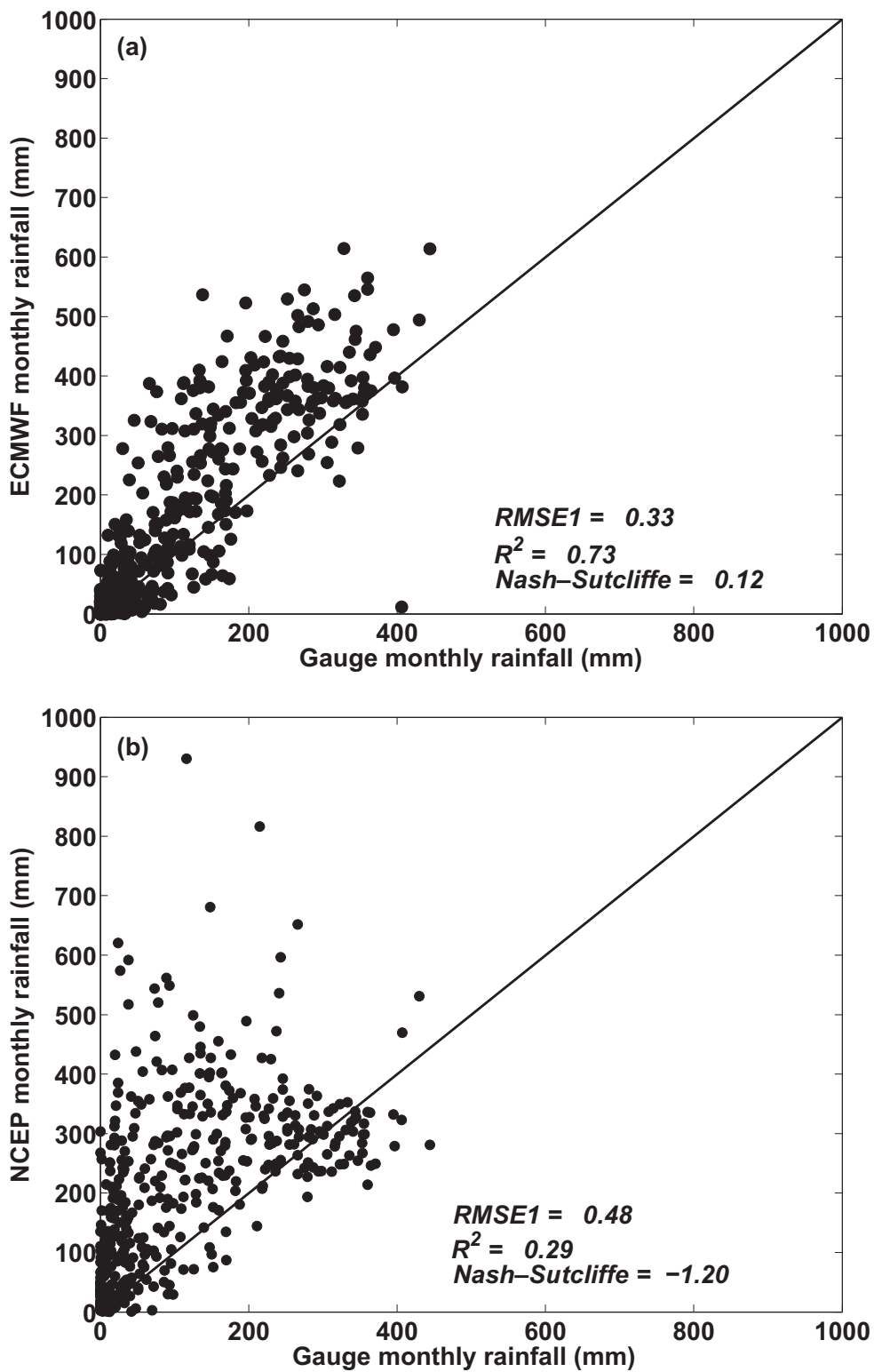


Figure 3.5: Scatterplots of the gauge rainfall data at Debremarcos station and two rainfall data sets (a) ERA-40 data, and (b) NCEP data.

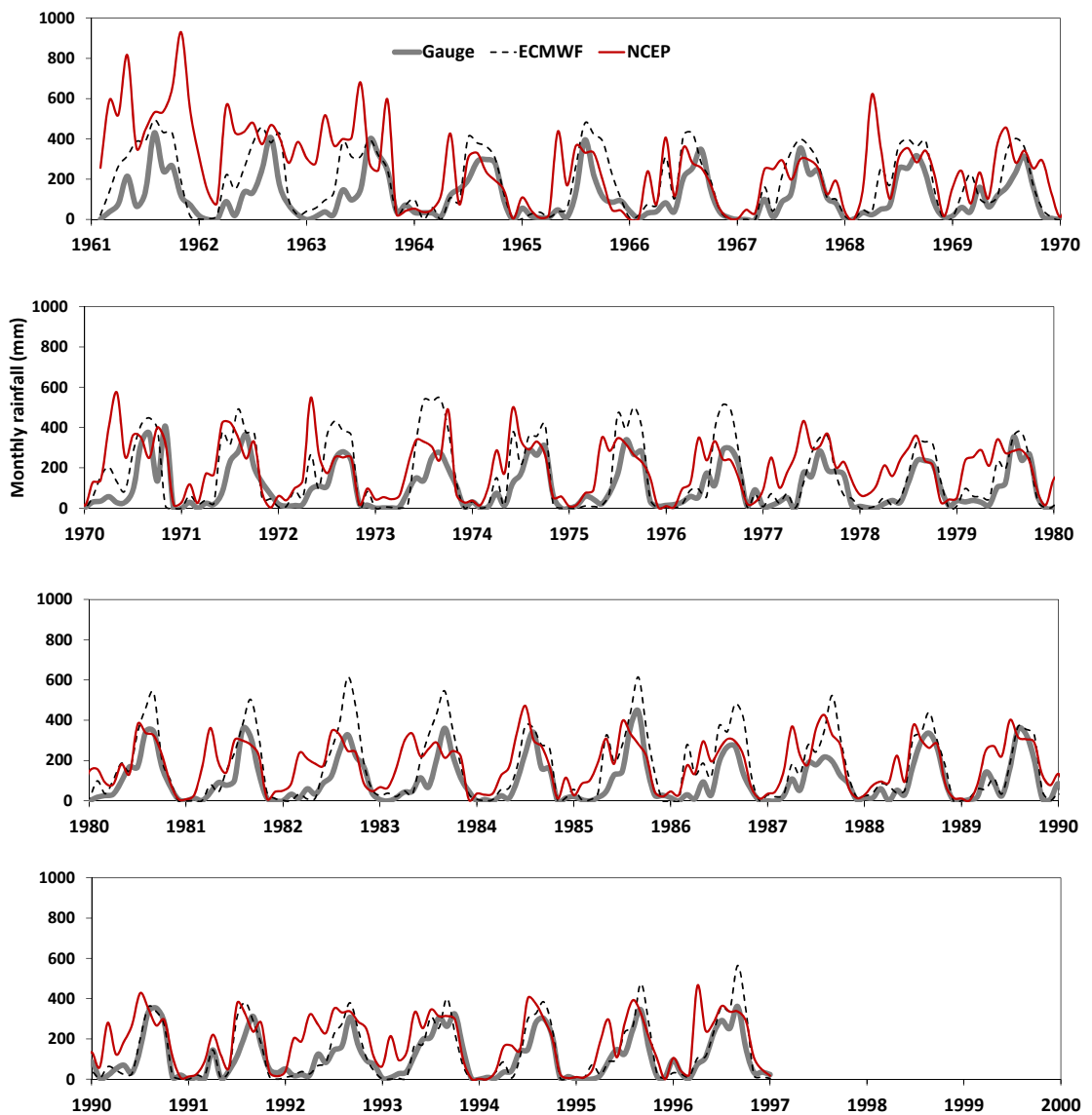


Figure 3.6: Comparison of Monthly rainfall time series between Gauge rainfall data at Debremarcos, ERA-40, and NCEP rainfall data.

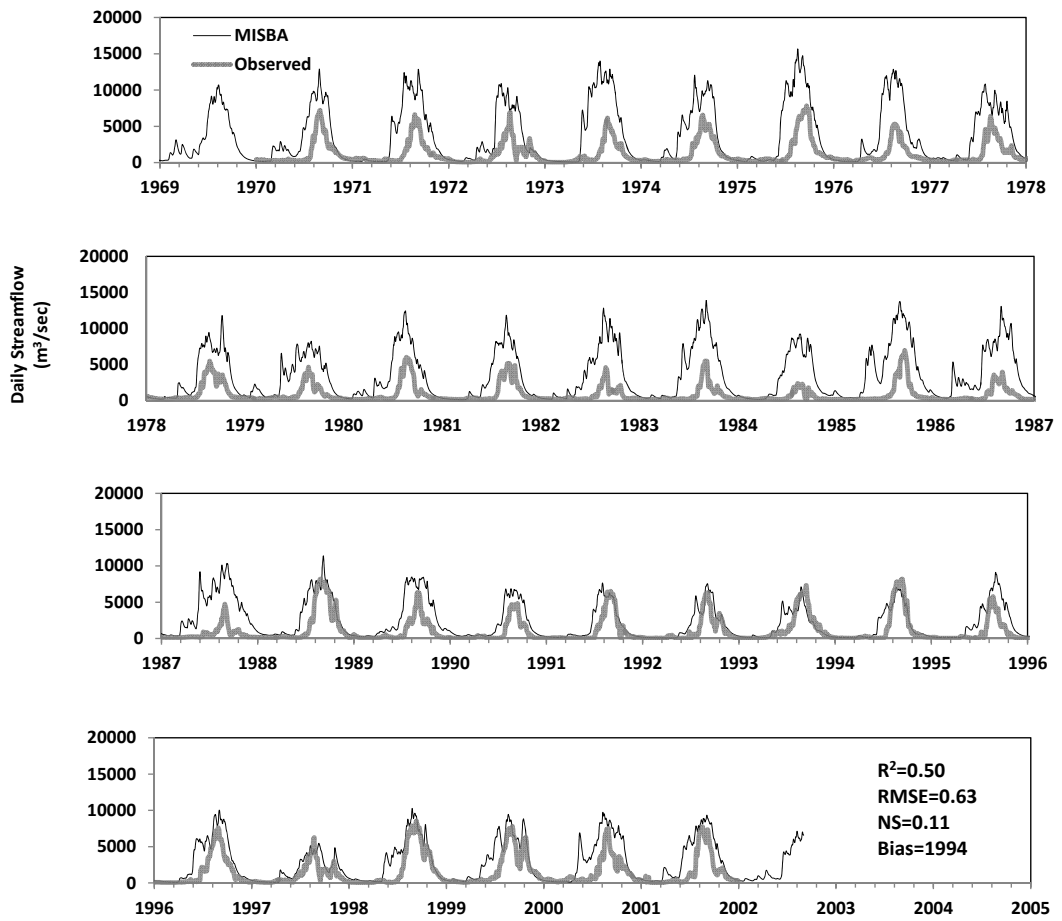


Figure 3.7: Streamflow simulation from MISBA model at daily time scale before rainfall, elevation, temperature corrections.

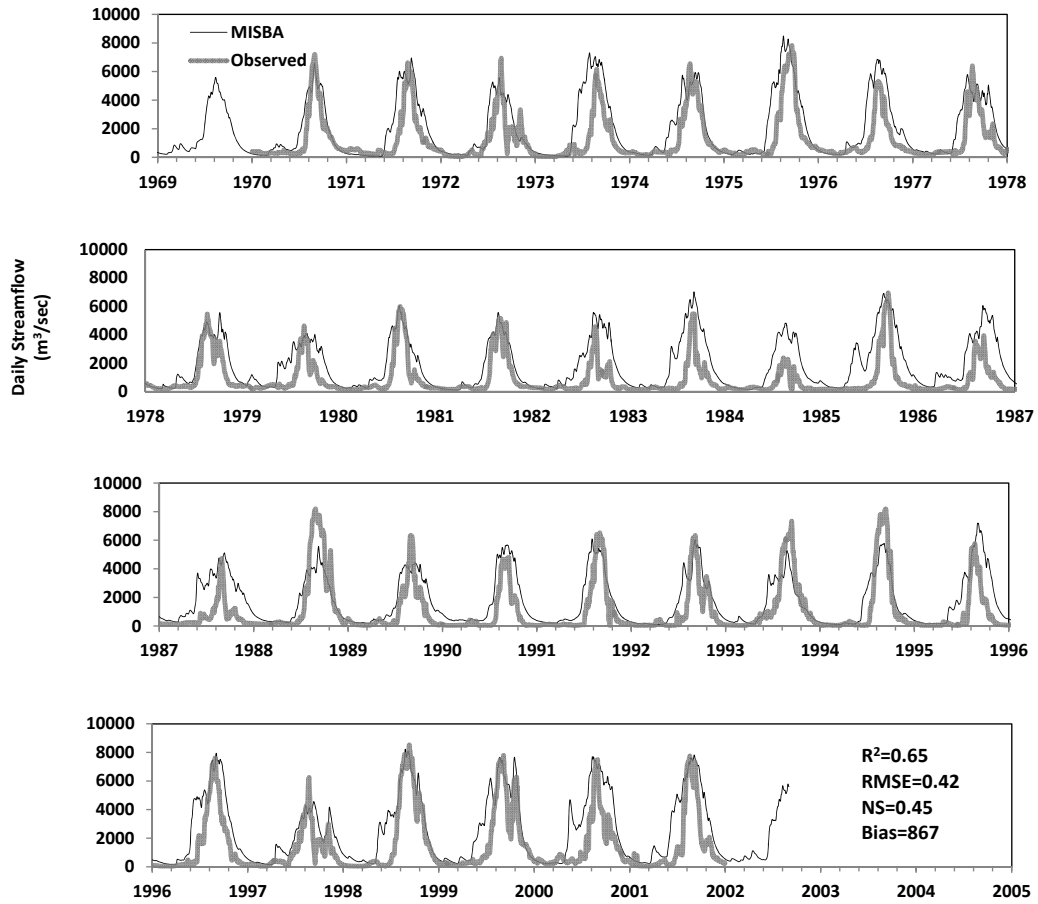


Figure 3.8: The UBNB streamflow simulation from MISBA model at daily time scale after adjusting the rainfall data by 3% increase with elevation .

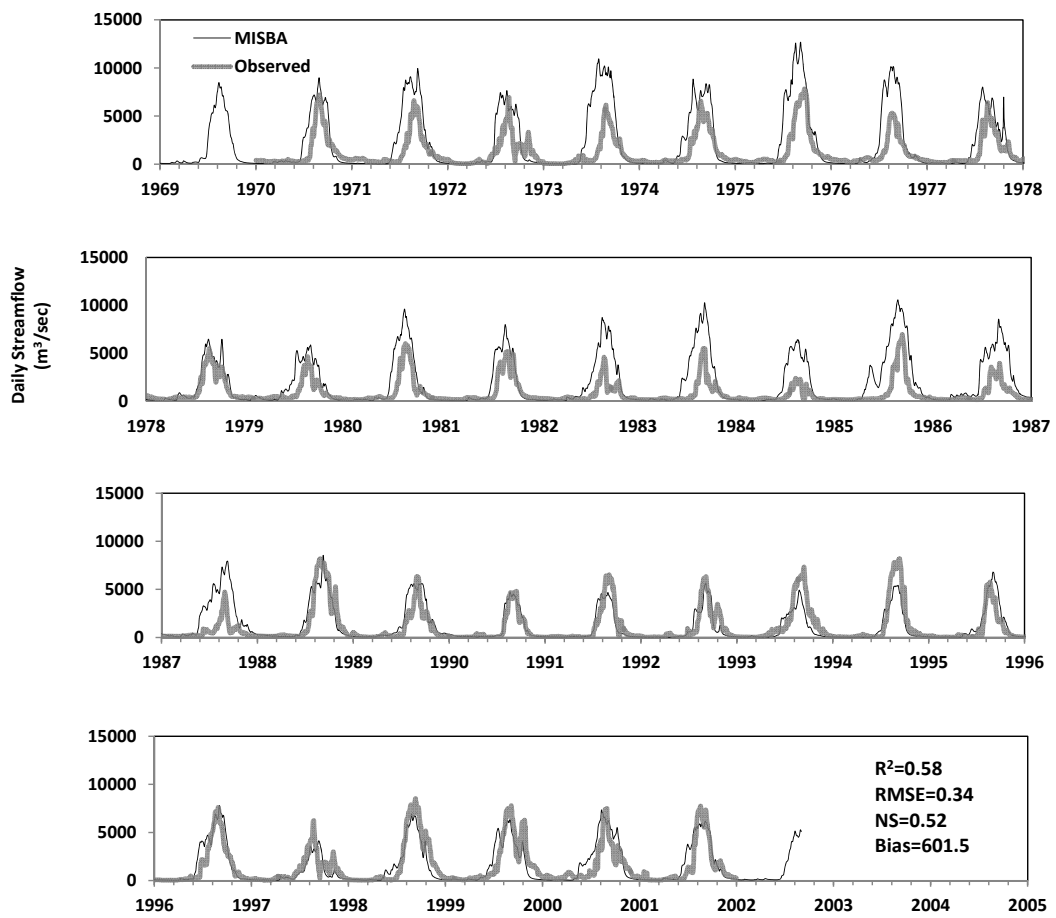


Figure 3.9: The UBNB streamflow simulation from MISBA model at daily time scale after modifying the evapotranspiration scheme.

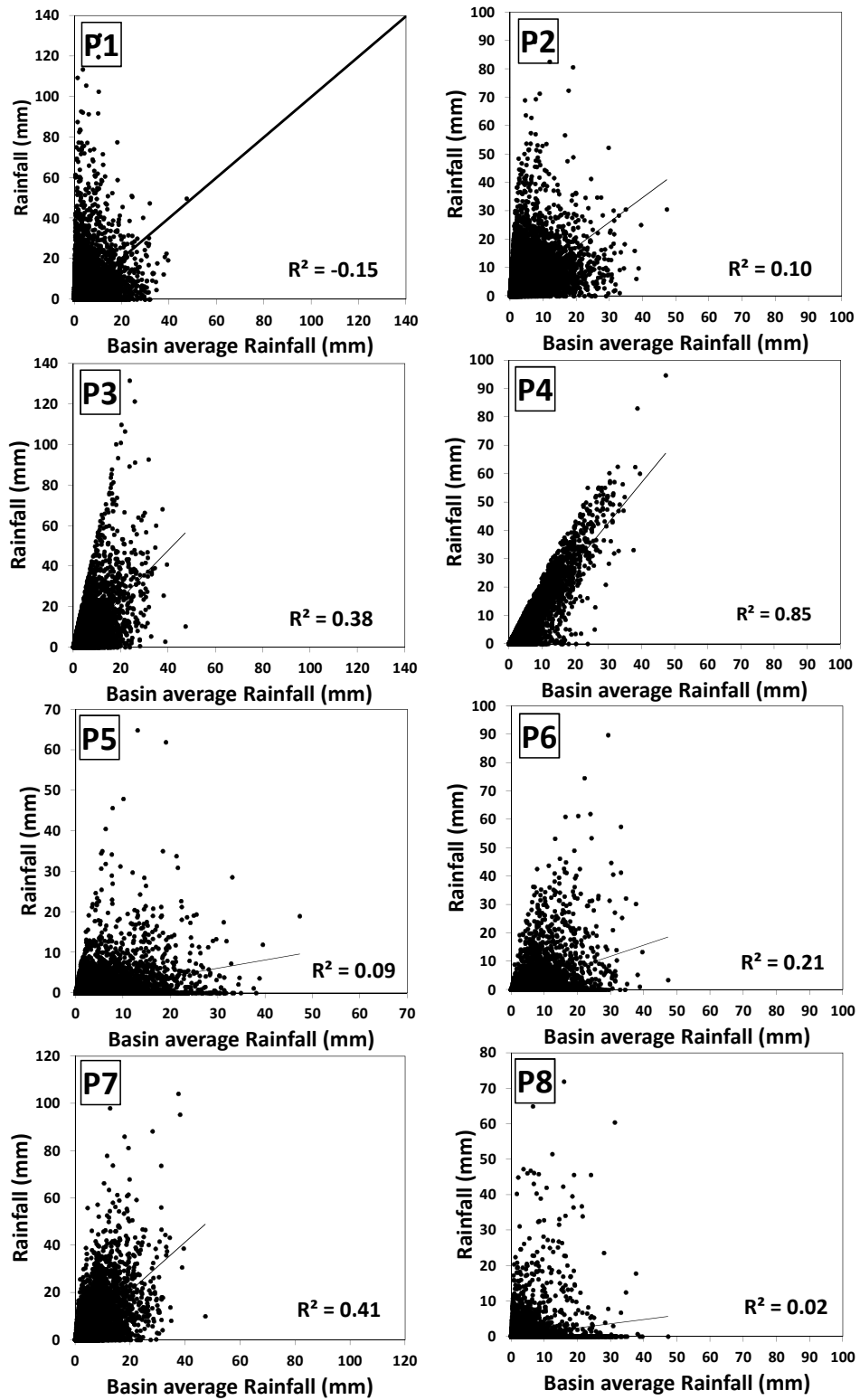


Figure 3.10: Scatterplots of the rainfall at each grid point of the ERA-40 data (Pt1 to Pt8) that cover the UBNB versus the whole basin average rainfall.

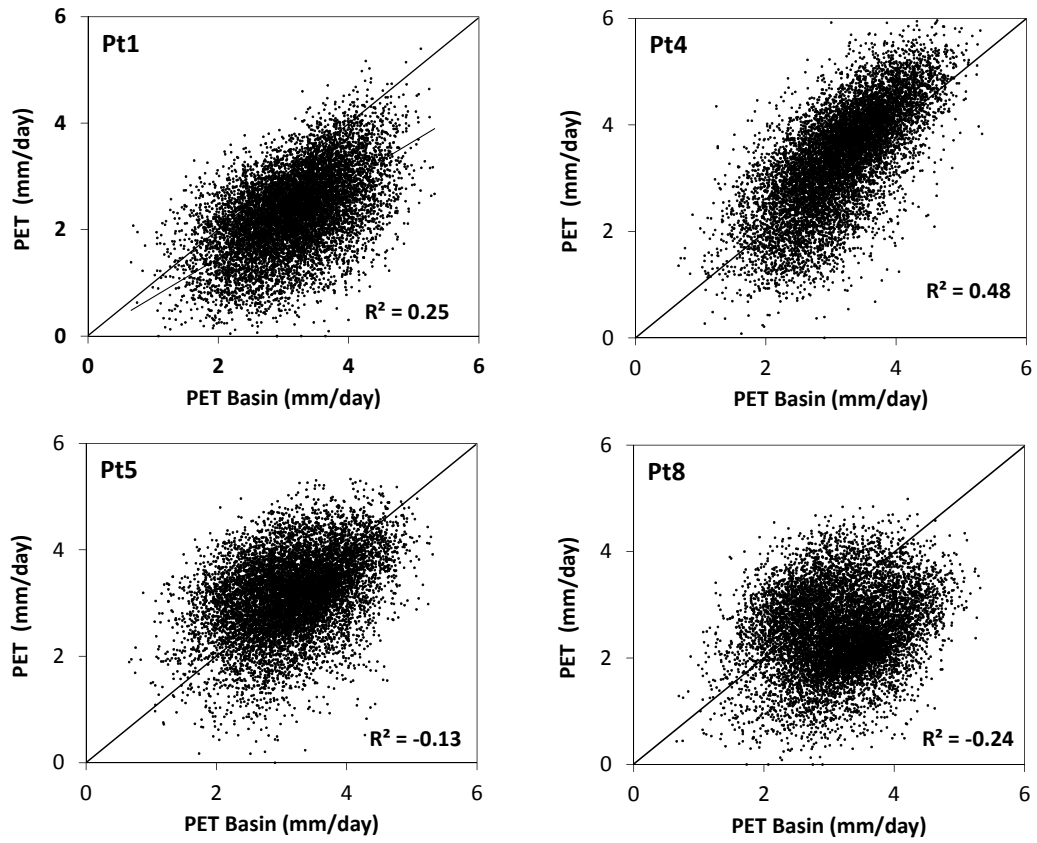


Figure 3.11: Scatterplots of the potential evapotranspiration (PET) at four different grid points (Pt1, Pt4, Pt5 and Pt8) of the UBNB versus the whole basin PET .

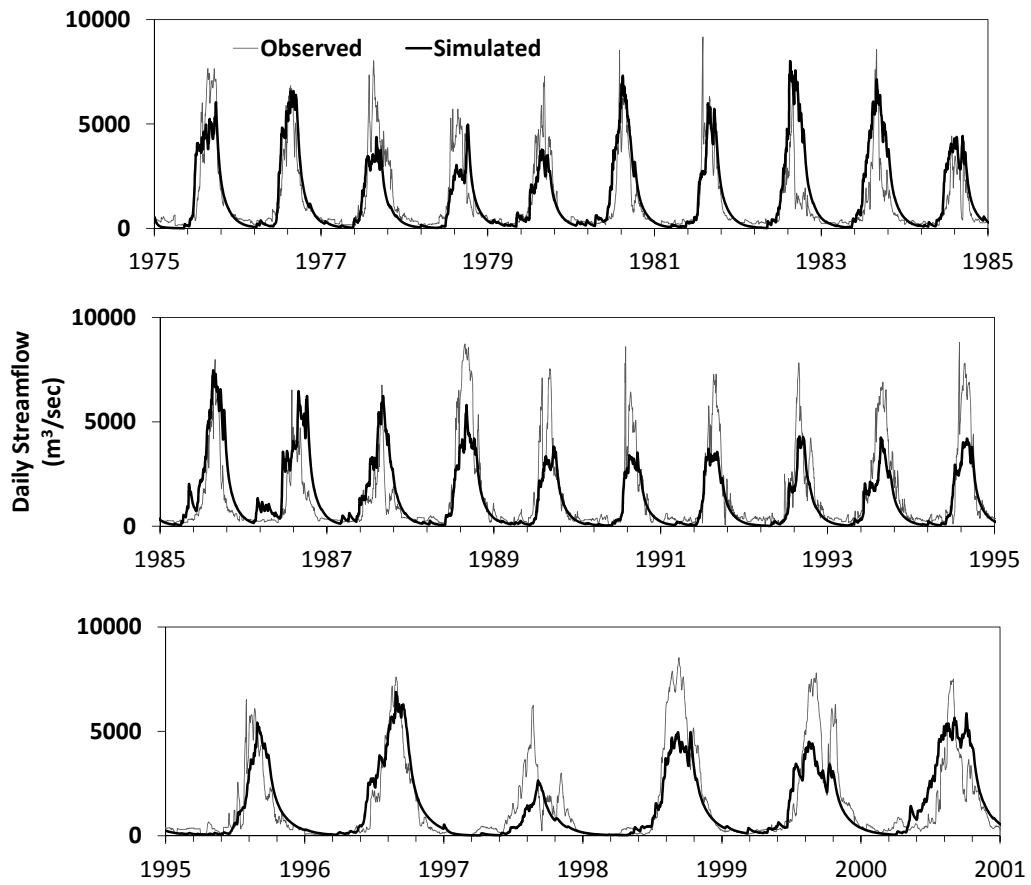


Figure 3.12: The UBNB streamflow simulation from SAC-SMA model.

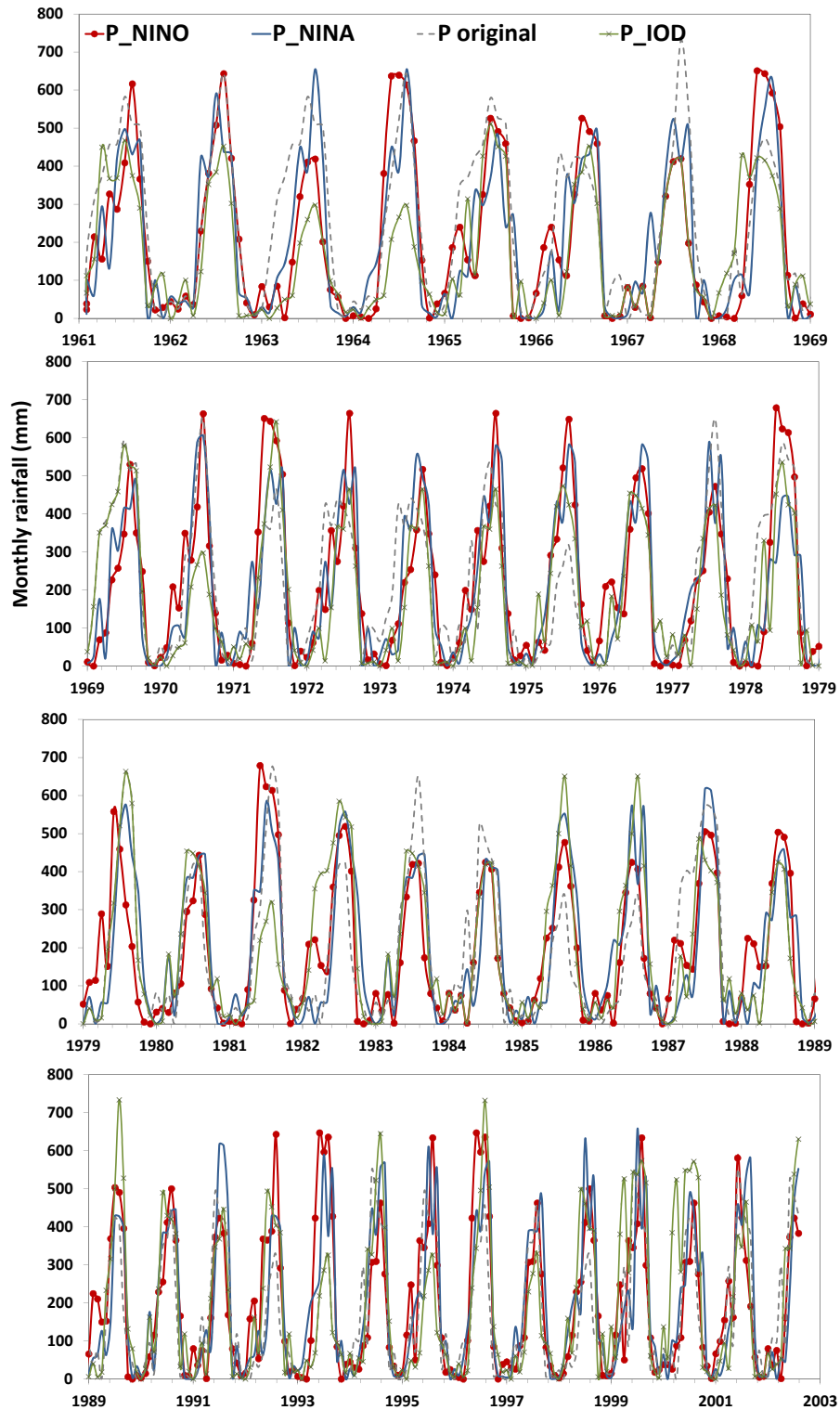


Figure 3.13: Monthly precipitation for grid point at 10° N- 37.5° E resampled by El Niño, La Niña, and IOD years.

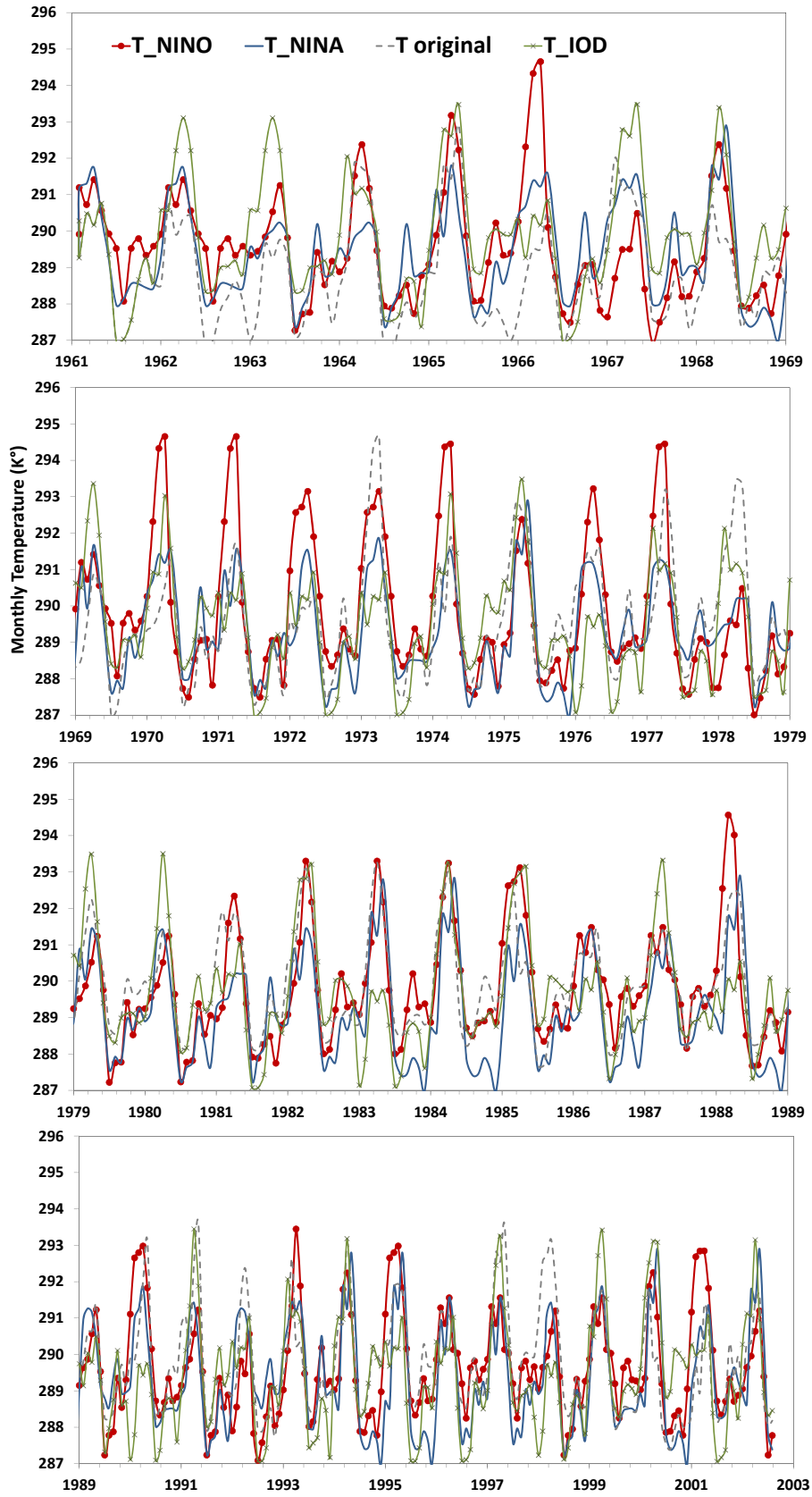


Figure 3.14: Monthly temperature for grid point at 10° N- 37.5° E resampled by El Niño, La Niña, and IOD years.

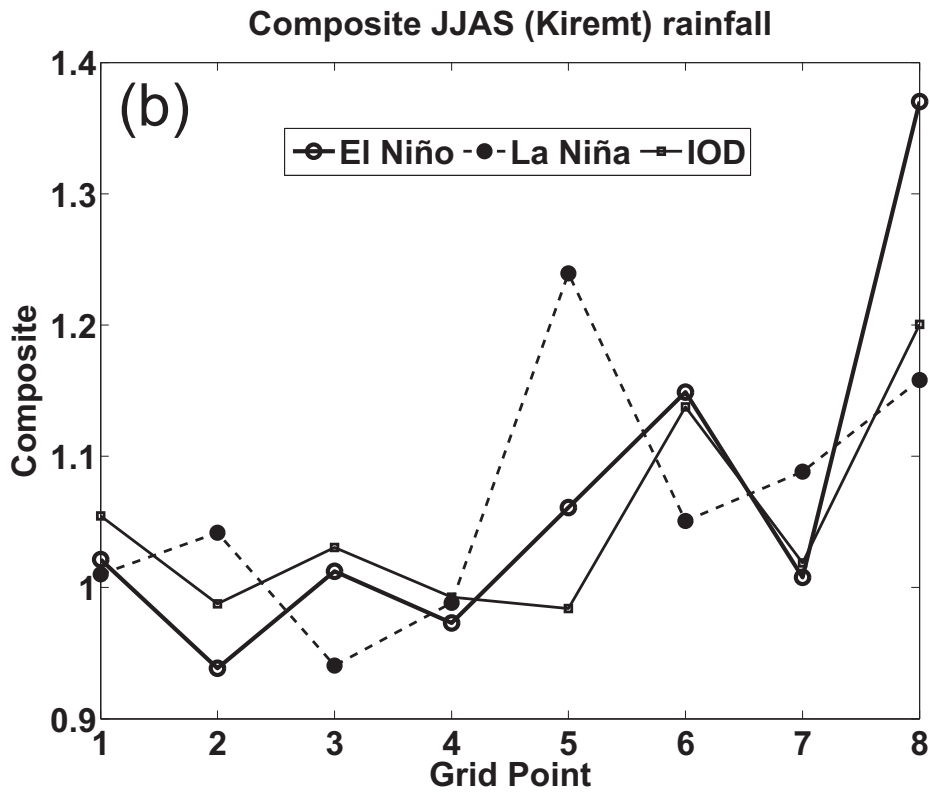
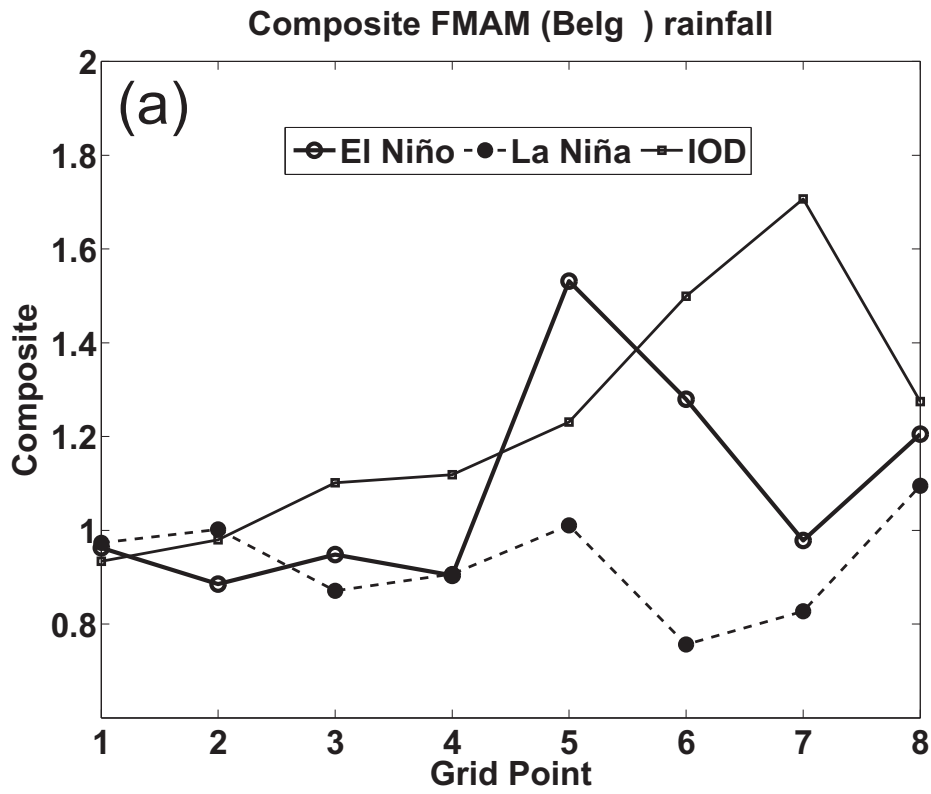


Figure 3.15: Composite analysis of the UBNB rainfall using the ERA-40 data at the eight grid points covering the basin. (a-b) for FMAM and JJAS for the whole grid points. (c-d) FMAM and JJAS averaging over three longitudes (35° E, 37.5° E, and 40° E).

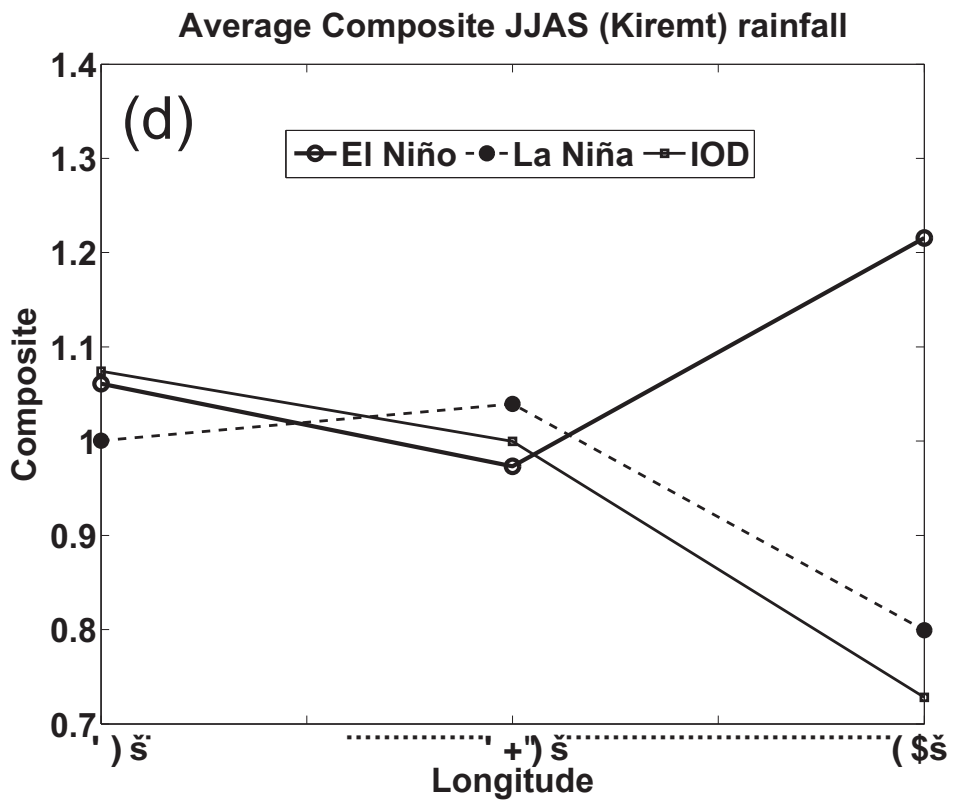
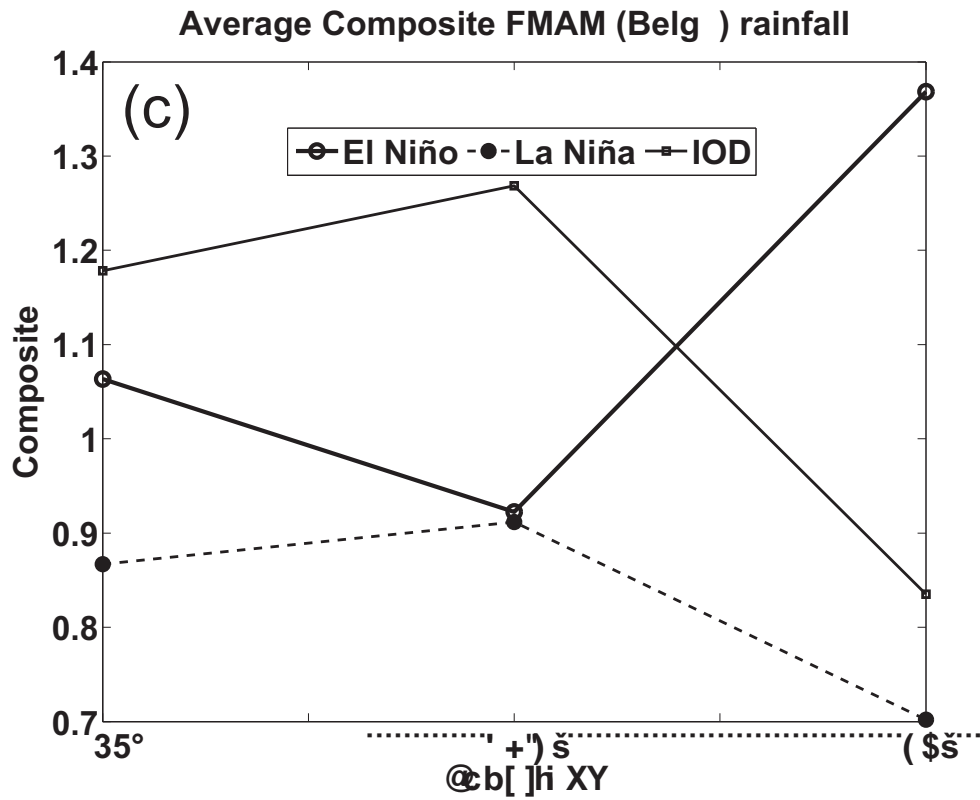


Figure 3.15: continued

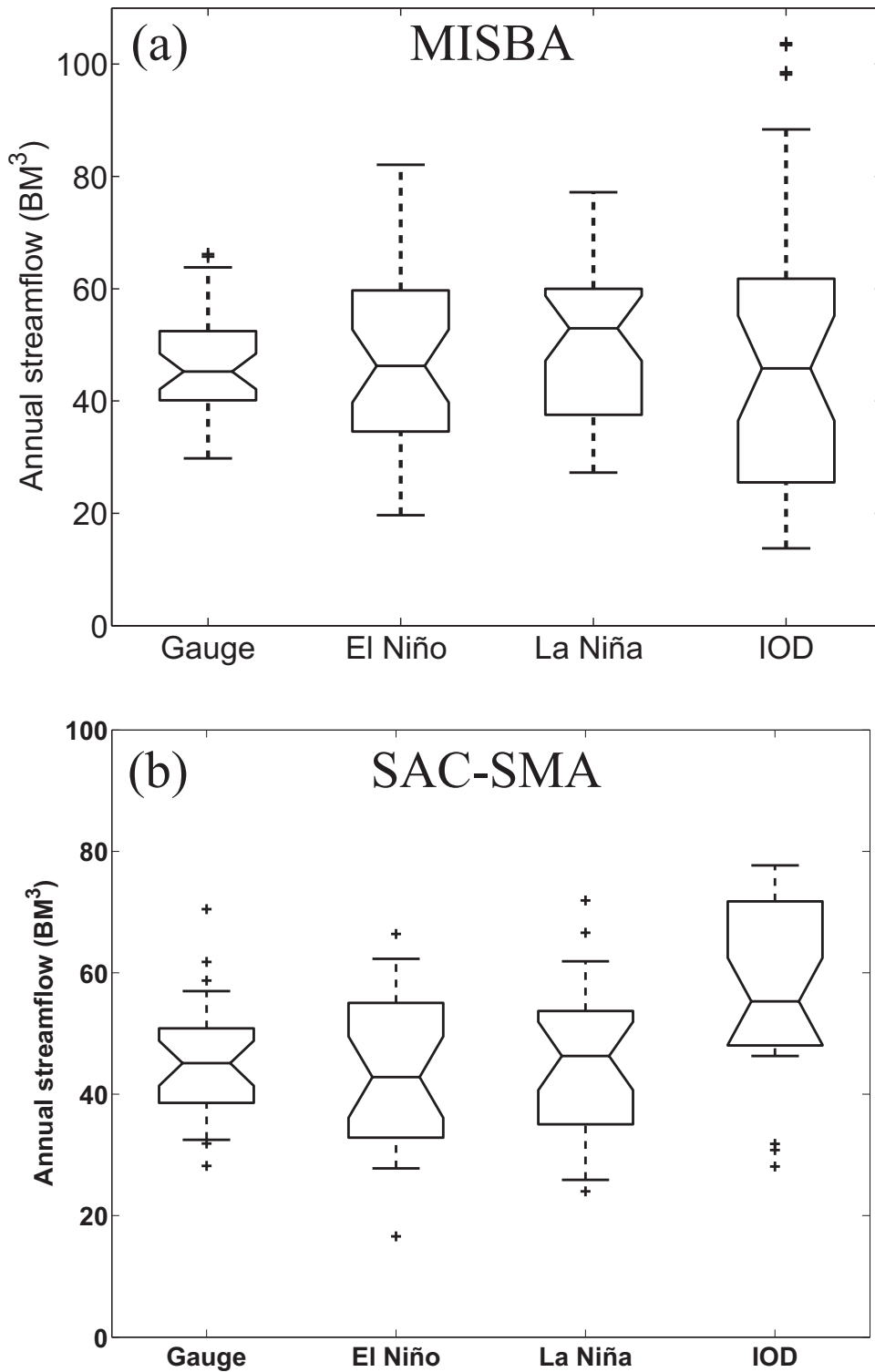


Figure 3.16: Box plot comparing the simulated streamflow distribution for the UBNB associated with El Niño, La Niña, and IOD periods (a) from MISBA simulation and (b) from SAC-SMA model.

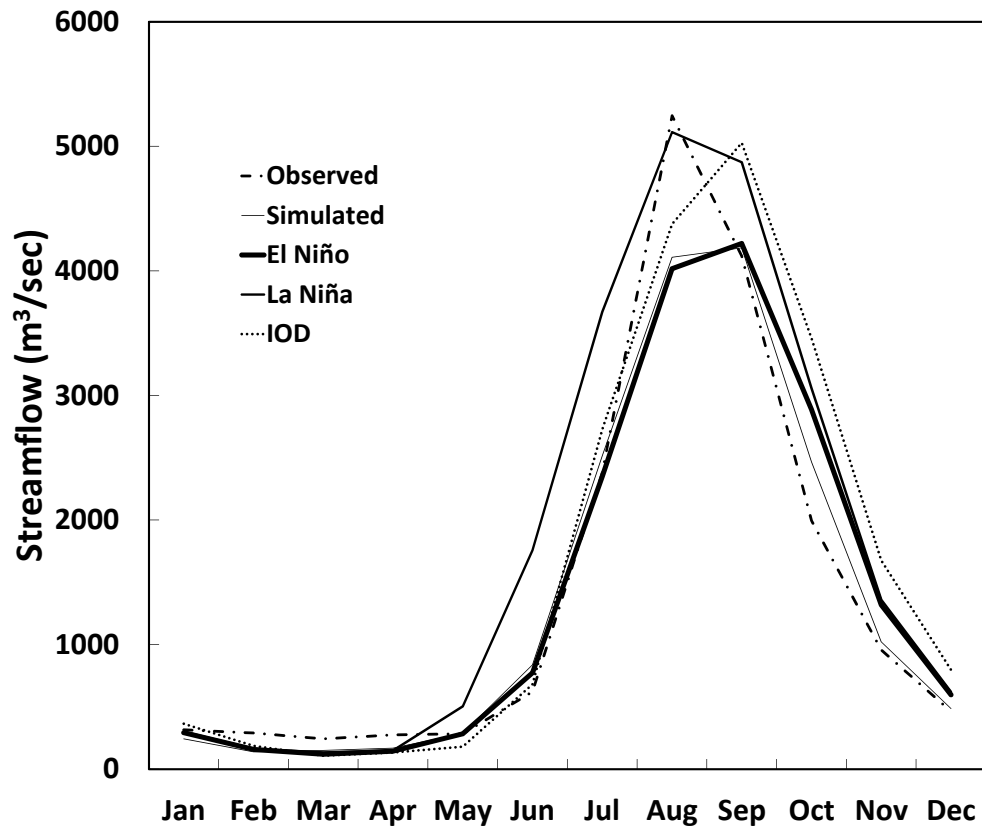


Figure 3.17: Average monthly of the UBNB streamflow hydrograph for the period (1970-2002) under different climate anomalies.

Chapter 4

The Upper Blue Nile Basin Rainfall, Teleconnection, and Prediction by an Artificial Neural Network ¹ ²

4.1 Introduction

The primary water supply of downstream countries of the Nile River, Egypt and Sudan, comes from the Nile River where one of the most important tributaries is located at the upper Blue Nile basin (UBNB) which contributes about 60% of the Nile's total streamflow reaching the Aswan High dam, Egypt (Seleshi and Demaree, 1995; Yates and Strzepek, 1998; Sutcliffe et al., 1999; Conway, 2000). Roughly 70% of the annual rainfall of the UBNB occurs during the Kiremt season, which is June to September (JJAS) (Conway, 2000), when about 85%-95% of the crops are grown annually (Degefu, 1987). Therefore the UBNB, located in Ethiopia, provides

¹A version of this chapter will be submitted for publication to the Monthly Weather Review

²Part of this chapter was accepted in the Proceeding conference, 2012 CSCE Annual General Conference, June 6-9, 2012, Edmonton, AB, CA.

the largest and economically crucial water resource for the country. While Ethiopia has been planning irrigation and hydro-power projects using the Blue Nile River, other neighboring countries also need to increase their allocations of Nile's water resources to sustain their population and economic development. Therefore, to avoid potential conflicts between competing countries, it will be necessary to establish equitable trans-boundary water sharing agreements and honorable implementation of such agreements.

Since the UBNB contributes a significant amount of water to the Nile River, it is important to predict its seasonal precipitation reliably. However, this can be challenging given that the UBNB had experienced hydrologic extremes, both floods and droughts, in the past few decades. Droughts and famines are endemic because agriculture, which accounts for approximately 50% of Ethiopia's Gross Domestic Product and employs 80% of Ethiopia's population, is heavily dependent on rainfall (Abegaz et al., 2007). Persistent droughts or long dry spells can be catastrophic, which for the last three decades has caused famines across Ethiopia, including most parts of the Ethiopian highlands (EH), which consequently affected the Blue Nile (Degefu, 1987; Elsanabary and Gan, 2012; Elsanabary et al., In review). In contrast, flooding may cause damages to the infrastructure and could lead to severe consequences, e.g. Sudan experienced heavy flooding in 1988 (Sutcliffe et al., 1989).

Segele et al. (2009) showed that Ethiopia's rainfall is nonstationary, particularly over UBNB. Because of the nonstationary characteristics inherent in most rainfall data, nonstationary techniques are generally needed to accurately analyze the variability of rainfall data, which because of teleconnections, has been found to be related to the variability of oceanic Sea Surface Temperatures (SST) (Diro et al., 2011; Elsanabary et al., In review). Degefu (1987) and Wolde-Georgis et al. (2001) found that the Indian and Atlantic Oceans provide primary sources of moisture for most rainfall

occurring over Ethiopia. [Camberlin \(1997\)](#) showed that monsoonal activity over India is a major trigger for the July-September rainfall variability in the East African highlands. [Jury \(2010\)](#) found that the rainfall mode in the northern part of Ethiopia that impacted the Nile River flow had been linked to the Atlantic zonal overturning circulation and the rainfall modes exhibited interdecadal (10-12 years) cycles throughout much of the 20th century.

Therefore, for Ethiopia, it will be useful to teleconnect the variability of its precipitation to oceanic SST. Knowledge of this teleconnection between selected oceanic SSTs and rainfall of Ethiopia would enhance Ethiopia's rainfall forecasting ability beneficial to its agriculture practices. Furthermore, knowledge of the variability of rainfall across the Blue Nile basin has the potential to assist downstream countries such as Egypt and Sudan that rely heavily on the water of the Nile River. Currently, the National Meteorological Agency (NMA) of Ethiopia issues seasonal summer rainfall forecasting for Ethiopia ([Gissila et al., 2004](#)). In Sudan, The Early Warning and Humanitarian Emergency Information Center (EWHIC) issues flood forecasts at key gauging stations of the Blue Nile up to 4 days of lead times ([Thiemig et al., 2011](#)).

With the motivation to develop a robust framework to forecast the JJAS rainfall at weekly time step, the objectives of this study are outlined in Section 4.2, the characteristics and climatology of the study site (UBNB) in Section 4.3, climate data in Section 4.4, research procedure and methodology in Section 4.5, discussions of results in Section 4.6, and summary and conclusions in Section 4.7.

4.2 Research Objectives

With the above statement of problem, this study has the objective of developing a framework to predict seasonal rainfall of UBNB driven by selected sectors of oceanic SSTs at one season lead time, and next to disaggregate the seasonal rainfall data to weekly rainfall for UBNB. This framework is developed on the basis of wavelet based principal component analysis (WPCA), artificial neural networks calibrated by a genetic algorithm (ANN-GA), and a statistical disaggregation algorithm. The steps involved to achieve the research objectives are:

- i) Analyze the nonstationary variability of June-September rainfall (JJAS; hereafter the four-month season will be abbreviated by the first letter of each month) over UBNB, and the February-May (FMAM) sea surface temperature (SST) of the global oceans, using wavelet analysis and wavelet based principal component analysis (WPCA);
- ii) From above results, identify sectors of SSTs that are strongly teleconnected to seasonal rainfall of the upper Blue Nile basin;
- iii) SSTs from the above selected sectors of the oceans are used to drive an artificial neural network calibrated by a genetic algorithm (ANN-GA) to predict the JJAS rainfall over UBNB at a one season lead time. The ANN-GA was calibrated using seasonal rainfall and SST data, and validated by assessing the accuracy of its predicted seasonal rainfall for periods independent of the calibration stage;
- iv) Using the Valencia and Schaake (VS) model ([Valencia and Schaake, 1973](#)), disaggregate the seasonal rainfall forecasted by ANN-GA to weekly rainfall.

4.3 Study site

4.3.1 Upper Blue Nile Basin(UBNB)

The UBNB (Figure 4.1) of (176000 km²) in area, which occupies 17% of Ethiopia and forms the western part of the Ethiopian Highlands, has an average annual precipitation of 1,600 mm (Sutcliffe et al., 1999), and a mean annual discharge volume of 48.5 cubic kilometers (Conway, 2000). The Blue Nile (Abay) begins at Tana Lake (2150 km² area) at an elevation of about 1800 a.m.s.l, then leaves the lake at the Tississat Falls that drop over 50 m vertically (Shahin, 1985). The UBNB generally receives more precipitation (1000-2400 mm/year) than the eastern, northern and southern parts of Ethiopia, and due to the orographic effect, precipitation generally increases with altitude (Kloos and Legesse, 2010).

4.3.2 Climatetic regime of UBNB

Over Ethiopia, the spatial distribution of seasonal rainfall is related to the migration of the ITCZ from south to north, which causes the rainfall to be more concentrated west of the Great Rift Valley (GRV) (Sutcliffe et al., 1999; Degefu, 1987; Gamachu, 1977). In the western highlands where the UBNB is located, rainfall occurs over much of the year, even though the wet season occurs predominantly between June to September. In the southern, central, and northern parts of Ethiopia, the dry season (called Belg) occurs in February-May (FMAM) while the wet season (called Kiremt) occurs in June-September (JJAS) (Kloos and Legesse, 2010) (Figure 4.2). Essentially, from February to May, the southeasterly winds that carry moisture from the Indian Ocean give rise to the first rainy season over most of Ethiopia, while from June to September the southwesterly and southeasterly winds are responsible for the second rainy season over Ethiopia. To show the wind speed variation from season to season and for different

time periods, (Figure 4.3). Figure 4.3 a-d shows the wind patterns for 3 months seasons (1970-1990), while Figure 4.3 f-h shows the wind patterns for 4 months seasons (1970-1990) and Figure 4.3 i-k shows the wind patterns for 4 months seasons (1990-2002).

4.4 Climate data

4.4.1 Rainfall Data

Historical monthly precipitation data (1900-1998), ‘*gu23wld0098.dat*’, Version 1.0, was supplied by Dr. Mike Hulme at the Climatic Research Unit, University of East Anglia in the United Kingdom. The data, gridded at a resolution of 2.5° latitude \times 3.75° longitude was extracted from the region 18° N- 2° N to 33° E- 48° E over Ethiopia and the surrounding areas (Figure 4.1). Data was extracted for 23 grids. This data is part of a historical monthly precipitation dataset for global land areas. These gridded data were constructed from station data using the Thiessen polygon method. No topographic weighting has been applied to the interpolation scheme. Because the method interpolates anomalies and not precipitation values, it is reasonable to exclude the effects of elevation. The data quality control of these gridded data is described in Hulme (1992, 1994); Hulme and New (1997); Hulme et al. (1998). Given that the focus of this study is the Kiremt season, the seasonal data for June to September (JJAS) were computed. The 6-hour (1961-2002) gridded data of ERA-40 at $2.5^{\circ} \times 2.5^{\circ}$ resolution was collected from the European Centre for Medium-Range Weather Forecasts (ECMWF) website (http://data-portal.ecmwf.int/data/d/era40_daily/) and aggregated to weekly data for JJAS for comparison with weekly rainfall data disaggregated from the predicted, seasonal JJAS rainfall data.

4.4.2 Sea Surface Temperature Data

Global mean monthly SST data of 1870-2008, at $1^\circ \times 1^\circ$ grid point resolution was extracted for about 65,000 grids from HadISST, Version 1.1 of Hadley Centre, United Kingdom Met Office. The monthly SST anomaly grid data were aggregated to seasonal February-May (FMAM) SST to be used as the SST predictors for predicting the seasonal precipitation of UBNB at one season lead time.

4.5 Research Procedure and Methodology

4.5.1 Wavelet Analysis

A wavelet is a “little” wave with limited duration in comparison to larger waves such as sinusoidal waves. Consider a precipitation time series that we want to study is X_t of equal time spacing δ and $t = 0 \cdots N - 1$, where N is the number of data points. A wavelet function, $\psi_\circ(\eta)$, that depends on a non-dimensional time parameter (η), chosen for this study is the Morlet wavelet (Torrence and Compo, 1998)

$$\psi_\circ(\eta) = \pi^{-1/4} e^{i\omega_\circ\eta} e^{-\eta^2/2}, \quad (4.1)$$

The Morlet wavelet is selected partly because it can effectively delineate characteristics of precipitation, temperature and SST data (Mwale et al., 2009). In this paper the continuous wavelet transform (CWT) is used. By varying the wavelet scale (s) and translating along the localized time index (n) over the x axis in the $x - y$ plane, we could generate a set of wavelets such as (Mallat, 1999; Addison, 2002):

$$\psi_{s,n}(t) = \frac{1}{\sqrt{s}} \psi \left(\frac{t-n}{s} \right), \quad (4.2)$$

The CWT or the wavelet spectrum $W_n(s)$ of a discrete time series x_t with a scaled and translated version of $\psi_{\circ}(\eta)$ is:

$$W_n(s) = \sum_{t=0}^{N-1} x(t) \psi^* \left[\frac{(t-n)\delta t}{s} \right], \quad (4.3)$$

Where $(*)$ indicates the complex conjugate of ψ . Also, the (\circ) on ψ from Equation 4.1 has been dropped to indicate that the wavelet has been normalized to have unit energy. By normalization, the wavelet transforms at each scale (s) are directly comparable to each other and to the transform of other time series (Torrence and Compo, 1998; Mallat, 1999). The non-orthogonal wavelet analysis is used because it enables us to choose arbitrarily a set of scales for building a comprehensive picture about the oscillation of precipitation events that occurred over the EH. For convenience, the scales were chosen as a fractional power of two (Torrence and Compo, 1998):

$$s_j = s_{\circ} 2^{j\delta_j} \quad j = 0, 1, \dots, J, \quad (4.4)$$

$$J = \delta_j^{-1} \log_2 \left(\frac{N\delta t}{s_{\circ}} \right), \quad (4.5)$$

Where s_{\circ} is the smallest resolvable scale and J the largest scale. The magnitude of $W_n(s)$ coefficients shows how well the wavelet matches with

the precipitation time series. For each scale, $W_n(s)$ coefficients also depict the amplitude of a time series at that scale. In a rainfall or SST time series, the power at each scale is an appropriate measure of the magnitude of the rainfall or SST anomalies. To investigate fluctuations in power over a range of scales (band), the scale-averaged wavelet power (SAWP) which represents the mean variance of wavelet coefficients over a range of scales s_1 to s_2 was also computed (Torrence and Compo, 1998) .

$$\overline{W}_n^2 = \frac{\delta_j \delta t}{C_\delta} \sum_{j=j_1}^{j_2} \frac{|W_n(s_j)|^2}{s_j} \quad (4.6)$$

Where C_δ is 0.776 for the Morlet wavelet, δ_j is a factor for scale averaging, and δt is the sampling period (Torrence and Compo, 1998).

Scale bands and time periods within which time series exhibits correlation with climate anomalies can be identified from the wavelet coherence (Torrence and Webster, 1999), which is defined as,

$$R_t^2(S) = \frac{|\langle S^{-1} W_t^{XY}(S) \rangle|^2}{\langle S^{-1} | W_t^X(S) |^2 \rangle \langle S^{-1} | W_t^Y(S) |^2 \rangle} \quad (4.7)$$

where $W_t^{XY}(S)$ is the cross-wavelet spectrum of X and Y , $\langle \cdot \rangle$ is a smoothing operator in both time and scale, and $0 < R_t^2(S) \leq 1$. Since the wavelet transform conserves variance, Equation 4.7 is an accurate representation of the normalized covariance between two time series.

4.5.2 Principal component analysis

Principal component analysis (PCA), a multivariate technique that orthogonally transforms a set of possibly correlated variables into a set of linearly uncorrelated variables called principal components (Abdi and

Williams, 2010), is widely used in atmospheric sciences (Wilks, 2006). In other words, PCA transforms multivariate data into independent PCs such that several leading PCs generally explain a large proportion of the total variance.

Imagine a data matrix x_n of N -variates or climate stations, and each with n observations ($n \times N$). PCA transforms x_n into another matrix of principal components (U) that accounts for all the variability of x_n , so that a few PCs (designated as u_m) account for majority of the joint variation of x_n . To examine the teleconnection between rainfall of UBNB and SST, PCA was applied to the SAWP (2-8 yrs.) of rainfall and SSTs (Mwale and Gan, 2005; Mwale, 2005), so that a few u_m account for majority of the SAWP variation. The SAWP signals (u_m) are computed as follows:

$$u_m = e_x^{T'} = \sum_{n=1}^N e_{nm} x'_n, \quad m = 1, \dots, M, \text{ (where } M \ll N \text{)} \quad (4.8)$$

Where, e_{nm} are the eigenvectors, x'_n are the n SAWP anomalies, and M represents a small subset of the N possible signals. The signals, u_m , are usually the major spatial and temporal patterns that account for the majority of the variations in the SAWP, and can be used to spatially delineate rainfall or SST variations into independent zones.

4.5.3 ANN-GA for forecasting seasonal rainfall

An Artificial Neural Network (ANN) composes of a large number of simple, highly interconnected processing elements known as “neurons”, typically arranged in layers, to relate inputs and outputs of a system. Originally inspired by biological nervous systems such as a brain, it is a nonlinear mathematical structure capable of representing complex nonlinear processes (Hsu et al., 1990; Chen et al., 2006). ANNs are data-driven

and non-parametric, and they do not necessarily require the enforcement of constraints or a prior solution structures (De Vos and Rientjes, 2005). An overview of ANNs, which have proven to be powerful in simulating non-linear and complex processes, is herein given (Mwale et al., 2004; Mwale and Gan, 2009). Figure 4.4 shows an ANN with a forward structure and three layers (input, hidden, and output layer). The model receives signals from the input nodes and transforms these signals through the network until they reach the output nodes. In this study, a hyperbolic tangent is used as the sigmoid function for the ANN model. Through a trial and error approach, a five-node hidden layer was adopted, while the number of input nodes depend on the number of input variables or predictors, and the output layer has only one node “predictand”, which is the seasonal rainfall. The input data was normalized to zero mean and scaled to unit variance.

The ANN model used is referred to as ANN-GA because a genetic algorithm (GA) is used to calibrate the parameters of the ANN model. The GA iteratively searched for optimal model parameters on the basis of maximizing an objective function that represents the correlation between simulated and observed seasonal rainfall. The GA consists of these operations: selection, crossover, and mutation. All the neural networks are ranked according to their respective performance evaluated in terms of objective function values computed in a descending order. Only the top 85% of the population (set at 200 for this study) is retained for further selection. In the next stage, a one point crossover scheme, weights and biases of neural networks are exchanged in pairs, such that one location is randomly chosen in the hidden layer and weights and biases on either side of the location are exchanged between the two neural networks. This procedure is repeated between all other pairs of neural networks in the selected population. After crossover, mutation is performed as an attempt to restore “good” weights and biases happened to be eliminated by selection. Only a small percentage of popu-

lation (1%) is randomly chosen for mutation in which the mutation point (weights or biases) are randomly assigned a number within the prescribed range of parameters. The above three operations are repeated for several generations. At each generation, the best neural network is kept until a better solution is found in successive generations.

To ensure the calibrated ANN model is valid or dependable, the weights and biases of the best surviving network found by the GA at the calibration stage were further tested by driving the model with input data independent of the calibration experience. If the performance of the ANN model at the validation stage is comparable to that of the calibration stage, there is basis to accept the calibrated ANN model as physically sound and useful for forecasting purposes.

4.5.4 Statistical Measures

To assess the forecasting skill of ANN-GA, five goodness-of-fit statistics were computed, which are Pearson correlation (r), root mean square error ($RMSE$), Nash-Sutcliffe coefficient of efficiency (Ns), $Bias$, and Hanssen-Kuipers (HK):

$$r = \frac{1}{k} \frac{\sum_{i=1}^k (X_i - \bar{X})(O_i - \bar{O})}{\sqrt{\sum_{i=1}^k (X_i - \bar{X})^2 \sum_{i=1}^k (O_i - \bar{O})^2}} \quad (4.9)$$

$$RMSE = \frac{1}{k} \sqrt{\sum_{i=1}^k (X_i - O_i)^2} \quad (4.10)$$

$$NS = 1 - \frac{\sum_{i=1}^k (X_i - O_i)^2}{\sum_{i=1}^k (X_i - \bar{X})^2} \quad (4.11)$$

$$Bias = \frac{1}{k} \sum_{i=1}^k (X_i - O_i) \quad (4.12)$$

$$HK = \frac{(H - N_c)}{(T - N_m)} \quad (4.13)$$

Where O_i and X_i are the observed and simulated rainfall respectively; \bar{O} and \bar{X} are their respective means; and K is the total number of data points. The Pearson correlation (r) ranges from -1 to 1 with a correlation of 1 (-1) being a perfect linear positive (negative) relationship between O_i and X_i , and a correlation of zero indicating no relationship between O_i and X_i , while the Nash-Sutcliffe coefficient efficiency (Ns) may range from $-\infty$ to 1 , with an efficiency of 1 corresponding to a perfect match, an efficiency of 0 indicating model simulation that are only as good as the mean of O_i , and an efficiency less than zero indicating that the prediction is as good as random.

To compute the HK skill score, the forecasted and observed rainfall data are grouped into three categories: dry, near normal, and wet. The percentages of the JJAS rainfall below 33%, 33-67%, and over 67% are used to compute the contingency table categories. Where H is the total number of correct forecasts, T is the total number of correct forecasts obtainable with a perfect forecast model, N_c is the number of correct hits expected

by chance, and N_m is the marginal number of correct (observation) hits expected by chance. HK values range from -1 to $+1$. Perfect forecasts receive a score of 1, random forecasts receive a score of 0, and forecasts inferior to random forecasts receive -1 .

4.5.5 Disaggregation of Seasonal precipitation

For the Blue Nile River the length 1400 km has a slope between the source (1800 m) and the gauging station (500 m) (Shahin, 1985) is about 10.77%. For “natural channels not well defined” with a slope of 8-11%, the approximate average flow velocity is between 1.22 to 2.13 m/s (see Chow et al., 1988, Page 164-165). Therefore, the “time of concentration”, which indicates the time needed for the whole UBNB to contribute runoff at the basin outlet (El Diem station), is about 7 to 8 days or a travel time of about a week. Therefore, it is reasonable to disaggregate the seasonal rainfall (JJAS) of UBNB into weekly rainfall, which can then be used to model the hydrology of the UBNB at weekly time steps. For simplicity’s sake, each month was divided to 4 weeks. For example, for June and September, the first two weeks were averaged over 8 days while the last two weeks were averaged over 7 days. For July and August, the first three weeks of each month were averaged over 8 days and the last week of each month was averaged over 7 days (see Figure 4.5).

The disaggregation of seasonal rainfall of the UBNB may be carried out using the temporal disaggregation model of Valencia and Schaake (1973), the Lane model of Lane and Frevert (1990), the Canonical Random Cascade Model of Gupta and Waymire (1993), or the analog approach of Lorenz (1969). In using the analog approach long data sets are required so that many similar episodes of weekly, monthly and annual aggregates can be found in the observations. Since the UBNB has only limited hydro-climatic data, only the disaggregation method of Valencia and Schaake (1973) has

been used in this study. Statistical properties between seasonal and weekly precipitation are used to disaggregate the seasonal precipitation to four weekly rainfall totals for each of the four months (i.e., for a total of 16 weekly precipitation totals). The disaggregation model of [Valencia and Schaake \(1973\)](#) is of the following form:

$$Z_t = AX_t + B\epsilon_t \quad (4.14)$$

Where Z_t is the $m \times 1$ vector of the weekly rainfall of the t^{th} year, X_t is the forecasted seasonal rainfall of the t^{th} year, m is the number of weeks for the main rainy season (JJAS) which in this case is 16 weeks, and ϵ_t is the $m \times 1$ vector of standard normal deviates (i.e. zero mean and unity variance). A is a $(m \times 1)$ vector of coefficients that sum to one and can be considered as weekly contributions to the seasonal rainfall of vector X_t , while B is a $(m \times m)$ matrix of coefficients. A and B were estimated using the SAMS version 2007 software developed by the US Bureau of reclamation and the Colorado State University ([Sveinsson et al., 2007](#)).

4.6 Discussion of Results

4.6.1 Wavelet analysis of seasonal rainfall

The Morlet wavelet analysis and the scale average wavelet power (SAWP) computed for the gridded seasonal rainfall of Ethiopia are herein discussed. It has been shown in Chapter 2 that the JJAS (Kiremt) seasonal rainfall data of Ethiopia exhibit interannual oscillations at 2-4 and 5-7 year cycles. Both the global and the local wavelet spectra for the JJAS seasonal rainfall in Ethiopia were computed (see an example in [Figure 4.6](#) for two grid points). The local wavelet spectra represent the changes of wavelet power of various periodicities over time, while the global wavelet spectrum shows

the averaging of all local wavelet spectra over time for each periodicity. Thick black contours in the figure indicate that the power is statistically significant at the 95% confidence level of the red noise process. The dashed line drawn encompassing the wavelet spectrum depicts the cone of influence (CI), for outside the CI the spectra may be affected by zero padding and should be treated with caution. Figure 4.6 shows that in the 1950s, 1960s and 1980s, strong power was detected at the interannual cycles of about 2 to 8 years. A strong interdecadal oscillation of about 16 years was also detected in the 1950s to 1980s for western parts of Ethiopia (see Figure 4.6a). Given that part of the interdecadal oscillation was outside the CI, and three episodes of statistically significant interannual oscillations of 2 to 8 years were detected, the SAWP for rainfall and SST are estimated between the 2- and 8-yr cycles.

Figure 4.7 shows the spatial correlation between WPC1 of the JJAS rainfall with the SAWP of all grid points over Ethiopia. The strong positive correlation over UBNB indicates that the variability of WPC1 mainly comes from this area of Ethiopia, which likely implies that the prediction skill of the ANN-GA model (Section 4.5.3) driven by SST of the surrounding oceans (selected on the basis of a strong correlation with the WPC1 of JJAS rainfall) should be higher in UBNB than in other parts of Ethiopia. From Figure 4.7, we also subjectively select a correlation coefficient of 0.5 as the threshold whereby we expect the prediction skill of the ANN-GA model will likely be adequate.

The power Hovmöller (PH) plot of 2-8 year cycles presented in a time-longitude framework (Figure 4.8) at a latitude 10.25° N for the Twentieth Century shows that in 1910-1920s, 1950-1960s and in 1980-1990s, the SAWP of the JJAS precipitation between longitude 37° E and 40.8° E had been statistically significant at 5% significant level over the white-noise, e.g., solid contours. To be able to draw the PH plot, we used the Uni-

versity of Delaware (UoD) data that are highly correlated with the UEA data (refer to chapter 2 for the highly correlated grid points). The PH of the JJAS rainfall at 2-8 years for all the grid points (the x-axis represents longitudes) over a section passing by the middle of the UBNB (e.g. latitude 10.25°N , where UoD and UEA are highly correlated) is presented in Figure 4.8. Figure 4.8a generally shows a strong spatial coherence across the UBNB (37°E and 40°E) at three different time periods, while Figure 4.8b shows zonally-averaged power over time, and Figure 4.8c shows the time averaged SAWP as a function of longitude. Overall, on the basis of three local maxima detected between 37°E and 40.8°E , significant interannual oscillations had occurred over the UBNB in the last century.

4.6.2 Wavelet analysis of seasonal SST

From a Morlet wavelet analysis applied to the global, seasonal SST (FMAM), some sectors of the global SST exhibit statistically significant interannual oscillations at 2-8 yr cycles. Figure 4.9a (b) shows the spatial correlation patterns between WPC1 (WPC2) of the SSTs and the SST SAWP of the FMAM season at 2-8 year spectral band. WPC1 (WPC2) accounted for 31% (12%) of the total SST variance of the FMAM season.

4.6.3 Teleconnection between WPC1 of JJAS rainfall WPC1 and SAWP of global FMAM SST

Figure 4.10a (b) shows the spatial correlation patterns between WPC1 of gridded precipitation of JJAS, Kiremt, season and each of the 65,000 SAWP of gridded global SST of the JFM (FMAM) season. As expected, WPC1 of rainfall is more strongly correlated to the SAWP of SST at one season than at two season lead time, and so the JJAS rainfall are linked to the FMAM SST (see Figure 4.10). Figure 4.10a shows that JJAS rainfall is correlated to the El Niño region (Equatorial Pacific Ocean (EPO)), and the

northern Atlantic Ocean (NAO) (west of the Sahara desert). Some other areas include areas east and west (South Pacific Ocean (SPO)) of South America and areas south of Indian Ocean (South Indian Ocean (SIO)). The correlation between rainfall WPC1 and JFM SST SAWP in the El Niño region appears to be relatively weak showing a causal relationship, but nonetheless a weak one (Elsanabary et al., In review). Figure 4.10b shows that JJAS rainfall is correlated to FMAM SST of northern and southern Indian Ocean, southern Atlantic Ocean and some sectors of the Pacific Ocean west of South America. From Figure 4.10b and from the correlation between SAWP of FMAM SST and WPC1 of JJAS rainfall WPCs, we found that SSTs explain up to 64% of the rainfall variability in the 2-8 yrs. frequency band. Since JFM hasn't yet surpassed the spring barrier we have to focus on the FMAM season as the forecasting season for the JJAS rainfall over the UBNB.

By linking wavelet transformed FMAM SSTs to JJAS rainfall, we can use the former as predictors to the ANN-GA model for predicting the JJAS rainfall at one-season lead time. Figure 4.10b shows that areas where the correlation between FMAM SST and JJAS rainfall are above 0.4 are located in the Equatorial Indian Ocean (EIO) (20° S- 11° N, 61° - 85° E), southern Indian Ocean (SIO) (59° - 43° S, 34° - 80° E), southern Atlantic Ocean (SAO) (48° - 35° S, 48° - 27° W), and southern Pacific Ocean (SPO) (41° - 26° S, 112° - 91° W). Therefore the FMAM SSTs data of the above ocean sectors were used as the predictors. The selected predictors are near to the four climate indices (Pacific Decadal Oscillation (PDO), the Southern Oscillation Index (SOI), The Indian Ocean Dipole (IOD), and Atlantic Multidecadal Oscillation (AMO)), that [Taye and Willems \(2012\)](#) used to explain anomalous rainfall over Ethiopia through temporal variability of extreme high and low flows and rainfall.

4.6.3.1 Wavelet coherence and phase differences

The WPC1 of JJAS rainfall at UBNB, that explained (64%) of the total variance, is used to represent the UBNB rainfall. While the PC1 of each SST sector for specific season was used to correlate with the JJAS WPC1 of the UBNB rainfall. Figure 4.11 and 4.12 show higher power in the 2-8 year except the SPO during JFM, it shows 8-16 year cycle (see Figure 4.11b).

The wavelet coherence between seasonal rainfall and PC1 of the identified SST sectors for JFM and FMAM are presented to provide more detailed information about their relationships that change over time. Figure 4.13 (4.14) shows the wavelet coherence and phase difference between WPC1 of the JJAS seasonal rainfall at UBNB and the PC1 of JFM (FMAM) SST for each sector of the four identified sectors (see Figure 4.9a and b). In Figure 4.13 and 4.14, the phase differences between the WPC1 of JJAS rainfall and each of the four SST-PC1s are plotted as vectors, where the arrows pointing towards the right indicate the two signals (rainfall and SST) are in phase while arrows pointing towards the left indicates the signals are out of phase. When arrows point upwards (downwards), it means that the rainfall WPC1 lags (leads) the PC1 of SST by 90° . If SST leads the rainfall, it likely means that SST can be a predictor for predicting seasonal rainfall at one season lead time. The thick contours enclose periods of statistically significant coherence with respect to a red-noise process simulated by a Monte Carlo experiment of Jevrejeva et al. (2003).

From figure 4.13a, WPC1 of the JJAS rainfall and the selected JFM SST in the Equatorial Pacific Ocean (EPO) exhibits statistically significant coherence in interannual scale (e.g. 1910s, 1930s, and 1960s), 4-8 year scale in the 1920s, and 8-16 year scale from 1930 to 1960. Notice that the existence of significant coherence between two signals does not necessarily depend on the existence of significant wavelet power in the two signals. The phase difference shows WPC1 of the UBNB rainfall generally changes from

90° to 0° in the 1920s (i.e. the rainfall leads the (SST) and be in phase with the EPO SST from 1930 to 1960.

In spite of the generally weak SPO activities between 1900s and 1960s, rainfall and SPO show high coherence in the 2-8 year scale. The inconsistency in the relationship between rainfall and SPO is clearly evident from the phase distribution in the interannual scale, where the phase difference changes from near 200° to 270° during 1920s and 1950s to near 90° after 1960s with 10-20 years cycle which means that the JJAS rainfall is leading the JFM SST from that sector of the Pacific Ocean (Figure 4.13b). Figure 4.13c shows that the phase distribution between JJAS rainfall and the NAO appears to be more inconsistency. From Figure 4.13d, the SST from the SIO is leading the rainfall by 90° during 1950s, and 1960s, which is a promising sector for forecasting the rainfall. The rainfall season was not quite affected by the JFM SST.

Since JFM season hasn't yet surpassed the spring barrier we have focused on the FMAM season as the forecasting season for the JJAS rainfall over the UBNB. Therefore, we tried to explore the SST just prior the JJAS rainfall season (i.e. FMAM SST). Figure 4.14a shows that the WPC1 of JJAS rainfall season exhibits statistically significant coherence in a 2-8 yr. scale in the 1910s and 1920s with SST leading the rainfall, 25-yr scale between 1940 and 1960 with rainfall leading the SST by 90° , and 2-4 year scale in 1980s with rainfall lagging the SST by 250° . From Figure 4.13b, WPC1 of the JJAS rainfall shows strong coherence with PC1 of the selected FMAM SST from SIO at a 2-4-yr scale in 1910s, 1920s, 1950s, and 1980s (Figure 4.14b). Also, Figure 4.14b shows a 15 year cycle (Elsanabary and Gan, 2012) from 1920 to 1940 and 4-8 year cycle from 1950s to 1990s, and 2-4 year cycle during only 1980s. For these three cycles the rainfall was almost lagging the SST by 90° . Also, figure 4.13c shows a promising indication for successful rainfall forecasting where the SST was leading the

rainfall by 90° with 4-10 year cycle from 1910 to 1920s and 2-4 year cycle in 1930s, 1950s, and 1970s. Finally, the WPC1 of JJAS rainfall season exhibits statistically significant coherence in a 4 yr scale in the 1910s and in 2-4 year in 1930s with SST leading the rainfall.

The above results reveal that the WPC1 of JJAS rainfall and JFM SST sectors have lower coherence at 2-8-yr scales; while the WPC1 of JJAS rainfall have a higher coherence with the selected FMAM SST at 2-8-yr scales. The results show generally high correlation between WPC1 of JJAS rainfall and SAWP of selected SST of the previous season. Therefore, the above sectors of FMAM of the global Oceans are selected as predictors for the statistical model (ANN-GA) for forecasting the JJAS rainfall.

4.6.4 Seasonal rainfall forecasting

Given that the JJAS rainfall over the UBNB was strongly correlated with FMAM SST sectors of the eastern and southern Indian (EIO, SIO), southern Atlantic Ocean (SAO), and southern Pacific Oceans (SPO) at interannual time scales (Figure 4.9b), it seems feasible to use these SST data to forecast the seasonal rainfall (JJAS) of UBNB at one-season lead time. As an attempt to eliminate unnecessary input data, only data that explain most amount of variance are retained. From the scree plot (figure not shown) that shows the percentage of explained variances of various principal components (PCs), we found that, from each sector, only the first PC of FMAM SST which explains \approx (80-90%) of the total variance was retained to forecast the JJAS rainfall. All input (SST- PC1s) and output data (seasonal rainfall) of the ANN-GA were normalized before the analysis. The structure of ANN-GA model for forecasting the seasonal rainfall is shown in Figure 4.4.

For the two grid points (pts. #4 and #7) located in the UBNB (Figure 4.1), the ANN-GA was first calibrated using 21 years of data (1975-1995)

to forecast the seasonal rainfall of the two grid points and independently validated using 6 years of data (1996-2001). The time series of the predicted and the observed seasonal rainfall of JJAS for the UBNB for both the calibration and validation stages are presented in Figure 4.15. Summary statistics on the performance of the ANN-GA at both stages are also given in Table 1. With a correlation coefficient (r) of about 0.7 (i.e. $R^2=0.49$) and a HK (Hanssen-Kuipers) score of 0.5 at the calibration stage, ANN-GA is considered adequately calibrated which is confirmed at the validation stage where both r and HK scores are maintained or even higher. However, at the Foothill of the GRV, r for the validation stage was only about 0.3. Apparently, even though the predicted JJAS rainfall for the central part of UBNB, near the foothill of the GRV, shows strong correlation with the observed data, the predicted JJAS rainfall for stations located at the edges of UBNB are not, which is expected because WPC1 of JJAS rainfall in the central UBNB is strongly correlated to the SAWP of individual grid points (r of 0.6-0.8), but it is poorly correlated (r of 0-0.5) to the SAWP of individual stations in the basin edges (Figure 4.7). Similar results are also found in terms of RMSE and HK scores.

Apparently, ANN-GA driven by the selected sectors of SST of some oceans has good predictability in central part of the UBNB. Next, the predicted JJAS rainfall of UBNB is disaggregated to weekly rainfall data of so that the data time scale, which will be of adequate time scale for hydrologic modeling of the UBNB.

4.6.5 Seasonal rainfall disaggregation

Observed seasonal (JJAS) rainfall of the two grid points were disaggregated by the algorithm of Valencia and Schaake (1973) (Figure 4.16a (b) for grid point #4 and #7). Among three disaggregation models tested, VS, Lane, and Canonical Random Cascade Model, (Kuo et al., 2010a,b)

found that VS has been more effective in disaggregating seasonal rainfall to 3-day time scale rainfall data. The rainfall data of the first 21 year (1975-1995) was used to calibrate parameters of the disaggregation model and the rainfall data of the last six year (1996-2001) was used to validate the calibrated disaggregation model. The results in terms of Pearson correlation (r), $RMSE$, Nash-Sutcliffe (NS) and $Bias$ are given in Table 4.2. The disaggregated rainfall at point #4 accounted for 45% of the observed weekly rainfall variability, while the $RMSE$ was 1.28 mm/week, NS (- 0.23) and $Bias$ was zero. Also, the disaggregated rainfall at point #7 accounted for 44% of the weekly rainfall variance, with $RMSE$ slightly higher (1.58 mm/week), NS (0.03) , and $Bias$ (0.01 mm). The disaggregated weekly rainfall at grid point #4 and #7 are shown in Figures 4.17 and Figure 4.18, respectively.

4.7 Summary and Conclusions

The June-September (JJAS) seasonal rainfall of the Upper Blue Nile Basin (UBNB) of Ethiopia is essential to the agriculture and water resource of western Ethiopia because it constitutes a significant proportion of the annual rainfall of Ethiopia. Therefore, for an effective management of the water resources of UBNB, it will be important to accurately predict its JJAS rainfall preferably at a seasonal lead time. The aim is to forecast the weekly rainfall through the teleconnect between the two climatic variations. Four main finding was reached from this study, which are:

1. Wavelet based principal component analysis (WPCA) was employed to analyze the non-stationary variability of UBNB's JJAS rainfall, and scale average wavelet power (SAWP) of the gridded rainfall data was computed. It was found that the Twentieth Century JJAS rainfall data of UBNB exhibited strong 2-8-yr cycles, and by mapping the

correlation pattern between WPC1 and SAWP of the JJAS rainfall data, it is found that the variability of WPC1 was mainly represented by rainfall of UBNB in western Ethiopia;

2. WPCs and SAWP of seasonal, FMAM SST of the Indian, Atlantic and Pacific oceans were also computed. Then, from the correlation field between SAWPs of the FMAM SST of the three oceans and WPC1 of JJAS seasonal rainfall over the UBNB, sectors of the Indian, Atlantic, and Pacific Oceans where SST showing strong teleconnection with the JJAS rainfall of UBNB ($r \geq 0.4$) were identified. High wavelet coherence was also found between WPC1 of selected sectors of FMAM SST and WPC1 of seasonal rainfall of the following season (JJAS), which is consistent with the correlation analysis between WPC1 of JJAS rainfall and SAWP of the selected sectors of FMAM SST;
3. Seasonal FMAM SST data in these identified sectors of the three oceans were used as predictors to a calibrated ANN-GA model to predict the seasonal JJAS rainfall of UBNB at one-season lead time. The sectors of FMAM SST fields chosen were located in the equatorial Indian Ocean (20° S- 11° N, 61° - 85° E), southern Indian Ocean (59° - 43° S, 34° - 80° E), southern Atlantic Ocean (48° - 35° S, 48° - 27° W), and southern Pacific Ocean (41° - 26° S, 112° - 91° W) for the FMAM SST to forecast JJAS rainfall. Results show that ANN-GA predicted seasonal rainfall that agree well with the observed data for the highlands of UBNB specifically, the UBNB ($RMSE$ between 0.72 and 0.82, correlation between 0.68 and 0.77, and HK scores between 0.5 and 0.77) but the results at the foothills region of GRV were poor which is expected since the variability of WPC1 mainly comes from the Highlands of Ethiopia;

4. The disaggregation models of Valencia and Schaake (1973) is used to disaggregate the seasonal rainfall to rainfall of one week time scale which can then be used to drive a hydrologic model to predict the streamflow of UBNB at one season lead time. Even though there are discrepancies, with a R^2 of 0.44, the weekly, disaggregated rainfall reasonably capture the characteristics of the observed weekly rainfall. The ability to predict the rainfall of UBNB at a season lead time will be useful for an optimal allocation of water usage among various competing users in the river basin. Our future research will be to predict the weekly streamflow of UBNB in Ethiopia at a season lead time.

Acknowledgements

This research was funded by the Egyptian Ministry of Higher education (MHE). The first author was also partly funded by graduate teaching assistantship of the University of Alberta. The authors thank Dr. Chun-Chao Kuo for his valuable discussions on ANN-GA. The Wavelet software was provided by Torrence and Compo. It may be downloaded from the following website. <http://atoc.colorado.edu/research/wavelets/> The Wavelet coherence software was provided by A. Grinsted, and found at <http://www.pol.ac.uk/home/research/waveletcoherence/>. The SAMS 2007 software is downloaded from <http://www.sams.colostate.edu/download.html> of the Colorado State University. Great appreciation is expressed to the two anonymous reviewers of this paper for their comments and suggestions.

References

Abdi, H., and Williams, L. (2010). Principal component analysis and model

- evaluation. *Wiley Interdisciplinary Reviews: Computational Statistics*, 2(4), 433-459.
- Abegaz, A., Keulen, H., Haile, M., and Oosting, S. (2007). Nutrient dynamics on smallholder farms in Teghane, Northern Highlands of Ethiopia. In A. Bationo, B. Waswa, J. Kihara, and J. Kimetu (Eds.), *Advances in integrated soil fertility management in sub-Saharan Africa: Challenges and opportunities* (p. 365-378). Springer Netherlands.
- Addison, P. S. (2002). *The illustrated wavelet transform handbook*. Institute of Physics Publishing.
- Camberlin, P. (1997). Rainfall anomalies in the source region of the Nile and their connection with the Indian summer monsoon. , 10, 1380-1392.
- Chen, S.-H., Lin, Y.-H., Chang, L.-C., and Chang, F.-J. (2006). The strategy of building a flood forecast model by Neuro-Fuzzy network. *Hydrol. Processes*, 20(7), 1525-1540.
- Chow, V. T., Maidment, D. R., and Mays, L. W. (1988). *Applied hydrology*. New York: McGraw-Hill.
- Conway, D. (2000). The climate and hydrology of the Upper Blue Nile river. *The Geographical Journal*, 166(1), 49-62.
- Degefu, W. (1987). Some aspects of meteorological drought in Ethiopia. In M. H. Glantz (Ed.), *Drought and hunger in Africa: Denying famine a future* (p. 23-36). Cambridge, England: Cambridge University Press.
- De Vos, N., and Rientjes, T. (2005). Constraints of Artificial Neural Networks for rainfall-runoff modelling: trade-offs in hydrological state representation and model evaluation. *Hydrol. Earth Syst. Sci. Discuss.*, 2(1), 365-415.

- Diro, G., Grimes, D., and Black, E. (2011). Teleconnections between Ethiopian summer rainfall and sea surface temperature: part I-observation and modelling. *Clim.Dyn.*, 37(1), 103-119.
- Elsanabary, M. H., and Gan, T. Y. (2012). Investigation of seasonal rainfall variability over the Ethiopian Highlands: Teleconnection between the Upper Blue Nile basin rainfall and the oceanic anomalies. *Proc. CSCE General Annual Conference, Canadian Society for Civil Engineering*. (Edmonton, Alberta, June 6-9, 2012)
- Elsanabary, M. H., Gan, Y. T., and Mwale, D. (In review). Application of wavelet empirical orthogonal function analysis to investigate the nonstationary character of Ethiopian rainfall and its teleconnection to nonstationary global sea surface temperature variations for 1900-1998. *Int.J.Climatol.*. (Submitted and under review)
- Gamachu, D. (1977). *Aspects of climate and water budget in Ethiopia*. Addis Ababa Univ. Press.
- Gissila, T., Black, E., Grimes, D. I. F., and Slingo, J. M. (2004). Seasonal forecasting of the Ethiopian summer rains. *Int.J.Climatol.*, 24(11), 1345-1358.
- Gupta, V. K., and Waymire, E. C. (1993). A statistical analysis of mesoscale rainfall as a random cascade. *J. Appl. Meteor.*, 32, 251-267.
- Hsu, K., H.V., G., and Sorooshian, S. (1990). Artificial Neural Network modeling of the rainfall-runoff process. *Water Resour.Res.*, 31(10), 2517-2530.
- Hulme, M. (1992). A 1951-80 global land precipitation climatology for the evaluation of General Circulation Models. *Clim. Dyn.*, 7, 57-72.

- Hulme, M. (1994). Validation of large-scale precipitation fields in General Circulation Models. In M. Desbois and F. Desalmand (Eds.), *Global precipitations and climate change*. Springer-Verlag.
- Hulme, M., and New, M. (1997). Dependence of large-scale precipitation climatologies on temporal and spatial sampling. *J.Clim.*, 10(5).
- Hulme, M., Osborn, T., and T.C.Johns. (1998). Precipitation sensitivity to global warming: Comparison of observations with HadCM2 simulations. *Geophys. Res. Letts.*, 25, 3379-3382.
- Jevrejeva, S., Moore, J. C., and Grinsted, A. (2003). Influence of the Arctic Oscillation and El niño-Southern Oscillation (ENSO) on ice conditions in the Baltic Sea: The Wavelet approach. *J.Geophys.Res*, 108(D21), 4677.
- Jury, M. (2010). Ethiopian decadal climate variability. , 101(1), 29-40.
- Kloos, H., and Legesse, W. (2010). *Water resources management in Ethiopia : implications for the Nile basin*. Amherst, NY: Cambria Press.
- Kuo, C., Gan, T., and Yu, P. (2010a). Seasonal streamflow prediction by a combined climate-hydrologic system for river basins of Taiwan. , 387(3), 292-303.
- Kuo, C., Gan, T., and Yu, P. (2010b). Wavelet analysis on the variability, teleconnectivity, and predictability of the seasonal rainfall of Taiwan. , 138, 162-175.
- Lane, W., and Frevert, D. (1990). *Applied stochastic techniques: Personal computer version : User manual*. Earth Sciences Division, Denver Office, Bureau of Reclamation, U.S. Department of the Interior.
- Lorenz, E. (1969). Atmospheric predictability as revealed by naturally occurring analogues. *J.Atmos.Sci.*, 26(4), 636-646.

- Mallat, S. G. (1999). *A Wavelet tour of signal processing*. Academic Pr.
- Mwale, D. (2005). *Nonstationary and nonlinear approaches for the analysis and prediction of hydroclimatic variables in eastern and southern Africa*. PhD thesis, University of Alberta, Edmonton, Alberta, Canada.
- Mwale, D., and Gan, T. (2009). Integrating Wavelet empirical orthogonal functions and statistical disaggregation for predicting weekly runoff for the Upper Kafue basin in Zambia, Africa. *J.Hydrol.Eng.*, 15, 822.
- Mwale, D., and Gan, T. Y. (2005). Wavelet analysis of variability, teleconnectivity, and predictability of the September-November East African rainfall. *J. Appl. Meteorol.*, 44(2), 256-269.
- Mwale, D., Gan, T. Y., Devito, K., Mendoza, C., Silins, U., and Petrone, R. (2009). Precipitation variability and its relationship to hydrologic variability in Alberta. *Hydrol. Processes*, 23(21), 3040-3056.
- Mwale, D., Gan, T. Y., and Shen, S. S. P. (2004). A new analysis of variability and predictability of seasonal rainfall of central southern Africa for 1950-94. *Int.J.Climatol.*, 24(12), 1509-1530.
- Segele, Z., Lamb, P., and Leslie, L. (2009). Seasonal-to-Interannual variability of Ethiopia/Horn of Africa Monsoon. part I: Associations of Wavelet-filtered large-scale atmospheric circulation and global Sea Surface Temperature. *J.Clim.*, 22(12), 3396-3421.
- Seleshi, Y., and Demaree, G. (1995). Rainfall variability in the Ethiopian and Eritrean highlands and its links with the Southern Oscillation Index. *J.Biogeogr.*, 945-952.
- Shahin, M. (1985). *Hydrology of the Nile basin* (Vol. 21). Amsterdam: Elsevier.

- Sutcliffe, J., Dugdale, G., and Milford, J. R. (1989). The Sudan floods of 1988. *Hydrol. Sci. J.*, 34(3), 355-364.
- Sutcliffe, J., Parks, Y., and of Hydrological Sciences, I. A. (1999). *The hydrology of the Nile*. International Association of Hydrological Sciences.
- Sveinsson, O., Salas, J., Lane, W., and Frevert, D. (2007). *Stochastic analysis, modeling, and simulation (SAMS Version 2007) User's Manual*. Department of Civil and Environmental Engineering, Colorado State University, Fort Collins, Colorado.
- Taye, M., and Willems, P. (2012). Temporal variability of hydroclimatic extremes in the Blue Nile basin. *Water Resour. Res.*, 48, W03513.
- Thiemig, V., De Roo, A., and Gadain, H. (2011). Current status on flood forecasting and early warning in Africa. *Intl.J.River Basin Management*, 9(1), 63-78.
- Torrence, C., and Compo, G. P. (1998). A practical guide to Wavelet analysis. *Bulletin of the American Meteorological Society*, 79(1), 61.
- Torrence, C., and Webster, P. J. (1999). Interdecadal changes in the ENSO-monsoon system. *J. Climate*, 12(8), 2679-2690.
- Valencia, D., and Schaake, J. (1973). Disaggregation processes in stochastic hydrology. *Water Resour.Res.*, 9(3), 211-219.
- Wilks, D. S. (2006). *Statistical methods in the atmospheric sciences*. Burlington, MA; London: Academic Press.
- Wolde-Georgis, T., Aweke, D., and Hagos, Y. (2001). The case of Ethiopia: reducing the impacts of environmental emergencies through early warning and preparedness. In G. MH (Ed.), . United Nations University Press.

Yates, D. N., and Strzepek, K. M. (1998). Modeling the Nile basin under climatic change. *J.Hydrol.Eng.*, 3(2), 98-108.

Table 4.1: Summary statistics of the forecasted JJAS rainfall season at the two grid points #4, #7

Grid Point	Bias	RMSE	r^2	HK
Point #4				
Calibration	-1.60	0.78	0.46	0.50
Validation	1.56	0.72	0.62	0.50
Point #7				
Calibration	-0.20	0.82	0.50	0.50
Validation	0.19	0.75	0.77	0.59

Table 4.2: Summary statistics of the statistically disaggregated weekly rainfall during JJAS rainy season at the two grid points #4, #7

Grid Point	r^2	RMSE	NS	Bias
Point #4	0.45	1.28	-0.23	0.00
Point #7	0.44	1.58	0.03	0.01

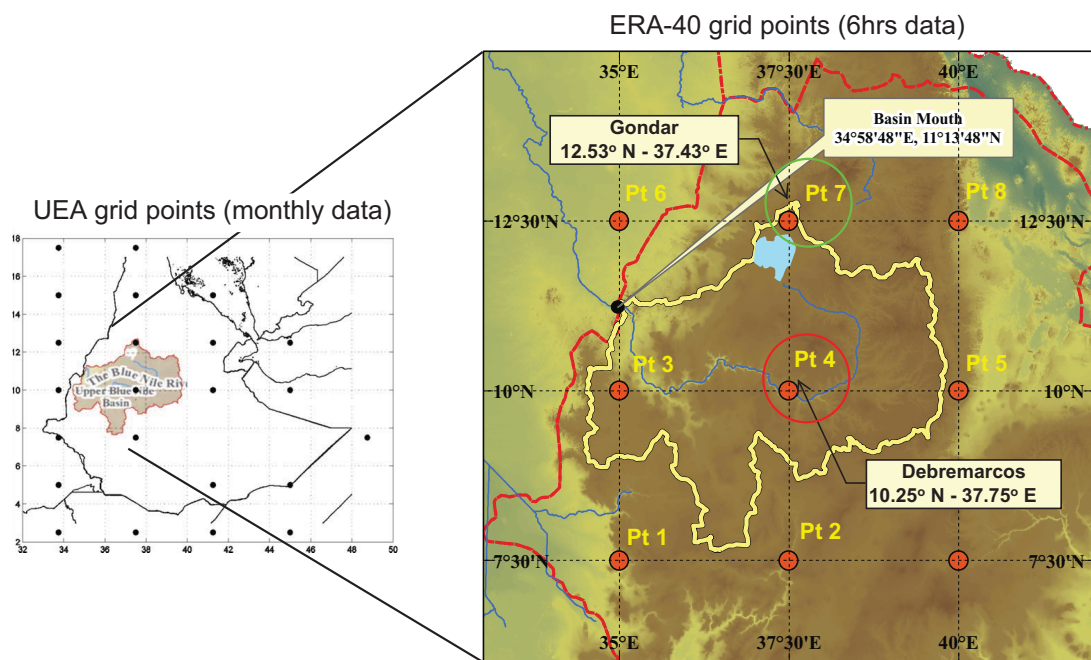


Figure 4.1: The Upper Blue Nile river basin, topography, UEA 23 grid points used for Wavelet analysis and ERA-40 nine grid points used for the hydrologic model. the closed circles indicating the two grid points (#4 and #7) out of nine, used for JJAS rainfall forecasting.

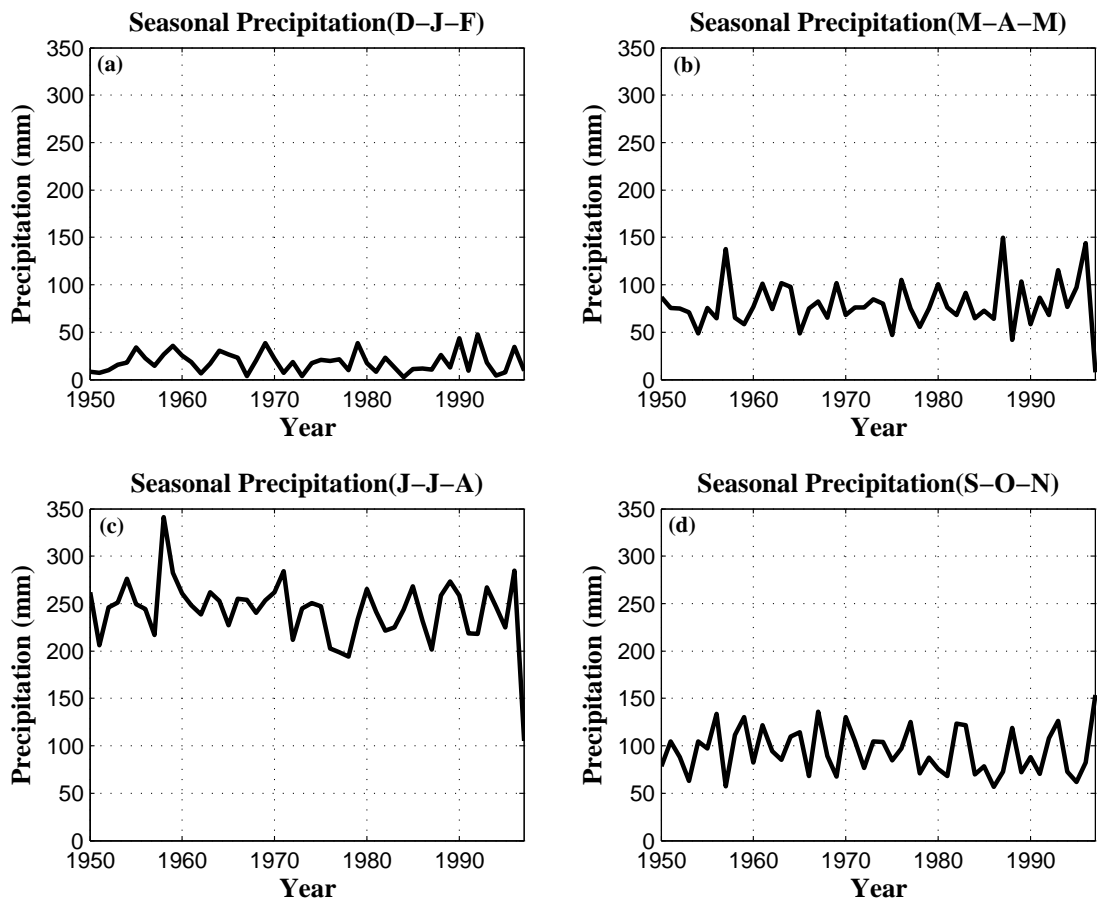


Figure 4.2: Seasonal rainfall variation at one grid point located at 10° N- 37.5° E for the period (1950-1998) from the UEA monthly gridded rainfall data.

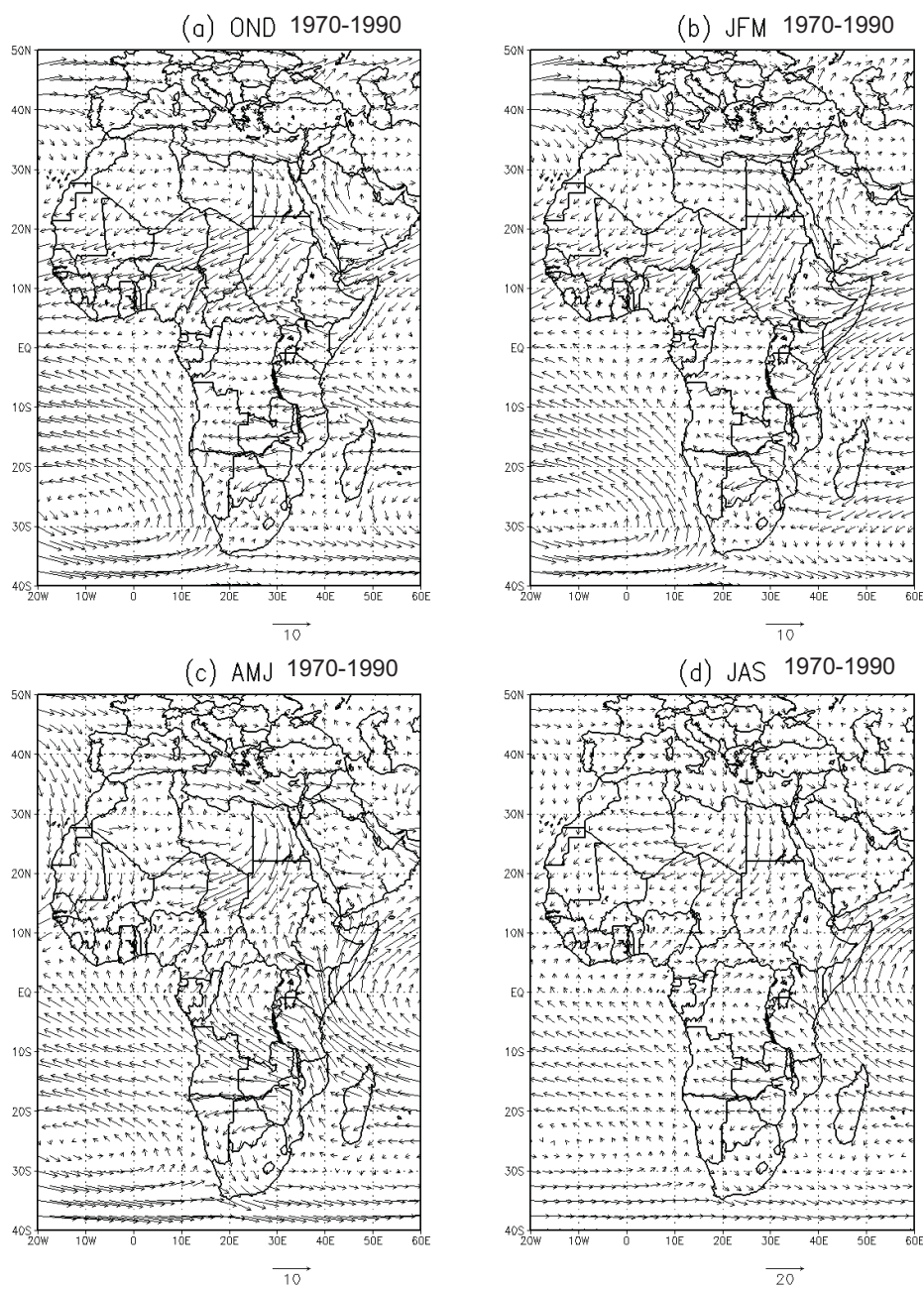


Figure 4.3: 850-hPa winds over Africa showing the prevailing atmospheric circulation and moisture transport in terms of wind speed (m/s) and direction throughout different seasons as indicated on each figure for a particular time period (ERA-40 data). (a-d) OND, JFM, AMJ and JAS for the period 1970-1990, (f-h) ONDJ, FMAM and JJAS for the period 1970-1990, and (i-k) ONDJ, FMAM and JJAS for the period 1990-2002.

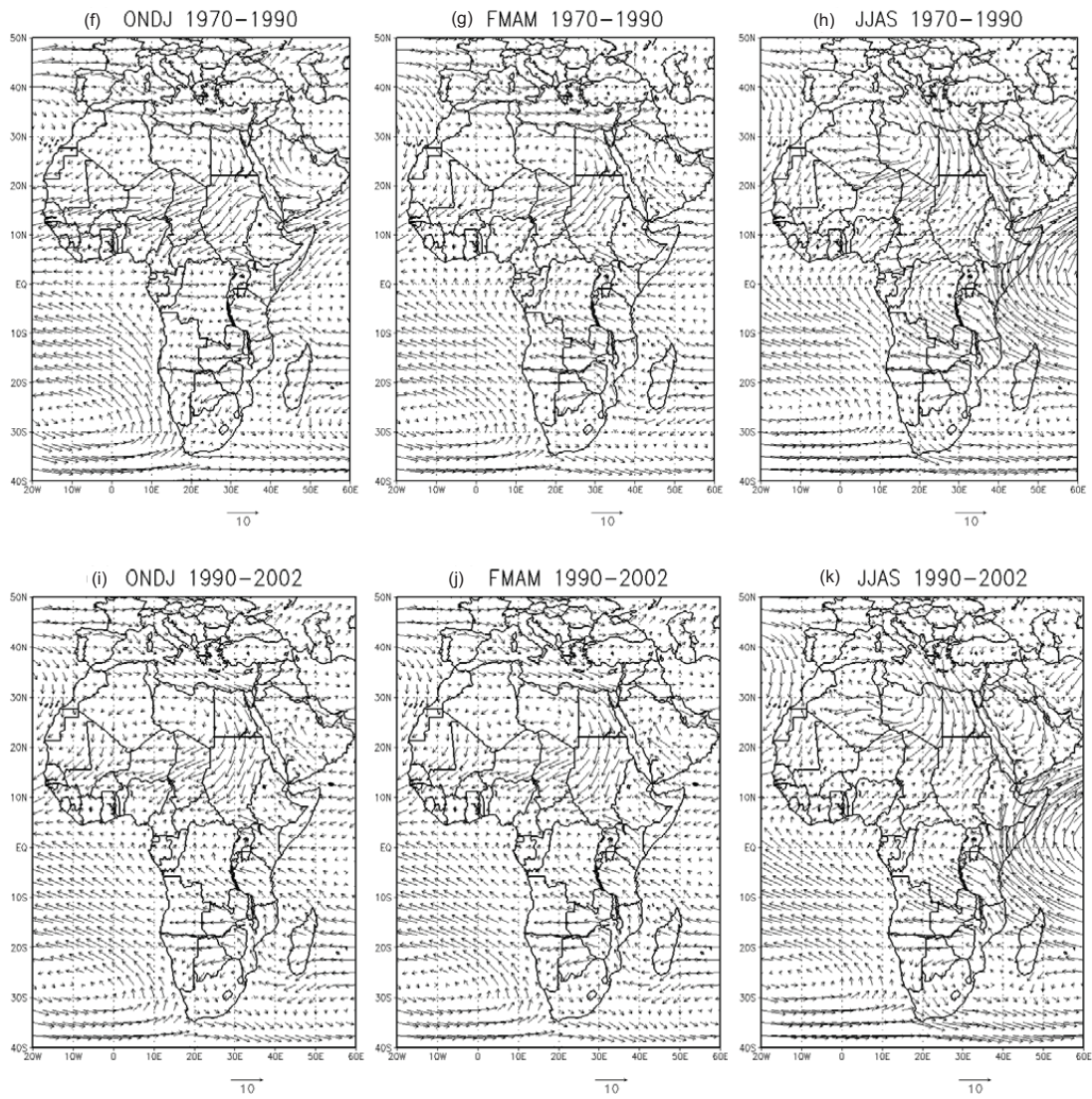


Figure 4.3: continued

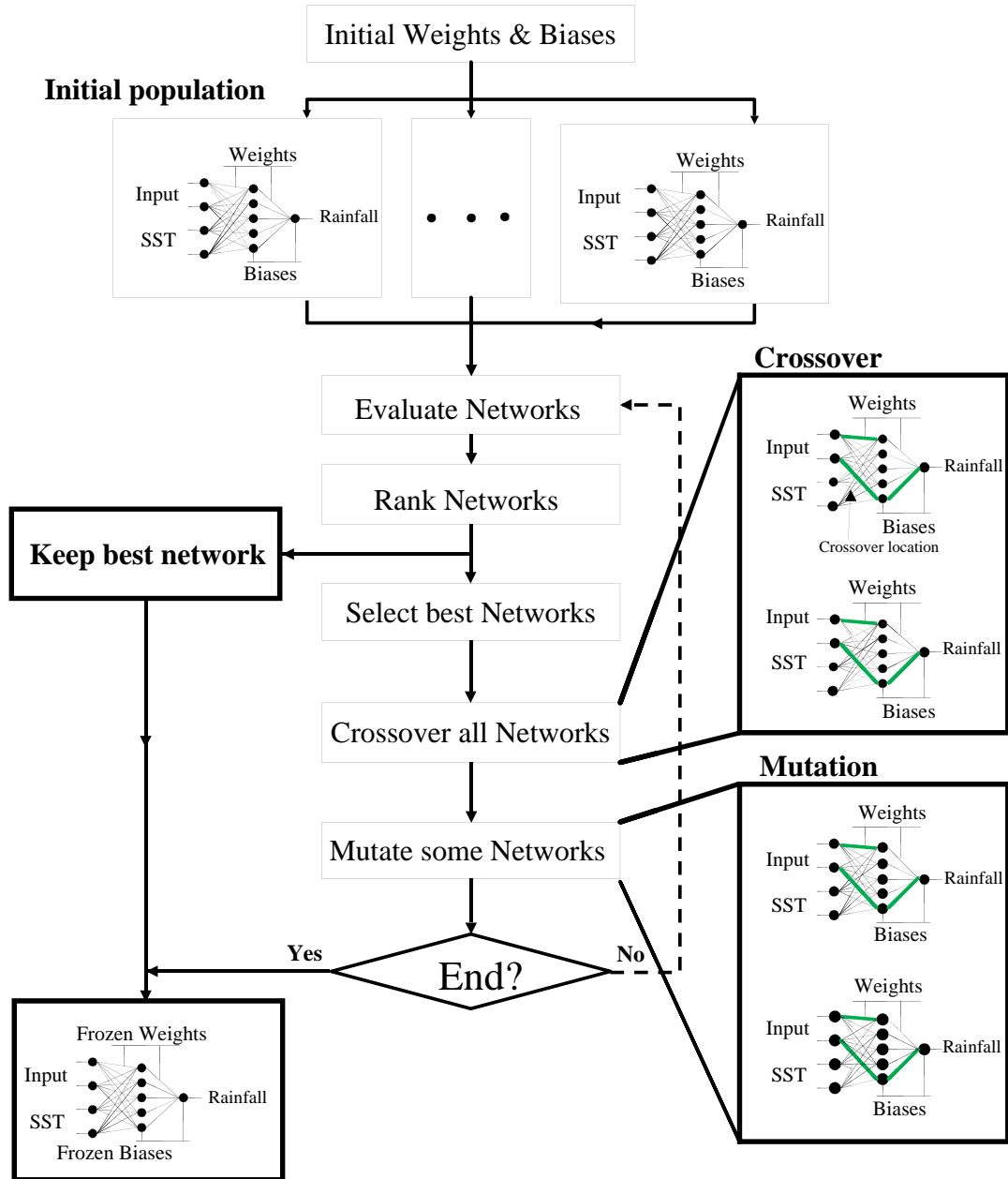


Figure 4.4: Flow chart of three-layer (input, hidden, and output) of the ANN-GA model. Three operations are shown: Selection, Crossover, and Mutation.

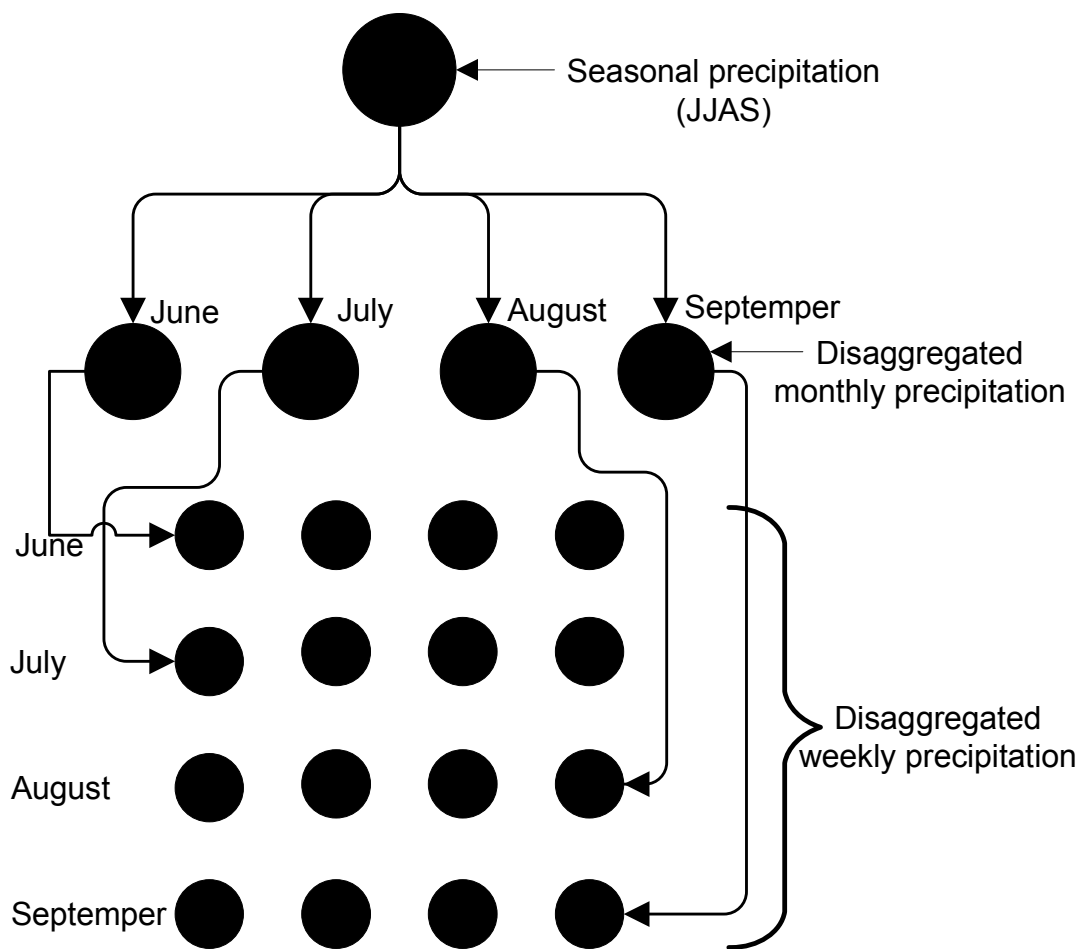


Figure 4.5: Seasonal disaggregation to weekly rainfall.

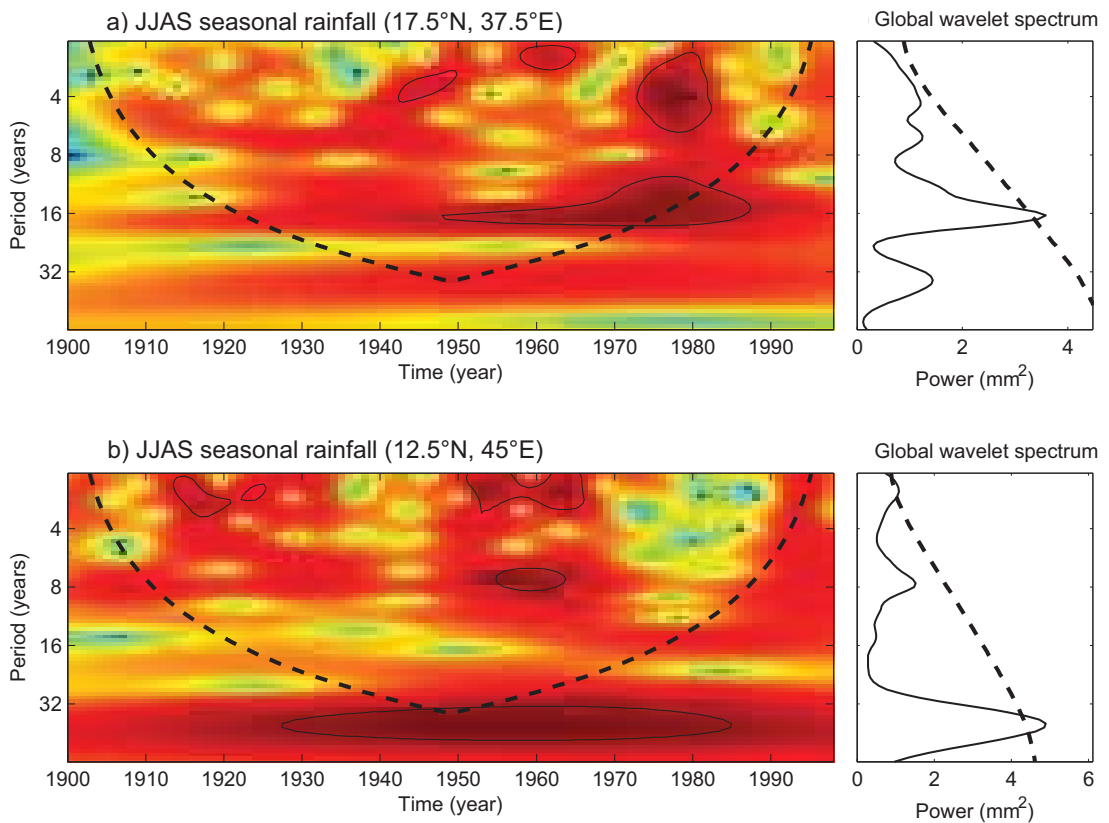


Figure 4.6: Examples of Continuous wavelet and global spectra of Ethiopian rainfall during June-September (JJAS) at two grid point: a) 17.5° N-37.5° E and b) 12.5° N-45° E. Each example presents the Morlet wavelet power spectrum, where the dashed line is the cone of influence beyond which the energy is contaminated by the effect of zero-padding and the thick black contours represent the 95% confidence level of local power relative to a red noise background, and Global wavelet power spectrum (solid line) with the 95% confidence level (dashed line).

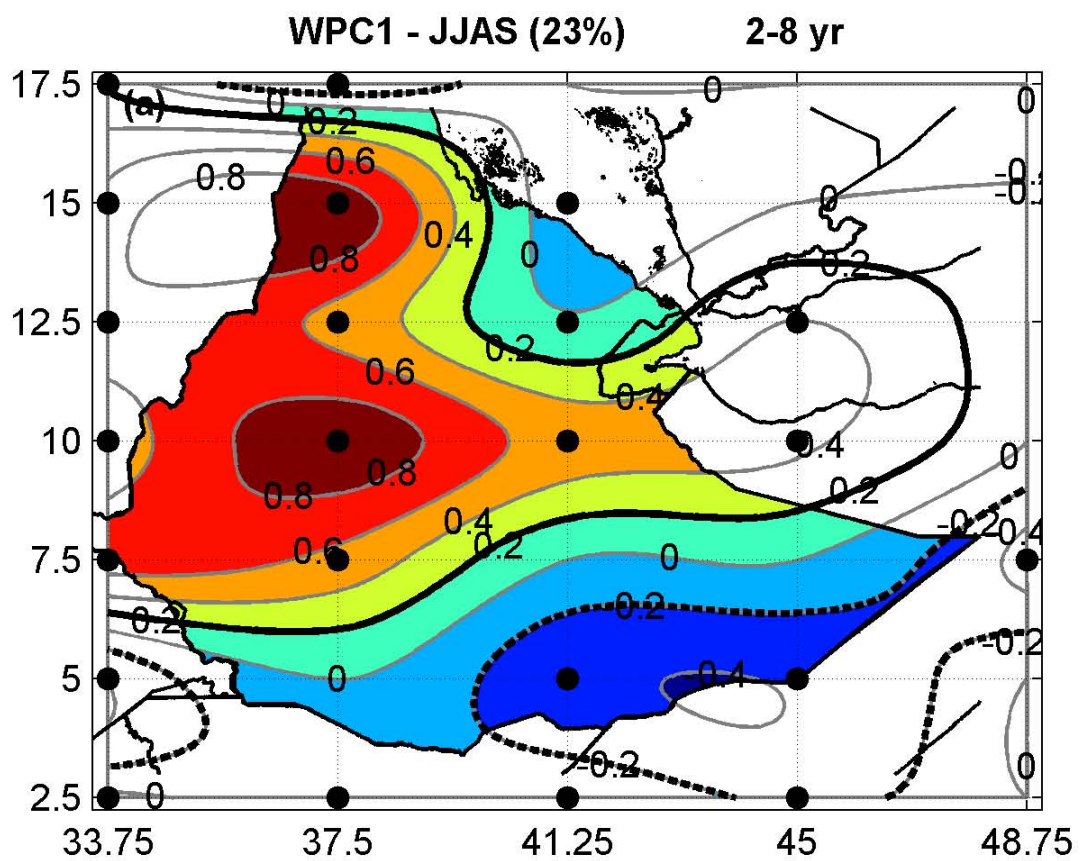


Figure 4.7: Contours of spatial correlation patterns between gridded rainfall SAWP and WPC1 of 2-8 year spectral band for the Kiremt season of UEA monthly gridded data (1900-1998).

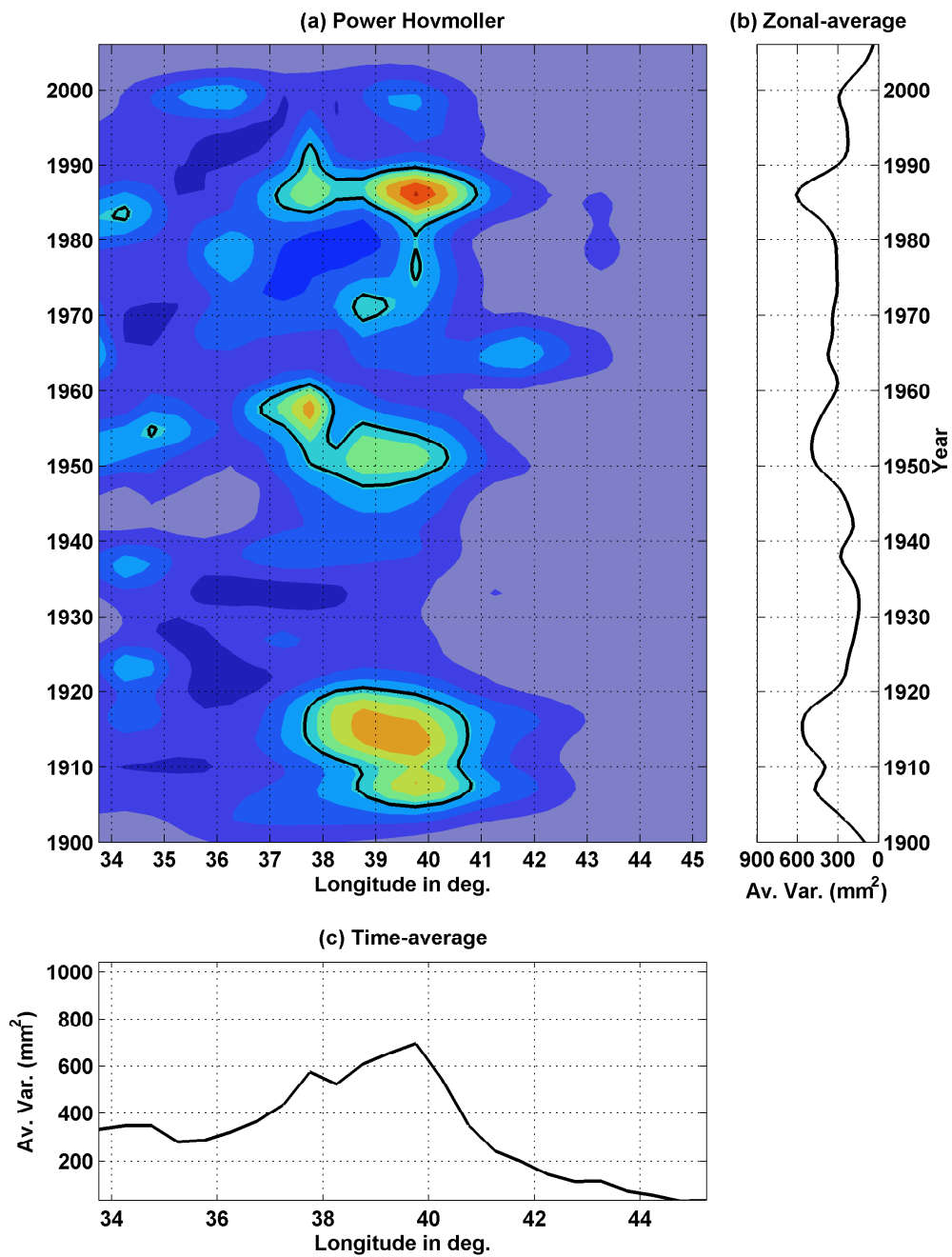


Figure 4.8: Power Hovmöller of 2-8 yrs. SAWP of the JJAS precipitation at lat. 10.25° N. the thick contour is the 95% confidence level, using the corresponding white noise spectrum at each longitude; (b) the average of (a) over all longitudes; (c) the average of (a) over all times. The data source is the UoD $0.5^\circ \times 0.5^\circ$ for the period (1900-2006).

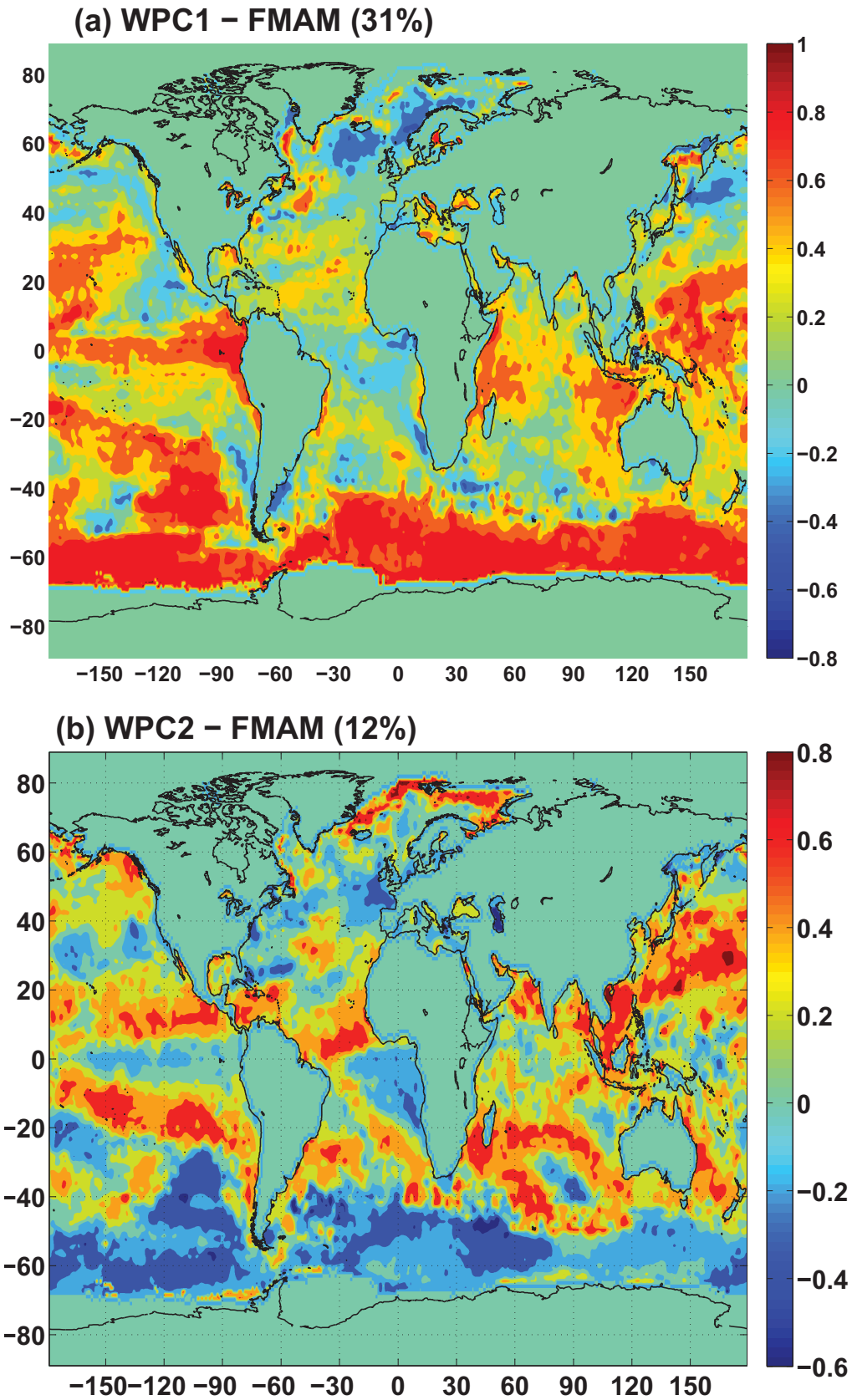


Figure 4.9: Contours of spatial correlation patterns between gridded SST SAWP and WPC1 from the SSTs of 2-8 year spectral band during FMAM season of 1870-2007 .

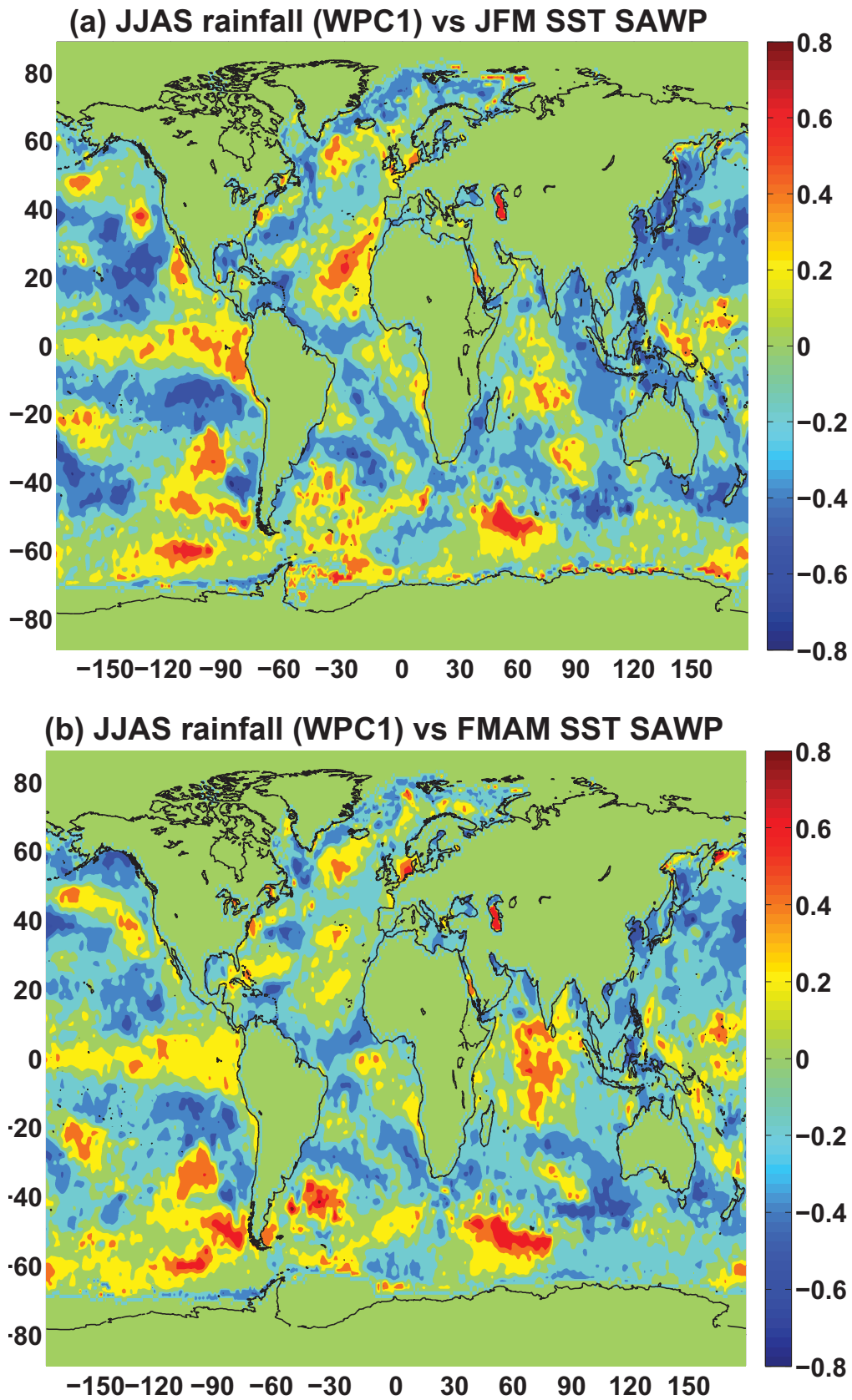


Figure 4.10: Contours of spatial correlation patterns between WPC1 of JJAS Ethiopian rainfall for 2-8 year spectral band during 1900-1998 and gridded SST SAWP during (a) JFM, and (b) FMAM.

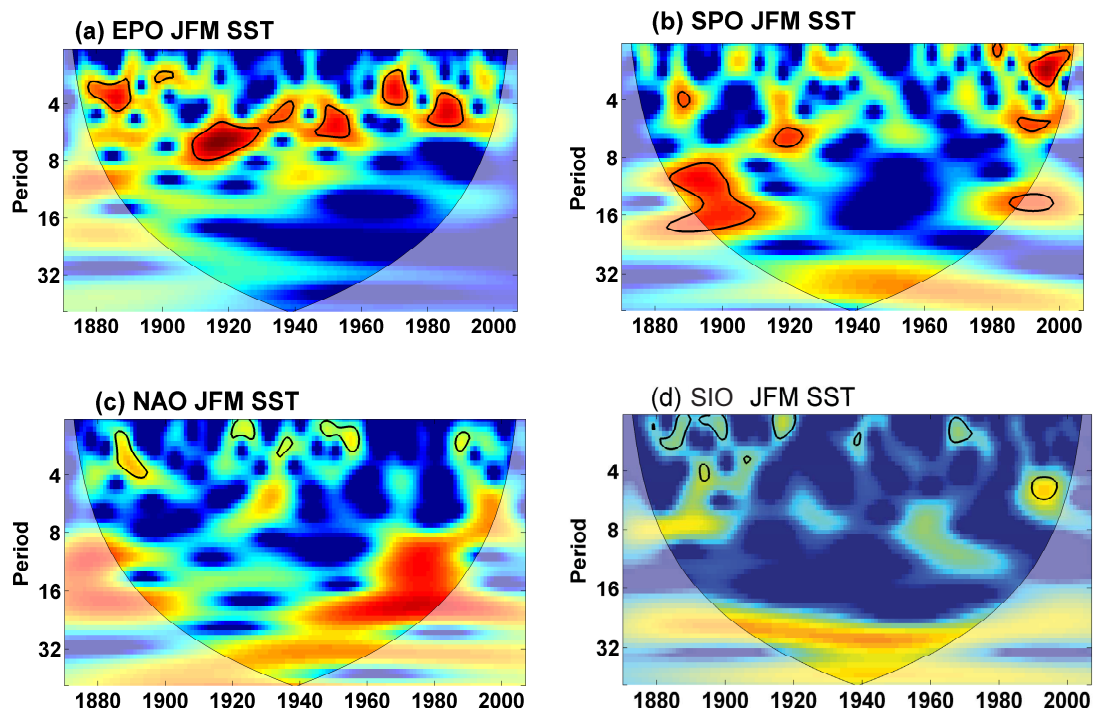


Figure 4.11: Wavelet Power Spectra of the leading first principal component for JFM seasonal Oceanic SST sectors (a) Equatorial Pacific Ocean (EPO), (b) South Pacific Ocean (SPO), (c) North Atlantic Ocean (NAO) and (d) South Indian Ocean (SIO). The thick black contours enclose statistically significant wavelet power at the 5% level of a red noise process, and the thin black curve is the cone of influence.

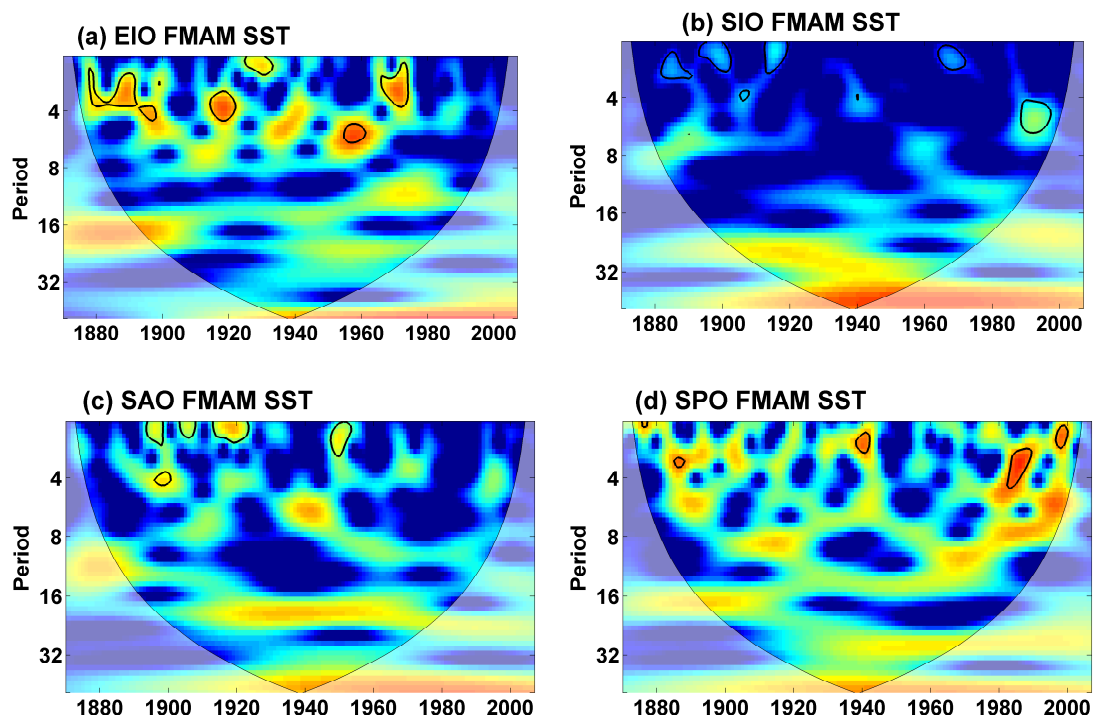


Figure 4.12: Wavelet Power Spectra of the leading first principal component for FMAM seasonal Oceanic SST sectors (a) Equatorial Indian Ocean (EIO), (b) South Indian Ocean (SIO), (c) South Atlantic Ocean (SAO) and (d) South Pacific Ocean (SPO). The thick black contours enclose statistically significant wavelet power at the 5% level of a red noise process, and the thin black curve is the cone of influence.

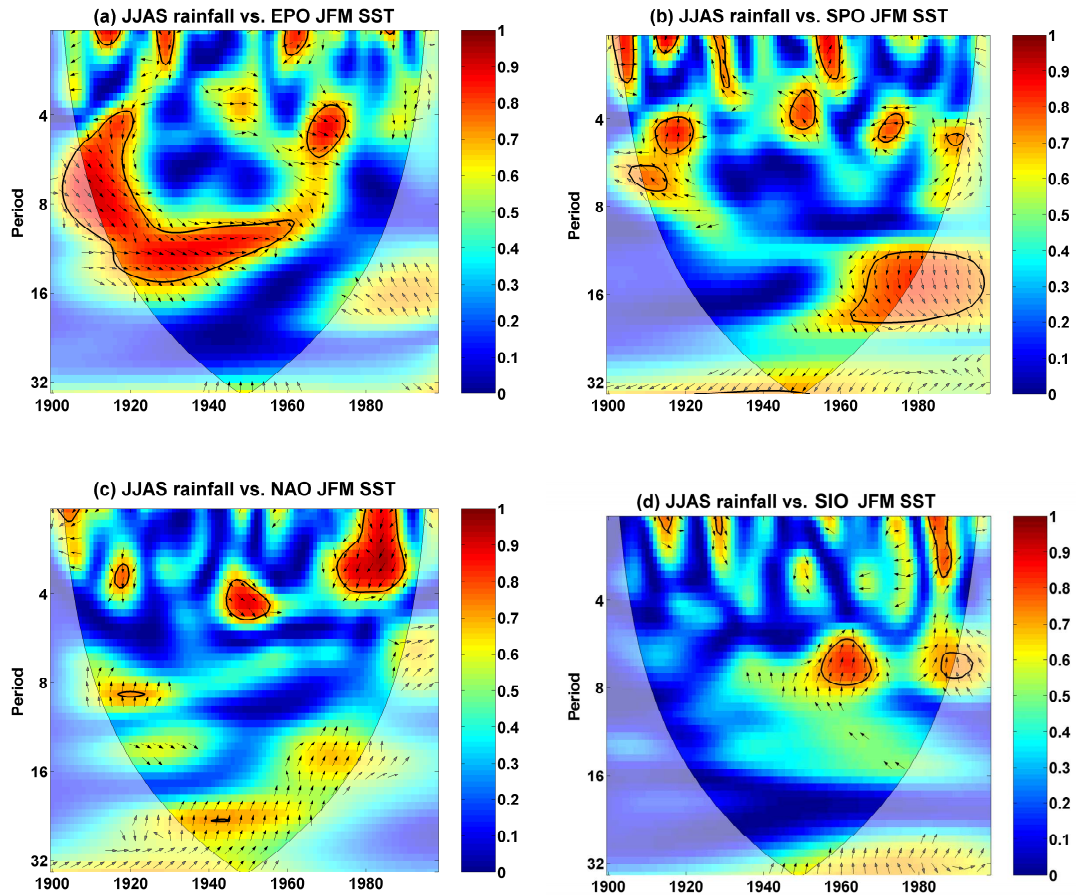


Figure 4.13: Wavelet coherence and phase difference between the UBNB rainfall PC1 and the leading PC1 for JFM seasonal Oceanic SST sectors (a) Equatorial Pacific Ocean (EPO), (b) South Pacific Ocean (SPO), (c) North Atlantic Ocean (NAO) and (d) South Indian Ocean (SIO). The thick black contours enclose statistically significant wavelet power at the 5% level of a red noise process, and the thin black curve is the cone of influence. The phase difference is plotted only for time periods and scales coherence over 0.5. Right pointing arrows indicate in-phase signals while left pointing arrows indicate anti phase signals.

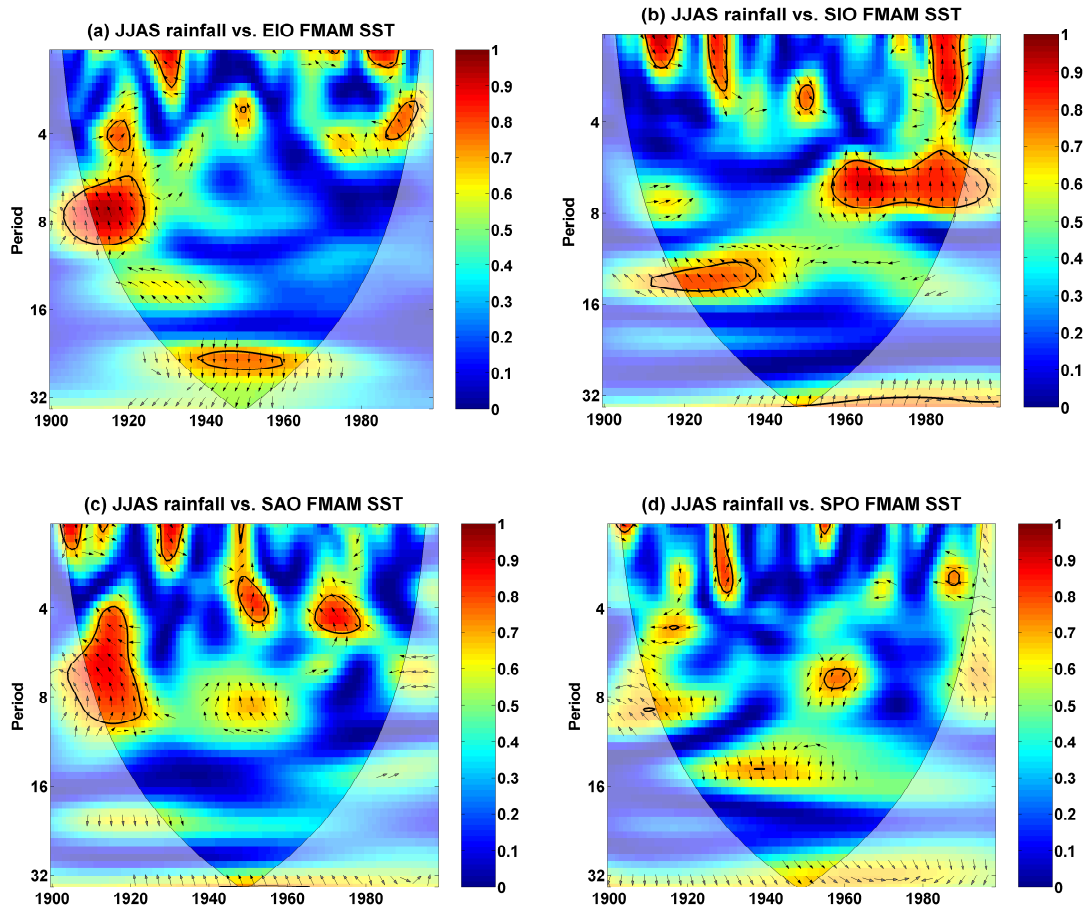


Figure 4.14: Wavelet coherence and phase difference between the UBNB rainfall PC1 and the leading PC1 for JFM seasonal Oceanic SST sectors (a) Equatorial Indian Ocean (EIO), (b) South Indian Ocean (SIO), (c) South Atlantic Ocean (SAO) and (d) South Pacific Ocean (SPO). The thick black contours enclose statistically significant wavelet power at the 5% level of a red noise process, and the thin black curve is the cone of influence. The phase difference is plotted only for time periods and scales coherence over 0.5. Right pointing arrows indicate in-phase signals while left pointing arrows indicate anti phase signals.

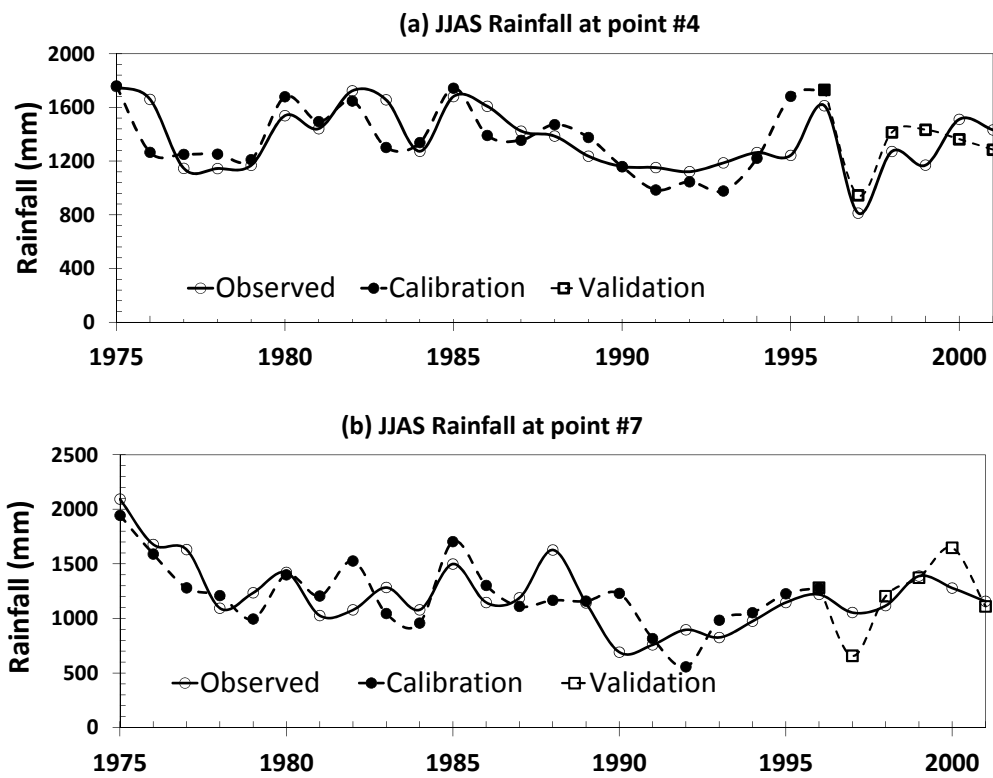


Figure 4.15: The observed (solid line) and forecasted (dotted and dashed) for JJAS seasonal rainfall at (a) grid point #4, (b) grid point #7. Calibration period is (1975-1995) and validation period is (1996-2001).

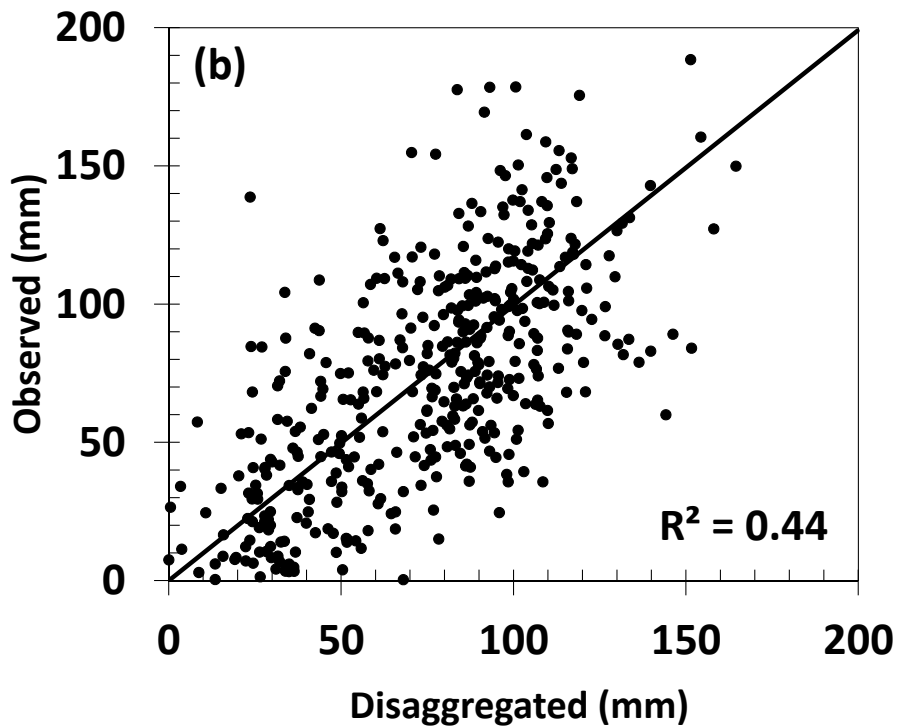
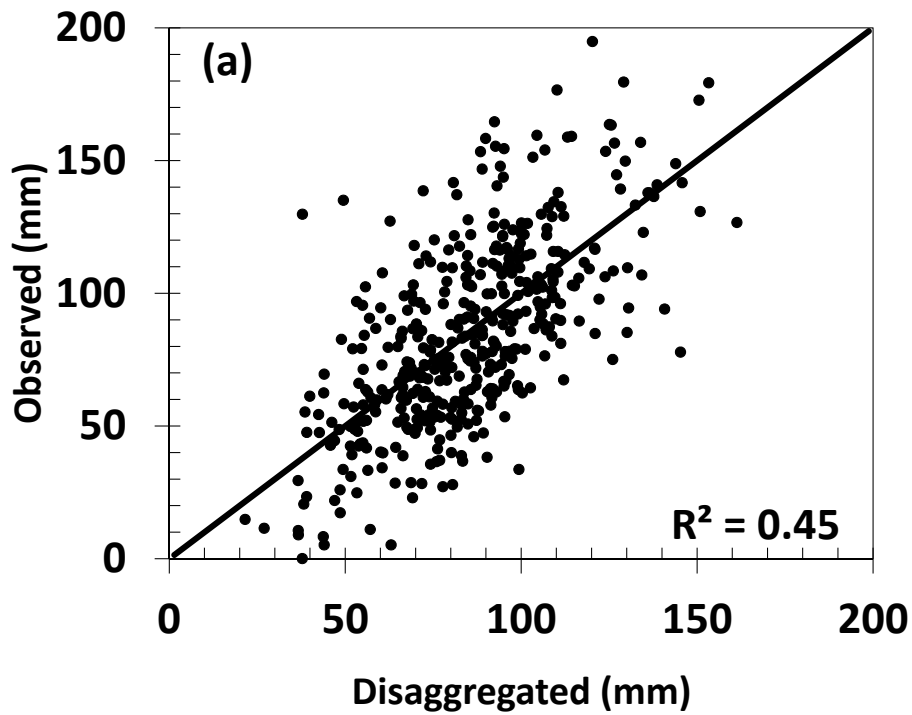


Figure 4.16: scatter plots for observed vs disaggregated weekly rainfall during JJAS rainy season at (a) grid point #4, (b) grid point #7.

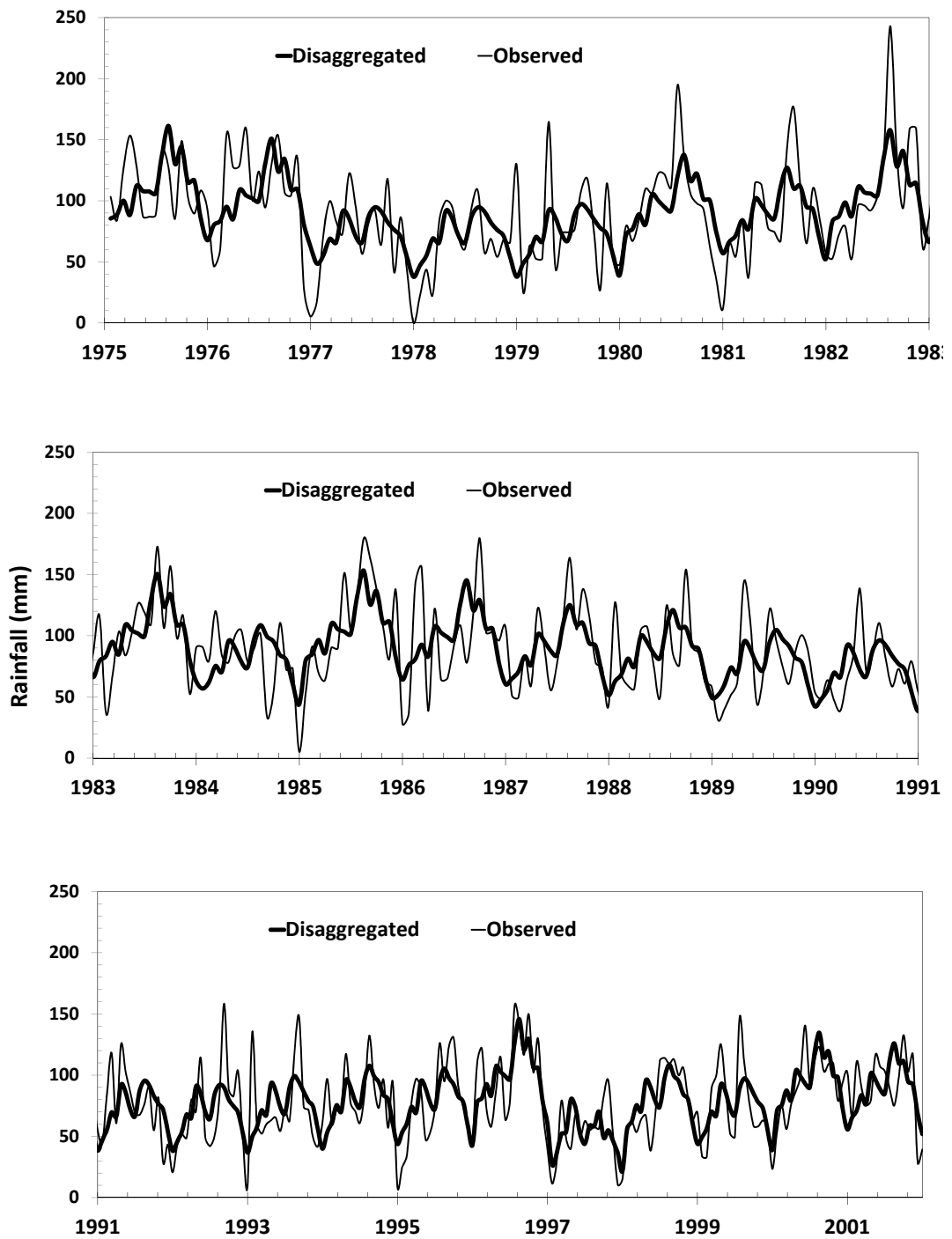


Figure 4.17: Observed and disaggregated weekly rainfall (mm) for grid point #4.

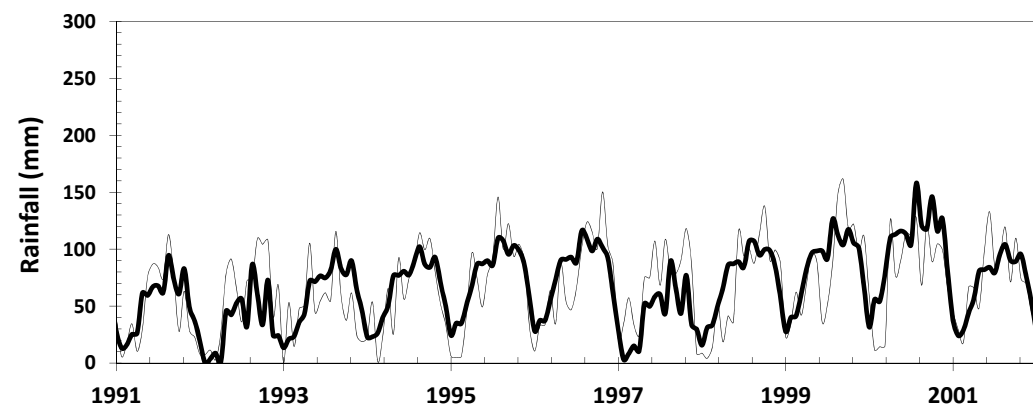
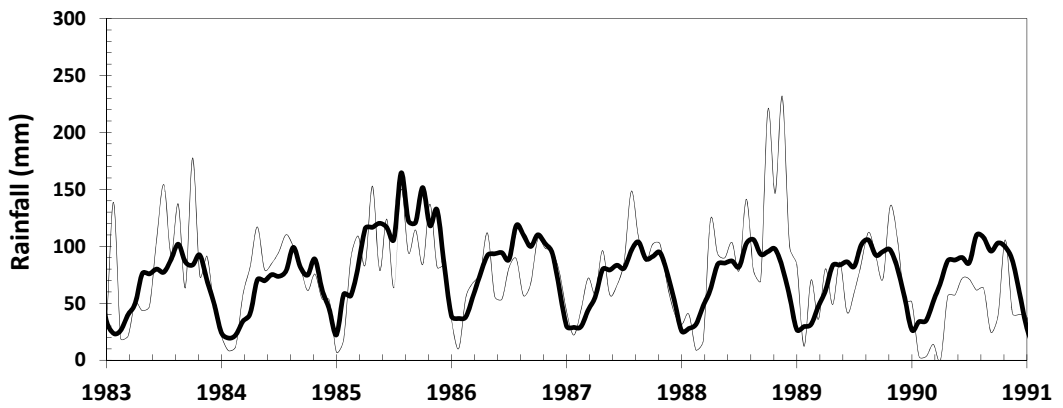
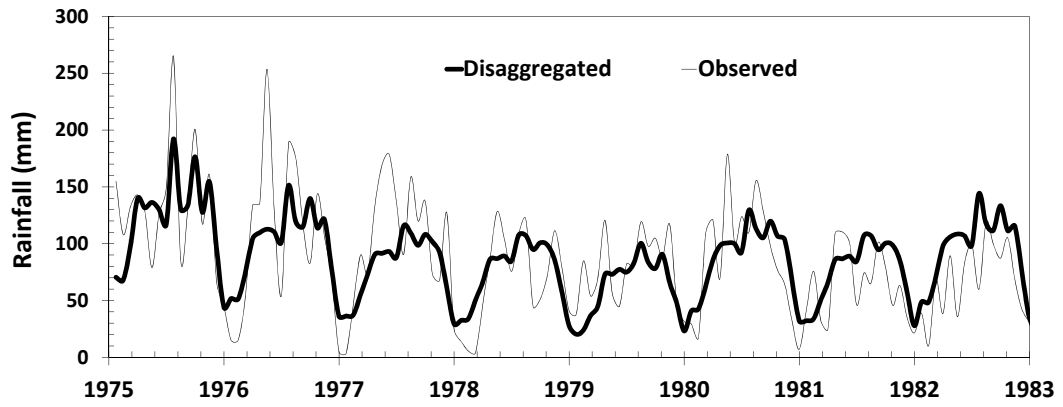


Figure 4.18: Observed and disaggregated weekly rainfall (mm) for grid point #7.

Chapter 5

Weekly Streamflow

Forecasting for the Upper

Blue Nile Basin, Ethiopia ¹

5.1 Introduction

The Nile River is the primary source of water supply and the artery to its downstream countries such as Egypt and Sudan. The upper Blue Nile basin (UBNB) in Ethiopia is one of the most important tributaries of the Nile River, contributing nearly 60% of the streamflow that reaches the Aswan High dam in Egypt (Figure 5.1) (Seleshi and Demaree, 1995; Yates and Strzepek, 1998; Sutcliffe et al., 1999; Conway, 2000). The Blue Nile has annual streamflow of about 48 Billion m^3 , which means it deliver more than 85% of the flow allocated to Egypt (Bishop, 2012). In recent years, Ethiopia experienced severe droughts which lead to adverse impacts on people's livelihood, agriculture, and industry. For the Blue Nile, the Kiremt season (June-September) yields substantial streamflow and serves as the main Ethiopian rain fed agricultural season, in which 85%-95% of

¹A version of this chapter will be submitted for publication to the Journal of Hydrology

the annual crops are produced of Ethiopia are produced (Degefu, 1987). As shown in Figure 5.2, roughly 70% of annual rainfall in the UBNB is delivered during June-September months (Conway, 2000).

It will be beneficial to develop a robust model that takes advantage of large scale, seasonal sea surface temperature (SST) data generated by climate models to credibly forecast the UBNB streamflow and preferably up to one season lead time. At seasonal time scale, the linkage between SST and streamflow can be represented by statistical models that can serve as tools to forecast seasonal streamflow useful for managing the water resources of the UBNB, given that UBNBs reservoirs are generally of limited capacity because of steep terrain which means that excessive water will tend to spill over. Because of limited reservoir storages, water shortages could happen if a dry season persists. The ability to reliably forecast streamflow at a season lead time will also help hydropower operators to manage hydropower production during low flow periods.

The teleconnection between the streamflow of Nile river basins and SST of certain oceans has been well studied. Amarasekera et al. (1997); Seleshi and Zanke (2004) found a negative correlation between the annual discharge of the NR and the warm phase of the El Niño Southern Oscillation (ENSO). (Eltahir, 1996) showed that 25% of the natural variability of the annual streamflow of the Nile is connected to ENSO. Quinn (1992) attributed the 7-years of famine in Egypt found in both the Bible and the Koran ¹

¹ (43) And the king (of Egypt) said: “Verily, I saw (in a dream) seven fat cows, whom seven lean ones were devouring, and seven green ears of corn, and (seven) others dry. O notables! Explain to me my dream, if it be that you can interpret dreams.” (44) They said: “Mixed up false dreams and we are not skilled in the interpretation of dreams.” (45) Then the man who was released (one of the two who were in prison), now at length remembered and said: “I will tell you its interpretation, so send me forth.” (46) (He said): “O Yûsuf (Joseph), the man of truth! Explain to us (the dream) of seven fat cows whom seven lean ones were devouring, and of seven green ears of corn, and (seven) others dry, that I may return to the people, and that they may know.” (47) [(Yûsuf (Joseph))] said: “For seven consecutive years, you shall sow as usual and that (the harvest) which you reap you shall leave it in the ears, (all) except a little of it which you may eat. (48) “Then will come after that, seven hard (years), which will devour what you have laid by in advance for them, (all) except a little of that which you have guarded (stored). (49)

to an anomalously cool period, resulted in a cold atmosphere and reduced precipitation.

There have been research studies conducted on forecasting NR streamflow, particularly the annual flood. For example, Wang and Eltahir (1999) developed an algorithm for medium- to long-range forecasting of the Nile flood by correlating ENSO and the Nile streamflow. (Awadallah and Rouselle, 2000) forecasted the summer runoff volume of the Nile using SSTs, ENSO and the SSTs in the South Indian Ocean. Their prediction at a 3-month lead time explained 63% of the variability of the Nile flood. Eldaw et al. (2003) forecasted the NR flow through different statistical models using SST zones from the Tropical Pacific Ocean (ENSO) at 11 months (approximately one year) of lead time. Both Gissila et al. (2004) and Saji et al. (1999) found that there is a strong correlation between East Africa (EA) and the IOD. Eltahir et al. (2004); Delude (2005) highlighted the sea-saw oscillation between the Amazon and Congo basins, which could lead to investigations of such phenomenon between the NRB and major rivers in the world, as well as, the oceanic anomalies. However, the influence of ENSO has generally been on the UBNB and the Atbara tributaries of the NR, which being north of the Equator, is more strongly correlated with ENSO than the two large tropical rivers, which are Congo and Amazon.

Since a reliable seasonal/weekly streamflow forecasting tool will be useful for an effective and sustainable management of water resources of the upper Blue Nile River basin, our objective is to develop a robust framework for generating a weekly streamflow forecast during July-October season to guide hydropower management, irrigated agriculture, and other water allocations of the basin.

“Then thereafter will come a year in which people will have abundant rain and in which they will press (wine and oil).”

5.2 Research Objectives

The goal of this study is to develop a framework that integrates wavelet analysis (WA), Principal component analysis (PCA), artificial neural networks with genetic algorithm (ANN-GA), and statistical disaggregation to forecast the weekly seasonal streamflow of the UBNB at a one-season lead time based on selected sectors of oceanic SST as the predictors. Essentially, the objectives of this study are as follows:

- i) To analyze the nonstationary variations of July-October (JASO) streamflow over the UBNB by wavelet analysis; ([Elsanabary and Gan, 2012](#); [Elsanabary et al., In review](#));
- ii) To analyze the nonstationary characteristics of January-March (JFM) and February-May (FMAM) sea surface temperatures (SST) using wavelet analysis, and identify linkage with the JASO streamflow of UBNB;
- iii) To develop an artificial neural network calibrated with a genetic algorithm (ANN-GA) driven by FMAM SST to forecast the JASO streamflow of UBNB. The ANN-GA was calibrated using the JASO streamflow and FMAM SST data of 1975-1995 and validated with the 1996-2001 data;
- iv) To disaggregate the forecasted seasonal streamflow of ANN-GA using the Use the [Valencia and Schaake \(1973\)](#) (VS) disaggregation model to weekly streamflow;
- v) To forecast weekly streamflow of UBNB based on the weekly rainfall data disaggregated from seasonal rainfall predicted by the ANN-GA model developed in Chapter 4 as predictors to another ANN-GA model;

The flowchart of the proposed modeling framework is shown in Figure 5.3. This paper is outlined as follows: UBNB hydrological characteristics and climatology of the basin are briefly described in section 5.3, rainfall and SST data in section 5.4, research methodology in section 5.5, discussions of results in section 5.6, and summary and conclusions in Section 5.7.

5.3 Upper Blue Nile Basin (UBNB)

The Blue Nile (Abay) begins at Tana Lake, (2150 km^2 area), and at an approximate elevation of 1800 m, with the water leaving the lake at the Tis-sissat Falls that drop over 50 m vertically (Shahin, 1985). The river course runs through a distance of 940 km (Conway, 1997) and the UBNB occupies 17% of Ethiopia (176,000 km^2) with a mean annual discharge volume of 48.5 billion m^3 (Conway, 2000) as shown in Figure 5.1. The precipitation of the UBNB is highly seasonal with a mean annual rainfall of 1600 mm (Sutcliffe et al., 1999). The Blue Nile streamflow is highly seasonal, with 81% (1912-2001) of the annual streamflow occurring in the summer months July to October (JASO) see Figure 5.2(a) and (c). Over Ethiopia, the seasonal rainfall distribution is governed by the migration of ITCZ from south to north, which causes the rainfall to be concentrated to the west of the Great Rift Valley (GRV) (Gamachu, 1977; Degefu, 1987; Sutcliffe et al., 1999). The UBNB, which is located west of the Ethiopian Highlands (EH), is one of the most important sub basins of the Nile River. The UBNB receives more precipitation (1000-2400 mm/year) than the eastern, northern and southern parts of the EH. Due to the orographic effect, precipitation generally increases with altitude (Kloos and Legesse, 2010), (see Figure 5.2 b).

Rainfall occurs over much of the year in the western highlands, but the wet season occurs between May-October. Essentially, from February to

May, the southeasterly winds that carry moisture from the Indian Ocean give rise to the first rainy season over most of Ethiopia, while from June to September the southwesterly and southeasterly winds are responsible for the second rainy season over Ethiopia. Since the Blue Nile is the leading contributor to the flow of the Nile, this study focuses on the seasonal to weekly streamflow forecasting of the UBNB.

5.4 Hydro-Climate data

5.4.1 Rainfall Data

Historical monthly precipitation data (1900-1998), ‘gu23wld0098.dat’, Version 1.0 (see Chapter 4 for details). A 6 hr (1961-2002) and more intense ($2.5^\circ \times 2.5^\circ$) rainfall re-analysis data set was also collected from the ECMWF, ERA-40. ERA-40 data was converted to weekly seasonal during JJAS for forecasting the seasonal rainfall and later to be used for forecasting the JASO seasonal streamflow. The main reason to use JJAS rainfall to forecast the JASO streamflow is to give us a one month in advance to effectively forecast the JASO streamflow of the UBNB.

5.4.2 SST Data

Global mean monthly SST data of 1870-2008, at $1^\circ \times 1^\circ$ grid resolution was extracted for about 65,000 grids points from Hadley Centre, HadISST Version 1.1, United Kingdom Met Office. The monthly SST anomaly grid data were transformed into seasonal SST (February-May, FMAM).

5.4.3 Streamflow Data

Daily natural streamflow (1971-2001) for the El Diem station was provided by Mr. Tazebe Beyenne of University of Washington while monthly

flow data were collected from the website (<http://dss.ucar.edu/datasets/ds553.2/data/>). The data came from several sources: Global Hydro Climate Data Network (GHCDN) of UNESCO/IHP, Cairo University (Shahin, 1985), Massachusetts Institute of Technology (1977), and Global Runoff Data Center of the World Metrological Organization (WMO) funded by Germany (<http://grdc.bafg.de/>)

5.5 Modeling Components and framework

5.5.1 Wavelet transformation

The wavelet is an oscillation (tiny wave) with limited duration in comparison to larger waves such as Sine or Cosine. The main purpose of using wavelet analysis is to understand and quantify the nonstationarity in the time-series. Consider a time series that we want to study is X_t , with equal time spacing δ and $t=0 \cdots N-1$, where N is the number of points. Assume a wavelet function, $\psi_o(\eta)$, that depends on a non-dimensional time parameter (η). The wavelet used in this study is the Morlet wavelet, which is used by [Torrence and Compo \(1998\)](#) for its ability to match with the hydroclimatic data.

$$\psi_o(\eta) = \pi^{-1/4} e^{i\omega_o\eta} e^{-\eta^2/2}, \quad (5.1)$$

[Gan et al. \(2007\)](#); [Mwale et al. \(2009\)](#) suggested the use of Morlet wavelet, when analyzing hydroclimatic data, because it resembles the stream-flow, temperature and SST time series. The continuous wavelet transform (CWT) is used for this study. When varying the wavelet scale (s) and transiting along the localized time index (n) over x axis in the x - y plane, we could generate a set of wavelets such as ([Mallat, 1999](#); [Addison, 2002](#)):

$$\psi_{s,n}(t) = \frac{1}{\sqrt{s}}\psi\left(\frac{t-n}{s}\right), \quad (5.2)$$

The CWT or the wavelet spectrum $W_n(s)$ of a discrete time series x_t with a scaled and translated version of $\psi_{\circ}(\eta)$ is:

$$W_n(s) = \sum_{t=0}^{N-1} x(t)\psi^*\left[\frac{(t-n)\delta t}{s}\right], \quad (5.3)$$

Where $(*)$ indicates the complex conjugate of ψ . Also, the (\circ) on ψ has been dropped to indicate that the wavelet has been normalized to have unit energy. The reason for this normalization is to ensure that the wavelet transforms at each scale (s) are directly comparable to each other and to the transform of other time series (Torrence and Compo, 1998; Mallat, 1999). The nonorthogonal wavelet analysis is used in this research to be able to choose arbitrarily a set of scales to build a complete picture about the magnitude of the rainfall and streamflow events over the EH. For convenience, the scales were chosen as a fractional power of two such as (Torrence and Compo, 1998):

$$s_j = s_{\circ}2^{j\delta_j}, j = 0, 1, \dots, J, \quad (5.4)$$

$$J = \delta_j^{-1}\log_2\left(\frac{N\delta t}{s_{\circ}}\right), \quad (5.5)$$

Where s_{\circ} is the smallest resolvable scale and J determines the largest scale. The magnitude of $W_n(s)$ coefficients shows how well the wavelet matches

with the precipitation time series. For each scale, $W_n(s)$ coefficients also depict the amplitude of a time series at that scale. For a streamflow or SST time series, the power at each scale will, therefore, be an appropriate measure of the magnitude of the rainfall or SST anomalies. To investigate the variations in the power over a range of scales (band) the scale-averaged wavelet power (SAWP), which represents the mean variance of wavelet coefficients over a range of scales s_1 to s_2 would also be used (Torrence and Compo, 1998).

$$\overline{W}_n^2 = \frac{\delta_j \delta t}{C_\delta} \sum_{j=j_1}^{j_2} \frac{|W_n(s_j)|^2}{s_j}, \quad (5.6)$$

5.5.2 Principal component analysis

The Principal component analysis (PCA) is defined as a multivariate technique in which observations are represented by several inter-correlated dependent variables (Abdi and Williams, 2010). PCA is mostly used in the atmospheric sciences (Wilks, 2006). The PCA reduces a data set with a large number of variables to a data set with fewer new variables. Its goal is to extract the important information from these variables, to represent it as a set of new orthogonal variables called principal components. PCA transforms data into independent PCs to reduce the numbers of variables by several leading PCs that explain a large proportion of the total variance. If we have multiple observations of a $(N \times n)$ data vector x_n , and the PCA give $(M \times n)$ vectors u , the u vector has fewer variables that represent a linear combinations of the original vector x_n . To examine the teleconnection between the rainfall/streamflow and SST, PCA was applied to the SAWP of rainfall, streamflow and SST separately (Mwale, 2005). Before applying the PCA, precipitation, streamflow, and SST time series were first converted to standardized anomalies (x') by subtracting the data with the mean and

dividing it with the standard deviation. Hence, there are usually a few U (or u_m) to account for the majority of the SAWP variation. The SAWP signals u_m , m^{th} principal component, are computed as follows:

$$u_m = e_m^T x' = \sum_{n=1}^N e_{nm} x'_n, \quad m = 1, \dots, M, \text{ (where } M \ll N \text{)} \quad (5.7)$$

Where, e_{nm} are the eigenvectors, X'_n are the k SAWP anomalies, and m represents a small subset of the k possible signals. The signals, u_m , are usually the major spatial and temporal patterns that account for the majority of the variations in the SAWP, and can be used to spatially delineate rainfall or SST variations into independent zones.

5.5.3 ANN-GA for predicting seasonal streamflow

Artificial Neural Networks (ANNs) are data-driven and non-parametric techniques, which mean that they do not necessarily require the assumption or enforcement of constraints or a priori solution structures (De Vos and Rientjes, 2005). ANNs have proven to be powerful in simulating non-linear and complex systems. ANN is a mathematical model that contains simple, densely interconnected elements known as “neurons” that are typically arranged in layers. An overview of the ANN-GA model described in this section is shown in Figure 4.4, (Mwale et al., 2004; Mwale, 2005; Mwale and Gan, 2009). The model has a forward structure with three layers (input, hidden, and output layer) as shown in Chapter 4. ANN-GA model receives signals at the input layer, and transforms these signals consequently through the hidden layer until they reach the output layer. Through trial and error, a five-node hidden layer was adopted in this study with a hyperbolic tangent used as the sigmoid function. The number of nodes for the input layer depend on the number of input variables, “predictors” (from

PCA), and the output layer has only one node, the “predictand”, which is the seasonal streamflow. The input data was normalized to zero mean and scaled to unit variance. Refer to Chapter 4 for more details.

5.5.4 Forecasting skill

To assess the performance of ANN-GA forecasting skill, five goodness-of-fit statistics were used, which are the Pearson correlation (r), root mean square error ($RMSE$), Nash-Sutcliffe coefficient of efficiency (Ns), and $Bias$, and Hanssen-Kuipers (HK) scores (Refer to Chapter 4).

5.5.5 Disaggregation of Seasonal streamflow

The Blue Nile River of length 1400 km, its average slope between the source (1800 m) and the gauging station (500 m) (Shahin, 1985) is about 10.77%. For natural channels with a slope of 8-11%, the approximate average velocity is between 1.22 to 2.13 m/s (Chow et al., 1988). Therefore, the “time of concentration”, which indicates the time needed for the whole basin of UBNB to contribute runoff at the basin outlet (El Diem station) is about 7 to 8 days, or a travel time of about a week. Therefore, it is reasonable to disaggregate the seasonal streamflow (JASO) of UBNB into weekly streamflow. For simplicity sake, each month was divided to 4 weeks. For example, for September, the first two weeks were averaged over 8 days while the last two weeks over 7 days. For July, August and October, the first three weeks of each month were averaged over 8 days while the last week of each month was averaged over 7 days (see Figure 5.4).

The disaggregation of seasonal streamflow of the UBNB can be carried out using a basic temporal disaggregation model of Valencia and Schaake (1973) or the analog approach of Lorenz (1969). In using the analog approach long data sets are required so that many similar episodes of weekly, monthly and annual aggregates can be found in the observations. Since UBNB

has only limited amount of hydro-climatic data, only the disaggregation method of [Valencia and Schaake \(1973\)](#) (VS) was used in this study. VS uses statistical properties between seasonal and weekly streamflow data to disaggregate the seasonal streamflow to four weekly streamflow totals per month for four months (i.e., a total of 16 weekly streamflow totals in four months). The VS disaggregation model takes the following form:

$$Z_t = AX_m + B\epsilon_m, \quad (5.8)$$

Where Z_t is the $m \times 1$ vector of the weekly streamflow of the t^{th} year, X_t is the forecasted seasonal streamflow of the t^{th} year, m is the number of weeks for the main season (JASO) which is 16 weeks for this study, and ϵ_t is the $m \times 1$ vector of standard normal deviates (i.e. zero mean and unity variance). A is a $(m \times 1)$ vector of coefficients that sum to one and can be considered as weekly contributions to the seasonal streamflow of vector X_t , while B is a $(m \times m)$ matrix of coefficients. A and B were estimated using the SAMS version 2007 software developed by the US Bureau of reclamation and the Colorado State University ([Sveinsson et al., 2007](#)).

5.6 Discussion of Results

5.6.1 Wavelet analysis of seasonal streamflow

The transformation of seasonal streamflow using wavelet analysis is summarized in this section. From the Morlet wavelet analysis and the scale average wavelet power (SAWP) computed for the seasonal rainfall of UBNB, [Elsanabary and Gan \(2012\)](#); [Elsanabary et al. \(In review\)](#) found that the JJAS rainfall data (Kiremt season) of Ethiopia exhibit interannual oscillations at 2-4 and 5-7 year cycles. As an example, global and local

wavelet spectra for seasonal streamflow (JASO) of the UBNB are shown in Figure 5.5. The local wavelet spectra represent the changes of wavelet power in terms of scale with respect to time while the global wavelet spectrum is the time average of all the local wavelet spectra for each scale. Thick black contours in the figure indicate that power is statistically significant at the 95% confidence level of a white noise process. The dashed line drawn through the wavelet spectrum depicts the cone of influence (CI), out of which the spectra may be affected by paddings and should be treated with caution. Figure 5.5 shows higher power in the 1910s and after 1980 between 2- and 8-yr cycles. Although the global (time averaged) spectra do not show statistically significant oscillations for all periods, the power between 2 and 8yr is still relatively high. Therefore, SAWP for the streamflow of UBNB and SST are estimated for the 2- and 8-yr cycles (Elsanabary and Gan, 2012; Elsanabary et al., In review).

5.6.2 Teleconnection between SAWP of JASO streamflow and SAWP of global SST

Figure 5.6a (b) shows the spatial correlation patterns between the UBNB JASO streamflow SAWP and each of the 65,000 SAWP of gridded global SST, during FMAM (JFM). To forecast at a one-season lead time, the SAWP of JASO streamflow is linked to the SAWP of FMAM SST (Figure 5.6). Figure 5.6(a) shows that JASO streamflow is correlated to SST of the Tropical Pacific, the northern Atlantic Ocean west of the Sahara desert. Some other areas include areas west of South America and areas south and north of Indian Ocean. The correlation between JASO SAWP and FMAM SST SAWP in the El Niño region appear comparatively strong. Figure 5.6(b) shows that JASO streamflow is correlated to areas in El Niño region, the southern Atlantic Oceans, and some other areas include areas west of South America during JFM seasonal SST. For AMJ, we found the

correlation between JASO and the SST is spatially similar but weaker to that of FMAM. Therefore, for robust forecasting it is better to use the FMAM as a leading season. Also, by comparing Figure 5.6 a(b) we noticed the change in the SST evolution specifically in the Indian Ocean. Apparently, correlation between JASO streamflow and the FMAM SST tend to increase after the IOD anomaly became mature which agrees with the finding of [Saji et al. \(1999\)](#). The correlations between FMAM SST SAWP and SAWP streamflow show that SST explains up to 64% (compared to 36% for JFM) of the streamflow variability. Since AMJ has crossed the summer barrier we have focused on the FMAM season as the forecasting season for the JASO streamflow over the UBNB to give adequate lead time.

By linking FMAM SST to JASO streamflow, we can use the wavelet transformed FMAM SSTs as predictors for the JASO streamflow at one-season lead time. In Figure 5.6(a), correlations above 0.4 used to identify areas of relatively high correlation. These areas were located in the north Equatorial Indian Ocean (18° S- 21° N, 45° - 95° E), south Indian Ocean (62° - 41° S, 16° - 92° E), south Pacific Ocean (66° - 34° S, 113° - 69° W) and equatorial Pacific Ocean (7.5° - 13° S, 163° - 82° W) (see Figure 5.7) . The SST data of these particular sectors were chosen as the predictors for JASO streamflow because the correlation coefficients were much higher than 0.4. Some of these sectors agree with those used by [Awadallah and Rousselle \(2000\)](#).

5.6.3 Seasonal streamflow forecasting

Given that the seasonal streamflow of the UBNB was strongly correlated with SST of some areas of the Equatorial and southern Indian ocean (EIO, SIO), north Atlantic (NAO), and south and equatorial Pacific Oceans(SPO, EPO) at interannual time scales, it makes sense to use these sectors of SST data to forecast the seasonal streamflow (JASO) of UBNB at one-season

lead time. Raw SST data of high correlated areas from the Indian, Atlantic, and Pacific Oceans were extracted. As an attempt to only retain data that explain most of the variances to eliminate unnecessary input data, from the scree plot that shows the percentage of explained variances of principal components (PCs), we found that, from each sector, only the first PC of FMAM SST with a total explained variances of $\approx 90\%$ was retained for forecasting the JASO streamflow see Figure 5.7. All input (SST- PC1s) and output data (seasonal rainfall) of the ANN-GA were normalized before the analysis. The structure of ANN-GA model for forecasting the seasonal rainfall is shown in Figure 4.4.

The ANN-GA was first calibrated using the 1975-1995 (21 yr) of data and independently validated using the 1996-2001 (6 yr) of data. The calibrated ANN-GA was applied to forecast the seasonal streamflow of the UBNB streamflow in Ethiopia. The time series of the predicted and the observed seasonal streamflow of JASO for the UBNB are presented in Figure 5.8a. The seasonal streamflow forecasted by the calibrated ANN-GA has a correlation (0.62) as shown in Figure 5.8a with the observed streamflow the basin at the calibration stage, which is generally of acceptable accuracy for water resources planning. Other goodness-of-fit statistics for the calibration stage, *Bias*, *RMSE* and the Hanssen-Kuipers (*HK*) scores which are 2.13 BM^3 , 0.86 BM^3 , and 0.33 respectively.

At the validation stage, the forecasted JASO streamflow (Figure 5.9a) showed a Pearson correlation (0.66). Similar results are shown by the *RMSE* and the Hanssen-Kuipers (*HK*) scores. Also, the *RMSE* of JASO streamflow prediction was acceptable (0.91 BM^3) as the Pearson correlation. The *HK* scores did exhibit promising score (0.57) as the Pearson correlation. Apparently, ANN-GA driven by the selected sectors of SST predictors in global Oceans has good predictability for the UBNB streamflow.

To improve the forecasting skill of ANN-GA, the forecasted seasonal rainfall of Chapter 4 was added as another predictor to the ANN-GA model (Figures 5.8b, and 5.9b). The combined predictors helped us in better forecasting the UBNB streamflow. The results are shown in Table 5.1 for the calibration and validation statistical test. The predicted seasonal streamflow from both cases is then disaggregated to streamflow of weekly time scale as shown in the following section.

5.6.4 Seasonal streamflow disaggregation

The observed seasonal (JASO) streamflow of the UBNB was disaggregated by the VS model (Figure 5.10, 5.11). The VS has been chosen because it was proven to be more effective in the disaggregation (Kuo et al., 2010). In terms of goodness-of-fit statistics for the forecasted streamflow, the Pearson correlation, *RMSE*, Nash-Sutcliffe (NS) and *Bias* are: 0.69, 0.04, 0.62 and 0.001; respectively. From the combined predictors run, the forecasting statistics which are: the Pearson correlation, *RMSE*, Nash-Sutcliffe (*NS*) and *Bias* are: 0.71, 0.04, 0.65 and 0.001; respectively (see Table 5.2).

5.7 Summary and Conclusions

This study investigated the predictability of the JASO weekly streamflow of UBNB using an ANN-GA statistical model driven by selected oceanic SST as predictors. We used wavelet transformed streamflow data to investigate the hydroclimatic variability of UBNB of western Ethiopia and its dynamic links with oceanic SST variability. The results of the study are summarized as follows:

1. The seasonal streamflow and global Oceans SST were wavelet transformed. It was found that the UBNB streamflow variability occurs at interannual scales of about 2-8 years;

2. From the correlation field between SAWP of JASO streamflow and SAWP of FMAM SST over the Indian, Atlantic, and Pacific Oceans, sectors where FMAM SST showing strong correlation with the UBNB JASO streamflow of ($r \geq 0.4$) were identified. For each sector, the most important SST is identified using the principal component analysis (PCA);
3. FMAM SST data in these identified sectors of the selected Oceans were used as predictors to an ANN-GA model to forecast the seasonal JASO streamflow of the UBNB at one-season lead time. The FMAM SST fields chosen were that of the Equatorial Indian Ocean (18° S- 21° N, 45° - 95° E), southern Indian Ocean (62° - 41° S, 16° - 92° E), southern Pacific Ocean (66° - 34° S, 113° - 69° W) and equatorial Pacific Ocean (7.5° - 13° S, 163° - 82° W) for the FMAM SST to forecast JASO streamflow;
4. Results show that ANN-GA gave good performance at the validation stage ($RMSE$ $0.91 BM^3$, correlation 0.66 , and HK scores 0.57). We improved the ANN-GA model performance by adding one more predictor which is the forecasted rainfall over the UBNB. Results show that the ANN-A with combined predictors gave a better performance ($RMSE$ $0.65 BM^3$, correlation 0.83 , and HK scores 0.79);
5. The Valencia-Schaake (VS) disaggregation model was used to disaggregate the seasonal streamflow to weekly streamflow. Parameters of VS was calibrated and independently validated to ensure that the disaggregated weekly streamflow data agree with the observed weekly streamflow data. Apparently, the ANN-GA model driven by the combined predictors (rainfall and SST) predicted more accurate JASO streamflow for UBNB than the ANN-GA model driven by the single SST predictors;

6. A water resources system guided by such a statistical streamflow forecast model (ANN-GA) that can predict weekly streamflow of a river basin (UBNB) at one-season lead time, especially during low flow seasons, could be crucial for an optimal allocation of water usage among various competing users.

References

- Abdi, H., and Williams, L. (2010). Principal component analysis and model evaluation. *Wiley Interdisciplinary Reviews: Computational Statistics*, 2(4), 433-459.
- Addison, P. S. (2002). *The illustrated wavelet transform handbook*. Institute of Physics Publishing.
- Amarasekera, K. N., Lee, R. F., Williams, E. R., and Eltahir, E. A. B. (1997). ENSO and the natural variability in the flow of tropical rivers. *J. Hydrol.*, 200(1-4), 24-39.
- Awadallah, A. G., and Rousselle, J. (2000). Improving forecasts of Nile flood using SST inputs in TFN model. *J. Hydrol. Eng.*, 5(4), 371-379.
- Bishop, K. (2012, July). The relationship between land use and water, water as the mirror of landscapes: How useful a hypothesis for resource management? *EOS*, 93(28), 259.
- Chow, V. T., Maidment, D. R., and Mays, L. W. (1988). *Applied hydrology*. New York: McGraw-Hill.
- Conway, D. (1997). A water balance model of the Upper Blue Nile in Ethiopia. *Hydrol. Sci. J.*, 42(2), 265-286.
- Conway, D. (2000). The climate and hydrology of the Upper Blue Nile river. *The Geographical Journal*, 166(1), 49-62.

- Degefu, W. (1987). Some aspects of meteorological drought in Ethiopia. In M. H. Glantz (Ed.), *Drought and hunger in Africa: Denying famine a future* (p. 23-36). Cambridge, England: Cambridge University Press.
- Delude, C. M. (2005, February). *Tropical seesaw: Flooded Amazon means drought in Congo* (Vol. 49) (No. 16). Retrieved from <http://web.mit.edu/newsoffice/2005/techtalk49-16.pdf> (Accessed: 05/15/2008)
- De Vos, N., and Rientjes, T. (2005). Constraints of Artificial Neural Networks for rainfall-runoff modelling: trade-offs in hydrological state representation and model evaluation. *Hydrol. Earth Syst. Sci. Discuss.*, 2(1), 365-415.
- Eldaw, A. K., Salas, J. D., and Garcia, L. A. (2003). Long-range forecasting of the Nile river flows using climatic forcing. *J. Appl. Meteorol.*, 42(7), 890-904.
- Elsanabary, M. H., and Gan, T. Y. (2012). Investigation of seasonal rainfall variability over the Ethiopian Highlands: Teleconnection between the Upper Blue Nile basin rainfall and the oceanic anomalies. *Proc. CSCE General Annual Conference, Canadian Society for Civil Engineering*. (Edmonton, Alberta, June 6-9, 2012)
- Elsanabary, M. H., Gan, Y. T., and Mwale, D. (In review). Application of wavelet empirical orthogonal function analysis to investigate the nonstationary character of Ethiopian rainfall and its teleconnection to nonstationary global sea surface temperature variations for 1900-1998. *Int.J.Climatol.*. (Submitted and under review)
- Eltahir, E. A. B. (1996). El Niño and the natural variability in the flow of the Nile river. *Water Resour. Res.*, 32(1), 131-137.

- Eltahir, E. A. B., Loux, B., Yamana, T. K., and Bomblies, A. (2004). A see-saw oscillation between the Amazon and Congo basins. *Geophys. Res. Lett.*, *31*(23), L23201.
- Gamachu, D. (1977). *Aspects of climate and water budget in Ethiopia*. Addis Ababa Univ. Press.
- Gan, T. Y., Gobena, A. K., and Wang, Q. (2007). Precipitation of southwestern Canada: Wavelet, scaling, multifractal analysis, and teleconnection to climate anomalies. *J. Geophys. Res. Atmos.*, *112*(D10), D10110.
- Gissila, T., Black, E., Grimes, D. I. F., and Slingo, J. M. (2004). Seasonal forecasting of the Ethiopian summer rains. *Int.J.Climatol.*, *24*(11), 1345-1358.
- Kloos, H., and Legesse, W. (2010). *Water resources management in Ethiopia : implications for the Nile basin*. Amherst, NY: Cambria Press.
- Kuo, C., Gan, T., and Yu, P. (2010). Seasonal streamflow prediction by a combined climate-hydrologic system for river basins of Taiwan. , *387*(3), 292-303.
- Lorenz, E. (1969). Atmospheric predictability as revealed by naturally occurring analogues. *J.Atmos.Sci.*, *26*(4), 636-646.
- Mallat, S. G. (1999). *A Wavelet tour of signal processing*. Academic Pr.
- Mwale, D. (2005). *Nonstationary and nonlinear approaches for the analysis and prediction of hydroclimatic variables in eastern and southern Africa*. PhD thesis, University of Alberta, Edmonton, Alberta, Canada.
- Mwale, D., and Gan, T. (2009). Integrating Wavelet empirical orthogonal functions and statistical disaggregation for predicting weekly runoff for the Upper Kafue basin in Zambia, Africa. *J.Hydrol.Eng.*, *15*, 822.

- Mwale, D., Gan, T. Y., Devito, K., Mendoza, C., Silins, U., and Petrone, R. (2009). Precipitation variability and its relationship to hydrologic variability in Alberta. *Hydrol. Processes*, *23*(21), 3040-3056.
- Mwale, D., Gan, T. Y., and Shen, S. S. P. (2004). A new analysis of variability and predictability of seasonal rainfall of central southern Africa for 1950-94. *Int.J.Climatol.*, *24*(12), 1509-1530.
- Quinn, W. H. (1992). A study of Southern Oscillation-related climatic activity for a.d. 622-1900. In H. F. Diaz and V. Markgraf. (Eds.), *El niño : historical and paleoclimatic aspects of the Southern Oscillation* (p. 119-149). New York, NY, USA: Cambridge University Press.
- Saji, N., Goswami, B. N., Vinayachandran, P. N., and Yamagata, T. (1999). A dipole mode in the tropical Indian Ocean. *Nature*, *401*(6751), 360-363.
- Seleshi, Y., and Demaree, G. (1995). Rainfall variability in the Ethiopian and Eritrean highlands and its links with the Southern Oscillation Index. *J.Biogeogr.*, 945-952.
- Seleshi, Y., and Zanke, U. (2004). Recent changes in rainfall and rainy days in Ethiopia. *Int.J.Climatol.*, *24*(8), 973-983.
- Shahin, M. (1985). *Hydrology of the Nile basin* (Vol. 21). Amsterdam: Elsevier.
- Sutcliffe, J., Parks, Y., and of Hydrological Sciences, I. A. (1999). *The hydrology of the Nile*. International Association of Hydrological Sciences.
- Sveinsson, O., Salas, J., Lane, W., and Frevert, D. (2007). *Stochastic analysis, modeling, and simulation (SAMS Version 2007) User's Manual*. Department of Civil and Environmental Engineering, Colorado State University, Fort Collins, Colorado.

- Torrence, C., and Compo, G. P. (1998). A practical guide to Wavelet analysis. *Bulletin of the American Meteorological Society*, 79(1), 61.
- Valencia, D., and Schaake, J. (1973). Disaggregation processes in stochastic hydrology. *Water Resour.Res.*, 9(3), 211-219.
- Wang, G., and Eltahir, E. A. B. (1999). Use of ENSO information in medium- and long-range forecasting of the Nile floods. *Journal of Climate*, 12(6), 1726-1737.
- Wilks, D. S. (2006). *Statistical methods in the atmospheric sciences*. Burlington, MA; London: Academic Press.
- Yates, D. N., and Strzepek, K. M. (1998). Modeling the Nile basin under climatic change. *J.Hydrol.Eng.*, 3(2), 98-108.

Table 5.1: Summary statistics of the forecasted seasonal streamflow during JASO season

SST	Bias	RMSE	r	HK
Calibration	2.13	0.86	0.62	0.33
Validation	-2.13	0.91	0.66	0.57
Combined				
Calibration	2.13	0.83	0.64	0.39
Validation	-2.13	0.65	0.83	0.79

Table 5.2: Summary statistics of the statistically disaggregated weekly streamflow during JASO season

	r^2	RMSE	NS	Bias
SST	0.69	0.04	0.62	0.001
Combined	0.71	0.04	0.65	0.001

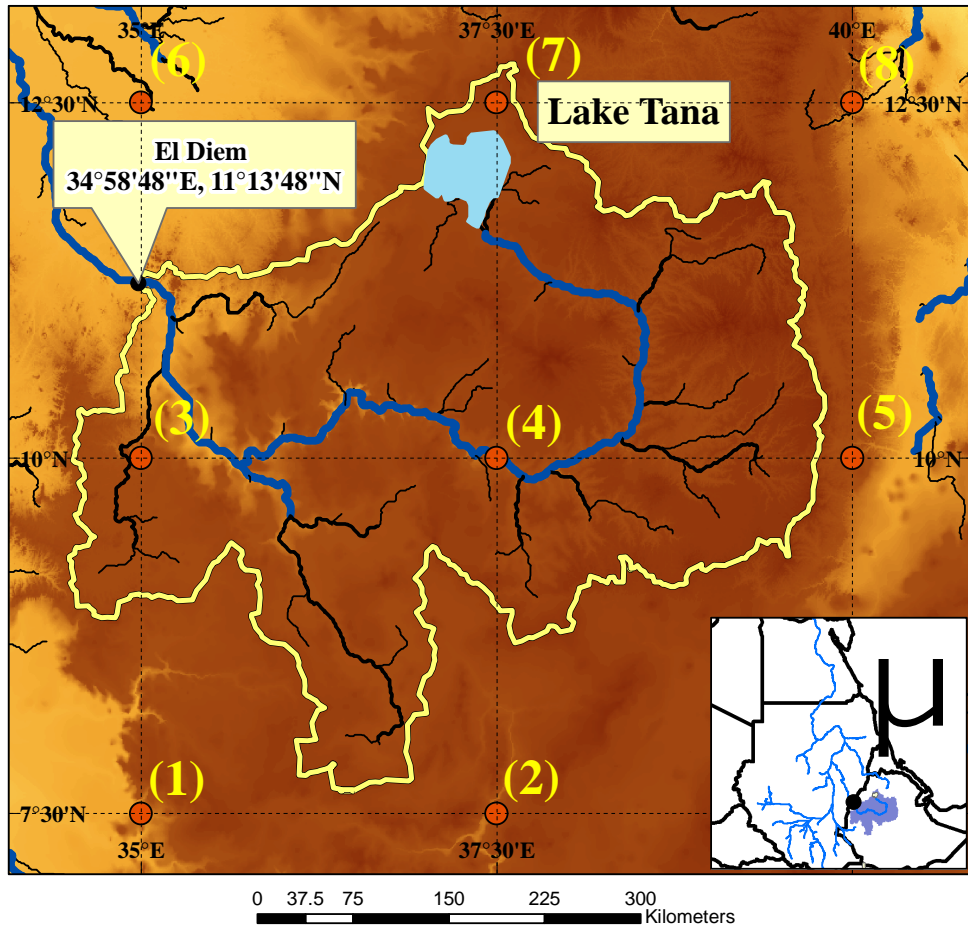


Figure 5.1: The Upper Blue Nile basin, location of the main streamflow gauge station at El Diem near to Ethiopia-Sudan boarder and the 2.5° ×2.5° grid pints from ERA-40

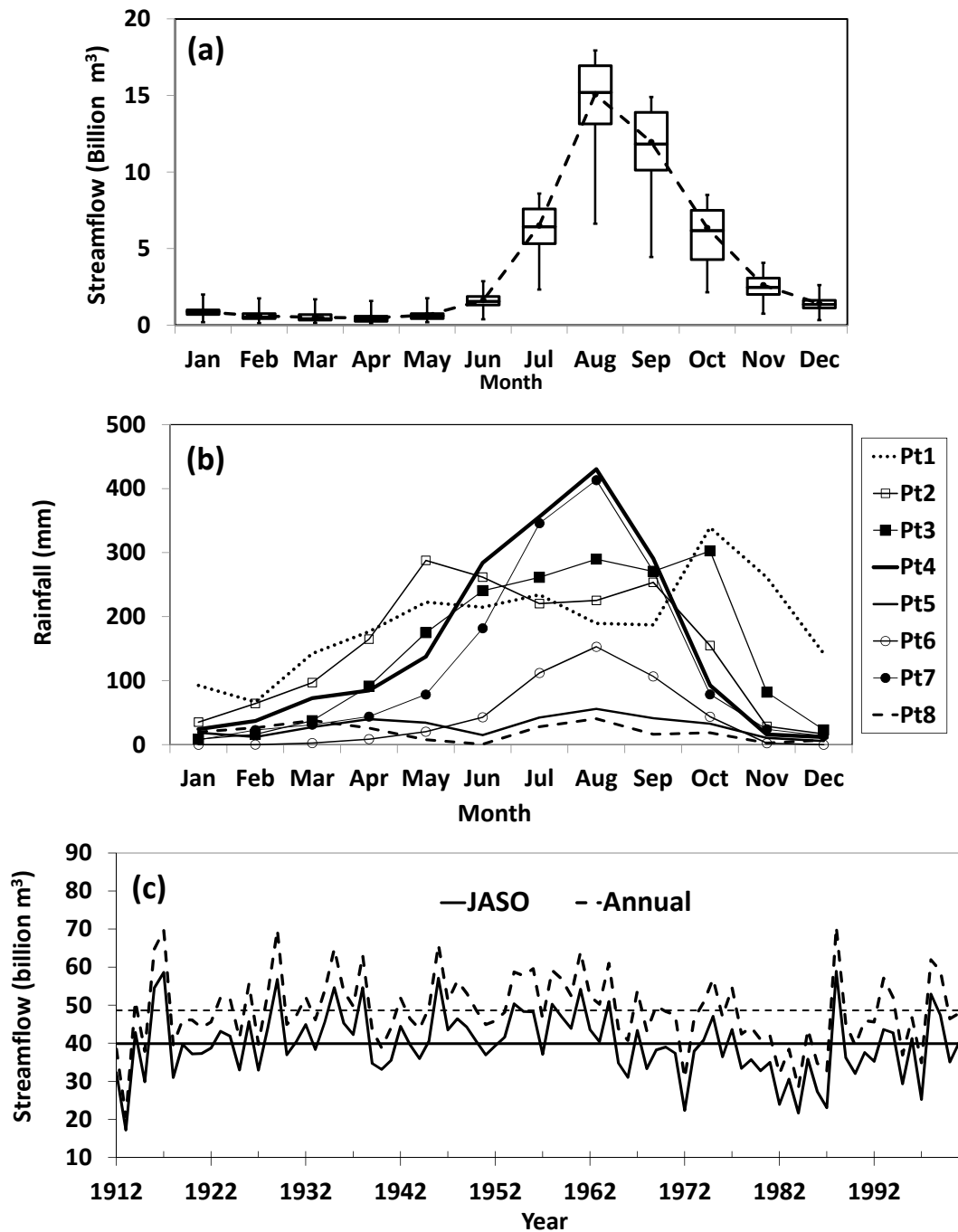


Figure 5.2: Streamflow time series at El Diem station, (1912-2001); (a) average monthly streamflow; (b) average monthly rainfall for each grid point in Figure 5.1; (c) Seasonal (annual) streamflow with solid (dashed) line and historical seasonal (annual) average solid (dashed) horizontal line.

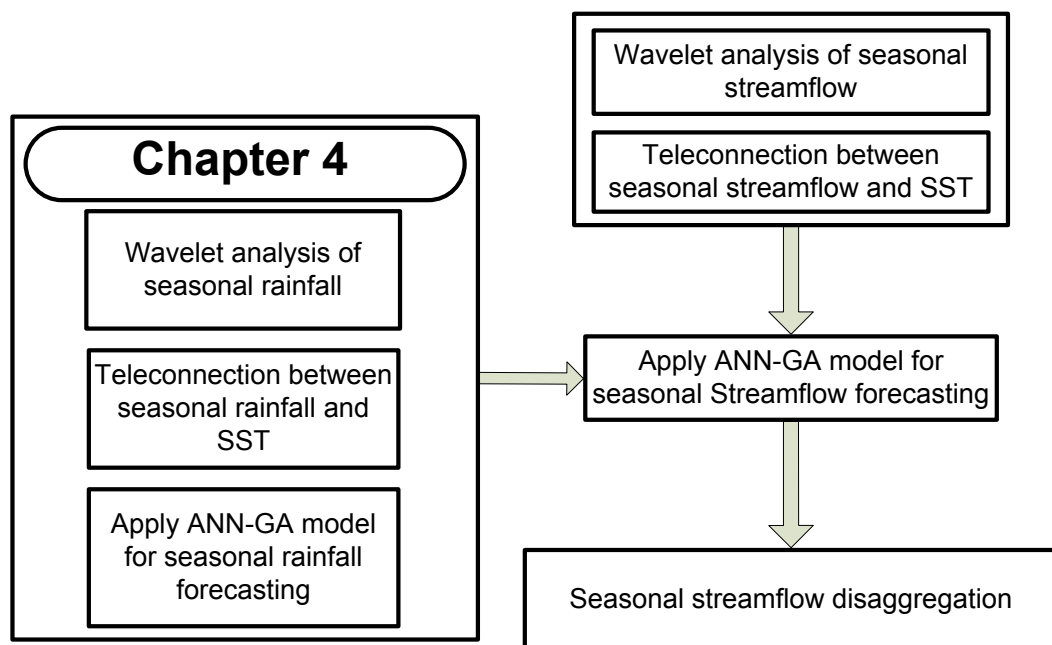


Figure 5.3: The flowchart of the study.

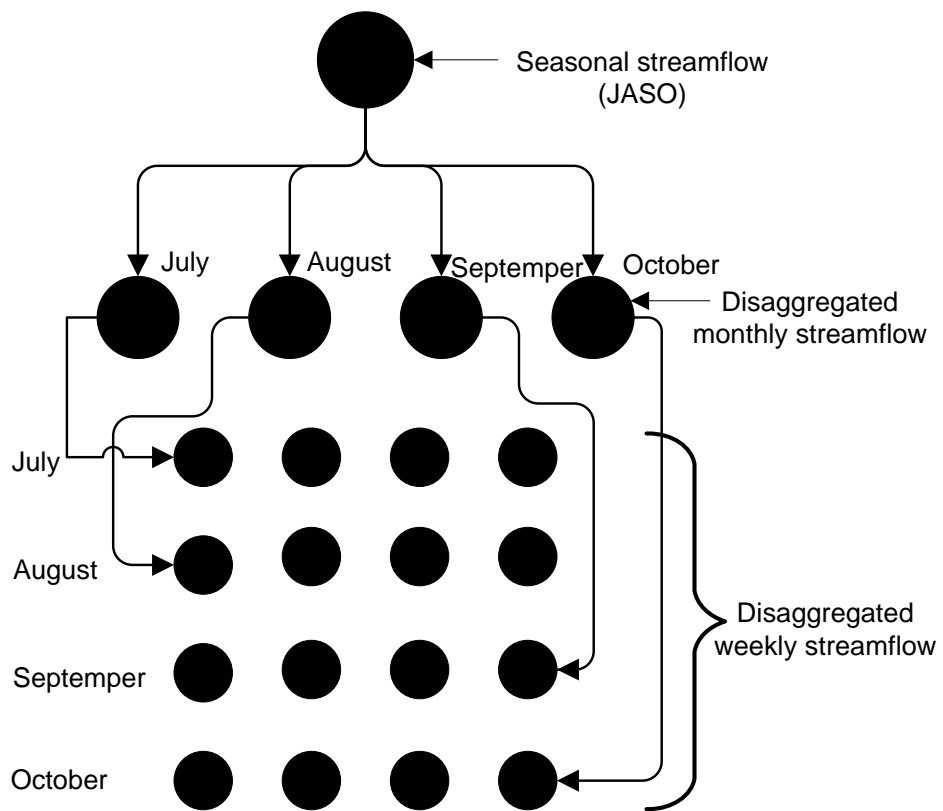


Figure 5.4: Seasonal disaggregation to weekly streamflow.

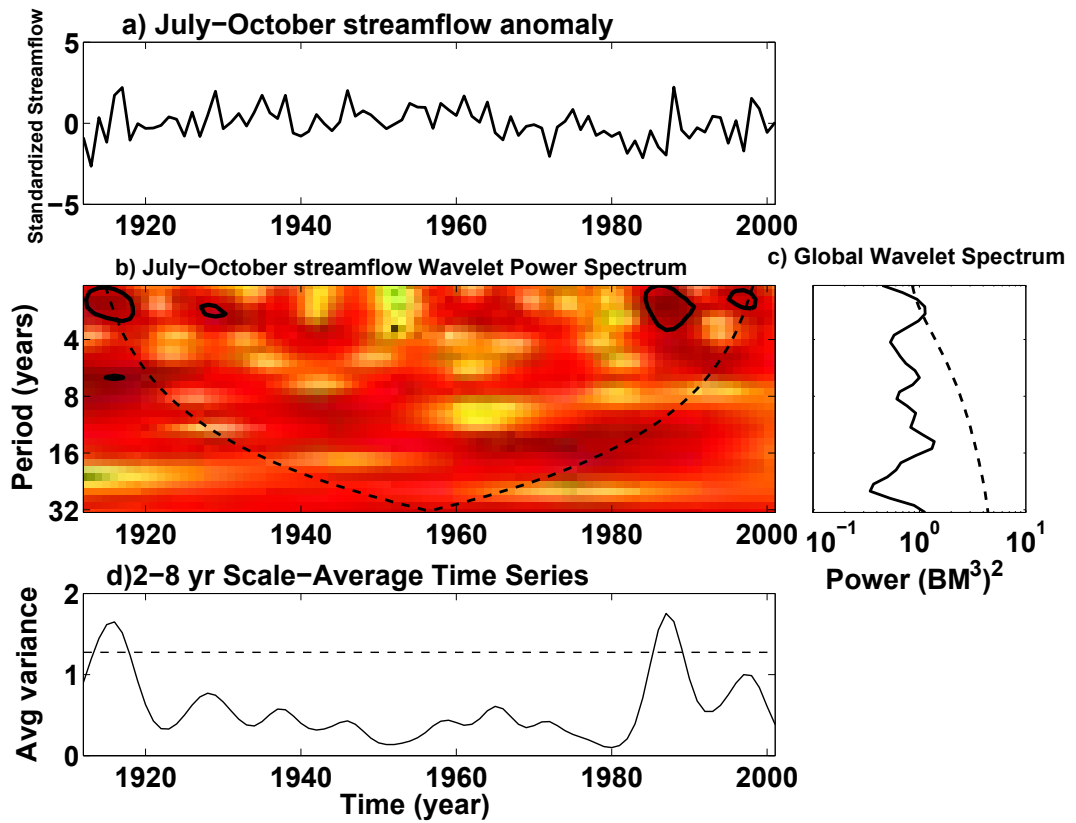
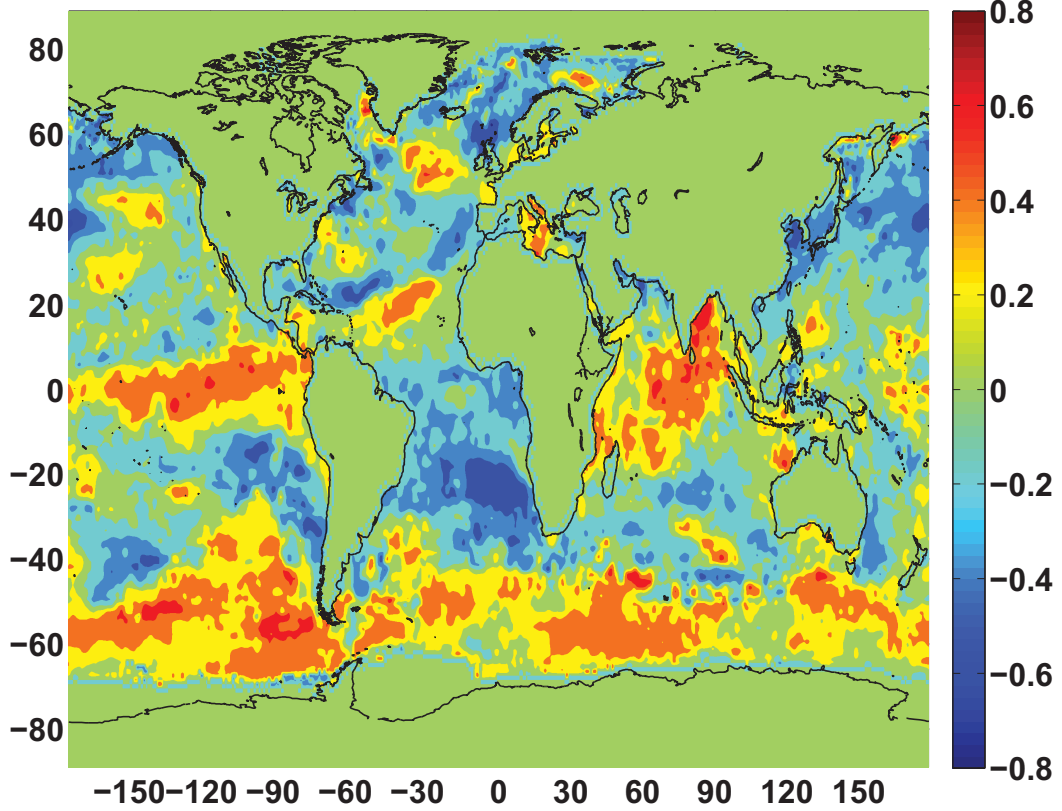


Figure 5.5: wavelet decomposition of the July-October streamflow of the UBNB. (a) Streamflow anomaly time series, (b) Wavelet power spectrum, (c) Global wavelet power spectrum. The solid lines in (b) enclose regions in the time-frequency domain where the streamflow power was statistically significant against a red-noise spectrum at the 10% level. The dashed line in (b) is the cone of influence outside which the effect of zero-padding may suppress the wavelet power. The dashed line in (c) is the 90% confidence level for the global wavelet power spectrum.

(a) JASO SAWP1-FMAM SST



(b) JASO SAWP1-JFM SST

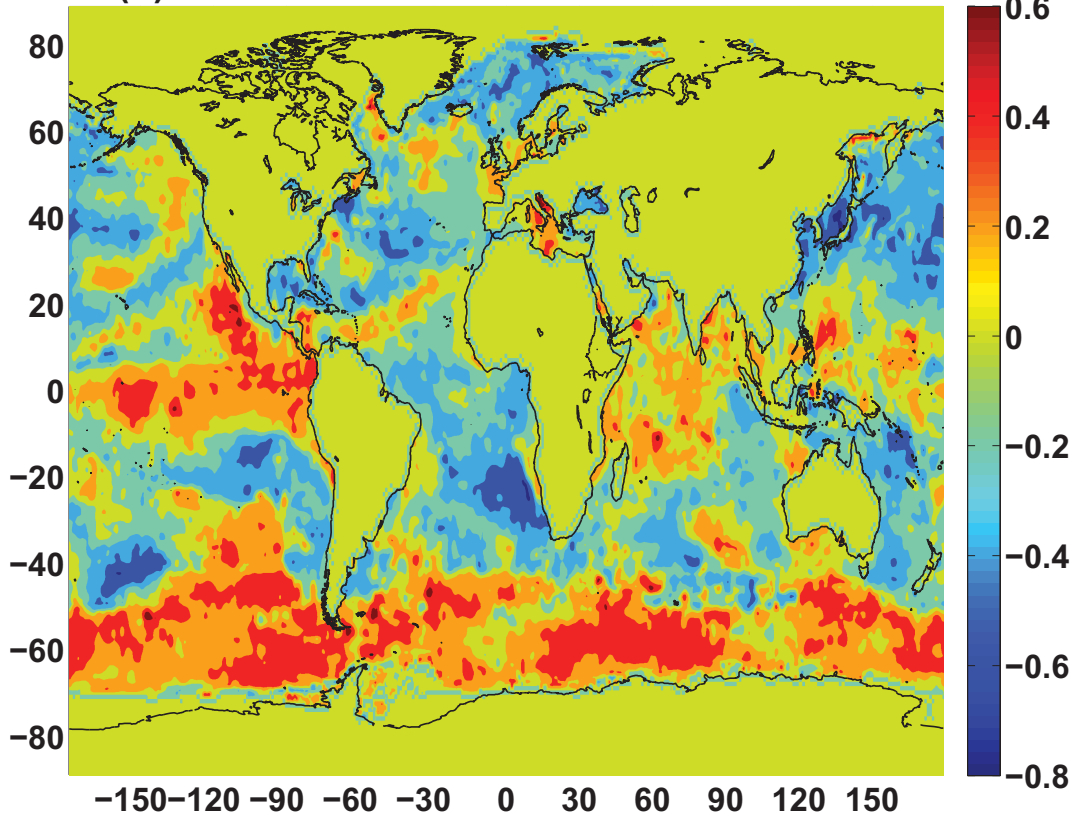


Figure 5.6: Contours of spatial correlation patterns between WPC1 of 2-8 year spectral band during JASO season of 1913-2001 and gridded SST SAWP during (a) FMAM, and (b) JFM.

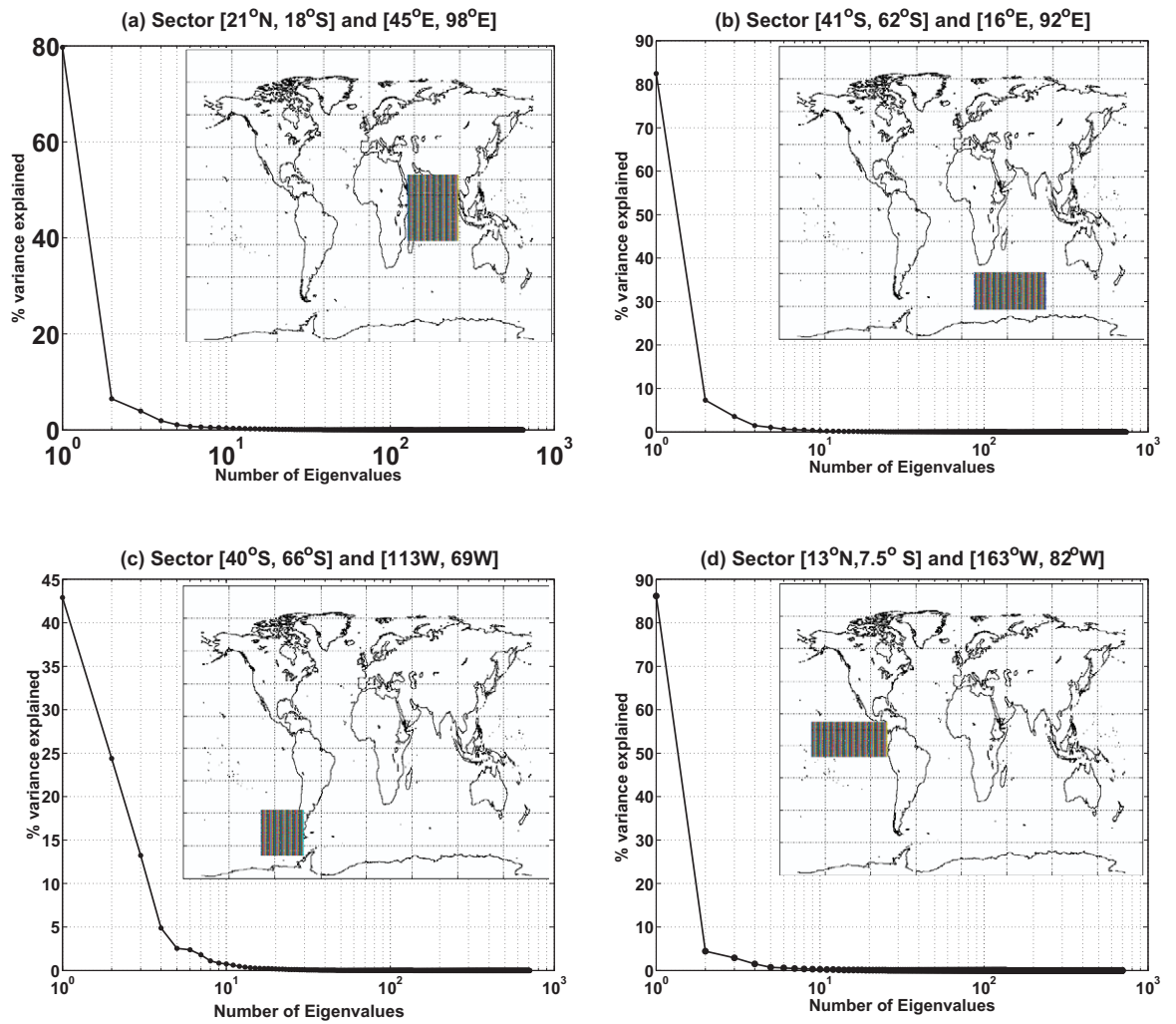


Figure 5.7: Scree plot from the principal component analysis of the four sectors from the global Oceans SST.

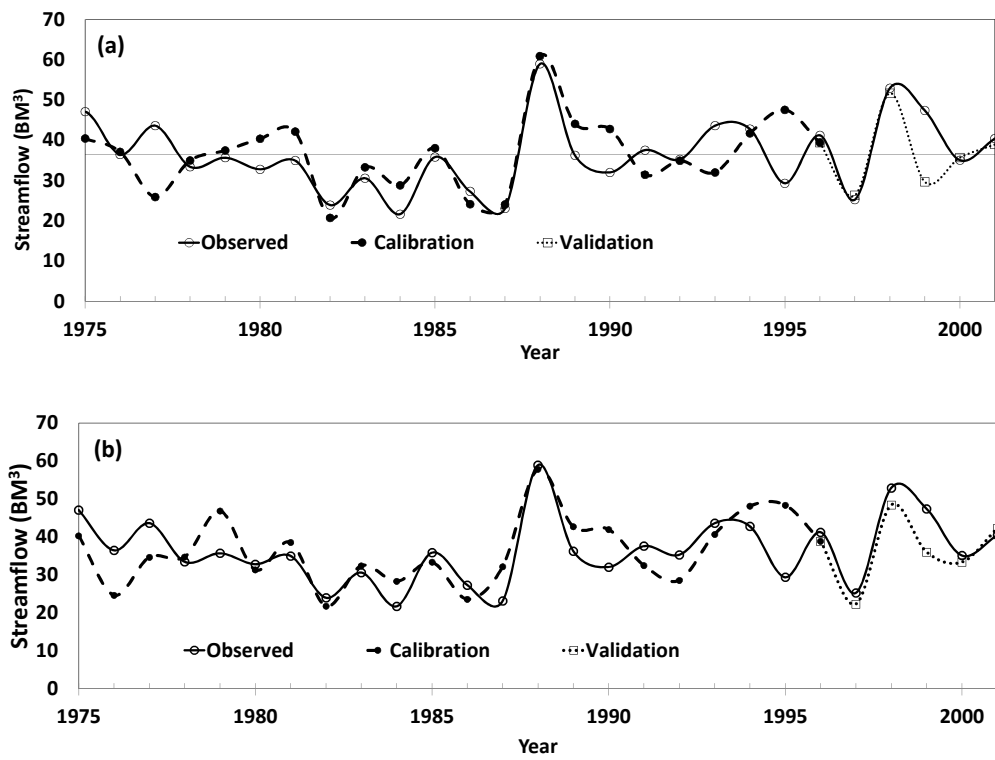


Figure 5.8: Observed and forecasted seasonal streamflow during JASO in BM^3 , a) using the SST predictors, b) using combined SST predictors and forecasted rainfall.

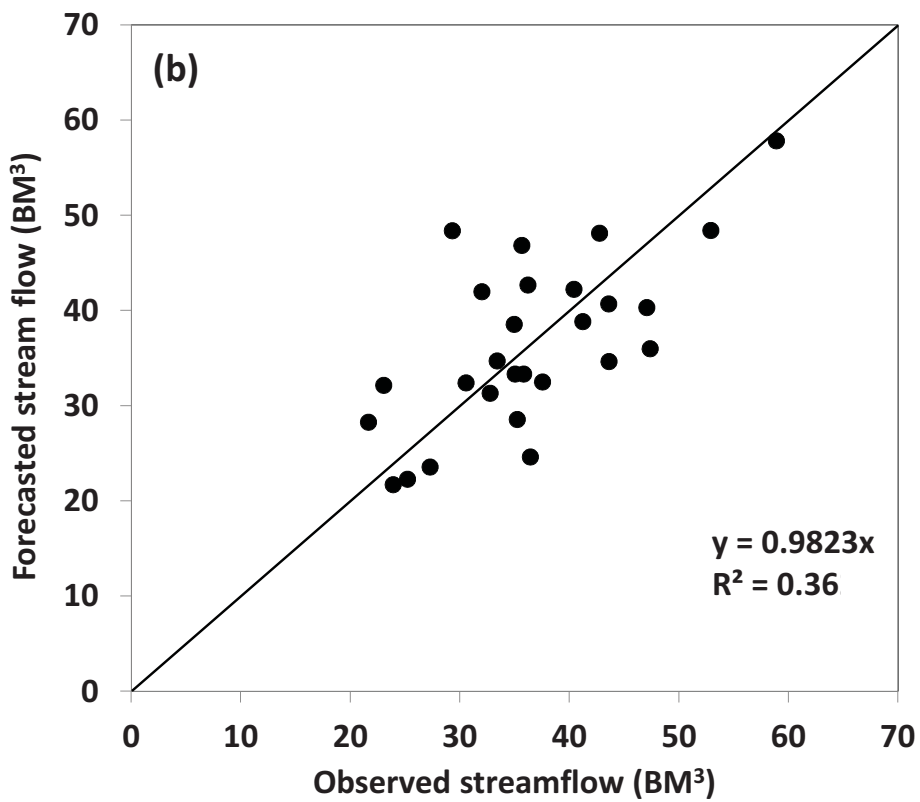
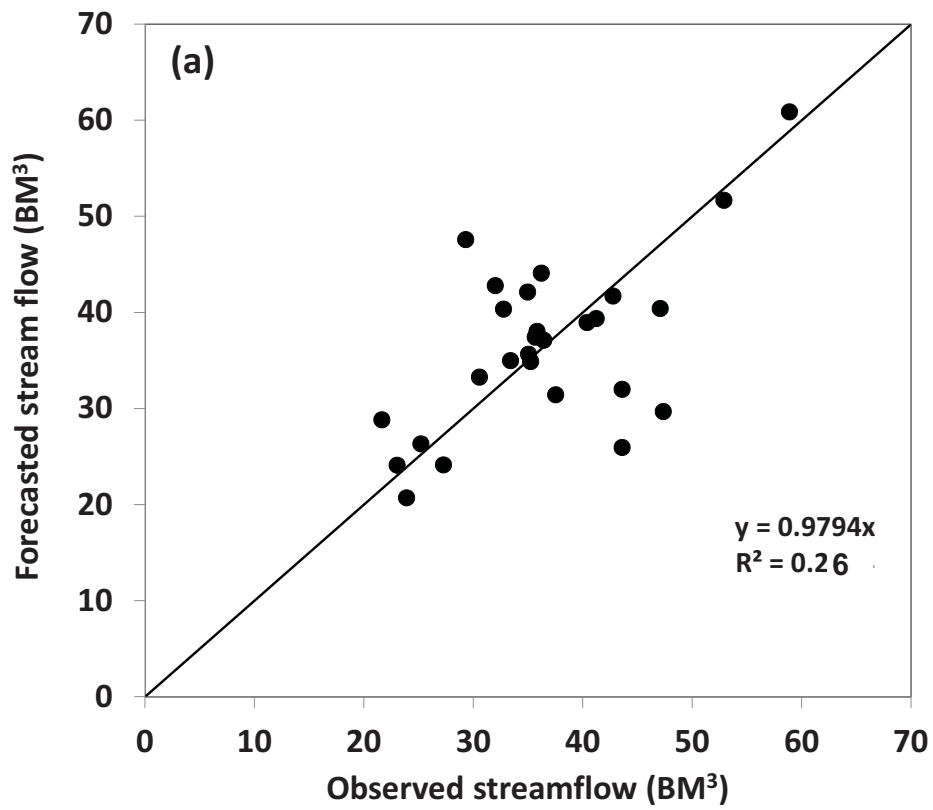


Figure 5.9: Scatter plots of Observed vs forecasted seasonal streamflow during JASO in BM^3 , a) using the SST predictors, b) using combined SST predictors and forecasted rainfall.

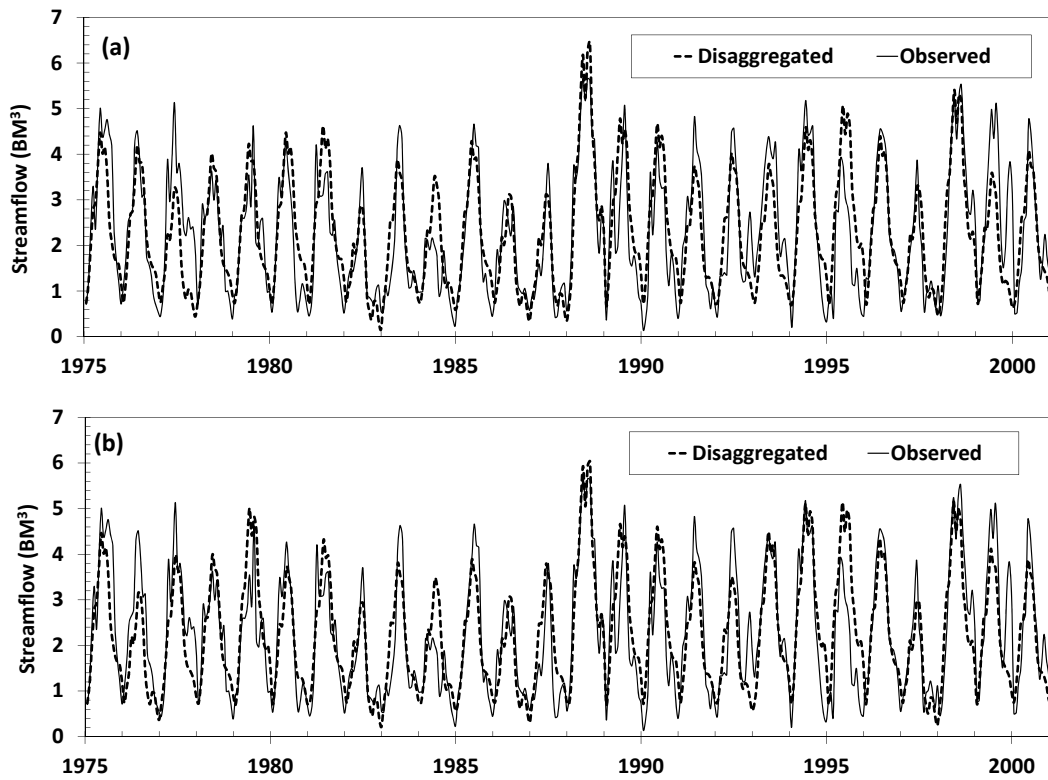


Figure 5.10: Observed and disaggregated weekly seasonal streamflow during JASO in BM^3 , a) using the SST predictors, b) using combined SST predictors and forecasted rainfall.

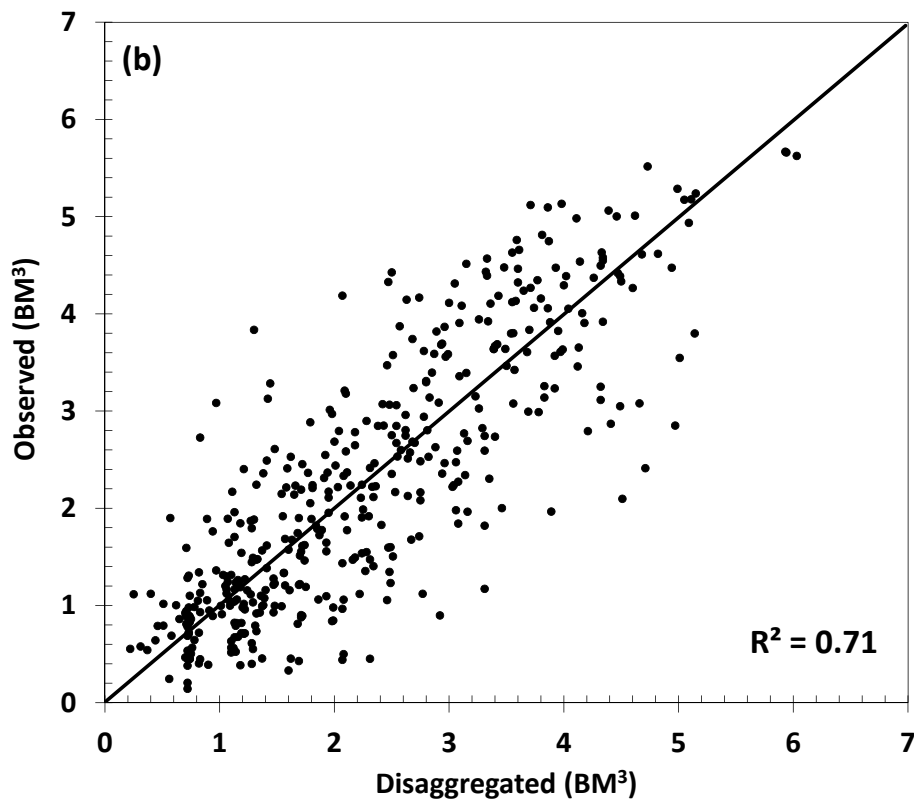
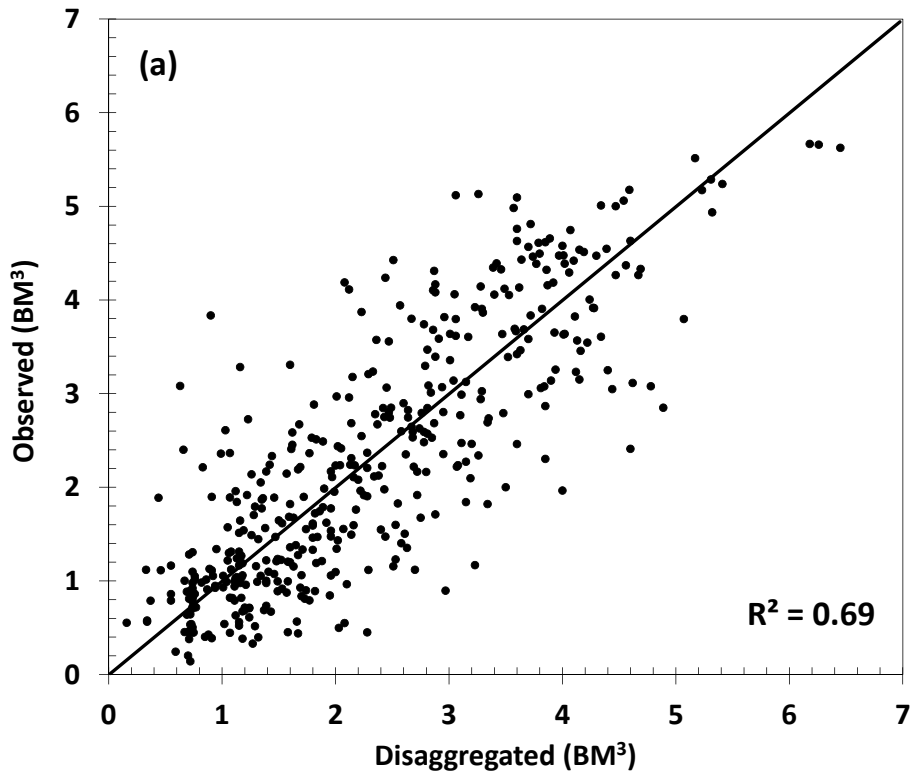


Figure 5.11: Scatter plots of Observed vs disaggregated weekly seasonal streamflow during JASO in BM^3 , a) using the SST predictors, b) using combined SST predictors and forecasted rainfall.

Chapter 6

Summary, Conclusions and Recommendations

6.1 Summary and Conclusions

Inspired by the Nile River basin and its water resources management and the effects of oceanic climate anomalies on them, the thesis conceptualized the integrated approaches of wavelet principal component analysis (WPCA), wavelet coherence, hydrological modeling, boot strap resampling technique and artificial neural network genetic algorithm (ANN-GA) model to forecast seasonal rainfall/ streamflow at weekly time steps from seasonal oceanic variability. The findings of the research are summarized in the following paragraphs.

Chapter two identified and analyzed the space-time and frequency variation of rainfall over the Ethiopian Highlands, which deliver more than 85% of the Nile flow in Egypt ([Bishop, 2012](#)), and global oceanic sea surface temperature (SST). The new findings of Chapter two are summarized below:

1. Both the June-September (JJAS) and February-May (FMAM) global SST variations espouse nonstationary characteristics. From a non-

stationary perspective, rainfall variability in Ethiopia was delineated into three zones. These are the western half of Ethiopia north of the Great Rift Valley (GRV), southern Ethiopia south of the GRV, and the GRV from the south-west to the Afar Triangle;

2. Temporal characteristics of the leading wavelet principal component signals showed Ethiopian rainfall in the doldrums for most of the century (1900-1998), with major periods of drought during the 1940s and 1980s. The temporal characteristics also showed that despite three peaks in the rainfall data (1913-1917, 1945-1955 and 1990-1998), these peaks were so irregular that Ethiopian rainfall exhibits a strong non-stationary character;
3. The dominant frequencies in the Ethiopian rainfall ranged between 2 and 8 years. In western Ethiopia north of the GRV, the 2-4 year rainfall frequencies dominated the rainfall variation within the 2-8 year frequency band, but their trends are modulated by the 5-7 year frequency band. Hence, when analyzing Ethiopian rainfall, it is necessary to simultaneously examine both the low (5-7 years) and the high (2-4 years) frequency regimes, to understand its nonstationary behavior;
4. In northeastern Ethiopia (Afar Triangle region), the 5-7 year frequencies dominate the rainfall, but the 2-4 year frequencies have limited influence in the variation of the 2-8 year frequency band. Between 1900 and 1998, northeastern Ethiopia experienced decreasing rainfall for 60 years (1900-1960), following the 5-7 year cycles of drought;
5. The non-stationary character of seasonal global SST (January-March-JFM, April-June-AMJ, July-September-JJS and October-December-OND) revealed that regardless of the time of year, the strongest global SST variations occur in the Antarctic Ocean region, the El Niño re-

gion of south America and the south western Pacific Ocean region followed by the Atlantic and the Indian oceans;

6. A comparison of leading signals in the oceans showed that increase in SST starts in the Atlantic and Indian oceans, which spread to the Antarctic Ocean, which probably contributes to the melting of Antarctic sea ice because of the large specific heat capacity of the oceans;
7. It is difficult to relate individual El Niño events to the rainfall deficits or droughts in Ethiopia.

Chapter three investigated the hydrologic modeling of the upper Blue Nile basin (UBNB) and the possible impact of climate anomalies on the water availability of the UBNB. The new findings of Chapter three are summarized below:

1. There are more discrepancies between rainfall data of ERA-40 and the gauged data before 1990 than after. In addition, partly due to the coarse resolution of GCM scale ($2.5^\circ \times 2.5^\circ$) ERA-40, the reanalysis data should be downscaled (bias correction) before it is applied to a hydrologic model;
2. The rainfall data should be corrected by a 3% reduction for the orographic effect of the mountainous terrain of UBNB;
3. The performance of MISBA applied to UBNB improved after MISBA was modified so that it could simulate evaporation loss from the canopy;
4. The performance of SAC-SMA at the calibration run and the validation run are better than that of MISBA even though it models the hydrology of UBNB in a lumped, conceptual framework as against

the physically-based, fully distributed framework of MISBA. This is because the SAC-SMA is a simple moisture accounting model while MISBA is a physically based model involving both energy and water fluxes in addition to the effects of data accuracy on the model performance;

5. ENSO warm and cold phases have variable effects on western Ethiopia (UBNB) rainfall spatially and temporally (i.e. from season to season). El Niño tends to decrease the JJAS rainfall but increase the FMAM rainfall, while La Niña has opposite effect on the UBNB rainfall;
6. In general, based on the simulations of MISBA and SAC-SMA for UBNB, La Niña and IOD tend to have wetting effects while El Niño has a drying effects on the UBNB streamflow, as found by [Eltahir \(1996\)](#). In addition, apparently ENSO and IOD increase the streamflow variability more than changing the magnitude of streamflow.

Chapter four, main objective was to accurately predict the weekly rainfall of UBNB at a seasonal lead time. The new findings of Chapter four are summarized below:

1. The SST predictors for forecasting the JJAS rainfall over UBNB were identified as: the Equatorial Indian Ocean (20°S-11° N, 61°-85° E), south Indian Ocean (59°-43°S, 34°-80° E), south Atlantic Ocean (48°-35°S, 48°-27° W), and south Pacific Ocean (41°-26°S, 112°-91° W) for the FMAM SST;
2. Results show that ANN-GA predicted seasonal rainfall that agrees well with the observed data for the highlands of UBNB, but the results at the foothills region of GRV were poor which is expected since the variability of WPC1 mainly comes from the Highlands of Ethiopia;

3. The disaggregated weekly rainfall reasonably captures the characteristics of the observed rainfall over the UBNB.

Chapter five main objective was to accurately forecast the weekly streamflow of UBNB at a seasonal lead time directly from the SST predictors. The new findings of Chapter five are summarized below:

1. The SST predictors for forecasting the JASO streamflow of UBNB were identified as: the north Equatorial Indian Ocean (18°S - 21°N , 45° - 95° E), south Indian Ocean (62° - 41° S, 16° - 92° E), south Pacific Ocean (66° - 34°S , 113° - 69° W) and equatorial Pacific Ocean (7.5° - 13° S, 163° - 82° W) for the FMAM SST;
2. The ANN-GA predicted seasonal streamflow that agreed well with the observed data for the highlands of UBNB. ANN-GA streamflow simulation can be improved by adding one more predictor which is the forecasted JJAS rainfall over the UBNB.

6.2 Recommendations

In the light of the results and conclusions reached during the course of this research, the following recommendations are made:

6.2.1 Nonlinear-Nonstationary techniques

1. Investigate the teleconnection that may exist between the UBNB and SST using a nonlinear non-stationary adaptive-empirical technique e.g. Hilbert Huang transform (needs mathematical foundations) ([Huang and Shen, 2005](#); [Cohen, 1995](#)) and the Wagner-Ville distribution method ([Cohen, 1995](#)) in combination with rotated principle components analysis or independent principal components analysis;

2. With the availability of the stable predictors for the UBNB streamflow, a further study should be conducted to investigate their potential predictability for other hydroclimatic variables, particularly the large rivers in Canada such as: Peace River, Athabasca River basin, Saskatchewan River, Churchill River, and Hayes River.

6.2.2 For Climate Variability Effects

1. Further study on the teleconnection (Seesaw) between the Nile River hydrology and the other major world rivers such as the Amazon, and the Mississippi (refer to the literature from Chapter 3 and 5);
2. For hydropower generation and operational purposes, this study should be extended to daily forecasting of the Upper Blue Nile River;
3. A study to extend the methodology developed during this research could be investigated for the other Nile River sub-basins;
4. Covering the whole Nile River basin with meteorological and hydrological gauges to have reliable data for further investigations (i.e. through cooperation between the riparian countries and the international funding agents).

6.2.3 For Better Rainfall Forecasting

1. Rainfall/streamflow forecasts could be improved by further improvement in the accuracy of local temperature and rainfall forecasts and hydrologic simulation;
2. Use remote sensing techniques to estimate rainfall in the Blue Nile region.

6.2.4 For Better streamflow Forecasting

1. Use of multiple hydrologic models in a multi-ensemble framework to reduce the effect of model structure uncertainty on the forecast skill.
2. Before going operational with the weekly seasonal streamflow forecast models proposed in this research, there is a need to evaluate the effects of climate change for the next century as well;
3. Detailed knowledge of sub-catchment characteristics and response times is required to forecast floods accurately in such a large and diverse basin.

6.2.5 General recommendations

1. Within the framework of the Nile Basin Initiative, starting from 1999, the chances that the Nile river riparian countries can benefit from trans-boundary cooperation have increased. For better river management, it is better to change from conflict to cooperation in the Nile basin, propose projects to satisfy the interests of development (e.g. the Irrigation improvement project (IIP) ([Elsanabary, 2004](#)), have ongoing discussion of legal issues to satisfy the interests of security, and establish a win-win agreement between the riparian countries to have all of them get use to the river's water;
2. Examining the availability of water resources and water use and management in the riparian countries and trying to afford new renewable water resources;
3. Politicians in the Nile Basin should consider the fact that the Nile basin residents are bound together by shared water and environmental resources. Such that the water resources for irrigation and hydroelectric power production are finite, erosion upstream effects

sedimentation of reservoirs downstream, floods and droughts are not confined by political boundaries, and water quality and pollution is a national challenge, international pollution can be avoided by early preventative action between the affected countries.

6.3 Suggestions for Future Work

Even though the systematic analysis carried out in this work has added substantial new perceptions to existing knowledge on the Nile River hydroclimatic variability, there still remain a number of issues that require further investigation. As with all techniques, there is always room for improvement. The following are some of the suggestions for future work

6.3.1 The Zero Padding (Truncation problem)

The famous problem for wavelet transformation is what is called the zero padding (truncation) problem. Since time series are limited in length, lots of zeros are added to the beginning and end of the time series to bring the length of the time series to the next high power-of-two (such as 1024), as this makes the Fourier transform (FFT) go faster. The addition of zeros conquers power computed at the two ends of the time series. Therefore, it is difficult to interpret the energy variability at the beginning and end of the time series. This difficulty might be solved by including more cosine or sine waves at the ends of the time series. Also, using a biorthogonal scaling function might help (see [Ruch and Van Fleet, 2009](#))

6.3.2 Application of WPCA to Global Scales and other Atmospheric Variables

An investigation into the effect of other climatic anomalies (e.g. the sea level pressure and the geopotential heights) on regional climate variability

will be helpful to provide a complete picture of climate systems at play in the Nile river sub-basins.

6.3.3 Seasonal forecasting

Regarding statistical seasonal rainfall/streamflow forecasting, a comparison of the ANN-GA model with other statistical forecasting methods such as local regression and kernel based approaches is useful. A multi-model ensemble strategy could be tried to explore the strength of each modeling approach.

6.3.4 Climate change effects

Next adjust the ensemble members with downscaled climate scenarios of multi-models (several) GCMs over three 30-year periods (2010-2039, 2040-2069, 2070-2100), and apply the adjusted ensemble members to the calibrated MISBA to simulate potential hydrologic impact of climate change to UBNB, White Nile Basin (WNB) and Victoria Lake Basin (VLB) under the simultaneous influence of climate anomalies. Comparing the above simulated streamflow of the ensemble members adjusted for climate change with that of non-adjusted ensemble members, we can examine the impact of climate change when certain climate anomalies have been active.

References

- Bishop, K. (2012, July). The relationship between land use and water, water as the mirror of landscapes: How useful a hypothesis for resource management? *EOS*, 93(28), 259.
- Cohen, L. (1995). *Time frequency analysis*. Englewood: Prentice Hall.

- Elsanabary, M. H. M. M. (2004). *Application of construction management in irrigation projects utilizing Value Engineering techniques*. Master's thesis, Department of Civil engineering, Faculty of Engineering, Suez Canal University, Port Said, Egypt.
- Eltahir, E. A. B. (1996). El Niño and the natural variability in the flow of the Nile river. *Water Resour. Res.*, 32(1), 131-137.
- Huang, N., and Shen, S. S. (Eds.). (2005). *Hilbert-Huang transform and its applications* (Vol. 5). Singapore: World Scientific.
- Ruch, D. K., and Van Fleet, P. J. (2009). *Wavelet theory: an elementary approach with applications*. Hoboken: John Wiley and Sons.

CURRICULUM VITAE – MOHAMED HELMY ELSANABARY

PERSONAL INFORMATION

Mohamed Helmy Elsanabary, PhD, Prov. Lic.
Eng. APEGA, AMASCE
W: 1-023 P. Markin/ CNRL NREF Building
Department of Civil and Environmental Engineering
University of Alberta
Edmonton, AB, Canada, T6G 2W2
tel: +1 7809662974
mohamed.elsanabary@ualberta.ca
[homepage](http://www.ualberta.ca/~elsanaba): <http://www.ualberta.ca/~elsanaba>



H: Faculty of Engineering
Civil Engineering Department
Port Said University
Port Fouad, Port Said, Egypt, 42523
tel: +2 01011125126
mohamed_elsanabary@p-eng.suez.edu.eg
[homepage](http://staff.psu.edu.eg/mhelsanabary): <http://staff.psu.edu.eg/mhelsanabary>

Mohamed Helmy Elsanabary was born on 29th September, 1974 in Port Said, Egypt. He received his Bachelor of civil Engineering with honor degree from Suez Canal University in 1997. After graduation, he worked in the Civil Engineering Department, of Suez Canal University as a demonstrator. In 2004, he received a Master of Science in Civil Engineering (Construction management). From 2004 to August 2006, he worked as lecturer assistance in the same department. In 2006 he was given a governmental scholarship from the Egyptian government to study at the Department of Civil and Environmental Engineering of the University of Alberta from which he received his Ph.D. in 2012.

EDUCATION

Ph.D. degree in Water Resources Engineering from the University of Alberta (2006 – 2012). Thesis advisor: Thian Yew Gan. Thesis title: *Teleconnection, Modeling, Climate Anomalies Impact and Forecasting of Rainfall and Streamflow of the Upper Blue Nile River Basin*. Studing the rainfall/ streamflow variability and teleconnection over the Ethiopian Highlands and the Upper Blue Nile hydrology.

MSc. in Civil Engineering from the Suez Canal University (2000 – 2004). Thesis advisor: Mohamed Ibrahim Balah. Thesis title: "Application of Construction Management in Irrigation Projects Utilizing Value Engineering techniques"

BSc. in Civil Engineering from the Suez Canal University (1992 – 1997). (Third rank over all, Very Good with honor Degree). Graduation project was on structural analysis and design of Concrete and Steel buildings (Excellent)

PROFESSIONAL EMPLOYMENT

2010 March → Present Professional Tutor with Northern Alberta Institute of Technology (NAIT)

2011 June → **Present** Professional Tutor with the University of Alberta

2010 July → **2011 November** Civil Engineering instructor with Global Innovative Campus (GIC)

2007 January → **2012 May** Teaching Assistant at the University of Alberta for: Principles of Environmental Modelling and Risk (CIVE 321), Plane Surveying (CIVE 250), Engineering Statics (ENGG 130), Engineering Drawing and Computer Graphics (CIVE 265) and Survey School (CIVE 251).

2006 September → **2007 August** Research Assistant at the University of Alberta, collecting data from meteorological station and snow surveying for the Paddle River basin, Alberta

COURSES TAKEN

2006 September → **2007 December** ENGINEERING FLUID MECHANICS, NUMERICAL METHODS HYDRAULICS, EXPERIMENTAL FLUID MECHANICS, HYDRAULIC STRUCTS, ADV REMOTE SENSING: APPL ALG, ADV DIGITAL REMOTE SENSING, ENGINEERING ETHICS INTEGRITY, and ADV SURFACE WATER HYDROLOGY

HONORS AND AWARDS

2012 June Best Poster Presentation Prize from Third Annual Graduate Research Symposium.

2012 May Professional Development Grant from the University of Alberta Graduate Students Association

2012 March Poster competition award, first place over all, Canadian Society for Civil Engineering (CSCE) poster competition, University of Alberta.

2011 April Professional Development Grant from the University of Alberta Graduate Students Association

2011 April First Place Best Poster award, The 1st Graduate Residence Student Conference.

2011 March Poster competition award, second place over all, Canadian Society for Civil Engineering (CSCE) poster competition, University of Alberta.

2011 February → Mary Louise Imrie Graduate Student Award, University of Alberta

2011 May Most Positive Influence Award by a Community Member, University of Alberta Residence Services

2006 September → **2010 September** Egyptian government scholarship for graduate studies

2006 September → **2007 April** University of Alberta, Graduate Assistantship

2006 March Egyptian Syndicate of Engineers prize for the Graduate students

2005 April Faculty prize for the Graduate students, Suez Canal University, Egypt

1998 May Faculty prize for the highest ranked students, Suez Canal University, Egypt
